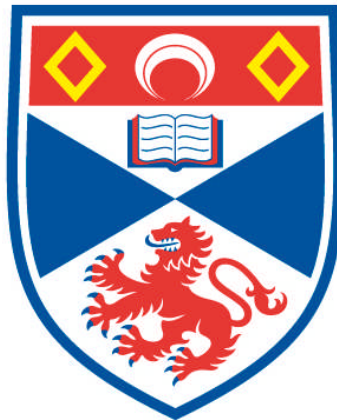


**INVESTIGATION OF INORGANIC POROUS SOLIDS AS
ADSORBENTS FOR THE SEPARATION OF CARBON
DIOXIDE FROM FLUE GAS**

Magdalena Malgorzata Lozinska

**A Thesis Submitted for the Degree of PhD
at the
University of St Andrews**



2013

**Full metadata for this item is available in
Research@StAndrews:FullText
at:**

<http://research-repository.st-andrews.ac.uk/>

Please use this identifier to cite or link to this item:

<http://hdl.handle.net/10023/3964>

This item is protected by original copyright

*Investigation of Inorganic Porous Solids
as Adsorbents for the Separation
of Carbon Dioxide from Flue Gas*

A thesis presented for the degree of
Doctor of Philosophy

in the Faculty of Science of the University of St Andrews
by *Magdalena Malgorzata Lozinska, MSc*

July 2013

Supervisor: Prof. Paul A. Wright



University of
St Andrews

Declarations

1. I, Magdalena Malgorzata Lozinska, hereby certify that this thesis, which is approximately 50 000 words in length, has been written by me, that it is the record of work carried out by me and that it has not been submitted in any previous application for a higher degree.

I was admitted as a research student in October 2009 and as a candidate for the degree of PhD in October 2010; the higher study for which this is a record was carried out in the University of St Andrews between 2009 and 2013.

Date..... Signature of Candidate.....

2. I hereby certify that the candidate has fulfilled the conditions of the Resolution and Regulations appropriate for the degree of PhD in the University of St Andrews and that the candidate is qualified to submit this thesis in application for that degree.

Date..... Signature of Supervisor.....

3. In submitting this thesis to the University of St Andrews I understand that I am giving permission for it to be made available for use in accordance with the regulations of the University Library for the time being in force, subject to any copyright vested in the work not being affected thereby. I also understand that the title and the abstract will be published, and that a copy of the work may be made and supplied to any bona fide library or research worker, that my thesis will be electronically accessible for personal or research use unless exempt by award of an embargo as requested below, and that the library has the right to migrate my thesis into new electronic forms as required to ensure continued access to the thesis. I have requested the appropriate embargo below. The following is an agreed request by candidate and supervisor regarding the electronic publication of this thesis:

Embargo on all of printed copy and electronic copy for the same fixed period of one year on the following ground: publication would preclude future publication.

Date Signature of Candidate

Signature of Supervisor

Acknowledgements

I owe a great many thanks to a great many people who helped and supported me during my PhD study.

First and foremost, I would like to thank my supervisor Prof. Paul A. Wright for giving me opportunity to work in his group, for his attention and time, and for sharing his knowledge, his ideas, and numerous tips all of which culminated in the completion of this PhD study.

I would like to express my gratitude for the numerous stimulating discussions, help with experimental setups and general advice provided by John Mowat.

My thanks and appreciations go to present and past PAW group members: Jürgen Kahr, Berenice Gonzalez, Laura Mitchell, Michael Wharmby, Lorena Picone, Alessandro Turrina and Alex Greenaway for their help, useful suggestions and wishes for the successful completion of this work.

I am grateful to many of the technical and scientific staff of the University of St Andrews, particularly Mrs. Sylvia Williamson for training in the use of equipment and collecting adsorption data.

I would like to thank the following people from outside of the University of St Andrews for their help and assistance with the collection of my data: Enzo Mangano and Prof. Stefano Brandani (ZLC method), Ashley Shepherd and Prof. Russell Howe (IR spectroscopy), Eric Masika and Prof. Robert Mokaya (nitridation), Miguel Palomino and Prof. Fernando Ray (CO₂ and CH₄ high pressure adsorption and selectivity), Dr. David Apperley (NMR service) and the EPSRC for financial support.

I also want to thank David who encouraged, supported and helped me in every trial that came my way during my PhD.

Last but not least, I wish to express my love and gratitude to my beloved family, my mother, father, brother and grandparents, for their understanding, support and endless love when it was most required.

*This thesis is dedicated to my grandmothers,
Janina and Zuzanna*

Abstract

Porous inorganic solids including mesoporous silicas, zeolites and silicoaluminophosphates have been investigated as adsorbents for carbon dioxide, particularly in relation to uptake from flue gases at 0.1 bar and *ca.* 298 K, but also at higher pressures.

The mesoporous silicas SBA-1 and SBA-2, with mesocages separated by narrower windows, have been prepared, calcined at various temperatures and also nitrated with ammonia at high temperature. Nitridation has resulted in framework nitrogen incorporation, but this gave only small increases in the uptake of CO₂ of these mesoporous silicas, which are very low (< 0.2 mmol g⁻¹) at flue gas conditions (0.1 bar, 298 K).

A series of cationic forms of the small pore zeolites, chabazite, ZK-5 and Rho, have been prepared by exhaustive cation exchange (and pre-calcination of the as-prepared form of Rho). In addition, a series of ultrastabilised zeolite Rho samples has been prepared to investigate the influence of extra-framework aluminium species on CO₂ uptake. For comparison, the silicoaluminophosphate versions of ZK-5 (SAPO STA-14) and Rho (SAPO(RHO)) have been prepared.

Adsorption on Li-, Na-, K- and Ca-forms of chabazite (Si/Al = 3.0) has been related to the crystal structures of their dehydrated forms, as determined by Rietveld refinement against powder X-ray diffraction data (PXRD). For Na- and K-chabazite the structure has been measured *in situ* by PXRD during CO₂ adsorption. Li-chabazite has the highest uptake from all chabazite cationic forms (4.3 mmol g⁻¹). PXRD of K-chabazite reveals cation migration from eight-membered ring sites to six-membered ring sites upon CO₂ adsorption. Na-chabazite shows partial transformation from rhombohedral to monoclinic symmetry upon prolonged evacuation at high temperature, with resultant non-Type I CO₂ adsorption behaviour.

Li-, Na- and K-forms of ZK-5 (Si/Al = 4.16) show high CO₂ uptakes at 0.1 bar and 298 K (Li-ZK-5, 4.7 mmol g⁻¹, which is the highest of the solids measured here). Like all H-forms, H-ZK-5 shows weaker uptake. None of the ZK-5 forms show high

selectivity for CO₂ over small hydrocarbons, because cations do not block eight-membered ring windows and the structures do not distort upon dehydration.

Uptake of CO₂ on univalent cation forms of zeolite Rho has been studied at low (up to 1 bar) and high (up to 10 bar) pressures. All cationic forms (but not H-Rho) show distortion ($Im\bar{3}m$ to $I\bar{4}3m$) upon dehydration. Forms of zeolite Rho in which cations occupy window sites in the eight-membered rings between α -cages show hysteresis in their CO₂ isotherms, the magnitude of which ($Na^+, NH_4^+ < K^+ < Cs^+$) correlates with the tendency of cations to occupy double eight-membered ring sites rather than single eight-membered ring sites. Additionally, reversible CO₂ uptake using the Zero Length Column method on fully and partially cation exchanged samples has been measured.

In situ synchrotron PXRD of CO₂ adsorption on Na-Rho indicates Na cations remain in window sites on the time average, indicating CO₂ uptake must occur by a 'trapdoor mechanism' by which Na cations move away from the windows to allow CO₂ to adsorb. In addition, *in situ* PXRD reveals the adsorption sites of CO₂ bound cations. Adsorption of small hydrocarbons does not occur on Rho, even at high pressure, indicating that adsorption is selective, and depends on the degree of interaction with the adsorbate rather than simply on the molecular size.

Na-Rho is therefore a selective adsorbent for CO₂ over CH₄ with selectivities of 150–25 at 1–9 bar and 298 K, predicted from the single component isotherms, and an uptake of 3.07 mmol g⁻¹ at 0.1 bar. High 'selectivities' are also observed over K-, Cs- and Ca-forms, examples of a novel type of adsorption selectivity.

Publications arising from this work

1. Wright P. A., Lozinska M. M.
Zeolites and ordered porous solids: Fundamentals and applications. Chapter 1: Structural chemistry and properties of zeolites,
3rd FEZA School on Zeolites, Editorial Universitat Politècnica de València, **2011**
<http://riunet.upv.es/handle/10251/11205>
2. Lozinska M. M., Mangano E., Mowat J. P. S., Shepherd A. M., Howe R. F., Thompson S. P., Parker J. E., Brandani S., Wright P. A.
Understanding carbon dioxide adsorption on univalent cation forms of the flexible zeolite Rho at conditions relevant to carbon capture from flue gases,
J. Am. Chem. Soc., **2012**, 134, 17628–17642, DOI: 10.1021/ja3070864

Information presented in this thesis has been published and has been adapted with permission from above authors. Copyright 2012, American Chemical Society.

3. Ferreiro-Rangel C. A., Lozinska M. M., Wright P. A., Seaton N. A., Düren T.
Kinetic Monte Carlo simulation of the synthesis of periodic mesoporous silicas SBA-2 and STAC-1: Generation of realistic atomistic models,
J. Phys. Chem. C, **2012**, 116, 20966–20974, DOI: 10.1021/jp307610a

Information presented in this thesis has been published and has been adapted with permission from above authors. Copyright 2012, American Chemical Society.

In preparation

4. Perez-Mendoza M., Ferreiro-Rangel C. A., Fairen-Jimenez D., Gonzalez J., Lozinska M. M., Seaton N. A., Düren T., Wright P. A.
Pore structure of the mesoporous structure SBA-2 and its modification for size selective separation of gases.
5. Lozinska M. M., Mowat J. P. S., Hu X., Brandani S., Palomino M., Jorda J. L., Valencia S., Rey F., Wright P. A.
Cation gating and selective carbon dioxide adsorption in flexible zeolite Rho.

Abbreviations

Abbreviation	Explanation
18-crown-6	1,4,7,10,13,16-hexaoxacyclooctadecane
2CLJQ	two-centre Lennard-Jones Quadrupoles
<i>a</i>	unit cell parameter
AAS	atomic absorption spectroscopy
AlPO	aluminophosphate
a.u.	arbitrary units
<i>b</i>	unit cell parameter
BET	Brunauer-Emmett-Teller theory
BJH	Barret-Joyner-Halenda theory
BOC	British Oxygen Company
<i>c</i>	unit cell parameter
C16-3-1	N-(3-trimethylammoniumpropyl)hexadecylammonium dibromide
<i>ca.</i>	approximately (latin: circa)
CCD	charge coupled device
CCS	carbon capture and storage
CHNX	carbon, hydrogen, nitrogen and heteroatoms analysis
CRT	cathode ray tube
CTAB	cetyltrimethylammonium bromide
CTEABr	cetyltriethylammonium bromide
D6R	double six-membered ring
D8R	double eight-membered ring
DEA	diethylamine
DTGS	deuterated triglycine sulfate
EDX	electron dispersive X-ray analysis
EFAL	extra-framework aluminium
EM	electron microscopy
<i>et al.</i>	and others (latin: et alii)
FEG	field emission gun
FT	Fourier transformation
FTC	framework type code
GC	gas chromatography
GSAS	General Structure Analysis System
HRTEM	high resolution transmission electron microscopy
ICDD	International Centre for Diffraction Data
IGA	intelligent gravimetric analysis
IR	infra-red spectroscopy
IUPAC	International Union of Pure and Applied Chemistry
IZA	International Zeolite Association
K222	4,7,13,16,21,24-hexaoxa-1,10-diazabicyclo[8.8.8]hexacosane
kMC	kinetic Monte Carlo method
MAS	magic angle spinning
MCM	Mobil Composition of Matter
MOF	metal organic framework
MQ	multiple-quantum
NMR	nuclear magnetic resonance
NSBA	nitrided Santa Barbara materials

PEI	polyethylenimine
PET	polyethylene
PMS	periodic mesoporous silica
PTFE	polytetrafluoroethylene
PXRD	powder X-ray diffraction
S4R	single four-membered ring
S6R	single six-membered ring
S8R	single eight-membered ring
SAPO	silicoaluminophosphate
SBA	Santa Barbara materials
SBU	secondary building unit
SEM	scanning electron microscopy
SFC	supercritical fluid chromatography
ST1	first set of steamed samples
ST2	second set of steamed samples
STA	St Andrews materials
TEA ⁺	tetraethylamine cation
TEAOH	tetraethylammonium hydroxide
TEOS	tetraethylorthosilicate
TEPA	tetraethylenepentamine
TGA	thermogravimetric analysis
TMAOH	tetramethylammonium hydroxide
US	ultra-stable
wt%	weight percent
ZLC	Zero Length Column method

Reagents used in this work

Reagent	Purity /%	Supplier
1,4,7,10,13,16-hexaoxacyclooctadecane (C ₁₂ H ₂₄ O ₆ ; 18-crown-6)	≥ 99	Sigma-Aldrich
1-bromohexadecane (C ₁₆ H ₃₃ Br)	97	Sigma-Aldrich
4,7,13,16,21,24-hexaoxa-1,10-diazabicyclo- [8.8.8]-hexacosane (K222; C ₁₈ H ₃₆ N ₂ O ₆)	97	ABCR
Acetone (C ₃ H ₆ O)	≥ 99.5	Sigma-Aldrich
Ammonium chloride (NH ₄ Cl)	99.9	Alfa Aesar
Aluminium isopropoxide (C ₉ H ₂₁ O ₃ Al)	≥ 98	Sigma-Aldrich
Cesium hydroxide (CsOH)	99.9	Sigma-Aldrich
Cetyltriethylammonium bromide (C ₂₂ H ₄₈ NBr; CTEABr)	–	PAW group
Diethylamine (C ₄ H ₁₁ N; DEA)	≥ 99.5	Sigma-Aldrich
Fumed silica (SiO ₂)	97	Fluka
Hexadecyltrimethylammonium bromide (C ₁₉ H ₄₂ NBr; CTAB)	≥ 99	Sigma-Aldrich
Metal (Ca, K, Li, Na) chlorides	99.5–99.9	Sigma-Aldrich
Metal (Ca, Cs, K, Li, Na) nitrates	99.5–99.9	Sigma-Aldrich
N-(3-trimethyl-ammoniumpropyl) hexadecylammonium dibromide (C16-3-1)	–	PAW group
Na-Y zeolite	–	Crosfield
Potassium hydroxide (KOH)	98.5	Fisher Chemicals
Sodium acetate (CH ₃ COONa)	99	Sigma-Aldrich
Sodium hydroxide (NaOH)	98.5	Fisher Chemicals
Strontium nitrate (Sr(NO ₃) ₂)	99.5	AnalaR
Tetraethyl orthosilicate (C ₈ H ₂₀ O ₄ Si, TEOS)	98	Sigma-Aldrich
Tetramethylammonium hydroxide (C ₄ H ₁₃ NO; TMAOH)	≥ 97	Sigma-Aldrich
Triethylamine (C ₆ H ₁₅ N)	≥ 99.5	Sigma-Aldrich
Reagent	Concentration /%	Supplier
Aluminium hydroxide (Al(OH) ₃)	50–57 (Al ₂ O ₃)	Sigma-Aldrich
Hydrochloric acid (HCl)	32–38	Fisher Chemicals
Ludox AS-40	40 (SiO ₂)	Sigma-Aldrich
Orthophosphoric acid (o-H ₃ PO ₄)	85	Prolabo
Sodium aluminate (NaAlO ₂)	31 (Na ₂ O) 38.5 (Al ₂ O ₃)	BDH Chemicals Ltd.
Tetraethylammonium hydroxide solution (C ₈ H ₂₁ NO; TEAOH)	34	Sigma-Aldrich

Contents

1. Introduction	1
1.1. Overview	1
1.2. Materials of Interest	5
1.2.1. Mesoporous Silicas	5
1.2.2. Zeolites	7
1.2.3. Silicoaluminophosphates (SAPOs)	12
1.3. Modification of the Framework Composition	13
1.3.1. Nitridation of Mesoporous and Microporous Materials	13
1.3.2. Dealumination of Zeolites	17
<i>References</i>	19
2. Characterisation of Materials	24
2.1. Basic Crystallography	24
2.2. Powder X-ray Diffraction	26
2.2.1. Introduction	26
2.2.2. X-ray Source	26
2.2.3. Bragg's Law	27
2.2.4. Principles of Powder X-ray Diffraction	28
2.2.5. Diffractometers	30
2.2.6. Synchrotron Radiation	31
2.2.7. Powder Structure Determination: Le Bail and Rietveld Refinement Methods	32
2.3. Adsorption	35
2.4. Electron Microscopy (EM)	38
2.4.1. Scanning Electron Microscopy (SEM)	38
2.4.2. High Resolution Transmission Electron Microscopy (HRTEM)	40
2.4.3. Energy Dispersive X-ray (EDX) Analysis	42
2.5. Fourier Transform (FT) Infra-red (IR) Spectroscopy	43
2.6. Solid State Magic Angle Spinning (MAS) Nuclear Magnetic Resonance (NMR) Spectroscopy	46
2.7. Other Techniques	50
2.7.1. Thermogravimetric Analysis (TGA)	50
2.7.2. Organic Elemental Analysis (CHNX)	51
2.7.3. Atomic Absorption Spectroscopy (AAS)	52
<i>References</i>	52

3.	Mesoporous Silicas SBA-1 and SBA-2: Materials with Large Pore Volume and Small Window Size	54
3.1.	Introduction	54
3.2.	Experimental	56
3.2.1.	Synthesis of SBA-1 and SBA-2	56
3.2.2.	Framework Modification by Calcination and Nitridation	58
3.2.3.	Characterisation	59
3.3.	Structural Characterisation of SBA-1 and SBA-2	60
3.4.	Modification of Mesoporous Silicas by Calcination	62
3.5.	Functionalisation of Mesoporous Silicas by Nitridation	67
3.6.	Realistic, Atomistic Model of SBA-2 and Simulation of Synthesis	75
3.7.	Conclusions	77
	References	78
4.	Preparing Zeolites as Carbon Dioxide Adsorbents	80
4.1.	Synthesis	80
4.2.	Ion Exchange	83
4.3.	Framework Modification and Dehydration	86
4.4.	Characterisation	88
	References	92
5.	Zeolite Chabazite: Structural Investigation of an Established Carbon Dioxide Adsorbent	94
5.1.	Introduction	94
5.2.	Characterisation of Different Cationic Forms of Chabazite	98
5.3.	Structural Studies of K-, Na-, Li- and Ca-Chabazite	103
5.4.	Carbon Dioxide Adsorption Study of Cationic Forms of Chabazite	110
5.5.	Conclusions	126
	References	129
6.	<i>ZK-5: Zeolite with High Carbon Dioxide Uptake at Ambient Temperature and Pressure</i>	131
6.1.	Introduction	131
6.2.	Characterisation of Different Cationic Forms of ZK-5	132
6.3.	Structural Studies of K-, Na-, and Li-ZK-5	136
6.4.	Carbon Dioxide Adsorption Study of K-, H-, Na- and Li-ZK-5	140
6.5.	Comparison of ZK-5 (KFI) with SAPO STA-14 (KFI)	142
6.6.	Conclusions	146

<i>References</i>	146
7. <i>Zeolite Rho: Potential Material for Selective Gas Capture</i>	148
7.1. Introduction	148
7.2. Characterisation of Different Cationic Forms of Rho	151
7.3. Functionalisation of H-Rho by Dealumination and Nitridation	156
7.4. Structural Studies of Na,Cs-, NH ₄ -, H-, Na-, Cs-, Li-, K- and Ca-Rho	165
7.5. CO ₂ Adsorption Related to Structure for Na,Cs-, Na- and Cs-Rho	170
7.6. CO ₂ Adsorption Related to Structure for H-, NH ₄ -, Li-, K- and Ca-Rho	172
7.7. N ₂ and CO ₂ Adsorption on Na,H-Rho, Li,H-Rho and Ca,H-Rho	175
7.8. <i>In situ</i> IR Spectroscopy of CO ₂ Adsorption	180
7.9. A Detailed Examination of CO ₂ Adsorption on Sodium Rho	183
7.10. High Pressure CO ₂ Adsorption and CO ₂ /CH ₄ Selectivity Studies	191
7.11. Comparison of Zeolite Rho with SAPO(RHO)	198
7.12. Conclusions	204
<i>References</i>	206
8. <i>General Conclusions and Future Work</i>	209
8.1. General Conclusions	209
8.2. Future Work	214
<i>Appendix</i>	216

1. Introduction

1.1. Overview

Carbon dioxide (CO₂) is emitted into the atmosphere from power stations by burning fossil fuels (for example coal, oil or gas), from automobile engines (for example cars or lorries), from furnaces used in commercial buildings and from some industrial and resource processes (for example the burning of forests during land clearance). A high concentration of CO₂ in the atmosphere is widely thought to be responsible for global warming and certainly causes ocean acidification.

Around 55% of global CO₂ emission is produced by power plants and heavy industry (for example petroleum, cement and steel industries). Flue gas is emitted into the atmosphere via a flue from a fireplace, oven, furnace, boiler or steam generator. It contains a low concentration of carbon dioxide among other gases, such as oxygen, sulphur oxides, water vapour and nitrogen. The CO₂ concentration in flue gas can vary from 7% to 30%, depending on the source.¹

Project Carbon Capture and Storage (CCS) aims to reduce the contribution of fossil fuel emissions by the capture of carbon dioxide and its storage away from the atmosphere.

To remove carbon dioxide from a flue gas, it must be preferentially separated by a capture process and subsequently concentrated and pressurised. Two processes² that are potential candidates for CO₂ capture are currently being used in industry (Figure 1.1):

- 1) Post-combustion capture (low-pressure adsorption) – CO₂ is separated, or removed, from a flue gas containing CO₂ mixed with other gases including N₂. Adsorption conditions $T \approx 298 \text{ K}$, $p_{\text{CO}_2} \approx 0.1 \text{ bar}$.
- 2) Pre-combustion capture (high-pressure adsorption) – the hydrocarbon fuel is first converted to CO₂ and H₂. The CO₂ can then be captured and stored, while the hydrogen is burnt to produce power. Adsorption conditions: $T \approx 313 \text{ K}$, $p_{\text{CO}_2} \approx 35 \text{ bar}$, CO₂ fraction $\approx 40\%$.

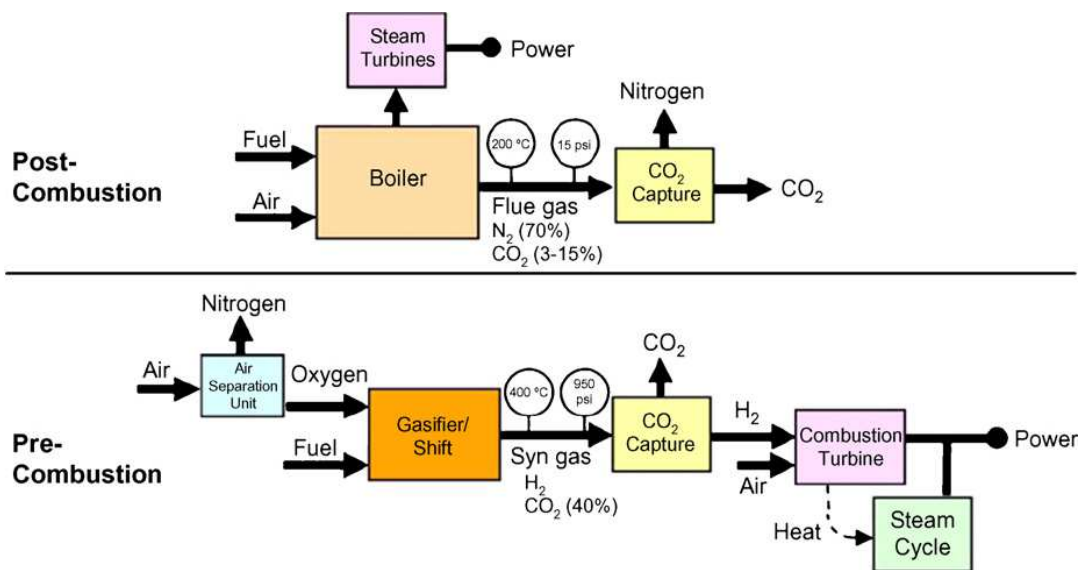


Figure 1.1. Block diagrams illustrating post-combustion and pre-combustion.²

The purpose of CCS is to compare methodologies and adsorbents (in particular the cost and efficiency) to establish an optimal process for CO₂ capture and storage from flue gases. The research teams which were collaborating in the CCS consortium, of which this project was a part, were groups from six British universities: St Andrews University, Cardiff University, University of Edinburgh, Imperial College London, University of Manchester and University College London. The research was focused on adsorption and membrane processes combining molecular modelling and advanced process modelling in order to develop reliable predictions of process performance. The main objectives of the consortium were to develop novel design and synthesis routes for materials and solvents for carbon capture technologies for use in power stations and screen them experimentally and via molecular modelling approaches.

CO₂ adsorbent should be selective with high adsorption capacity, possess fast adsorption/desorption kinetics, and good thermal and mechanical stability.³ Adsorbents which have been applied to CO₂ capture include, for example, activated carbons,⁴ silica gel,⁵ ion exchange resins,⁶ zeolites,⁷ porous silicates (for example SBA-15, MCM-41),⁸ metal oxides (for example CaO, K₂O, Li₂O)⁹ and metal-organic frameworks (MOFs).¹⁰

The aim of this PhD study was to investigate inorganic porous solids, with and without framework modification, for use in the removal of CO₂ from post-combustion (low-pressure adsorption) gas streams. The materials which were chosen for this study were:

mesoporous silicas SBA-1 and SBA-2 (chapter 3), the zeolites chabazite (CHA), ZK-5 (KFI) and Rho (RHO) (chapters 5, 6 and 7, respectively), and silicoaluminophosphates (SAPO) STA-14 and SAPO(RHO) (chapters 6 and 7, respectively).

Pore/window aperture of mesoporous silicas, zeolites and silicoaluminophosphates must be larger than the kinetic diameters of the molecules that are being adsorbed. Besides the size, quadrupole moment and polarisability of molecules often point to the most appropriate mechanism for the separation in porous materials. Selective CO₂ adsorption (over for example N₂ or CH₄) in porous materials is very often not only due to the small kinetic diameter of CO₂ but also its strong interactions with the structure due to its large quadrupole moment and polarisability. Polarisability of an atom or a molecule is a measure of the ease with which the electrons and nuclei can be displaced from their average positions. When the electrons occupy a large volume of space, which occurs in an atom or molecule with many electrons, the polarisability of the substance is large. The polarisability of a molecule increases with both increasing size and increasing number of atoms in the molecule.¹¹ Large polarisability for an atom or molecule results in producing a stronger attraction between particles. The kinetic diameters, two-centre Lennard-Jones Quadrupoles (2CLJQ), quadrupole moment and polarisability of some molecules are presented in Table 1.1.

Table 1.1. Kinetic diameters, two-centre Lennard-Jones Quadrupoles (2CLJQ), quadrupole moment (Θ) and polarisability of molecules.¹¹⁻¹³

Molecule	Molecular weight	Kinetic diameter /Å	2CLJQ model /Å		Θ /10 ⁻⁴⁰ C m ²	Polarisability /Å ³
			σ	L		
H ₂ O	18	2.46	–	–	3.03	1.45
CO ₂	44	3.30	2.98	2.42	13.4	2.65
N ₂	28	3.64	3.32	1.05	4.70	1.76
CH ₄	16	3.80	–	–	0.0	2.60
C ₂ H ₆	30	4.40	–	–	3.34	4.47

Small window sizes of mesoporous silicas, SBA-1 and SBA-2, could allow them to act as molecular sieves. Separation based on geometry is possible, when zeolite or mesoporous silica has a pore/window size large enough to take up CO₂ but too small to adsorb small hydrocarbons. A previous study¹⁴ suggests that this might be possible

for mesoporous silica by using a calcination temperature that reduces nitrogen uptake but not CO₂ uptake.

Small pore zeolites may facilitate strong interactions with adsorbed molecules, even at the highest levels of pore filling. Larger and more polar molecules interact strongly with zeolites having smaller univalent cations, or divalent cations. The advantages of zeolites chabazite, ZK-5 and Rho are: 3-dimensionally connected pore structures, high chemical, thermal and hydrothermal stabilities, fast and easy synthesis and many easily exchangeable extra-framework cations. It will be demonstrated that the CO₂ adsorption preference of zeolites depends on many factors, for example Si/Al ratio, the size distribution and the form of the pores and the number of extra-framework cations.

It is also known that zeolites will adsorb H₂O in preference to CO₂ in their usual cation exchanged form and the competitive adsorption is typically of the order H₂O > CO₂ > N₂ > O₂ at ambient temperature and pressure.¹⁵ Possible approaches to modify a zeolite able to take up CO₂ in preference to H₂O, ultrastabilisation and nitridation, have been also investigated in this study.

Both as-prepared zeolites and mesoporous silicas require modification before they will be able to capture CO₂. Possible modification routes are: (i) control of framework Si/Al ratio and number of extra-framework cations in zeolites, (ii) pore size modification in mesoporous silicas and (iii) framework nitridation of mesoporous silicas and zeolites.

All materials which have been chosen in this study could be prepared economically and have high surface areas. A key criterion of their application in CO₂ removal from flue gas is that they should show appreciable uptake of CO₂ at temperatures close to ambient (298 K) and at relatively low partial pressures (*ca.* 0.1 bar). High uptakes at high pressures are of interest as adsorbents in pre-combustion processes, but that was not the primary concern of this PhD study.

1.2. Materials of Interest

1.2.1. Mesoporous Silicas

Mesoporous materials contain pores with diameters between 2 and 50 nm. They are typically amorphous or paracrystalline solids (no long-range order).

The first mesoporous material, kanemite, was reported in 1990 by Japanese researchers.¹⁶ In the same year Mobil researchers presented the synthesis, characterisation and proposed mechanism of formation of a new family of mesoporous silicas designated as MCM (Mobil Composition of Matter).^{17,18} This family of materials possesses a regular array of pores with uniform diameter, high specific surface areas and pore volumes. The best known members of the MCM family are MCM-41 and MCM-48. The first, MCM-41, has a hexagonal arrangement of pores while the second, MCM-48, has a cubic structure. Characteristic properties of these materials are large surface areas (1000–1500 m²g⁻¹) and a narrow pore-size distribution.

Soon after the discovery of MCM materials Huo *et al.*^{19,20} synthesised the first two mesoporous materials from the SBA (Santa Barbara materials) family – SBA-1 and SBA-2. SBA mesoporous silicas possess well-ordered channel and cage structures. Among the SBA family, SBA-15 and SBA-16 are considered to be the most interesting mesostructures and most work has been done on this materials.²¹⁻²⁵ This work was focused on the less studied but also very interesting structures of SBA-1 and SBA-2, as potential candidates for CO₂ capture. More details about these materials are given in introduction to chapter 3.

Mesoporous materials are prepared in the presence of surfactants that lead to different micellar arrangements. Surfactants are materials which can reduce the surface tension of liquids. Mesoporous solids can be prepared with cationic, anionic or neutral surfactants of different types and under alkaline, acid or neutral pH (Table 1.2).

In the first fast stage of the reaction silicate oligomers, formed in the aqueous solution, interact with the surfactant at the micelle surface and transform the micelles into a hexagonal array separated by a partially condensed silica matrix. During the second

slow stage of the reaction further condensation and dehydration take place. The porous solid can be achieved by template removal (calcination between 673 K and 873 K) or by extraction with solvent under reflux conditions.

Table 1.2. Mechanisms of the synthesis of mesoporous solids.

Mechanism	Surfactant type	Synthesis pH	Example of mesoporous solid
$S^+ I^-$	Cationic	Basic	SBA-2
$S^+ X^- I^+$	Cationic	Acidic	SBA-1
$S^- I^+$	Anionic	5–10	AMS-n
$S^0 H^+ X^- I^+$	Neutral (block copolymers)	Acidic	SBA-15

I^- , I^+ - inorganic matrix; S^+ - surfactant (cationic); S^- - surfactant (anionic); S^0 - surfactant (uncharged); X^- - anions from solution

Mesoporous silicas possess a stable structure, a high surface area and a large uniform pore size that makes them promising CO₂ adsorbents. However, due to their neutral silica framework, pure mesoporous silicas are physical adsorbents characterised by weak CO₂-adsorbent interactions. Modification of the silica framework is necessary to enhance CO₂ uptake. There has been a large amount of research effort devoted to the functionalisation of the surfaces of these materials.^{8,14,21,22,25-33} The results show that amino-functionalised mesoporous silicas are good candidates for CO₂ capture from combustion flue gas, due to the reversible formation of ammonium carbonates during CO₂ adsorption, as well as the uniform, large pores and high surface area.^{34,35} Upon amine functionalisation, the CO₂ uptake is significantly improved, particularly at low CO₂ concentration, and the mesoporous solids are capable of both chemical and physical adsorption.²⁶ So far, several amine incorporated mesoporous silica materials have been reported with promising CO₂ capture at room temperature, for example MCM-41 impregnated with polyethylenimine (PEI),⁸ SBA-15 impregnated with tetraethylenepentamine (TEPA)²³ and MCM-41 and MCM-48 post-synthetically grafted with aminopropylsilanes.^{28,33} Impregnation with PEI or TEPA helps to obtain CO₂ sorbents with high amine loadings. It was also shown that, in contrast to zeolites, the functionalised mesoporous silicas show high CO₂ uptake in the presence of humidity.²⁶ This is a big advantage for gas purification and separation processes. Mesoporous silicas may be also functionalised by the co-condensation and post-grafting. However, both of these methods have many disadvantages, for example the

post-grafting method typically results in an inhomogeneous surface coverage³⁴ and the co-condensation method may lead to situations where some of the functional groups are embedded in the silica network.³¹ Due to the limited number of incorporated atoms and the restricted reactivity of introduced groups for all of the above modification processes, a new approach was needed. The substitution of N atoms for the framework O atoms, in the process called ‘nitridation’, leads not only to an increase in the number of functional sites but also to more extended functionalisation. Nitridation is an easy and fast process. Nitrided mesoporous silicas, KCC-1, SBA-15 and MCM-41, have very recently been reported to exhibit good thermal stability and regenerability and higher CO₂ uptake, at 1 bar and room temperature, than pure mesoporous silicas.²² In this study SBA-1 and SBA-2 were nitrided for the first time and their N₂ and CO₂ sorption abilities have been measured. The mechanism of nitridation of mesoporous silicas will be discussed in more details in section 1.3.1.

The discovery of the MCM and SBA families of mesoporous materials has opened new opportunities for the synthesis of novel organic-inorganic hybrid materials that combine the structural properties of the rigid silica framework and the chemical reactivity of the attached organic groups.

1.2.2. Zeolites

The term zeolite appeared in 1756. The Swedish mineralogist, Axel Fredrik Cronstedt, noticed that the stilbite material produced large amounts of steam from water when rapidly heated and called it *zeolite*, from the Greek ζέω (*zeō*), meaning "boil" and λίθος (*lithos*), meaning ‘stone’.¹³

Zeolites are a large group of natural and synthetic microporous crystalline solids with well-defined structures. Zeolites typically contain silicon, aluminum and oxygen in their framework, but other elements, such as germanium, titanium or gallium, can also occupy framework cation sites. Zeolites possess a framework formed by a 3-dimensional assemblage of corner-sharing tetrahedra [SiO₄] and [(AlO₄)⁻]. The Commission on Zeolite Nomenclature of the International Union of Pure and Applied Chemistry (IUPAC) labeled zeolites framework types by a ‘framework type code’ (FTC) denoted by three capital letters, for example CHA for chabazite, KFI

for ZK-5 and RHO for Rho. FTCs are assigned and curated by the Structure Commission of the International Zeolite Association (IZA). Additionally, for each observed topology the Zeolite Atlas gives complete details of unit cell dimensions and symmetry, fractional atomic coordinations, coordination sequences of tetrahedral nodes, pore connectivity and dimensions, and secondary building units found in the frameworks.³⁶ The secondary building units (SBUs) are frequently used to describe the number of framework cations in the zeolite rings, for example S6R – single six-membered ring that contains six cations and six oxygen atoms, or D8R – double eight-membered ring that contains two eight-membered rings (eight cations and eight oxygen atoms) linked together. More examples of SBUs are given in Figure 1.2, where only the topology of the tetrahedral cations is given. These are linked by oxygen atoms in the structures. In this study, the α -cage (Figure 1.2g) is of importance because it is a key SBU in two zeolites, Rho and ZK-5, which have been investigated. Additional forms of building units in zeolitic structure include different types of unbranched and branched chains.

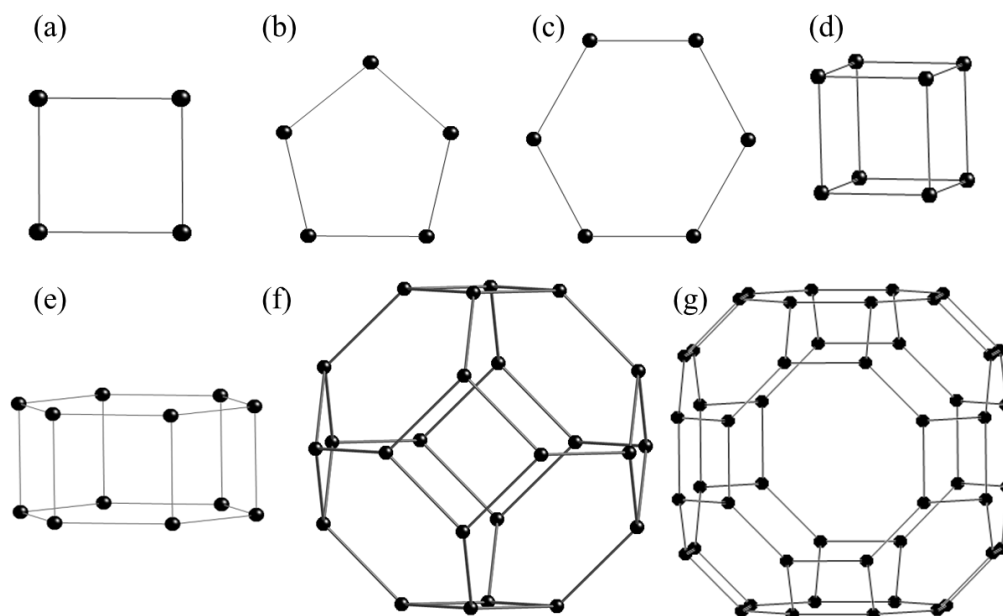


Figure 1.2. SBUs including (a) single four-membered ring, S4R, (b) single five-membered ring, S5R, (c) single six-membered ring, S6R, (d) double four-membered ring, D4R, (e) double six-membered ring, D6R, (f) sodalite or β -cage and (g) α -cage.

In contrast to mesoporous silicas, the framework composition of aluminosilicate zeolites allows the presence of charge-balancing extra-framework cations, for example Li^+ , Na^+ ,

K^+ , Ca^{2+} , Ba^{2+} , Cu^{2+} , Zn^{2+} and Mg^{2+} . Cations are located within the cavities to balance the negative charge introduced into the framework by the substitution of aluminium atoms for silicon atoms. The extra-framework cations can readily be exchanged. For many low silica zeolites, complete ion exchange is possible, for example with zeolites X, ZK-5 or Rho,³⁷⁻⁴⁰ whereas for some, such as zeolite L,⁴¹ it is possible to exchange extra-framework cations in the main channels but not those held within the cages. Ion exchange can effectively enhance the adsorption capacity of zeolites.

For flexible zeolites (for example zeolite Rho or chabazite), the ion exchange and dehydration can cause structural effects.³⁸ For zeolites that contain only inorganic cations, heating results in loss of water with resultant effects on the location of cations and the position of framework atoms. Dehydration of zeolites reduces the coordination of the cations, which then move to achieve better coordination by framework oxygen atoms. This results in cation migration either closer to framework oxygen atoms or to different cation sites.⁴² Some zeolites show marked changes in framework geometry and symmetry (by rotation and twisting) in order to achieve better coordination of cations when they lose water.⁴³ Ion exchanged forms of zeolites show reversible dehydration upon heating, except for the ammonium forms, which upon heating to around 573 K convert to the H-form, along with framework dealumination, the mechanism and structural consequences of which are described in section 1.3.2.

Many studies have demonstrated the ability of zeolites to selectively separate gases based on molecular size and shape because of their small pore size (3–10 Å) and their narrow pore size distribution.⁴⁴⁻⁴⁸ Cationic zeolites with relatively high extra-framework cation content are effective CO₂ adsorbents that can adsorb significant amounts of this greenhouse gas even at the low partial pressure (0.1 bar) and ambient temperature relevant to carbon capture from flue gases.^{40,49-51}

Adsorption preference of zeolites depends on Si/Al ratio, size and form of their pores, size, distribution and the number of extra-framework cations, the polarisability and size of adsorbed molecules, the presence of water and other gas and presence of carbonates at their surface. Pressure and temperature also strongly influence the uptake of CO₂ on zeolites.⁵²

Yamazaki *et al.*⁵³ and Khelifa *et al.*⁵⁴ showed that the energy of the interaction between the CO₂ and the cation sites of zeolites decreases with increased cation radius (Li⁺ < Na⁺ < K⁺ < Rb⁺ < Cs⁺).⁵⁵ The polarising power of the cations is inversely proportional to its ionic radius. Small cations interact more strongly with the CO₂ due to their higher charge density, for example for group 1 A: Cs⁺ (3.3 Å) < Rb⁺ (2.9 Å) < K⁺ (2.7 Å) < Na⁺ (1.9 Å) < Li⁺ (1.4 Å).

The CO₂ adsorption also depends on the framework composition. Calleja *et al.*⁵⁶ showed that the CO₂ adsorption of zeolites increases as the Si/Al ratio decreases because of the increasing electric field in the zeolite pores induced by the increasing of framework density charge caused by the substitution of Si⁴⁺ by Al³⁺. Inui *et al.*⁵⁷ found that the shape of pores is important for the selective adsorption of CO₂ and zeolites which possess a pore structure that is connected in three-dimensions show the highest CO₂ sorption. Gallei and Stumpf⁵⁸ noticed that the chemical adsorption of CO₂ is accompanied by the formation of carbonates (for example stable monodentate, unidentate carbonates and bidentate carbonates), due to the interaction of CO₂ with framework oxygen atoms.

The optimisation of structural characteristics of zeolites includes: (i) size, distribution and the number of extra-framework exchangeable cations, (ii) size of the pores, (iii) the Si/Al ratio, (iv) the formation of carbonates species at the surface of zeolites, and (v) presence of water.

Zeolites A, X and Y which have relatively low Si/Al ratios and high extra-framework cation content adsorb CO₂ strongly at ambient temperature.^{51,59,60} Currently, the zeolite 13X (Figure 1.3a) is used in industry as the benchmark for CO₂ uptake at 0.1 bar and 298 K. Under these post-combustion conditions, the CO₂ uptake of zeolite 13X is 3.05 mmol g⁻¹ (Figure 1.3b). However, much of its open space is inaccessible to CO₂, which it cannot pass through the single six-membered ring (S6R) windows of the sodalite cage and only extra-framework cations in the supercage (site II and III, Figure 1.3c) are accessible for CO₂ adsorption. The approach for high CO₂ adsorption in this study is to use zeolites that have a larger fraction of their pore volume accessible but still have relatively small cages that facilitate strong interactions with adsorbed molecules, even at the highest levels of pore filling. The zeolites chabazite, ZK-5

and Rho are attractive in this regard. In chabazitic zeolites, chabazite and ZK-5, pore volumes of *ca.* $0.30 \text{ cm}^3 \text{ g}^{-1}$ are available if no pore space is taken up by extra-framework cations, whereas in Rho, where all pore space is available, this value is *ca.* $0.40 \text{ cm}^3 \text{ g}^{-1}$.⁷

In this study, CO_2 adsorption on chabazite, ZK-5 and Rho samples fully exchanged with a range of univalent and divalent cations (for example Li^+ , Na^+ , K^+ and Ca^{2+}), prepared by cation exchange, was measured. The CO_2 adsorption behaviour of all chabazite, ZK-5 and Rho materials is discussed with reference to the crystal structures of the dehydrated forms. More information about chabazite, ZK-5 and Rho structures and their applications are given in the introductions to chapters 5, 6 and 7, respectively.

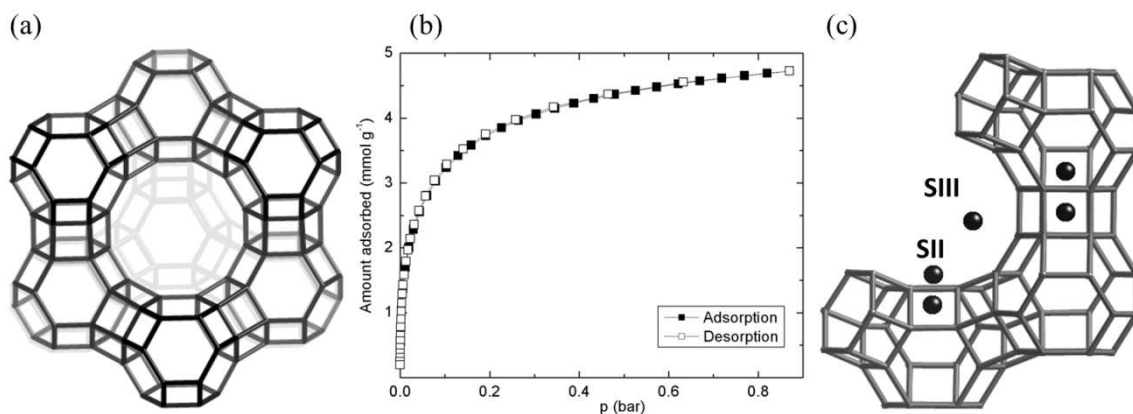


Figure 1.3. (a) Structure of zeolite 13X which is formed from β -cages, joined through double six-membered rings (D6Rs), (b) CO_2 sorption isotherms for zeolite 13X at 298 K up to 0.9 bar, and (c) extra-framework cation sites in zeolite 13X showing site II and site III which are accessible for CO_2 adsorption.

Zeolites are synthesised from reactive gels in a solvent (usually water) at temperatures between about 353 K and 473 K.^{13,61} Until 1961, zeolites (and some zeotypes) were mainly made using inorganic reactants. Since the 1960s much use has also been made of organics as structure directing agents, or templates, around which the inorganic framework crystallises. Most high-silica zeolites are synthesised using organic templates, which have to be removed from the structure, usually by calcination at temperatures in the range of 723–873 K, to produce porous solids. The most important of hydrothermal synthesis parameters are: gel composition and source of chemicals, gel aging, pH, temperature and time.

Hydrothermal synthesis is a multiphase reaction and crystallisation process in which amorphous reactants are converted to the crystalline product through the agency of hydroxyl ions acting as a catalyst by breaking and remaking Si,Al–O–Si,Al bonds. In hydrothermal synthesis reactants are heated at high pressures in autoclaves (Figure 1.4). Hydrothermal synthesis involves at least one liquid phase and both amorphous and crystalline solid phases. In this study hydrothermal synthesis was used for the synthesis of all zeolites.

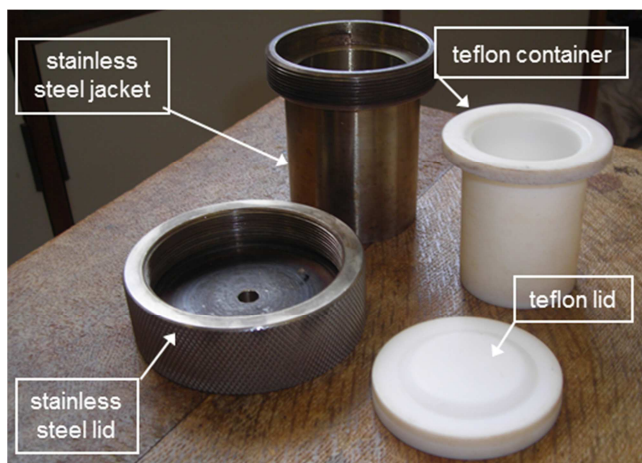


Figure 1.4. An autoclave consisting of a teflon container within a stainless steel jacket.

1.2.3. Silicoaluminophosphates (SAPOs)

Microporous silicoaluminophosphate solids (SAPOs), which belong to the class of ‘zeolite-like’ materials, were discovered by Flanigen and co-workers.⁶² They are composed of TO_4 tetrahedra of Al, P and Si. SAPOs can be considered to be derived from replacing some of the phosphorus atoms (and sometimes also Al atoms) in aluminophosphates (AIPOs) with silicon atoms. The main mechanism of replacement of P atoms by Si atoms involves production of isolated $\text{Si}(\text{OAl})_4$ units or larger aluminosilicate domains.⁶³ AIPOs are solids with neutral frameworks so that by this replacement of P atoms by Si atoms negative charges are inducted which are charge-balanced with protons that act as Brønsted acid sites (the bridging Si–OH–Al sites). Protons in SAPOs can be exchanged for different extra-framework cations.^{64,65} The maximum number of univalent extra-framework cations is equal to the number of silicon atoms. SAPOs possess catalytic properties similar to zeolites, what makes them potential candidates for catalysis and adsorption.

Small-pore SAPO-34 (CHA) is the most studied material from the silicoalumino-phosphate family. It has received great attention due to its high selectivity to CO₂/CH₄ separation^{66,67} and the methanol to olefin reaction.^{68,69} It has been recently reported that ion exchanged SAPO materials are promising adsorbents for the selective removal of CO₂ at ambient temperatures and pressures.^{70,71}

In this study, SAPO STA-14 (KFI) and SAPO(RHO) (RHO) were synthesised, characterised, ion exchanged and their CO₂ uptake was compared with zeolites ZK-5 (KFI) and Rho (RHO), respectively. SAPO STA-14 and SAPO(RHO) were ion exchanged with Na cations for the first time in this study and the CO₂ uptake on the Na-forms was measured. More information about these SAPO materials can be found in chapters 6 and 7.

1.3. Modification of the Framework Composition

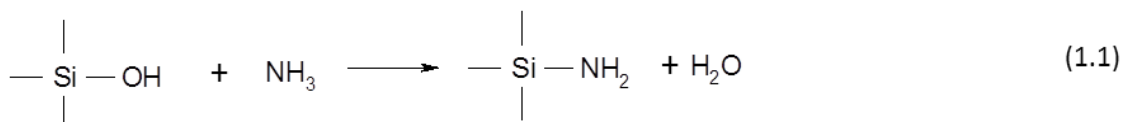
1.3.1. Nitridation of Mesoporous and Microporous Materials

The properties of porous materials are determined by the framework topology, the framework composition and the presence of extra-framework charge-balancing cations. By replacing atoms, or groups of atoms, of the porous structures with selected groups, new active sites may be created of interest in adsorption and catalysis. There is increasing evidence that the framework composition of zeolites and mesoporous solids can be modified by replacement of the oxygen atoms.^{22,29,30,72,73} One modification that may be of interest for improving CO₂ uptake is the replacement of lattice oxygen atoms with nitrogen atoms in a process called 'nitridation'.³⁰

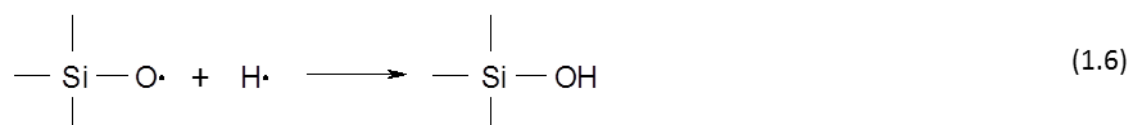
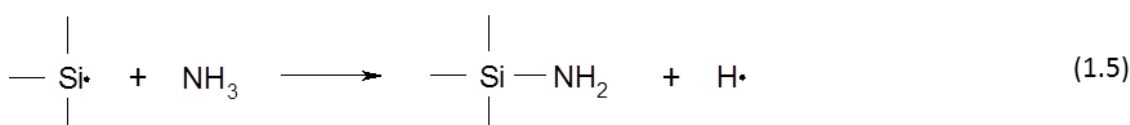
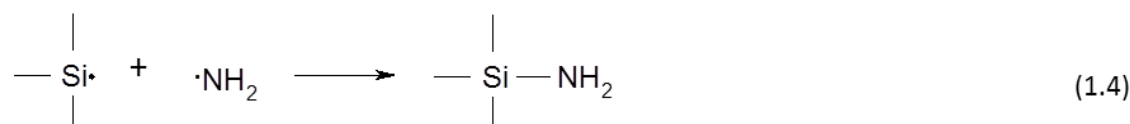
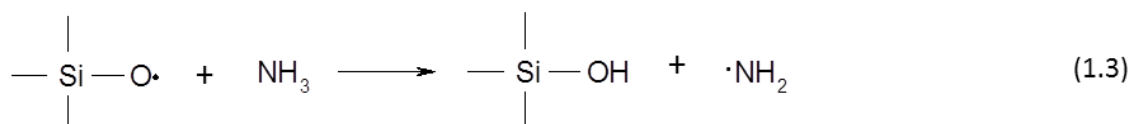
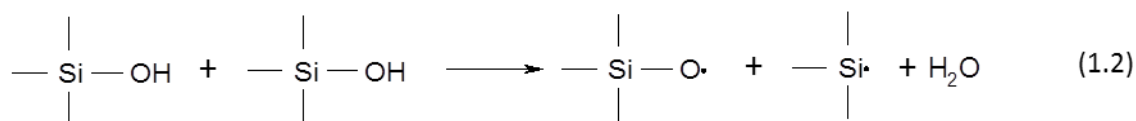
In 1968 Kerr and Shipman⁷⁴ first obtained the substitution of nitrogen for oxygen in crystalline porous materials using zeolite Y as the substrate. In 1993 Stein *et al.*⁷⁵ presented the nitridation of AlPO at temperatures up to 1173 K. Since then, nitridation has been studied on zeolites and on mesoporous silicas.^{21,30,32,73} The substitution of oxygen atoms by nitrogen atoms in the silica framework leads to an increase of the Lewis basicity, as a result of the lower electronegativity of nitrogen with respect to oxygen.

The nitridation process of mesoporous silicas and zeolites in this study was carried out at the University of Nottingham in collaboration with Eric Masika and Prof. Robert Mokaya. The nitridation was conducted in a tube furnace under ammonia gas flow.

The nitridation mechanism of mesoporous silicas, based on the example of SBA-15, was suggested by Chino *et al.*²¹ In the first stage, at 1073 K, ammonia molecules react with hydroxyl groups to form $\equiv\text{Si}-\text{NH}_2$ bonds (reaction 1.1).



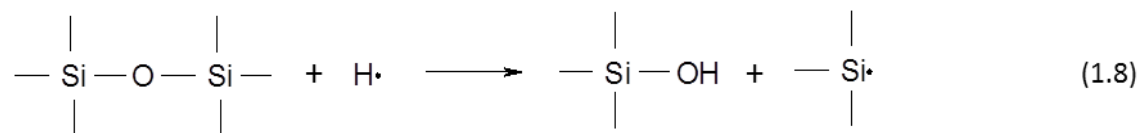
The mechanism of reaction 1.1 is speculated to occur as follows: $\equiv\text{Si}\cdot$ and $\equiv\text{Si}-\text{O}\cdot$ are generated through dehydration of isolated hydroxyl groups according to reaction 1.2 and then $\equiv\text{Si}\cdot$ and $\equiv\text{Si}-\text{O}\cdot$ generate $\cdot\text{NH}_2$ from NH_3 molecules (reaction 1.3). If $\equiv\text{Si}\cdot$ is located next to $\equiv\text{Si}-\text{O}\cdot$, $\equiv\text{Si}-\text{NH}_2$ can be generated according to reaction 1.4 or $\equiv\text{Si}\cdot$ can be reacted with NH_3 molecules according to reaction 1.5, where $\equiv\text{Si}-\text{OH}$ can be generated according to reaction 1.6.



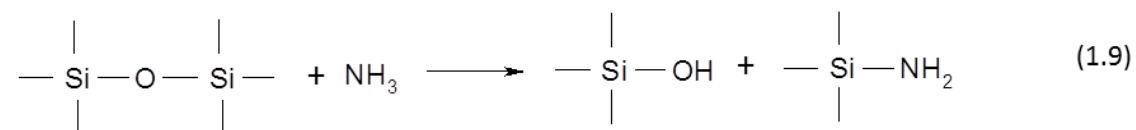
During the nitridation at higher temperature (> 1173 K) $\equiv\text{Si}-\text{NH}-\text{Si}\equiv$ groups are formed and $\equiv\text{Si}-\text{NH}_2$ groups disappear, reaction 1.7.



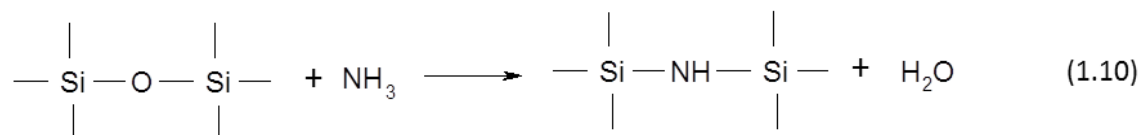
Atomic hydrogen (H \cdot) which is produced during the decomposition of NH $_3$ molecules around the silica surface (see reaction 1.5) can play an important role in removing oxygen atoms of siloxane bridging bonds and producing the defect species at high temperatures, as demonstrated in reaction 1.8.



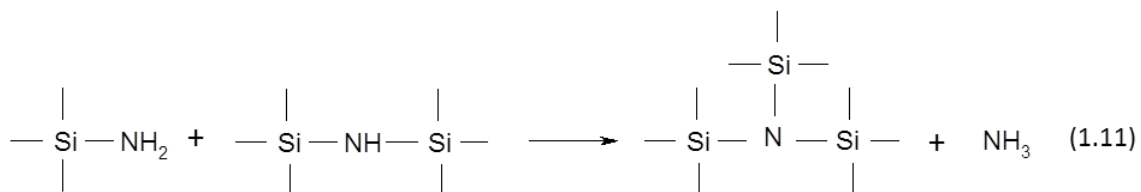
Combination of reactions 1.5 and 1.8 can be presented as reaction 1.9.



At 1273 K the decomposition of NH $_3$ leads to the incorporation of nitrogen atoms into siloxane bridging bonds, reaction 1.10.

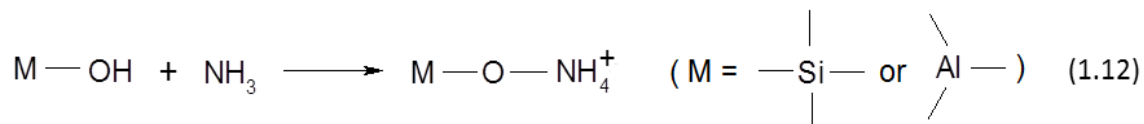


Concurrently with reactions 1.1 to 1.10, the pore diameter of the mesoporous structure is decreasing. This suggests that the mesoporous structure is drastically condensed by reaction 1.11, where SiN $_4$ or SiN $_3$ O components are formed around the surface.

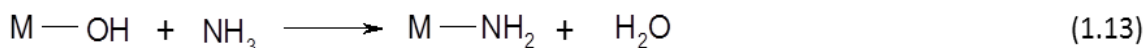


The nitridation mechanism of zeolites, based on example of zeolite Y, was suggested by Srasra *et al.*⁷³

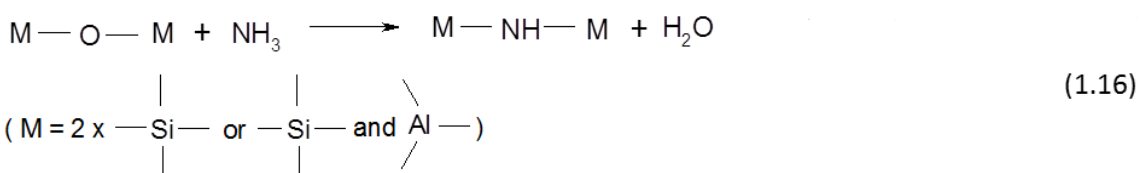
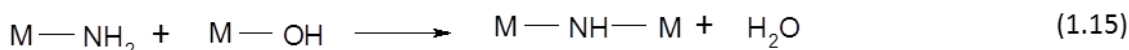
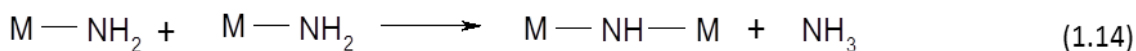
At low temperature (873 K) ammonia molecules first react with hydroxyl groups to form -O-NH $_4^+$ ionic bonds as presented in reaction 1.12.



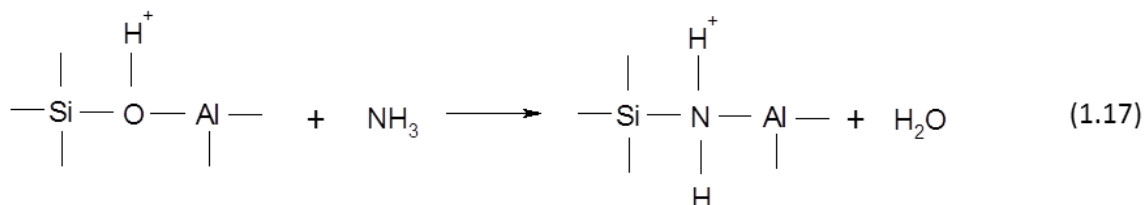
Ammonia may also react with hydroxyl groups to form amido groups, -NH $_2$ (reaction 1.13).



At higher temperatures (1073 K) the formation of the bridging imido >NH can be explained in three ways by the condensation: of two amide groups (reaction 1.14), of an amide with another hydroxyl group (reaction 1.15) or the direct attack of bridging oxygen by ammonia (reaction 1.16).



In zeolites at temperatures between 1023 K and 1073 K the substitution of oxygen at Si-OH-Al sites occurs according to reaction 1.17.



The increase of the amount of nitride species provokes a decrease of the crystallinity and the formation of an amorphous phase.⁷³

In this study powder X-ray diffraction (PXRD), energy dispersive X-ray (EDX) analysis and ²⁹Si magic angle spinning nuclear magnetic resonance (MAS NMR) spectroscopy were used to determine the changes that occurred to the structures of the mesoporous solids and zeolites after nitridation. More about these techniques and their application to the characterisation of nitrated samples is described in chapter 2.

In summary, the studies show that the nitridation routes are dependent on the temperature of the thermal treatment, the time of the nitridation process and the flow rate of the ammonia. Increasing the temperature of nitridation causes an increase of the nitrogen content in mesoporous silicas and zeolites.^{27,32} It is also known that, for example zeolite Y is stable during heating to 773 K, above this temperature its structure collapses, whereas during nitridation it can be heated until 1123 K and is still highly crystalline.^{76,77} This suggests that high temperatures in the absence of ammonia

cause minor structural deformations of the Si–O and Al–O bonds whereas the presence of ammonia can either prevent the formation of defects or heal some of them via dealumination.⁷⁷ In this case it is also important to introduce ammonia before the furnace reaches the reaction temperature.⁷⁸ Longer nitridation time may be an effective way of increasing the nitrogen content without compromising the textural properties.³² The surface area of the nitrated materials decreases at higher nitridation temperatures. The best flow rate of ammonia is between 300–600 mL min⁻¹ but it is recommended to keep the flow rate as high as possible.⁷⁸ At high temperatures (1023–1073 K) in zeolites there is a preference for substitution at Si–OH–Al sites.⁷⁷ The nitridation of crystalline microporous zeolites is more difficult than nitridation of mesoporous silica because zeolites contain fewer silanol groups and the nitrogen substitution reaction starts from these defect sites. The increase of the amount of nitride species can occur with minor decreases in crystallinity and porosity.⁷³ The presence of extra-framework cations (other than protons) in zeolites requires higher temperatures and/or longer times to show similar levels of substitution to those seen in comparably treated H-forms of zeolite Y, and the materials with higher Si/Al ratios shows higher levels of substitution and stability than high-aluminum zeolites.⁷⁷

Nitrated mesoporous silicas and microporous solids are of interest because of their high thermal stability and low density. It is possible that nitridation can create new adsorption sites in mesoporous silicas and zeolites and enhance CO₂ uptake.

1.3.2. Dealumination of Zeolites

The heating of the ammonia form of a zeolite at high temperature (> 823 K) results in preparation of the protonic form and loss of framework aluminium. This process, called ‘dealumination’, creates the Brønsted acid sites as well as Lewis acidic extra-framework aluminium (EFAL) species.⁷⁹ This strong acidity of zeolites, together with their regular structure, is responsible for their widespread use as catalysts. Dealumination was used in this study to create new CO₂ adsorption sites in H-Rho and to make it more hydrophobic.

Dealumination is most readily applicable for zeolites with Si/Al > 2, because for zeolites with Si/Al < 2 it usually results in loss of the crystallinity. The H-form of

a zeolite produced by dealumination can be prepared by using ‘deep-bed calcination’ conditions⁸⁰ or by heating under high H₂O vapor pressures (steaming).⁸¹ Under these conditions, it is possible for Si to migrate to fill some of the Al vacancies, allowing the framework Si/Al ratio to be increased while the crystal structure is retained. During the migration of Si atoms secondary mesoporosity is developed, which improves molecular diffusion in these materials. Many ultrastable zeolites have been prepared by dealumination, for example zeolite Y.⁸²

²⁹Si and ²⁷Al magic angle spinning nuclear magnetic resonance (MAS NMR) spectroscopy is a powerful tool to study the local environments of silicon in the zeolite frameworks. It was used to investigate the dealumination of zeolite Rho in this study. More information about the technique and its use for measuring the degree of dealumination are given in chapter 2.

In a process of dealumination, aluminium species are removed from the lattice in two stages, during deammoniation and also during rehydration and hydrolysis at defect sites upon cooling.^{83,84} The formation of EFAL develops in the progression: Al(OH)₃ (six-fold coordinated Al, reaction 1.19), Al(OH)₂⁺ (five-fold coordinated Al, reaction 1.20) and AlOH²⁺ (four-fold coordinated Al, reaction 1.21) species, according to Scheme 1.1.⁸³ The EFAL is coordinated to oxygen atoms and bounded to framework Al species. These species are thought to be able to be further coordinated by water molecules. It is very difficult to remove all Al during dealumination, even from zeolite Y. To prepare Y with very high Si/Al ratio, or as a pure silica, chemical treatment is required, giving direct replacement by Al atoms with Si atoms.⁸⁵

11. Miller K. J., *J. Am. Chem. Soc.*, **1990**, *112*, 8533-8542
12. D'Alessandro D. M., Smit B. and Long J. R., *Angew. Chem. Int. Edit.*, **2010**, *49*, 6058-6082
13. Wright P. A., '*Microporous Framework Solids*', The Royal Society of Chemistry, UK, **2008**
14. Gonzalez J., *Adsorption properties of organically functionalised mesoporous solids and dynamics of adsorbed molecules in microporous organic-inorganic hybrid solids*, University of St Andrews, **2005**
15. Breck D., '*Zeolite Molecular Sieves: Structure, Chemistry and Use* ', John Wiley & Sons, Inc, New York, **1974**
16. Yanagisawa T., Shimizu T., Kuroda K. and Kato C., *B. Chem. Soc. Jpn*, **1990**, *63*, 1535-1537
17. Beck J. S., Vartuli J. C., Roth W. J., Leonowicz M. E., Kresge C. T., Schmitt K. D., Chu C. T. W., Olson D. H., Sheppard E. W., McCullen S. B., Higgins J. B. and Schlenker J. L., *J. Am. Chem. Soc.*, **1992**, *114*, 10834-10843
18. Kresge C. T., Leonowicz M. E., Roth W. J., Vartuli J. C. and Beck J. S., *Nature*, **1992**, *359*, 710-712
19. Huo Q. S., Leon R., Petroff P. M. and Stucky G. D., *Science*, **1995**, *268*, 1324-1327
20. Huo Q. S., Margolese D. I., Ciesla U., Feng P. Y., Gier T. E., Sieger P., Leon R., Petroff P. M., Schuth F. and Stucky G. D., *Nature*, **1994**, *368*, 317-321
21. Chino N. and Okubo T., *Micropor. Mesopor. Mat.*, **2005**, *87*, 15-22
22. Patil U., Fihri A., Emwas A. H. and Polshettiwar V., *Chemical Science*, **2012**, *3*, 2224-2229
23. Yue M. B., Chun Y., Cao Y., Dong X. and Zhu J. H., *Adv. Funct. Mater.*, **2006**, *16*, 1717-1722
24. Carta D., Bullita S., Casula M. F., Casu A., Falqui A. and Corrias A., *ChemPlusChem*, **2013**, *78*, 364-374
25. Andrade G. F., Soares D. C. F., dos Santos R. G. and Sousa E. M. B., *Micropor. Mesopor. Mat.*, **2013**, *168*, 102-110
26. Belmabkhout Y. and Sayari A., *Adsorption*, **2009**, *15*, 318-328
27. Hayashi F., Ishizu K. and Iwamoto M., *J. Am. Ceram. Soc.*, **2010**, *93*, 104-110
28. Huang H. Y., Yang R. T., Chinn D. and Munson C. L., *Ind. Eng. Chem. Res.*, **2002**, *42*, 2427-2433

29. Sanz R., Calleja G., Arencibia A. and Sanz-Pérez E. S., *Micropor. Mesopor. Mat.*, **2012**, *158*, 309-317
30. Wang J. C. and Liu Q., *Micropor. Mesopor. Mat.*, **2005**, *83*, 225-232
31. Wang X., Lin K. S. K., Chan J. C. C. and Cheng S., *J. Phys. Chem. B*, **2005**, *109*, 1763-1769
32. Xia Y. D. and Mokaya R., *J. Mater. Chem.*, **2004**, *14*, 2507-2515
33. Yokoi T., Yoshitake H. and Tatsumi T., *J. Mater. Chem.*, **2004**, *14*, 951-957
34. Richer R., *Chem. Commun.*, **1998**, *0*, 1775-1777
35. Kim C. O., Cho S. J. and Park J. W., *J. Colloid Interf. Sci.*, **2003**, *260*, 374-378
36. McCusker L. B., Liebau F. and Engelhardt G., *Micropor. Mesopor. Mat.*, **2003**, *58*, 3-13
37. Siporin S. E., McClaine B. C. and Davis R. J., *Langmuir*, **2003**, *19*, 4707-4713
38. Corbin D. R., Stucky G. D., Eddy M. M., Prince E. E., Abrams L. and Jones G. A., *Abstr. Pap. Am. Chem. Soc.*, **1987**, *193*, 300-INOR
39. Dyer A. and Enamy H., *Zeolites*, **1981**, *1*, 66-68
40. Ridha F. N., Yang Y. and Webley P. A., *Micropor. Mesopor. Mat.*, **2009**, *117*, 497-507
41. Newell P. A. and Rees L. V. C., *Zeolites*, **1983**, *3*, 22-27
42. Jackowski A., Zones S. I., Hwang S. J. and Burton A. W., *J. Am. Chem. Soc.*, **2009**, *131*, 1092-1100
43. Corma A., Diaz-Cabanas M. J., Jorda J. L., Rey F., Sastre G. and Strohmaier K. G., *J. Am. Chem. Soc.*, **2008**, *130*, 16482-16483
44. Shin J., Cambor M. A., Woo H. C., Miller S. R., Wright P. A. and Hong S. B., *Angew. Chem. Int. Edit.*, **2009**, *48*, 6647-6649
45. Palomino M., Corma A., Jorda J. L., Rey F. and Valencia S., *Chem. Commun.*, **2012**, *48*, 215-217
46. Miyamoto M., Fujioka Y. and Yogo K., *J. Mater. Chem.*, **2012**, *22*, 20186-20189
47. Campo M. C., Ribeiro A. M., Ferreira A., Santos J. C., Lutz C., Loureiro J. M. and Rodrigues A. E., *Sep. Purif. Technol.*, **2013**, *103*, 60-70
48. Remy T., Peter S. A., Van Tendeloo L., Van der Perre S., Lorgouilloux Y., Kirschhock C. E. A., Baron G. V. and Denayer J. F. M., *Langmuir*, **2013**
49. Ridha F. N. and Webley P. A., *Sep. Purif. Technol.*, **2009**, *67*, 336-343
50. Ridha F. N. and Webley P. A., *Micropor. Mesopor. Mat.*, **2010**, *132*, 22-30

51. Palomino M., Corma A., Rey F. and Valencia S., *Langmuir*, **2009**, 26, 1910-1917
52. Bonenfant D., Kharoune M., Niquette P., Mimeault M. and Hausler R., *Sci. Technol. Adv. Mater.*, **2008**, 9, 1-7
53. Yamazaki T., Katoha M., Ozawaa S. and Oginoa Y., *Mol. Phys.*, **1993**, 80, 313-324
54. Khelifa A., Derricheb Z. and Bengueddache A., *Micropor. Mesopor. Mat.*, **1999**, 32, 199-209
55. Huang M. and Kaliaguine S., *J. Chem. Soc., Faraday Trans.*, **1992**, 88, 751-758
56. Calleja G., Pau J. and Calles J. A., *J. Chem. Eng. Data*, **1998**, 43, 994-1003
57. Inui T., Okugawa Y. and Yasuda M., *Ind. Eng. Chem. Res.*, **1988**, 27, 1103-1109
58. Gallei E. and Stumpf G., *J. Colloid Interf. Sci.*, **1976**, 55, 415-420
59. Pirngruber G. D., Raybaud P., Belmabkhout Y., Cejka J. and Zukul A., *Phys. Chem. Chem. Phys.*, **2010**, 12, 13534-13546
60. Barrer R. M. and Gibbons R. M., *Trans. Faraday Soc.*, **1965**, 61, 948-961
61. Cundy C. S. and Cox P. A., *Chem. Rev.*, **2003**, 103, 663-702
62. Lok B. M., Messina C. A., Patton R. L., Gajek R. T., Cannan T. R. and Flanigen E. M., *J. Am. Chem. Soc.*, **1984**, 106, 6092-6093
63. Ashtekar S., Chilukuri S. V. V. and Chakrabarty D. K., *J. Phys. Chem.*, **1994**, 98, 4878-4883
64. Tang B., Lu X. H., Zhou D., Tian P., Niu Z. H., Zhang J. L., Chen X. and Xia Q. H., *Catal. Commun.*, **2013**, 31, 42-47
65. Arevalo-Hidalgo A. G., Almodovar-Arbelo N. E. and Hernandez-Maldonado A. J., *Ind. Eng. Chem. Res.*, **2011**, 50, 10259-10269
66. Talesh S. S. A., Fatemi S., Hashemi S. J. and Ghasemi M., *Separ. Sci. Technol.*, **2010**, 45, 1295-1301
67. Venna S. R. and Carreon M. A., *Langmuir*, **2011**, 27, 2888-2894
68. Liang J., Li H. Y., Zhao S., Guo W. G., Wang R. H. and Ying M. L., *Appl. Catal.*, **1990**, 64, 31-40
69. Barger P. T. and Lesch D. A., *Arab. J. Sci. Eng.*, **1996**, 21, 263-272
70. Rivera-Ramos M. E., Ruiz-Mercado G. J. and Hernandez-Maldonado A. J., *Ind. Eng. Chem. Res.*, **2008**, 47, 5602-5610
71. Arevalo-Hidalgo A. G., Santana J. A., Fu R. Q., Ishikawa Y. and Hernandez-Maldonado A. J., *Micropor. Mesopor. Mat.*, **2010**, 130, 142-153

72. Narasimharao K., Hartmann M., Thiel H. H. and Ernst S., *Micropor. Mesopor. Mat.*, **2006**, *90*, 377-383
73. Srasra M., Delsarte S. and Gaigneaux E. M., *J. Phys. Chem. C*, **2010**, *114*, 4527-4535
74. Kerr G. T. and Shipman G. F., *J. Phys. Chem.*, **1968**, *72*, 3071
75. Stein A., Wehrle B. and Jansen M., *Zeolites*, **1993**, *13*, 291
76. Luz Z. and Vega A. J., *J. Phys. Chem.*, **1987**, *91*, 374-382
77. Dogan F., Hammond K. D., Tompsett G. A., Huo H., Conner W. C., Auerbach S. M. and Grey C. P., *J. Am. Chem. Soc.*, **2009**, *131*, 11062-11079
78. Hammond K. D., Gharibeh M., Tompsett G. A., Dogan F., Brown A. V., Grey C. P., Auerbach S. M. and Conner W. C., *Chem. Mater.*, **2010**, *22*, 130-142
79. Li S., Zheng A., Su Y., Zhang H., Chen L., Yang J., Ye C. and Deng F., *J. Am. Chem. Soc.*, **2007**, *129*, 11161-11171
80. Kunkeler P. J., Zuurdeeg B. J., Van der Waal J. C., Van Bokhoven J. A., Koningsberger D. C. and Van Bekkum H., *J. Catal.*, **1998**, *180*, 234-244
81. De Lucas A., Canizares P., Durán A. and Carrero A., *Appl. Catal. A-Gen.*, **1997**, *154*, 221-240
82. Engelhardt G., Lohse U., Samoson A., Mägi M., Tarmak M. and Lippmaa E., *Zeolites*, **1982**, *2*, 59-62
83. Agostini G., Lamberti C., Palin L., Milanesio M., Danilina N., Xu B., Janousch M. and Van Bokhoven J. A., *J. Am. Chem. Soc.*, **2009**, *132*, 667-678
84. Yu Z., Zheng A., Wang Q., Chen L., Xu J., Amoureux J. P. and Deng F., *Angew. Chem. Int. Edit.*, **2010**, *49*, 8657-8661
85. Beyer H. K., Belenykaja I. M., Hange F., Tielen M., Grobet P. J. and Jacobs P. A., *J. Chem. Soc., Faraday Trans.*, **1985**, *81*, 2889-2901

2. Characterisation of Materials

2.1. Basic Crystallography¹⁻³

A ‘lattice’ is a periodic arrangement of points in space. A lattice with an atom or a group of atoms associated with each lattice point (motif or basis) is called a ‘crystal’. The smallest and simplest unit of the crystal by which periodic repetition generates the entire crystal (without overlaps or gaps) is called a ‘unit cell’. The unit cell is described by three edge vectors a , b and c , and the angles between them α , β and γ which are together called ‘the unit cell parameters’. The positions of the atoms inside the unit cell are described by the set of atomic positions x , y and z .

In three dimensions there are seven crystal systems which differ in unit cell parameters: triclinic, monoclinic, orthorhombic, tetragonal, trigonal, hexagonal and cubic (Table 2.1), and four lattice centering types: primitive (P) – lattice points only at the corners of the unit cell; body-centred (I) – lattice points at the corners and one lattice point in the middle of the unit cell; face-centred (F) – lattice points at the corners and at centres of all faces of the unit cell and end-centred or base-centred (C) – lattice points at the corners and at the centres of a pair of opposite faces (Figure 2.1).

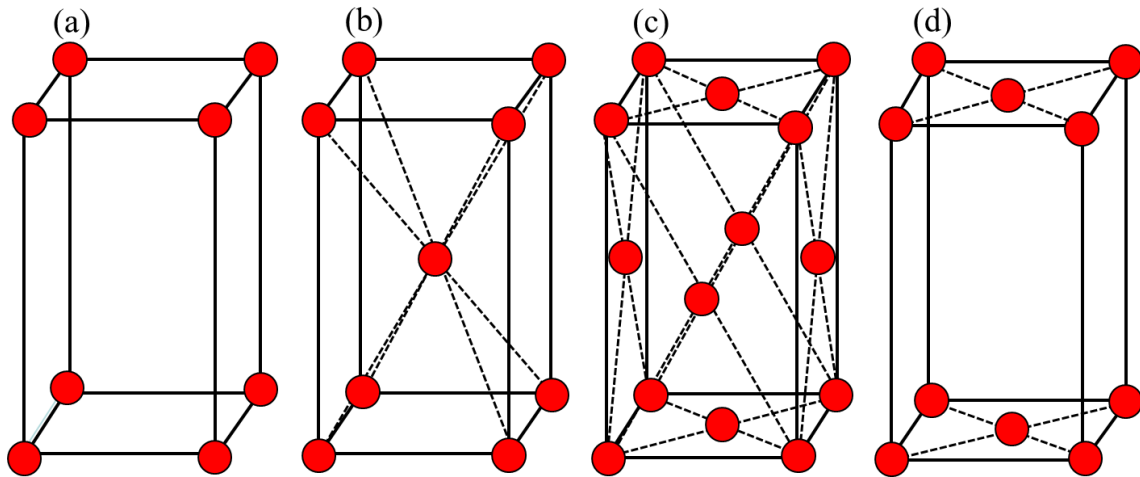


Figure 2.1. Four lattice centerings: (a) primitive (P), (b) body-centred (I), (c) face-centred (F) and (d) end-centred or base-centred (C).

The combination of the seven crystal systems and four lattice centering types produces 14 unique Bravais lattices (Table 2.1), introduced by Auguste Bravais in 1850.

Table 2.1. The seven crystal systems with unit cell parameters and Bravais lattices.

Crystal system	Unit cell parameters	Bravais lattices
Cubic	$a = b = c;$ $\alpha = \beta = \gamma = 90^\circ$	$P \quad I \quad F$
Tetragonal	$a = b \neq c;$ $\alpha = \beta = \gamma = 90^\circ$	$P \quad I$
Hexagonal	$a = b \neq c;$ $\alpha = \beta = 90^\circ; \gamma = 120^\circ$	P
Trigonal or rhombohedral	$a = b = c;$ $\alpha = \beta = \gamma \neq 90^\circ$	P
Orthorhombic	$a \neq b \neq c;$ $\alpha = \beta = \gamma = 90^\circ$	$P \quad I \quad F \quad C$
Monoclinic	$a \neq b \neq c;$ $\alpha = \gamma = 90^\circ; \beta \neq 90^\circ$	$P \quad C$
Triclinic	$a \neq b \neq c;$ $\alpha \neq \beta \neq \gamma$	P

Lattices are classified on the basis of their symmetry. The space groups represent a description of the symmetry of the crystal. The 14 Bravais lattices were combined with point (for example symmetry around the point or rotation axes) and space (for example screw axes or glide planes) symmetry elements in the derivation of the 230 space groups in 1891. The space group symmetry elements and their symbols are listed in Table 2.2. For example, the space group symbol $Pnma$ indicates a primitive (P), orthorhombic space group with the n -glide plane perpendicular to the a -axis, a mirror plane perpendicular to the b -axis, and the a -glide plane perpendicular to the c -axis.

Table 2.2. Space group symmetry elements and their symbols.

Symmetry element	Symbol
Inversion (or a centre of symmetry)	$\bar{1}$
Mirror plane (or plane of symmetry)	$m (\equiv \bar{2})$
Glide planes	a, b, c, d, n
Rotation axis (or n -fold rotation)	$2, 3, 4, 6$
Screw axis	$2_1, 3_1, 3_2, 4_1, 4_2, 4_3, 6_1, 6_2, 6_3, 6_4, 6_5$
Rotary inversion axis	$\bar{3}, \bar{4}, \bar{6}$

The planes in lattices and crystals are characterised by their Miller indices, introduced by British mineralogist William Hallows Miller in 1839. The Miller indices describe how the crystal planes intersect the main crystallographic axes of the crystal. They are quoted as set of numbers hkl and specify only orientation in space and not the position or sense of the plane. For example, when the first plane out from the origin cuts x axis at

$a/2$, the y axis at $b/2$ and the z axis at $c/3$, the Miller indices for this plane are (223). Zero represents that the plane is parallel to the corresponding axis and a negative sign indicates that the plane cuts the axis in the negative direction (the intercept has a negative value).

2.2. Powder X-ray Diffraction^{1,3-7}

2.2.1. Introduction

The properties of porous materials are dependent on their structure. It is necessary to fully characterise these structures to understand the factors that govern these properties and gain the insight necessary for the development of new porous materials. Porous materials may have complex structures, and often have large unit cells, which can make the determination of their structure difficult, particularly for powder data. Structure solution of zeolite can be achieved by using single crystal X-ray diffraction, but this requires single crystals at least 150–250 μm in size, whereas the zeolites analysed in this study are polycrystalline – they do not produce high quality large single crystals but rather many tiny crystals, some exhibiting intergrowth. Mesoporous silicas SBA-1 and SBA-2 are paracrystalline (no long-range atomic order). For all materials investigated in this study, powder X-ray diffraction (PXRD) was used as the primary method for determining whether a sample is pure, quantitatively analysing the composition of a bulk sample and obtaining diffraction data for refinement of crystal structures.

2.2.2. X-ray Source

X-rays are electromagnetic radiation with wavelengths in the range of 0.01–10 nm. In laboratory diffractometers X-ray are generated in an X-ray tube (Figure 2.2a), where a high energy electron beam (produced by passing a current through a tungsten filament – cathode) is accelerated towards a metal target (anode). Some of the electrons collide with the electrons of the metal anode, expelling them from inner shells. Electrons of higher energy from an outer orbital drop down to occupy the vacant shell, losing excess energy as X-ray radiation (Figure 2.2b). Continuous ‘white radiation’, as well as lines characteristic of K-shell electronic transitions, induced in the metal target, are emitted from an X-ray tube through a ‘window’ made of beryllium.

A monochromator is commonly used to isolate the K_{α} wavelength, which is the most intense X-ray spectral line for an element bombarded with energy sufficient to cause maximally intense X-ray emission. The most common metal used as an anode (also in this study) is copper. For copper, there are two K-shell electronic transitions, K_{α} and K_{β} , where the K_{α} ($\lambda = 1.5418 \text{ \AA}$), $2p \rightarrow 1s$ transition, is more intense than the K_{β} ($\lambda = 1.3922 \text{ \AA}$), $3p \rightarrow 1s$ transition. Depending on spin states of the $2p$ electron which makes the transition, relative to the spin of the vacant $1s$ orbital, two K_{α} transitions with different energy, K_{α_1} ($\lambda = 1.54051 \text{ \AA}$) and K_{α_2} ($\lambda = 1.54433 \text{ \AA}$), are generated (Figure 2.2c). Values of the K_{α} for other (than copper) common metal anodes are: 0.7107 \AA for Mo, 1.9373 \AA for Fe, 2.2909 \AA for Cr and 1.7902 \AA for Co.

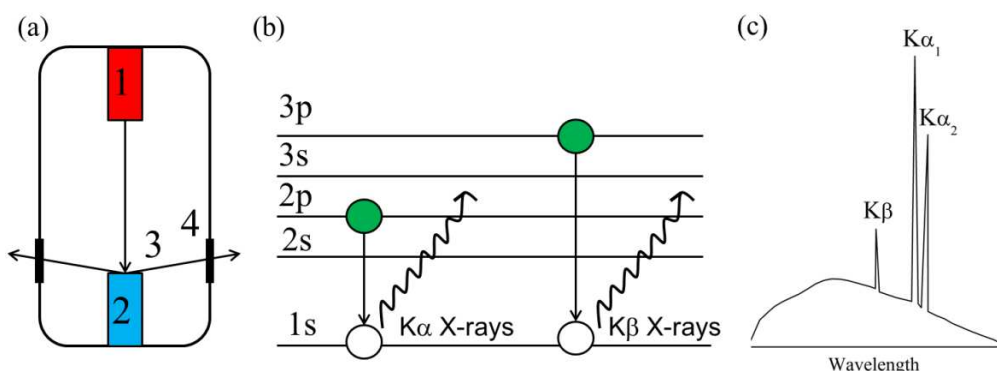


Figure 2.2. (a) Schematic illustration of a laboratory X-ray tube, showing (1) cathode, (2) anode, (3) X-rays and (4) Be windows. (b) Generation of Cu K_{α} and K_{β} X-rays, where $2p$ and $3p$ electrons fall into the empty $1s$ levels and the excess energy is released as X-radiation. (c) X-ray emission spectrum of Cu (background ‘hump’ is white radiation, or bremsstrahlung’).

2.2.3. Bragg’s Law

Diffraction occurs when a wave encounters an obstacle of a size that is comparable to the wavelength of the radiation. In 1912, Max von Laue, a German physicist, proposed that X-rays will be diffracted by a crystalline material because the wavelength is similar to the spacing between atoms in crystals (*ca.* 1 \AA). A year later, William H. Bragg and his son, William L. Bragg, deduced the equation:

$$n\lambda = 2AB = 2d_{hkl} \sin\theta \quad (2.1)$$

where n is an integer, λ is the wavelength of incident wavefront, d is the spacing between the planes in the atomic lattice, and θ is the angle between the incident ray and

the scattering planes. It describes diffraction as ‘reflection’ from lattice planes, where incident and reflected X-rays are making the same angle θ with the (hkl) planes (Figure 2.3). X-rays with incidence θ different from the Bragg angle are not scattered in such a way to give constructive interference. The path difference (red arrows, Figure 2.3) between ‘reflected’ X-rays must be an integral number of wavelengths and the d-spacing should be greater than half the wavelength of the X-rays used (if $d < \lambda/2$, then $\sin\theta > 1$, which is impossible).

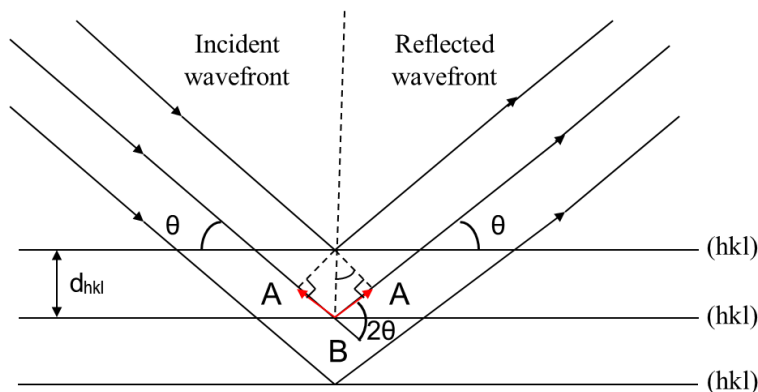


Figure 2.3. Condition for Bragg reflection from (hkl) planes with spacing d_{hkl} , where the path difference between incident and reflected X-rays is $2AB$ and X-ray incident on a set of planes at the Bragg angle θ are diffracted through an angle 2θ .

2.2.4. Principles of Powder X-ray Diffraction

A powder sample contains crystals arranged in all possible orientations and the set of planes in different crystals will be oriented at different angles around the incident beam. Some of the planes in crystals must be oriented at the Bragg angle, θ , to the incident beam, the diffraction occurs from these planes and a pattern of spots will be produced. Spots which are obtained by X-ray diffraction from the same (hkl) plane with the same Bragg angle but different orientation will form the surface of a cone (the Debye diffraction cones, Figure 2.4). Crushing (before measurement) or spinning/rotating (during measurement) the sample increases the number of the (hkl) planes orientations and more crystallites satisfy the Bragg conditions.

Patterns on powder diffractometers are typically obtained by scanning cones in the radial direction and are usually presented as plots of diffracted intensity versus 2θ . Every crystalline material (for example zeolite and zeotypes) will give a characteristic

diffraction pattern which can act as a unique ‘fingerprint’, with sharply defined diffraction peaks (Figure 2.5a). The diffraction peaks can be used for qualitative and quantitative analysis of crystalline structures. The diffraction patterns of crystalline materials may be compared against those in a computerised database, for example that of the International Centre for Diffraction Data (ICDD),⁸ to find a match. By this method, identification of any crystalline compound, even in a complex sample or in a mixture of crystalline phases, can be made. If it is possible to index an unknown crystalline diffraction pattern, the structure of a new crystalline material may be determined and refined. The diffraction patterns of mesoporous silicas (Figure 2.5b) show only broad peaks in the low angle region (below $10^\circ 2\theta$), which is due to the amorphous nature (no long-range atomic order) of the silica walls. It is possible to calculate the unit cell parameters for these materials but atomic positions cannot be determined.

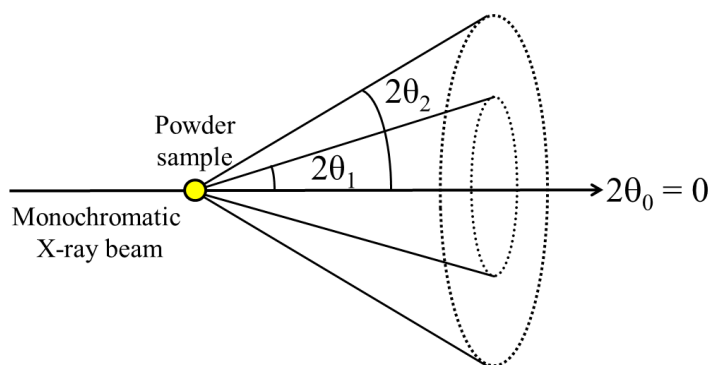


Figure 2.4. Diffraction from a powder sample showing the Debye diffraction cones of X-rays.

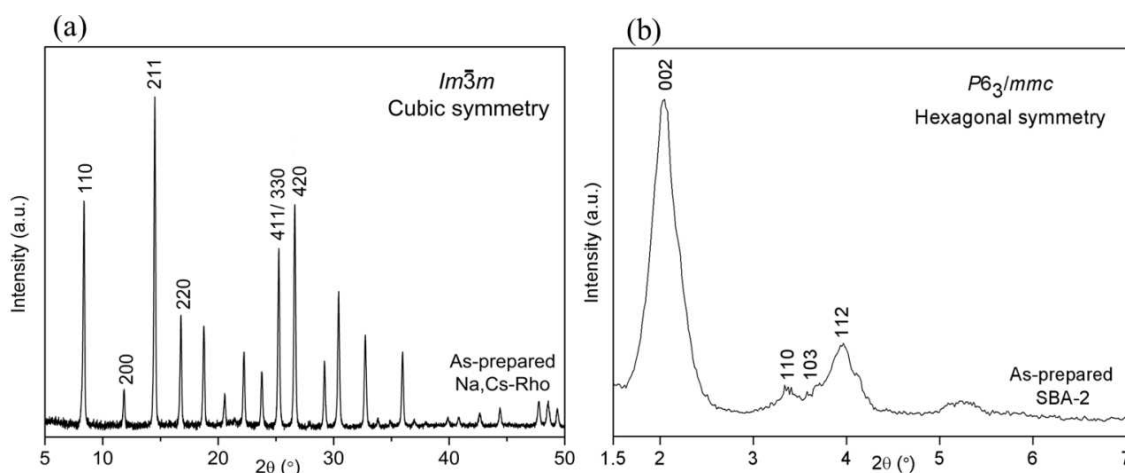


Figure 2.5. X-ray powder diffraction patterns of (a) as-prepared zeolite Na,Cs-Rho and (b) as-prepared SBA-2, collected at the University of St Andrews and indexed with cubic and hexagonal symmetry, respectively.

2.2.5. Diffractometers

Diffractometers for powder diffraction can be operated in transmission and in reflection configurations. A Stoe STAD i/p diffractometer working in capillary (transmission) mode using Debye-Scherrer geometry and a PANalytical diffractometer working in reflection mode using Bragg-Brentano geometry were used to characterise materials in this study. The advantages and disadvantages of both diffractometers are presented in Table 2.3.

Table 2.3. Advantages and disadvantages of diffractometer with Debye-Scherrer geometry and capillary (transmission) mode, and diffractometer with Bragg-Brentano geometry and reflection mode.

	Debye-Scherrer geometry	Bragg-Brentano geometry
Intensities	low	high
Absorption correction	yes	no
Low angle measurement	yes	yes
Small sample sizes (0.01–0.1 mg)	yes	no
Sensitive or dehydrated samples measurement	yes	no

The Debye-Scherrer geometry (Figure 2.6a) is one of the oldest known powder diffraction geometries. In the diffractometer with capillary (reflection) mode and Debye-Scherrer setup the sample is held in a glass or quartz capillary, which spins on its axis to increase the number of accessible crystallite orientations. Sealing the capillary with the powder sample before measurement allows dehydrated or air-sensitive samples to be studied. The monochromator is used to select only the Cu $K_{\alpha 1}$ radiation and the divergence slit restricts the size of the monochromatic beam.

In the diffractometer operating with reflection mode and Bragg-Brentano geometry (Figure 2.6b), the detector is always at 2θ and the sample surface is always at θ to the incident X-ray beam. In the theta-2:theta geometry the tube is fixed, the sample rotates at θ°/min and the detector rotates at $2\theta^\circ/\text{min}$. In the theta:theta geometry the sample is fixed and the tube rotates at a rate $-\theta^\circ/\text{min}$ and the detector rotates at a rate of θ°/min . The goniometer (platform) is used to hold and move the sample, optics and detector. Slits restrict the size of the beam. The divergence and scattering slits limit beam spread parallel to the diffraction plane, where Soller slits for incident and

scattered beam limit beam spread perpendicular to the diffraction plane. The sizes of the slits determine the intensity and shape of the diffraction peaks. Narrow slits will reduce the peak intensity but the instrumental resolution will be improved.

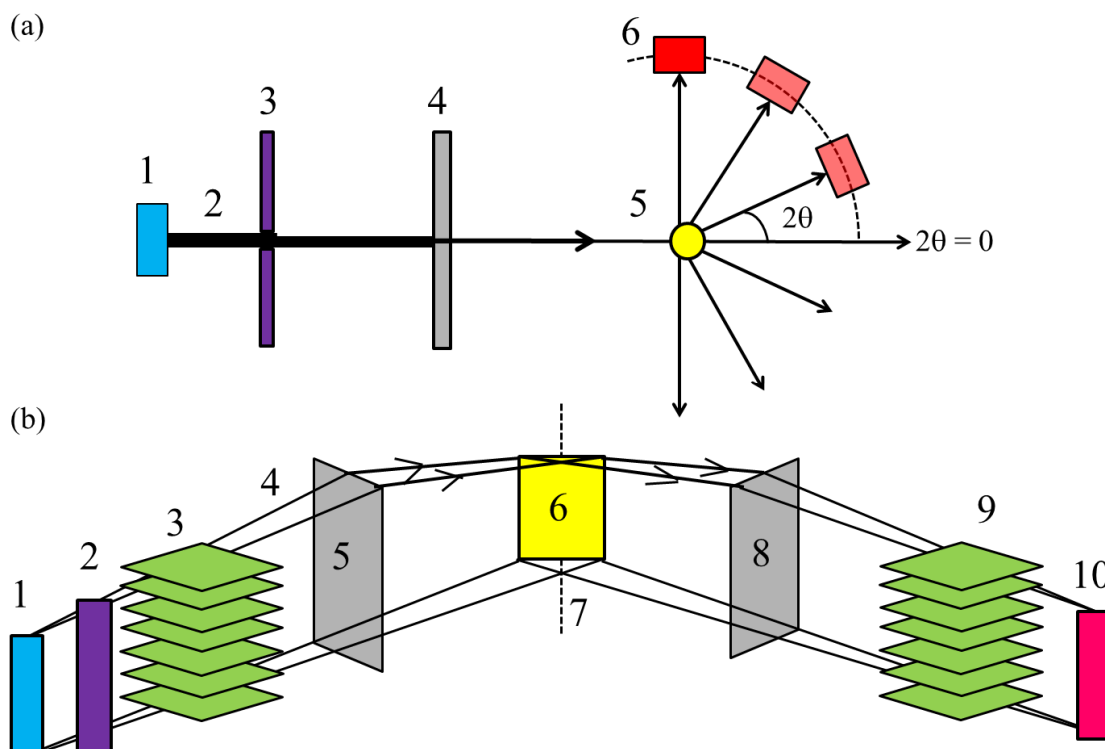


Figure 2.6. Schematic illustrations of diffractometers used at the University of St Andrews with (a) Debye-Scherrer geometry showing (1) Cu X-ray tube, (2) beam of X-rays, (3) primary monochromator, (4) divergence slit (5) capillary with a sample, (6) detector (movable counter), and (b) with Bragg-Brentano geometry showing (1) X-ray source, (2) primary monochromator (3) Soller slits for incident beam, (4) beam of monochromatic X rays, (5) divergence slit, (6) sample, (7) goniometer (platform) axis, (8) scattering slit, (9) Soller slits for scattered beam and (10) detector.

2.2.6. Synchrotron Radiation

An alternative source of X-rays, suitable for determining the structure of very small crystals and for getting high resolution data (for structure refinement) is synchrotron radiation. A synchrotron accelerates electrons at a speed close to the speed of light, generating an intense beam of X-rays. The electrons are directed around a circular path (storage ring) by magnets and the required wavelength of radiation is selected using

a monochromator and it is directed to experimental stations located on different beamlines. Beamline I11 uses X-ray radiation for high resolution powder diffraction at the Diamond Light Source, located at the Harwell Science and Innovation Campus in Oxfordshire,⁷ and it was used for examining Na-chabazite and Na-Rho samples in this study. Prior to X-ray diffraction measurement, it was possible to dehydrate the sample *in situ* (using heat gun and cryostream) and adsorb CO₂ at low pressures, up to 1 bar. High quality, high resolution powder patterns were recorded with short scan times via multi-element analyser stages while fast, wide-angle position sensitive detectors allowed the rapid collection of powder patterns (Figure 2.7).

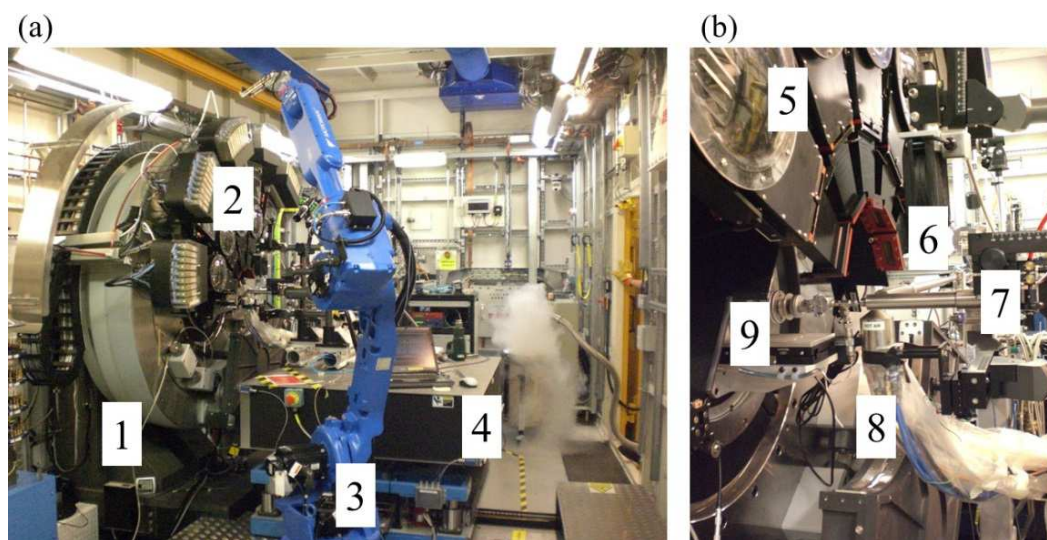


Figure 2.7. (a) Beamline I11 experimental hutch showing: (1) heavy duty diffractometer, (2) five arms on 2θ circle with multi-analysing crystal-detectors (9 detectors on top of each arm), (3) robotic-arm and (4) heavy duty table. The magnified image (b) shows (5) Si(111) analysing crystals ($\times 9$), (6) beam pipe, (7) cryostream for heating and cooling, (8) heat gun, and (9) sample stage.

2.2.7. Powder Structure Determination: Le Bail and Rietveld Refinement Methods

The Rietveld method is a least squares whole-pattern fitting structure refinement technique that has been used successfully for quantification and characterisation of crystalline structures. It can give information about framework topology, unit cell parameters, atomic coordination, bond lengths and angles.

In this study, the Rietveld method was used to refine the structures (including the positions of extra-framework cations and CO₂ molecules) of dehydrated zeolites and zeotype before and after CO₂ adsorption.

Before Rietveld refinement, the Le Bail method was applied. The Le Bail fitting is a whole pattern structureless fitting useful for refining unit cell lattice parameters, instrumental parameters and identifying impurities. Using the Le Bail method before Rietveld refinement helps to establish the instrumental parameters (especially background and profile) before fitting the structure; to estimate best possible fit when profiles are irregular (for example asymmetric peak shape); and to fit an additional phase when the structure is not known but it may be indexed. Le Bail and Rietveld methods are a part of the General Structure Analysis System (GSAS) software package.⁴

Rietveld refinement compares an observed diffraction pattern with a calculated diffraction pattern for the model using a least squares method. The method of least squares assumes that the best-fit curve of a given type is the curve that has the minimal sum of the deviations squared from a given set of data.

$$S = \sum w_i |y_{i0} - y_{ic}|^2 \quad (2.2)$$

where:

$$(w_i)^{-1} = \sigma_{ip}^2 + \sigma_{ib}^2 \quad (2.3)$$

and y_{i0} – observed intensity at the i^{th} step, y_{ic} – calculated intensity at the i^{th} step, w_i – weight factor, σ_{ip} – standard deviation associated with the peaks and σ_{ib} – standard deviation associated with background.

The Rietveld method refines a theoretical line profile until it matches the measured profile. It minimises the difference between observed and calculated powder patterns and takes overlapping peaks into account. The difference between the profile calculated from the model and that observed experimentally is quantified by the goodness of fit: weighted profile R value (R_{wp}) and chi squared (χ^2).⁹

$$R_{wp} = \left[\frac{\sum w_i (y_{i0} - y_{ic})^2}{\sum w_i y_{i0}^2} \right]^{\frac{1}{2}} \quad (2.4)$$

$$\chi^2 = \left(\frac{R_{wp}}{R_{exp}} \right)^2 \quad (2.5)$$

Expected R factor (R_{exp}) is called “best possible R_{wp} ” quantity. R_{wp} factor values vary according to the statistics of the experimental data set. The optimum value for χ^2 is 1.0. Refinement of the instrumental and structural parameters of the model minimises R_{wp} and χ^2 . Missing atoms, for example extra-framework cation or adsorbed gas, can be found on the basis of electron density peaks in the difference Fourier analyses which compare ‘experimental’ electron density with that of the model. The structure refinement improves the fit until further modifications give no significant improvement. More details about this technique are given in the text edited by Young.⁶ Figure 2.8 illustrates the final observed, calculated and difference Rietveld plot for the powder data refinement of dehydrated Na-Rho with CO₂ molecules adsorbed, studied by synchrotron X-ray powder diffraction at the Diamond Light Source in United Kingdom, where refinement enables the sodium cations and CO₂ molecules to be located.

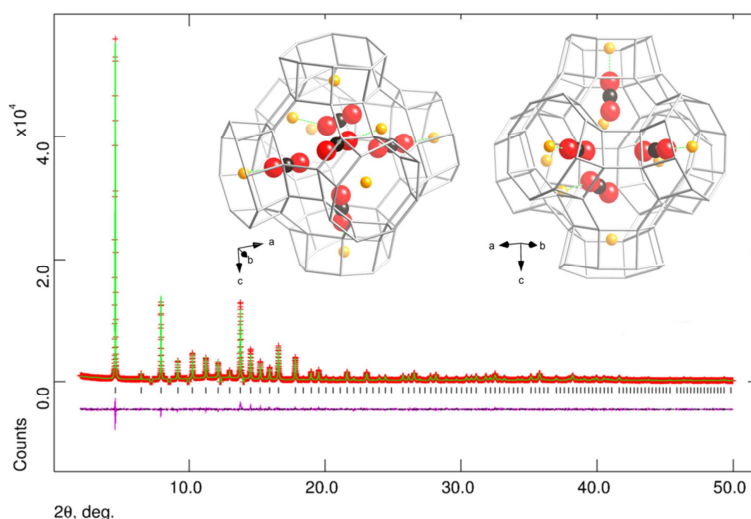


Figure 2.8. Final observed, calculated and difference Rietveld plot for the powder data refinement of dehydrated Na-Rho with CO₂ molecules adsorbed (insert), studied by synchrotron X-ray powder diffraction.

In the Rietveld refinement determination of site-occupancy parameters is considered to be less accurate than the determination of positional parameters. There is a correlation between the site-occupancy and thermal parameters (UISO), because both parameters are primarily $\sin\theta/\lambda$ dependent. For this reason thermal parameters are often fixed at literature values or constrained to have a common value for several independent atoms.¹⁰

2.3. Adsorption^{5,11-14}

In this study, adsorption measurements were used to determine the porosity of a structure. The porosity was initially determined by the adsorption of N₂ at 77 K. The CO₂ uptakes at low (up to 1 bar), and CO₂ and CH₄ uptakes at high (up to 9 bar) pressures were also measured.

Adsorption is the process of binding of molecules or particles from an adjacent gas or liquid to an exposed surface. Zeolites, zeotypes and mesoporous solids have strong abilities to take up molecules from the liquid or gas phase. Small molecules diffuse through the pore windows of these solids to an internal surface area many times greater than the external surface area. The adsorbed molecules may diffuse between adsorption sites in different cages and along channels.

Adsorption can be measured in two different ways by gravimetric and volumetric methods. Gravimetric methods measure the uptake as the increase in weight of a sample as the adsorbate pressure is varied. In volumetric methods the changes in pressure upon dosing a known amount of gas into a volume containing the sample are measured and the uptake is calculated from this.

Adsorption can be classified according to the nature of the interaction between adsorbate molecule and adsorbent into two categories: physical adsorption (physisorption) and chemical adsorption (chemisorption) (Table 2.4). During physisorption weak bonds between molecules and surface are created, through the interactions of induced or permanent dipoles or quadrupoles (commonly classified as van der Waals forces). During chemisorption a charge-transfer between adsorbate and surface takes place. For the adsorption of molecules such as N₂ or CO₂ on microporous solids weak or strong physisorption occurs, whereas adsorption of basic molecules onto acid sites is an important type of chemisorption. In 1938, Stephen Brunauer, Paul Hugh Emmett, and Edward Teller developed *Brunauer-Emmett-Teller* (BET) theory. The BET theory is based on a simplified model of multilayer physisorption.

Table 2.4. Differences between physisorption and chemisorption.

Physisorption	Chemisorption
Low heat of adsorption (20–40 kJ/mol)	High heat of adsorption (50–400 kJ/mol)
Van der Waals forces	Chemical bond forces
Reversible	Irreversible
Takes place at low temperature	Takes place at high temperature
No changes	Leads to chemical changes
Forms multimolecular layers	Forms monomolecular layers
No activation energy	Requires high activation energy
High pressure is favorable	High uptake at low adsorbate pressure
Decrease of pressure results in desorption	Decrease of pressure does not cause desorption

Adsorption is typically measured as an isotherm. An adsorption isotherm is the equilibrium uptake of a sorbate measured at a constant temperature as a function of its pressure (gas) or concentration (liquid).

In 1940 Brunauer, Deming and Teller introduced the first interpretation of adsorption isotherms for gas-solid equilibria. One of the methods for measuring surface areas and pore size distributions of crystalline microporous solids is the physical adsorption of nitrogen at 77 K. There are six types of isotherms (Figure 2.9) in the International Union of Pure and Applied Chemistry (IUPAC) classification. Isotherms of Type I characterise adsorption for microporous materials. These show a sharp initial increase followed by a plateau as the micropores and surface sites become filled. Type II isotherms describe adsorption on macroporous or open surface materials with strong adsorbate-adsorbent interaction, and Type III isotherms are observed for weak sorbate-adsorbent interactions. Types IV and V isotherms display hysteresis, which is also seen during the adsorption on mesoporous silicas, and is due to capillary condensation effects. The adsorption hysteresis arises from the metastability of a confined phase and the temperature at which the hysteresis disappears (hysteresis critical temperature) is lower than the critical temperature of vapor-liquid equilibrium in pores (pore critical temperature). The hysteresis occurs on the desorption rather than on the adsorption branch, irrespective of the pore geometries. Type VI isotherms possess steps, as well-defined cages are filled stepwise with increasing pressure.

Figure 2.10 presents experimental adsorption isotherms of N₂ at 77 K on mesoporous solids: MCM-41, SBA-1 and SBA-2. MCM-41 has cylindrical channels and gives N₂ adsorption isotherms of Type IV (see Figure 9), where initial monolayer coverage is

followed by multilayer adsorption. At a higher pressure capillary condensation of liquid nitrogen within the similarly sized mesopores takes place, resulting in a sharp increase in uptake. For SBA-1 and SBA-2 the capillary condensation step occurs at a low partial pressure because those materials possess mesoporosity on a length scale that bridges the microporous and mesoporous regimes. From the adsorption isotherm of a mesoporous material its surface area, a pore size distribution (from the condensation pressure range) and a total pore volume (from the maximum uptake before nitrogen condenses in the voids between particles) can be calculated.

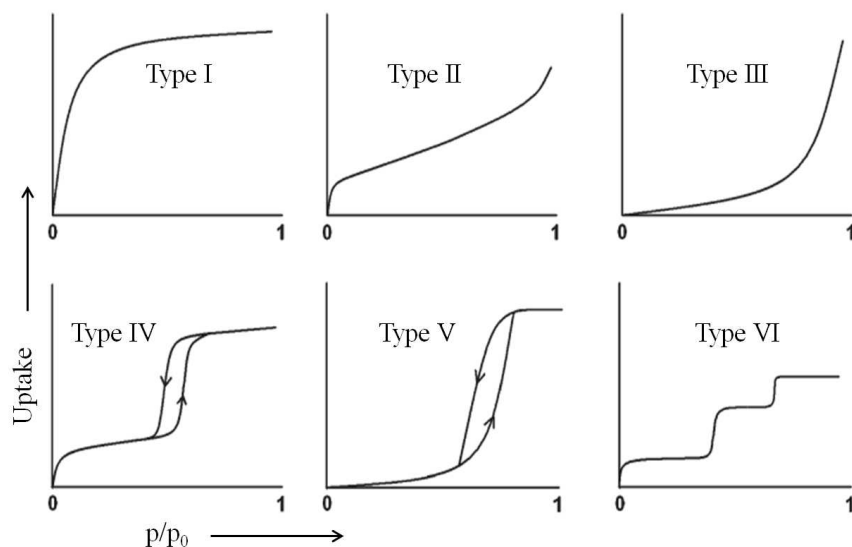


Figure 2.9. The Brunauer-DeMing-Teller classification of isotherms Type I to VI. P is the absorbate pressure and p_0 is the saturated vapour pressure of the pure liquid adsorbate at the isotherm temperature.⁵

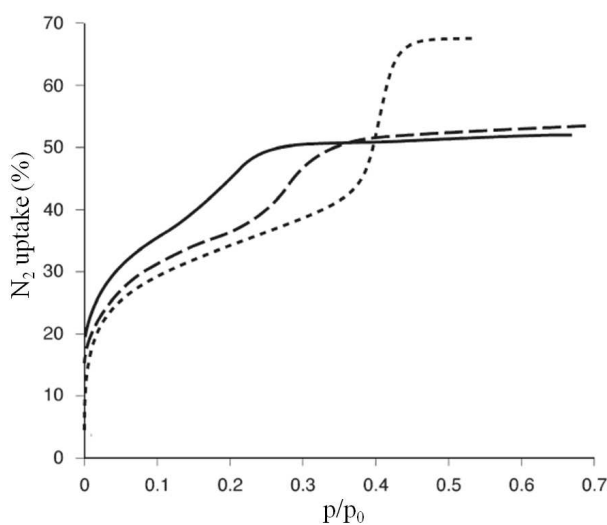


Figure 2.10. Experimental adsorption isotherms of N_2 at 77 K on: MCM-41 (•••), SBA-2 (--) and SBA-1 (—).⁵

The CO₂ adsorption at 0.1 bar and 298 K in this study was measured using the Zero Length Column (ZLC) method at the University of Edinburgh in collaboration with Enzo Mangano and Prof. Stefano Brandani. The ZLC method is a simple and relatively inexpensive technique for obtaining the required physical properties. It is a chromatographic technique which is based on following the desorption curve of a sample previously saturated with a mixture of 10% of CO₂ (sorbate) in He (carrier). When equilibrium between the gas phase and the adsorbed phase is reached, the flow is switched to pure He (purge) and the outlet gas phase concentration from the column is monitored. An on-line quadrupole mass spectrometer is connected to the ZLC to monitor the outlet gas concentration. The apparatus is provided with drying columns to ensure pre-dried gases entering the system. A very small amount of material (*ca.* 10 mg) is required to fill a ZLC. Before measurement, samples are dehydrated overnight under a flow of pure He.

2.4. Electron Microscopy (EM)^{5,15-17}

Electron microscopy (EM) was used in this study to obtain the topographical, morphological (which includes the size, shape and arrangement of detectable surface particles), compositional (energy dispersive X-ray analysis, EDX) and crystallographic information (electron diffraction) of as-prepared and ion exchanged materials. The primary advantage of EM is its powerful magnification but the disadvantages include its cost, size, maintenance, researcher training and image artifacts resulting from sample preparation.

2.4.1. Scanning Electron Microscopy (SEM)

In the scanning electron microscope (SEM, Figure 2.11), the electron beam is produced by a heated tungsten filament. The first and second condenser lenses form a thin and tight beam. The scan coils and objective lens direct and position the beam onto the sample surface. The electron beam is scanned over the surface of sample. When the electron beam hits the sample it generates low-energy secondary electrons, backscattered electrons, and characteristic X-rays, from near the sample surface. Low-energy secondary electrons are collected by a secondary electron detector. The number of electron interactions is counted and a pixel is displayed on a cathode ray tube (CRT)

screen. Thus, for each point on the sample there is a conjugate point on the CRT screen. This process is repeated until the scan is finished.

SEM images can show the topography of surface features a few nm across. The image displayed by an SEM maps the sample surface and shows the brightness variation (colours from grey to black), which depends on the number of detected secondary electrons. Thus, areas producing lots of electrons appear bright, where areas not producing many electrons appear dark (Figure 2.12). The number of secondary electrons depends on the topography of the sample.

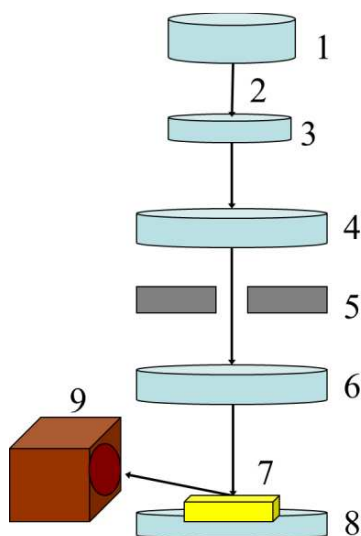


Figure 2.11. Schematic diagrams of the SEM showing (1) electron gun, (2) electron beam, (3) anode, (4) condenser, (5) scan coils, (6) objective lens, (7) sample, (8) stage and (9) secondary electron detector.

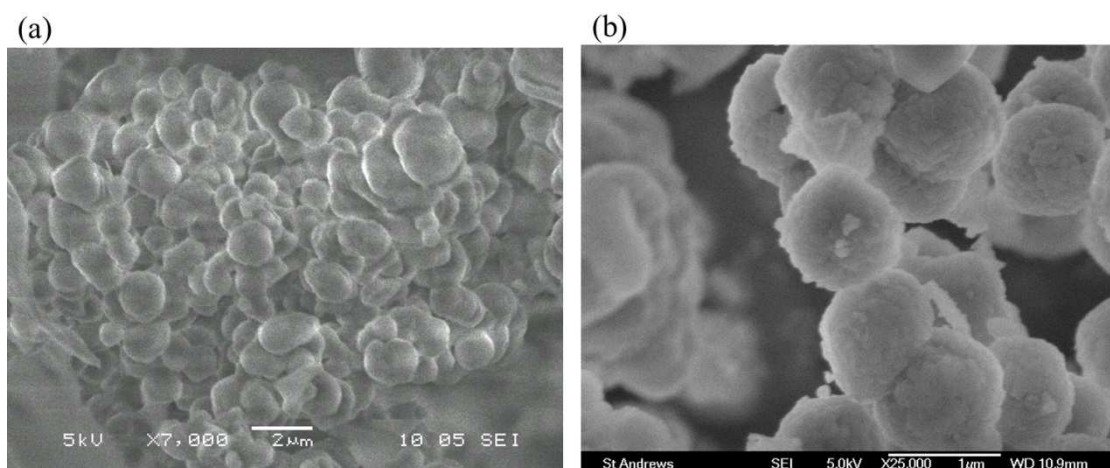


Figure 2.12. SEM micrographs of (a) mesoporous silica SBA-2 showing small particles with a spherical shape and (b) as-prepared zeolite Na,Cs-Rho showing particles built up from smaller crystallites.

2.4.2. High Resolution Transmission Electron Microscopy (HRTEM)

In contrast to SEM, in high resolution transmission electron microscopy (HRTEM, Figure 2.13) a beam of electrons is interacting with an ultra-thin sample (a thick sample decreases the number of electrons detected) as it passes through. The electrons (produced by a heated lanthanum hexaboride, LaB₆, filament) from electron gun travel to a condenser lens which focuses them into a very thin beam. The electron beam goes through a sample. Some of the electrons are absorbed and scattered. The transmitted electrons are focused by the objective lens into an image which is enlarged by a projector lens. The projector lens focuses electrons onto an imaging device, such as a fluorescent screen or charge coupled device (CCD) camera. The continuous image of the sample, usually green in colour, can be seen through a viewing window. Fine adjustments to the image are made while viewing it with an externally mounted binocular microscope.

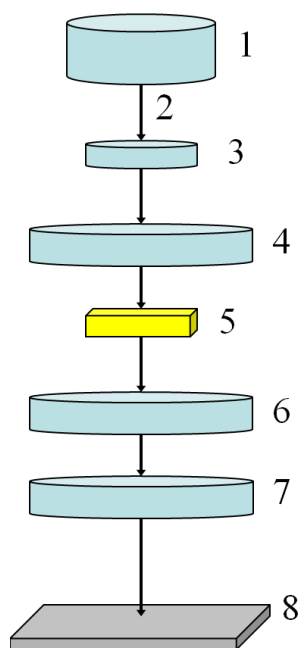


Figure 2.13. Schematic diagrams of the HRTEM showing (1) electron gun, (2) electron beam, (3) anode, (4) condenser, (5) sample, (6) objective lens, (7) projector lens and (8) fluorescent screen or charge coupled device (CCD) camera.

The HRTEM image is a two-dimensional projection of the density of scattering electrons in the sample, focused with the objective lens. Zeolites are very electron beam sensitive where the transformation from crystalline phase to amorphous phase occurs so

easily that it is difficult (but possible) to obtain HRTEM images of zeolites. This problem does not exist for mesoporous silicas (Figure 2.14) for which HRTEM is one of the main characterisation techniques.

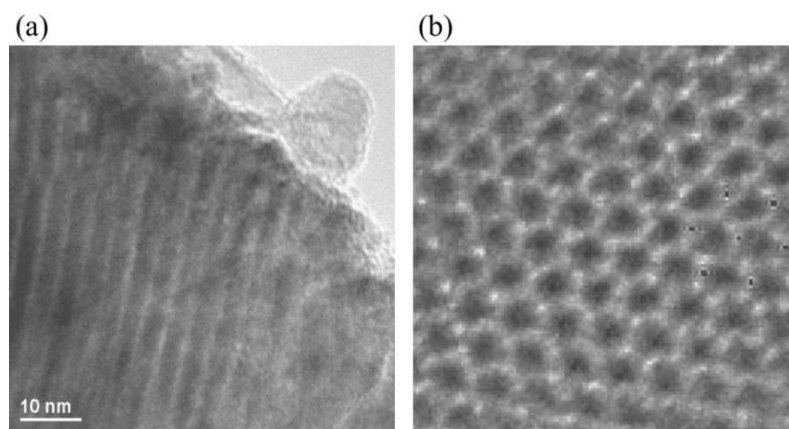


Figure 2.14. HRTEM images of (a) ordered pore arrays and (b) hexagonal pore arrangement in mesoporous silica SBA-2.

The most powerful use of HREM is in determining disordered structures or defects in the structures which are impossible to detect by other techniques.

Electron Diffraction

HRTEM allows not only structural information to be obtained, but it is also possible to establish the unit cell parameters and symmetry of material by investigating its electron diffraction pattern. The manipulation of lenses allows diffracted electrons to be focused into a regular arrangement of diffraction spots that are projected and recorded as the electron diffraction pattern. Diffraction spots are formed on the back focal plane and the image is formed on the image plane (Figure 2.15). It is possible to obtain electron microscope images and diffraction patterns simultaneously for the same region.

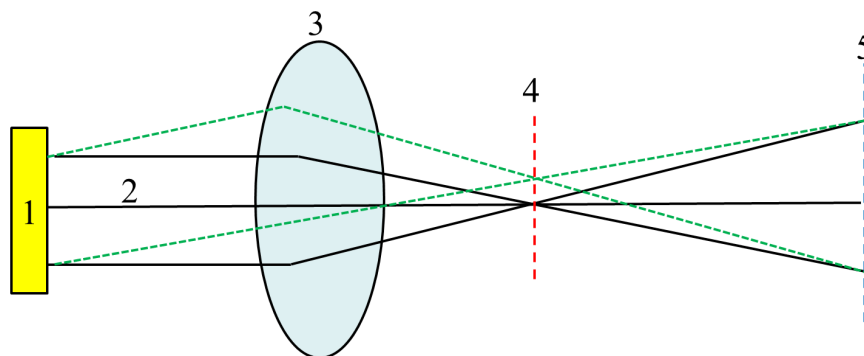


Figure 2.15. TEM's optical ray diagram showing (1) sample, (2) electron beam, (3) optical lens, (4) backfocal plane and (5) image plane.

For crystalline zeolites and zeotypes an electron pattern that consists of a pattern of dots (Figure 2.16) is obtained.

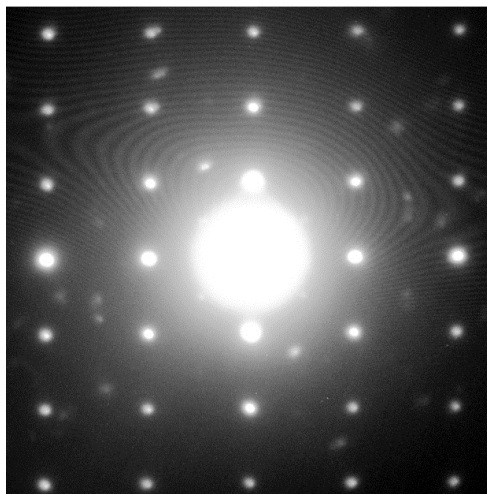


Figure 2.16. HRTEM electron pattern of zeolite Li-chabazite.

2.4.3. Energy Dispersive X-ray (EDX) Analysis

Energy dispersive X-ray (EDX) analysis works as an integrated part of the scanning electron microscopy (SEM) and high resolution transmission electron microscopy (HRTEM). EDX is a technique used for identifying the elemental composition of the materials. In this study it was used to confirm the amount of extra-framework cations that were exchanged and that no other unexpected elements are present after ion exchange.

In EDX analysis, the material is bombarded with an electron beam inside the electron microscope. The bombarding electrons collide with the electron from the atom, as a result knocking some of them out. Electrons transfer from a higher-energy shell occurs to fill the vacancies. During this transfer electrons emit X-ray radiation. By measuring the energy of the emitted characteristic X-ray the identity of the atom from which the X-ray was emitted can be established. The results of an EDX analysis are presented in the form of peaks on EDX spectrum (Figure 2.17). The position of the peaks is characteristic for each element. The more intense peak in a spectrum, the more concentrated the element is in the material. EDX calibration is performed using standard reference materials.

The precision of EDX is usually better than $\pm 1\%$ (relative error), but the overall analytical accuracy is commonly nearer $\pm 2\%$, due to the uncertainties in the

compositions of the standards and errors in the various corrections which need to be applied to the raw data. Detection limits are typically about 1000 ppm (by weight) but can be reduced by using long counting times.

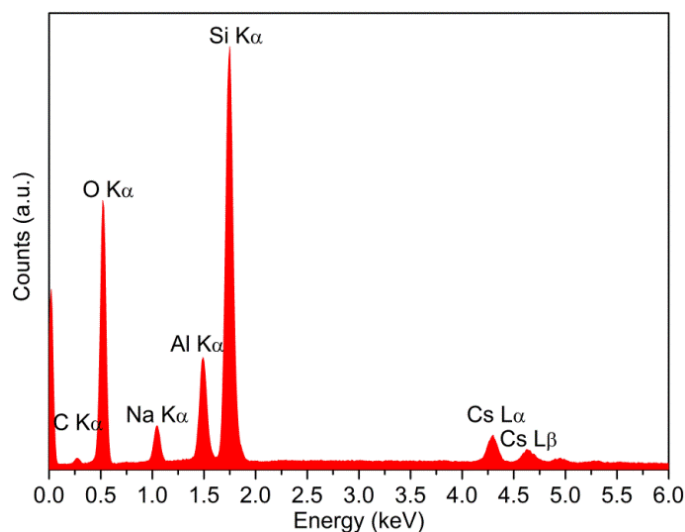


Figure 2.17. EDX spectrum of as-prepared Na,Cs-Rho showing framework Si, Al and O and extra-framework cations (Na and Cs).

2.5. Fourier Transform Infra-red (FTIR) Spectroscopy^{1,17,18}

Infra-red (IR) spectroscopy is one of the most common spectroscopic techniques used for sample analysis by organic and inorganic chemists. It is used to determine the chemical functional groups in the sample. Electromagnetic radiation in the IR region has wavelengths longer than visible waves (around 390–750 nm) and shorter than microwaves (around 1 mm – 1 m). The infra-red region is divided into: near-infra-red (closest to visible light), mid-infra-red (between near and far-infra-red) and far-infra-red (closest to the microwave region).

The bonds within molecules all vibrate at temperatures above absolute zero. The typical frequencies of these vibrations match the frequencies of IR radiation. Vibrations fall into the two main categories of stretching (change in inter-atomic distance along bond axis) and bending (change in angle between two bonds). Bending can be further divided into: rocking, scissoring, wagging and twisting. The vibrations which change the dipole moment of molecules (IR active), for example asymmetrical stretching and bending, will absorb in the infra-red region. Symmetrical stretching and bending do not change the dipole moment of molecules and they are usually not IR active. If the frequency

of the IR radiation matches the vibrational frequency of the IR active molecule then radiation will be absorbed, causing a change in the amplitude and energy of molecular vibration. The result of IR absorption is the release of heat since absorption increases molecular vibrational energy. Therefore absorption of IR is restricted only to excite vibrational and rotational states of a molecule. A molecule can be identified by its molecular vibrations during IR absorption, based on the absorption and intensity of specific infra-red wavelengths. Therefore the IR spectrum represents the set of IR active molecular vibrations in the sample.

In the interferometer (Figure 2.18), the beamsplitter takes the incoming infra-red beam and divides it into two optical beams where one beam reflects off a fixed mirror and the second beam reflects off a moving mirror (this mirror moves typically a few millimeters away from the beamsplitter). The two beams meet back at the beamsplitter where they are re-combined. Because the path that one beam travels is a fixed length and the other is constantly changing as the mirror moves, the signal which exits the interferometer is the result of these two beams interfering with each other and the resulting signal is called an 'interferogram'. The interferogram is measured and the recorded data contains information about every infra-red frequency that comes from the source. The resulting signal coming from the interferometer is then passed through the sample which absorbs (when the frequency of the signal is the same as the vibrational frequency of the bonds between atoms in the sample) and transmits (different frequency for signal and the bonds) some of the specific wavelengths which are subtracted from the interferogram. The resulting interferogram represents the molecular absorption and transmission and it creates a molecular fingerprint of the sample which is unique for every molecular structure. Because the analysis requires a frequency spectrum (a plot of the intensity at each individual wavelength) in order to make an identification, the measured interferogram signal cannot be interpreted directly and the 'decoding' can be accomplished via a mathematical technique called the Fourier transformation (FT). This transformation is performed by the computer which then presents the user with the desired spectral information for analysis. Usually, a 'background spectrum' is run and automatically subtracted from every spectrum is typically collected between 400 cm^{-1} and 4000 cm^{-1} . Analysis of the position, shape and

intensity of peaks in the subtracted spectrum reveals details about the molecular structure of the sample.

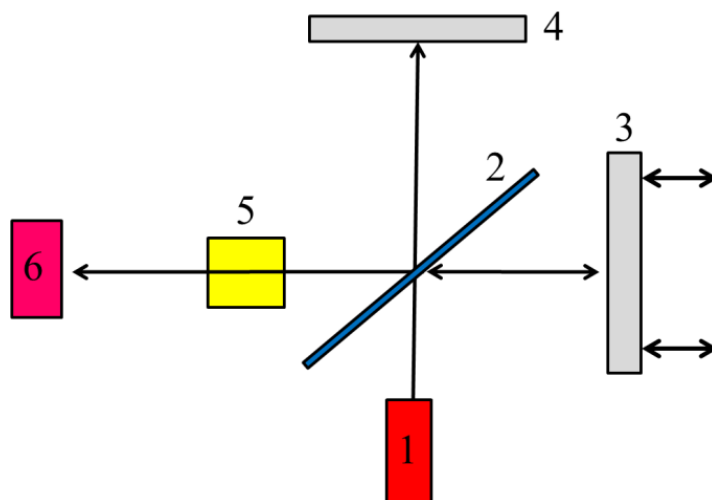


Figure 2.18. Diagram of basic FTIR system showing: (1) IR source, (2) beam splitter, (3) moving mirror, (4) fixed mirror, (5) sample cell and (6) detector.

In situ FTIR spectroscopy was used in this study to better characterise and understand the interactions of CO₂ with the framework and extra-framework cations in fully exchanged zeolites chabazite and Rho. The ν_3 asymmetric stretching vibration (red colour, Figure 2.19) is observed in the CO₂ infra-red spectrum which is due to an uneven distribution of charge which gives the CO₂ molecule a temporary dipole moment, enabling it to absorb infra-red radiation. Direct evidence for a CO₂:cation interaction in zeolites comes from observation of the ν_1 symmetric stretching CO₂ vibration as a weak band at 1378 cm⁻¹ (green colour, Figure 2.19). This vibration is infra-red forbidden for the gas phase molecule (at 1388 cm⁻¹) and it is not observed in CO₂ spectrum, but becomes weakly allowed due to interaction of CO₂ with zeolite cations.

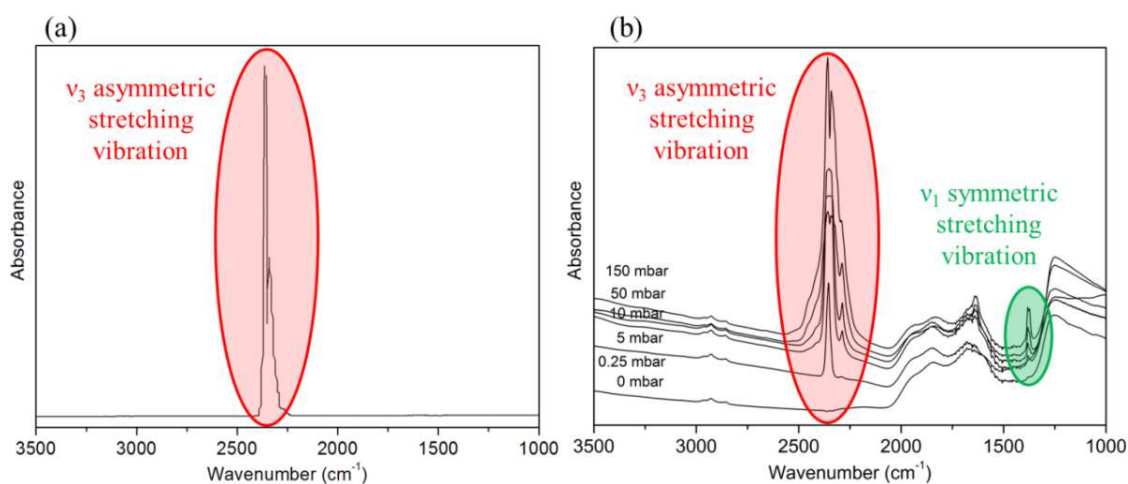


Figure 2.19. $3550\text{--}1000\text{ cm}^{-1}$ range of the infra-red spectra of (a) CO_2 and (b) CO_2 adsorbed on zeolite Li-Rho showing the ν_3 asymmetric stretching vibration for CO_2 (red colour) and the ν_1 symmetric stretching vibration for CO_2 :cation interaction (green colour).

2.6. Solid State Magic Angle Spinning (MAS) Nuclear Magnetic Resonance (NMR) Spectroscopy^{1,5,18-20}

Solid state magic angle spinning (MAS) nuclear magnetic resonance (NMR) spectroscopy is a structural tool which gives information on local environments and mobility that cannot be obtained from X-ray diffraction or IR spectroscopy. MAS NMR spectroscopy deals with energy states in the nuclei of atoms and their interactions with radio waves when an intense magnetic field is applied.

In solid state MAS NMR the sample is spun rapidly at the magic angle θ_m (54.74° , where $\cos^2\theta_m = 1/3$) with respect to the direction of the magnetic field. Spinning at this angle helps to increase the resolution (the normally broad lines become narrower) for better identification and analysis of the spectrum.

The position of the signal in a solid state MAS NMR spectrum is called the ‘chemical shift’. Chemical shift defines the frequency of absorption for a nucleus of interest relative to the frequency of absorption of a standard. The position and intensity of the resonance gives information on the chemical environment of the nucleus and, so about the structure. The chemical shift depends on the local structural environment and it is sensitive to structural modifications and symmetry changes.

In this study solid state ^{27}Al and ^{29}Si MAS NMR were used to obtain the framework Si/Al ratio of as-prepared, ion exchanged and dealuminated zeolites, and to investigate the local environment of Si or Al atoms in mesoporous silicas and zeolites.

The presence of other elements within the silicate framework has a strong effect on the ^{29}Si spectra. It can cause broadening of the Si resonance and changes in the chemical shift. In general, the chemical shifts become less negative with increasing Si-O bond length, decreasing average T-O-T bond angle or decreasing electronegativity of the surrounding atom, for example substitution of aluminum for silicon in the framework causes a shift of approximately 5 ppm per aluminum.

The lack of atomic long-range order in mesoporous silicas makes NMR the most important local structural method for these solids. In mesoporous silicas where amorphous silica walls are not fully tetrahedrally connected ^{29}Si MAS NMR gives important information on the $\text{Q}^1\text{-Q}^4$ silicon environments ($\text{R-Si}-(\text{OSi})_n(\text{OH})_{3-n}$, with n from 0 to 3, Figure 2.20a).

In zeolites silicon can be close to 1, 2, 3 or 4 Al atoms in nearest tetrahedral positions ($\text{Si}(n\text{Al}) = (\text{Si}(\text{OSi})_n(\text{OAl})_{4-n}$, with n from 4 to 1, Figure 2.20a). The environment of aluminium atoms in the zeolite can be measured using ^{27}Al MAS NMR. ^{27}Al MAS NMR gives rather broad signals with quadrupolar line shapes (Figure 2.20c) which can be further resolved by using the isotropic projection of the ^{27}Al multi quantum (MQ) MAS NMR (Figure 2.20d).

The chemical shifts for the different Si local environments in mesoporous silicas, and Si and Al local environments in zeolites are presented in Figure 2.21. They were used to identify the structure changes upon dealumination and nitridation and to calculate the framework Si/Al ratio in this study.

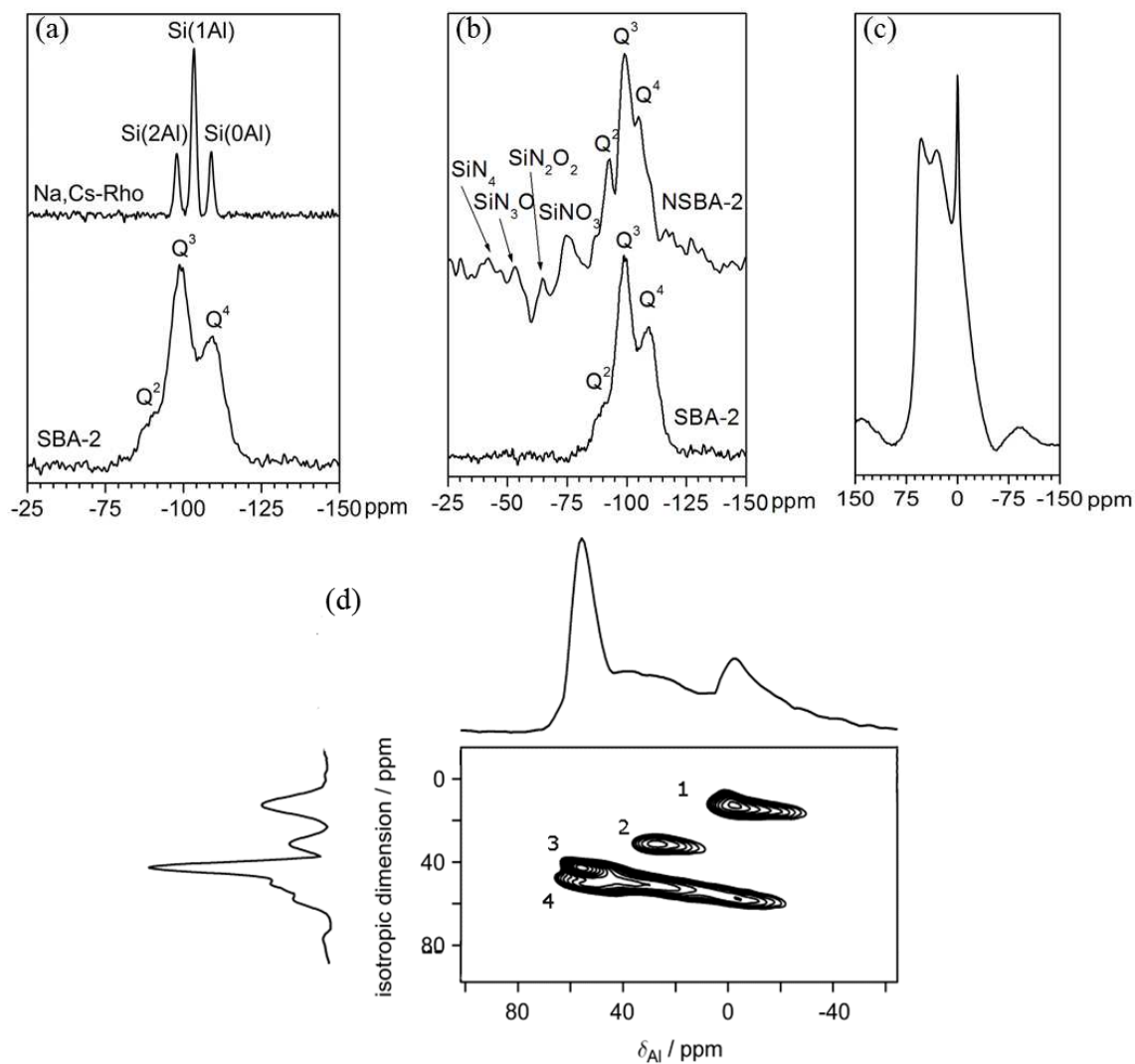


Figure 2.20. (a) ^{29}Si MAS NMR of SBA-2 and Na,Cs-Rho, (b) ^{29}Si MAS NMR of SBA-2 before and after nitridation, (c) ^{27}Al MAS NMR of steamed H-Rho and (d) its ^{27}Al MQ MAS NMR projection showing 1 – octahedral Al in extra-framework positions, 2 – five-coordinate Al in extra-framework positions, 3 – tetrahedral framework Al, 4 – Al in a distorted tetrahedral extra-framework environment.

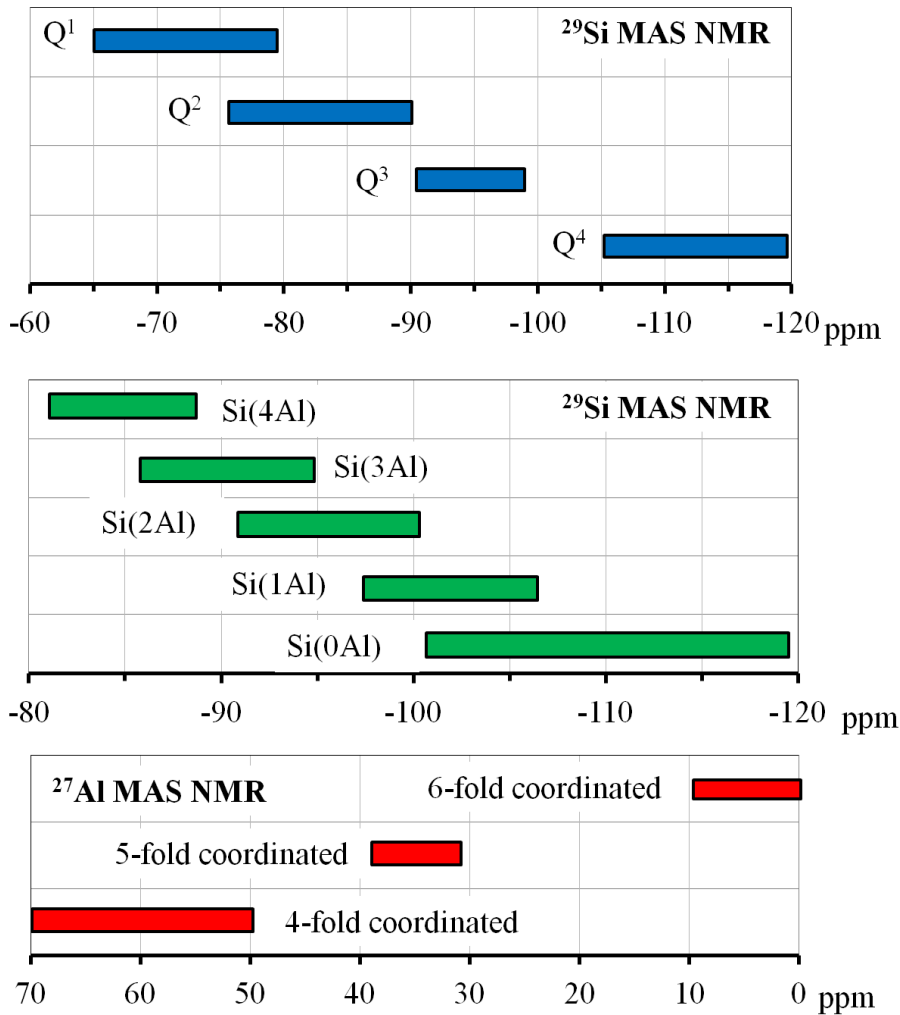


Figure 2.21. The chemical shifts for the different Si local environments in mesoporous silicas (blue, top), and Si (green, middle) and Al (red, bottom) local environments in zeolite.^{5,20}

In the case of single T-site zeolites (all zeolites in this study) and after taking into account Lowenstein's rule (which excludes the possibility of alumina as nearest neighbors), it is possible to calculate the Si/Al ratio of the framework using the formula:

$$\frac{Si}{Al} = \frac{\sum_{n=0}^4 I_{nAl}}{\sum_{n=0}^4 0.25nI_{nAl}} \quad (2.6)$$

where I_{nAl} denotes the intensity of the ^{29}Si peak corresponding to a $\text{Si}[n\text{Al},(4-n)\text{Si}]$ environment. It is very important to measure framework Si/Al ratio in zeolites because it may be very different from the bulk composition, for example when framework dealumination occurs during ultrastabilisation or ion exchange. The framework Si/Al

ratio obtained from ^{29}Si MAS NMR measurement helps to calculate the number of expected extra-framework cations in zeolites.

The nitridation of zeolites and mesoporous silicas, investigated in this study, where oxygen atoms are substituted for nitrogen atoms, causes larger changes in chemical shift in the ^{29}Si MAS NMR spectrum of these materials, providing a sensitive method to study the degree of nitridation (see Figure 2.20b). The changes in chemical shift reduce as the number of nitrogen atoms added per silicon atoms gets larger because the substitution changes not only the atoms bound to the silicon but also the bond angles around it. The shifts for the basic $\text{SiN}_x\text{O}_{4-x}$ local environments in silicon oxynitrides fall in the ranges presented in Table 2.5. There are also several local environments whose shifts lie outside these ranges, which were studied in more details by Dogan *et al.*²⁰

Table 2.5. The chemical shifts for the different $\text{SiN}_x\text{O}_{4-x}$ local environments in silicon oxynitrides.²⁰

$\text{SiN}_x\text{O}_{4-x}$	Chemical shift /ppm
x= 1	-71 to -89
x= 2	-58 to -71
x= 3	-44 to -55
x= 4	-44 and higher

2.7. Other Techniques

2.7.1. Thermogravimetric Analysis (TGA)²¹

Thermogravimetric analysis (TGA, Figure 2.22) measures weight loss (or weight gain) in a material in relation to a change in temperature (or time) under a controlled atmosphere (for example air or O_2). During the heating materials can change weight from a simple process such as drying, template removal or chemical reaction with the atmosphere in the testing environment.

In this study TGA was used to determine: the temperature at which template is completely removed from the materials, the content of organic template in the materials, the decomposition points of the materials and the temperature of water desorption from the porous structures, which was later used in dehydration processes prior to structure refinement and gas adsorption.

The thermal stability of aluminosilicate zeolites and mesoporous materials is generally very high, 1073 K and 1773 K, respectively. Physisorbed water is lost reversibly from all these solids at temperatures around 423 K. Samples with Li cations demand higher temperature for water removal, around 573 K.

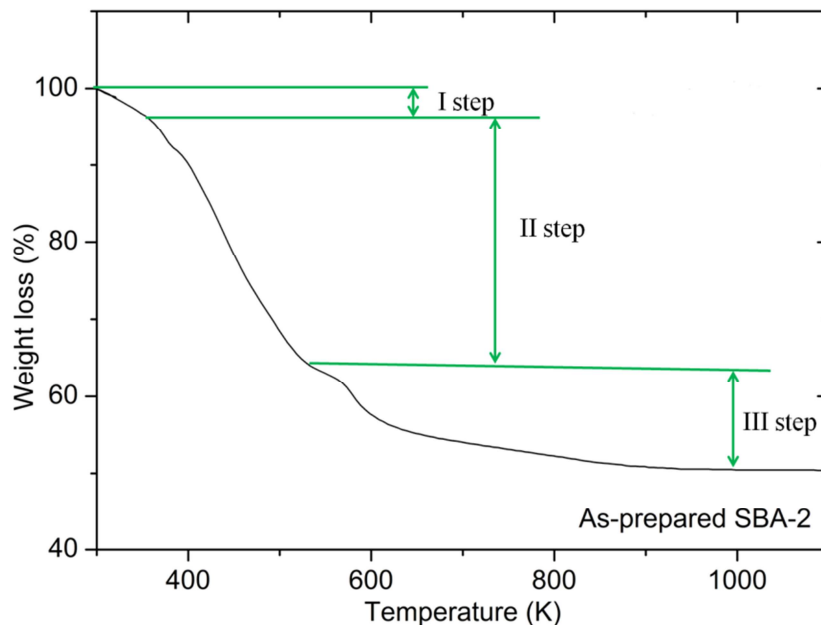


Figure 2.22. Thermogram of as prepared SBA-2 showing removal of water and decomposition of template in three steps of weight loss. The first weight loss (I step), ca. 2 wt%, occurs below 370 K is due to the desorption of physisorbed water. The second weight loss (II step), ca. 31 wt% between 370 K and 550 K, is caused by the decomposition of the surfactant head group. The last weight loss (III step), ca. 15 wt%, occurs at 550–800 K and it is attributed to the decomposition of the alkyl chain of the surfactant.

2.7.2. Organic Elemental Analysis (CHNX)²²

Organic elemental analysis (CHNX) was used for calculating the amount of template in mesoporous silicas.

CHNX analysis is a qualitative and quantitative technique which gives the percentage weights of carbon (C), hydrogen (H), nitrogen (N) and heteroatoms (X = for example halogens or sulfur) of a sample. The most common form of elemental analysis is accomplished by combustion analysis. A sample is burnt in an oxygen-rich environment, and various traps collect the combustion products (CO_2 , H_2O , NO_x and

N₂). Detection of the gases can be carried out in a variety of ways, for example by gas chromatography (GC) with thermal conductivity detection. The mass of each product is used to work out a chemical formula of the combusted substance.

2.7.3. Atomic Absorption Spectroscopy (AAS)²³

Atomic absorption spectrometry (AAS) is an analytical technique that measures the concentrations of elements in the sample. The valence electrons of the atoms in the atomiser (flame) are promoted to higher orbitals for a short period of time (nanoseconds) by absorbing radiation of a given wavelength. Each metal absorbs radiation at a characteristic frequency and then emits the same radiation in the form of (visible) light as the electron falls back into the lower energy orbital. The intensity of the absorbed light is proportional to the concentration of the element in the flame. Concentrations of elements in the samples are usually determined from a working curve after calibrating the instrument with standards of known concentrations. AAS is a very accurate technique and can measure concentration as small as parts per billion of a gram ($\mu\text{g dm}^{-3}$) in a sample.

In this study AAS was used to determine lithium in ion exchanged zeolitic samples. Lithium is out of reach in EDX analysis due to the low energy of its characteristic X-rays.

References

1. West A. R., *'Basic Solid State Chemistry'*, John Wiley & Sons Ltd, UK, **1999**
2. Giacovazzo C., Monaco H. L., Artioli G., Viterbo D., Milanesio M., Gilli G., Gilli P., Zanotti G. and Ferraris G., *'Fundamentals of Crystallography'*, Oxford University Press, USA, **1992**
3. Hammond C., *'The Basics of Crystallography and Diffraction'*, Oxford University Press, USA, **2006**
4. Larson A. C. and Von Dreele R. B., *'General Structure Analysis System (GSAS)'*, Los Alamos National Laboratory, USA, **1994**
5. Wright P. A., *'Microporous Framework Solids'*, The Royal Society of Chemistry, UK, **2008**
6. Young R. A., *'The Rietveld Method'*, Oxford University Press, USA, **1996**

7. Thompson S. P., Parker J. E., Potter J., Hill T. P., Birt A., Cobb T. M., Yuan F. and Tang C. C., *Rev. Sci. Instrum.*, **2009**, *80*
8. The International Centre for Diffraction Data, www.icdd.com
9. Toby B. H., *Powder Diffr.*, **2006**, *21*, 67-70
10. Yamazaki S. and Toraya H., *J. Appl. Crystallogr.*, **1999**, *32*, 51-59
11. Sing K., *Colloid. Surface. A*, **2001**, *187-188*, 3-9
12. Sing K. S. W., *Adv. Colloid. Interfac.*, **1998**, *76-77*, 3-11
13. Morishige K., *Adsorption*, **2008**, *14*, 157-163
14. Brandani S. and Ruthven D. M., *Ind. Eng. Chem. Res.*, **1996**, *35*, 315-319
15. Williams D. B. and Carter C. B., '*Transmission Electron Microscopy*', Plenum Press, USA, **1996**
16. Bendersky L. A. and Gayle F. W., *J. Res. Natl. Inst. Stand. Technol.*, **2001**, *106*, 997-1012
17. Putnis A., '*Introduction to Mineral Sciences*', Cambridge University Press, UK, **1992**
18. Cheetham A. K. and Day P., '*Solid State Chemistry: Techniques*', Oxford University Press, USA, **1987**
19. Zhang C. M., Liu Q. and Xu Z., *J. Non-Cryst. Solids*, **2005**, *351*, 1377-1382
20. Dogan F., Hammond K. D., Tompsett G. A., Huo H., Conner W. C., Auerbach S. M. and Grey C. P., *J. Am. Chem. Soc.*, **2009**, *131*, 11062-11079
21. Coats A. W. and Redfern J. P., *Analyst*, **1963**, *88*, 906-924
22. Fadeeva V. P., Tikhova V. D. and Nikulicheva O. N., *J. Anal. Chem.*, **2008**, *63*, 1094-1106
23. Skoog D. A., West D. M., Holler F. J. and Crouch S. R., '*Fundamentals of Analytical Chemistry*', Brooks/Cole Pub Co, USA, **2003**

3. Mesoporous Silicas SBA-1 and SBA-2: Materials with Large Pore Volume and Small Window Size

3.1. Introduction

In the early 1990s Huo *et al.*^{1,2} synthesised the mesoporous materials, SBA-1 (Santa Barbara-1) and SBA-2 (Santa Barbara-2), which are of interest in this study. SBA-1 and SBA-2 may be considered to be made up of large ordered silicate cages, with windows of controllable dimensions, that are formed by condensation around spherical micelles. SBA-1 (Figure 3.1a) is a cubic ($Pm\bar{3}n$), highly symmetric three dimensional cage-type structure with two kinds of cages, larger cages (diameter *ca.* 4.0 nm) and smaller cages (diameter *ca.* 3.3 nm), and small windows (diameter *ca.* 0.8 nm).^{3,4} The pore network of SBA-2 (Figure 3.1b) is made up of interconnected spherical cavities, arranged in a hexagonal ($P6_3/mmc$) or a cubic ($Fm\bar{3}m$) close-packed array. SBA-2 has been studied less than other mesoporous silica materials since it was discovered,^{4,15} at least partly because of its small window size (*ca.* 0.4 nm).⁴ The size of windows between the cages in SBA-2 is much smaller than the diameter of the cage (2.5–4 nm) and it may be modified for example by changing the conditions of its synthesis⁴ or its calcination at high temperatures.¹⁶ The small window sizes of mesoporous silicas could act as molecular sieves. Separation based on geometry is possible, when mesoporous silica has a pore/window size large enough to take up CO₂ but too small to adsorb small hydrocarbons. The PhD thesis of Jorge Gonzalez,¹⁶ suggests this might be possible for mesoporous silica by using a calcination temperature that begins to reduce nitrogen uptake but does not reduce the CO₂ uptake. This will also have a strong effect on molecules with bigger kinetic diameter than nitrogen, for example methane. Hunter *et al.*⁸ discussed in detail the synthesis and characterisation of SBA-2, and determined the synthetic conditions necessary to modify its pore size. In a later study they also identified SBA-2 as small solid spheres, flat sheet particles with complex and irregular domain structures, and larger spherical hollow forms.⁹ In 2002 Garcia-Bennett *et al.*⁴ noticed that under basic conditions the SBA-2 phase is observed with hollow sphere morphology while under strongly acidic conditions, a mixture of SBA-1 and SBA-2 is observed, depending on the surfactant and silicate content of the original gel.

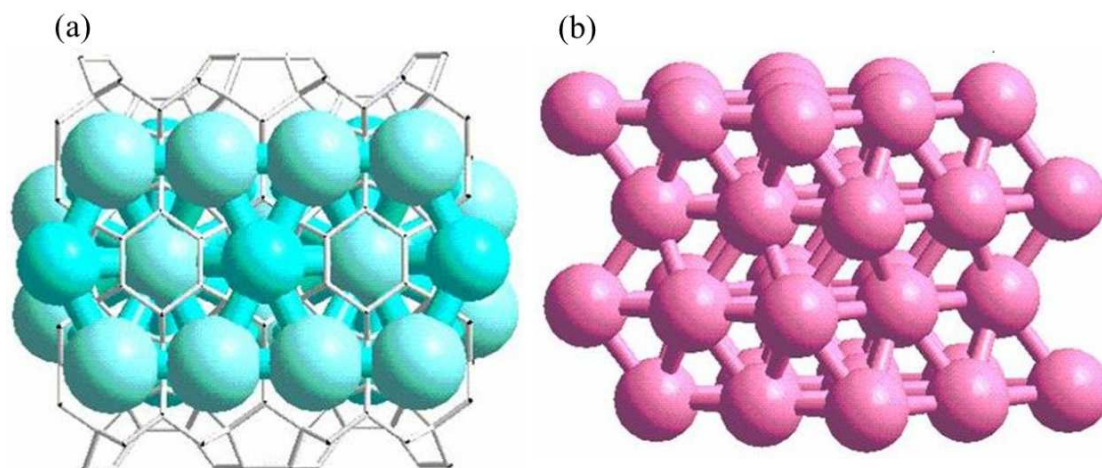


Figure 3.1. Schematic drawing of close packed arrays of super-cages connected by micropores in (a) SBA-1 and (b) SBA-2.

The SBA materials can be prepared economically and possess good physical, hydrothermal, mechanical and chemical properties. Their relative hydrophobicity, compared to zeolites and metal organic frameworks (MOFs), is a potential advantage for CO₂ adsorption from flue gas. Furthermore, manipulation of pore size and the dimension of supercages in SBA materials can be achieved through the use of an organic template during synthesis or by varying the calcination temperature.⁸ Reducing the pore size by calcination at different temperatures may have a strong effect on adsorption of molecules with bigger kinetic diameter than carbon dioxide (including N₂ and CH₄) and may allow these materials to act as a molecular sieve. The literature suggests that the silica framework of mesoporous silica materials could be nitrified in ammonia, and silicon oxynitrides offer potentially stronger CO₂ adsorption sites.¹⁷ These features make these materials promising candidates for CO₂ capture and storage from flue gases or other CO₂-containing gas streams.

This chapter includes an investigation on the physicochemical properties and modification of SBA-1 and SBA-2. Series of SBA-1 and SBA-2 calcined at different temperatures have been prepared. For the first time SBA-1 and SBA-2 have been modified by nitridation. All solids have been characterised by PXRD, TEM, SEM, TGA and ²⁹Si MAS NMR. The effect of thermal treatment and nitridation upon porosity of the solids has been investigated by means of N₂ and CO₂ adsorption. Furthermore, for the first time, the framework density of SBA-2 has been followed as a function

of calcination temperature, enabling a structural model of SBA-2 to be developed in collaboration with modellers at the University of Edinburgh.

3.2. Experimental

3.2.1. Synthesis of SBA-1 and SBA-2

During the synthesis mesoporous silicas were stirred within the polyethylene (PET) bottle (Figure 3.2a and b). As-prepared and calcined samples gave white powders (Figure 3.2c).

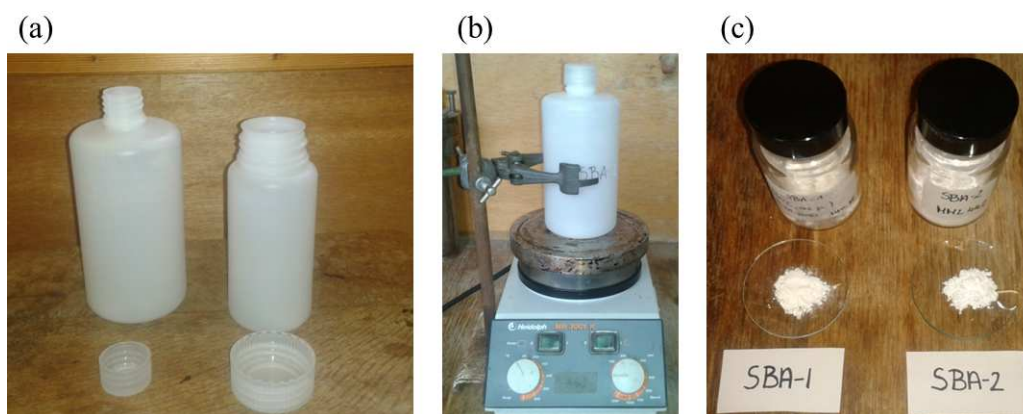


Figure 3.2. (a) Polyethylene bottles used for mesoporous silicas synthesis, (b) set up for mesoporous silica synthesis and (c) as-prepared white powder of SBA-1 and SBA-2.

The length of the hydrophobic tail of the surfactant used in the synthesis of mesoporous materials has a direct effect on the pore size of the final material. SBA-1 was prepared with a cationic surfactant, cetyltriethylammonium bromide with one quaternary ammonium head group attached to a hydrophobic tail ($[(C_{16}H_{33})N(CH_3)_3]^+ Br^-$, CTEABr, Figure 3.3a). SBA-2 was prepared with a dicationic gemini surfactant, N-(3-trimethylammoniumpropyl)hexadecylammonium dibromide with two quaternary ammonium head groups separated by a trimethylene chain attached to a hydrophobic tail ($[(C_{16}H_{33})N(CH_3)_2(CH_2)_3N(CH_3)_3]^{2+} 2Br^-$, C16-3-1, Figure 3.3b). The mechanism for the synthesis of mesoporous solids is described in more detail in chapter 1.

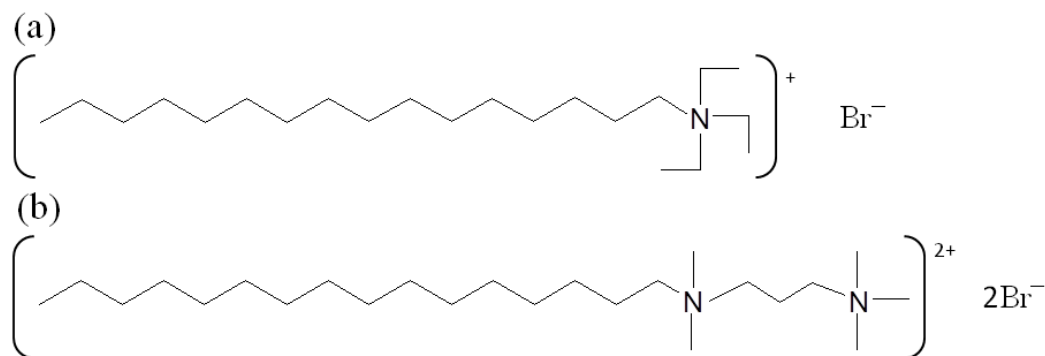


Figure 3.3. Surfactants used for mesoporous silicas synthesis (a) cetyltriethylammonium bromide (CTEABr, SBA-1 formation) and (b) N-(3-trimethylammonium-propyl)hexadecylammonium dibromide (C16-3-1, SBA-2 formation).

The synthesis of the cetyltriethylammonium bromide (CTEABr) and the mesoporous silica SBA-1 were carried out according to published procedures.^{18,19} CTEABr was synthesised by the reaction of 1-bromohexadecane (C₁₆H₃₃Br; 152.7 g; 0.50 mol; 97%; Sigma-Aldrich) with triethylamine (C₆H₁₅N; 75.9 g; 0.75 mol; ≥ 99.5%; Sigma-Aldrich) in acetone (C₃H₆O; 400 mL; ≥ 99.5%; Sigma-Aldrich). The product was decanted and purified by recrystallisation from an acetone solution. The resulting product was separated by filtration and dried for several hours at 333 K. Synthesis of SBA-1 was performed as follows: the CTEABr (0.23 g; 1.20 mmol), distilled water (10 mL), and hydrochloric acid (HCl; 0.41 g; 22.20 mmol; 32–38%; Fisher Chemicals) were mixed to obtain a homogeneous solution. The solution was stirred for 30 minutes prior to the drop wise addition of tetraethyl orthosilicate (TEOS; C₈H₂₀O₄Si; 0.93 g; 8.90 mmol; 98%; Sigma-Aldrich). The reaction mixture was kept at 268 K under static conditions for five days. The white precipitate was filtered and dried at 333 K.

The synthesis of SBA-2 was prepared according to a published procedure⁸ as follows: N-(3-trimethyl-ammoniumpropyl)hexadecylammonium dibromide (C16-3-1; 0.50 g; 0.95 mmol; PAW group) was mixed with water (70 mL) and tetramethylammonium hydroxide (TMAOH; C₄H₁₃NO; 5.0 g; 13.70 mmol; ≥ 97%; Sigma-Aldrich). The reaction mixture was homogenised in a PET bottle at ambient temperature for 30 minutes. To this solution tetraethyl orthosilicate (TEOS; C₈H₂₀O₄Si; 5.7 g; 27.40 mmol; 98%; Sigma-Aldrich) was slowly added dropwise at room temperature and stirred for 3 hours. The solid product was recovered by filtration and dried at 333 K.

3.2.2. Framework Modification by Calcination and Nitridation

Calcination. The porosity and framework modification of SBA materials were achieved by surfactant removal during calcination of as-prepared materials. The samples were heated at different calcination temperatures between 823 K and 1173 K at a ramp rate of 3 K min⁻¹. The samples were first heated at 823 K under nitrogen for 5 hours to remove most of the organic template, before being switched to oxygen for a further 6 hours. Calcination was carried out in a tube furnace with flowing gas (Figure 3.4). From now on, SBA-1 and SBA-2 calcined at 823 K, 973 K, 1073 K, 1173 K are referred to as SBA-1(823), SBA-1(973), SBA-1(1073), SBA-1(1173), SBA-2(823), SBA-2(973), SBA-2(1073), SBA-2(1173), respectively.



Figure 3.4. The tube furnace designed for heating materials under oxygen, nitrogen or air up to 1473 K.

Nitridation. The nitridation of SBA materials was carried out in a tube furnace under ammonia gas flow (Figure 3.5a and 3.5b). They were prepared in collaboration with the University of Nottingham. The starting materials used for nitridation were SBA-1(823) and SBA-2(823). The resulting nitrided materials were white powders (Figure 3.5c). Nitridation was carried out according to a published procedure.²⁰ The mesoporous silicas SBA-1(823) and SBA-2(823) were placed in an alumina boat and inserted into a tube furnace. The tube furnace was subjected to purging by N₂ for 30 minutes. After 30 minutes the gas flow was switched to ammonia with a flow rate of 100 mL min⁻¹. The temperature of the furnace was increased, at a ramp rate of 5 K min⁻¹, to desired nitridation temperature of 973 K, 1073 K and 1173 K. The samples were maintained at those temperatures for 20 hours under the NH₃ atmosphere. The furnace was cooled to about 373 K under NH₃ and the gas flow switched to N₂ until it cooled to room temperature. From now on, SBA-1 nitrided at 1073 K and 1173 K and SBA-2 nitrided

at 973 K, 1073 K and 1173 K will be referred as NSBA-1(1073), NSBA-1(1173), NSBA-2(973), NSBA-2(1073) and NSBA-2(1173), respectively.

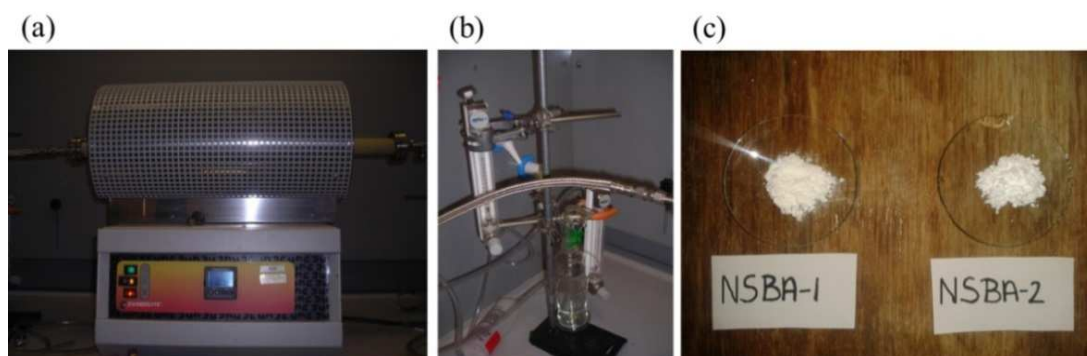


Figure 3.5. Set up for mesoporous nitridation: (a) a tube furnace under ammonia gas flow (heating up to 1473 K), (b) ammonia flow meters and (c) white powders of NSBA-1 and NSBA-2 samples.

3.2.3. Characterisation

The identity of as-prepared, calcined and nitrated mesoporous materials was confirmed by laboratory PXRD using a PANalytical diffractometer operating in reflection geometry with Cu $K_{\alpha 1}$ X-ray radiation (1.54056 Å). Thermogravimetry of SBA-1 and SBA-2 was performed using a Netzsch TG 209 instrument with a heating rate of 3 K min⁻¹ up to 973 K in flowing air, in order to determine the temperature at which water and template were removed from the structure. Analysis of the template was done in a Perkin Elmer 2400 CHNX-analyzer. The morphology of SBA materials was performed using a JEOL JSM 5600 scanning electron microscopy (SEM) and a Jeol JEM 2011 high resolution transmission electron microscopy (HRTEM) operating at 200 keV. EDX analysis was performed in a JEOL JSM 5600 SEM, with an Oxford INCA Energy 200 EDX analyser. The EDX area scans were performed over three different regions and averaged. Solid-state ²⁹Si MAS NMR of as-prepared, calcined and nitrated SBA materials was performed using a Varian VNMRS spectrometer operating at 79.44 MHz at the University of Durham, as part of the Engineering and Physical Sciences Research Council (EPSRC) collaboration. N₂ adsorption isotherms were measured volumetrically at 77 K using a Micromeritics Tristar II 3020 up to p/p₀ = 1.0, where p₀ is the saturation pressure. CO₂ adsorption isotherms were measured volumetrically using a Micro-meritics 2020 porosimeter. This was performed at 0–1 bar at 298 K. Prior to N₂ and CO₂ adsorption/desorption isotherms being measured, the samples were degassed

under high vacuum at 623 K. Density analysis was carried out on a Micromeritics AccuPyc 1340 helium pycnometer. The AccuPyc works by measuring the amount of displaced gas. The material is ground to powder and the volume is determined by the mass difference between a certain pycnometer filled with helium and the same pycnometer filled with a sample and helium.²¹

3.3. Structural Characterisation of SBA-1 and SBA-2

The mesoporous structure of SBA materials was confirmed by low-angle powder X-ray diffraction (PXRD). The diffraction peaks for mesoporous materials occur only in the low angle region (below $10^\circ 2\theta$) due to the amorphous nature of mesoporous solids and the absence of long-range ‘crystalline’ order. The PXRD pattern of SBA-1 (Figure 3.6a) shows three well-resolved sharp (200), (210) and (211) diffraction peaks in the region of $2.0\text{--}3.0^\circ 2\theta$ and (320), (321) and (400) peaks in the region of $4.0\text{--}6.0^\circ 2\theta$. All of the reflections are associated with $Pm\bar{3}n$ cubic symmetry, $a = 66 \text{ \AA}$. The PXRD pattern of SBA-2 (Figure 3.6b) is consistent with a hexagonal arrangement of the mesopores, $P6_3/mmc$, with $a = 50 \text{ \AA}$ and $c = 82 \text{ \AA}$, shows an intense (002) diffraction peak in range of $1.5\text{--}3.0^\circ 2\theta$ and (110), (103) and (112) peaks in the range of $3.0\text{--}6.0^\circ 2\theta$.

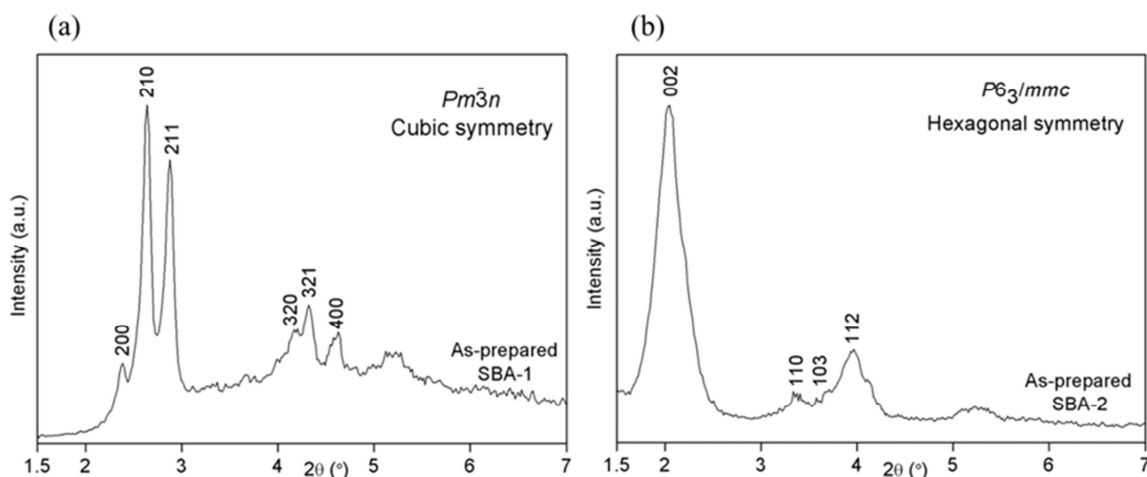


Figure 3.6. PXRD patterns of (a) as-prepared SBA-1 and (b) as-prepared SBA-2. Patterns are indexed according to the cubic and hexagonal symmetry, respectively.

The thermal stability and the most effective temperature for template removal for SBA-1 and SBA-2 were determined by thermogravimetric analysis (TGA,

Figure 3.7). CHNX analysis was used to confirm the percentage of template. Weight loss for the as-prepared SBA materials is observed to occur in three steps. The first weight loss, *ca.* 2 wt% for SBA-1 and 3 wt% for SBA-2, occurs below 370 K and it is due to the desorption of physisorbed water. The second weight loss, *ca.* 40 wt% for SBA-1 and 31 wt% for SBA-2 between 370 K and 550 K, is caused by the decomposition of the surfactant head group. The last weight loss step, *ca.* 20 wt% for SBA-1 and *ca.* 15 wt% for SBA-2, occurs between 550 K and 800 K and it is attributed to the decomposition of the alkyl chain of the surfactant. CHNX analysis of as-prepared SBA-1 confirms that the content of the template is *ca.* 58% (%C = 47.17, %H = 7.87, %N = 2.94) and *ca.* 47% (%C = 38.01, %H = 6.89, %N = 3.88) for as-prepared SBA-2. The TGAs suggest that the lowest temperature at which the surfactant is completely removed from as-prepared SBA materials is 823 K. The TGAs of SBA-1(823) and SBA-2(823) confirm that at this temperature no template remains.

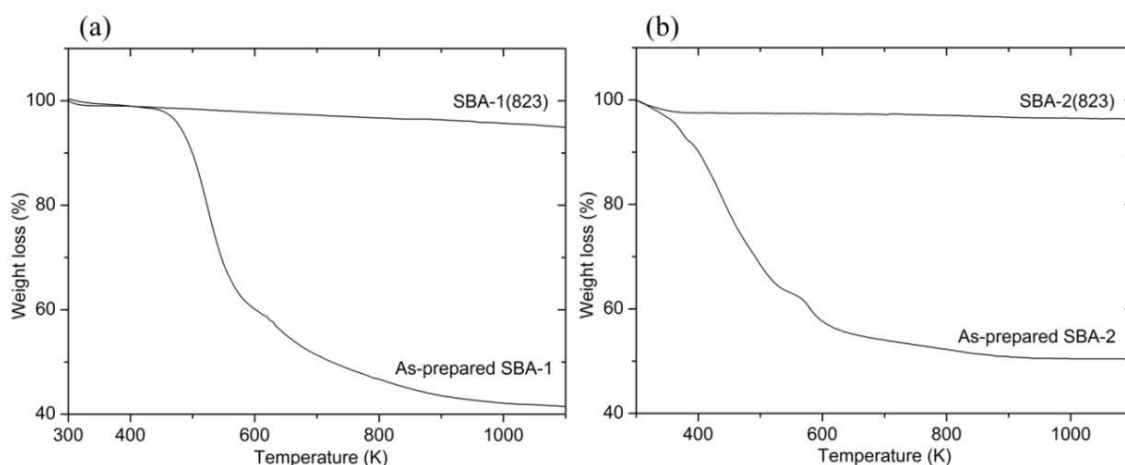


Figure 3.7. TGA curves of (a) SBA-1, SBA-1(823) and (b) SBA-2, SBA-2(823).

SBA-1(823) and SBA-2(823) were characterised by scanning electron microscopy (SEM) and high-resolution transmission electron microscopy (HRTEM) to observe the morphology and arrangement of pores (Figure 3.8). The micrographs of SBA-1(823) and SBA-2(823) show small particles with a spherical shape, between 1 μm and 5 μm in size (SEM) and a well-ordered uniform arrangement of pores (HRTEM).

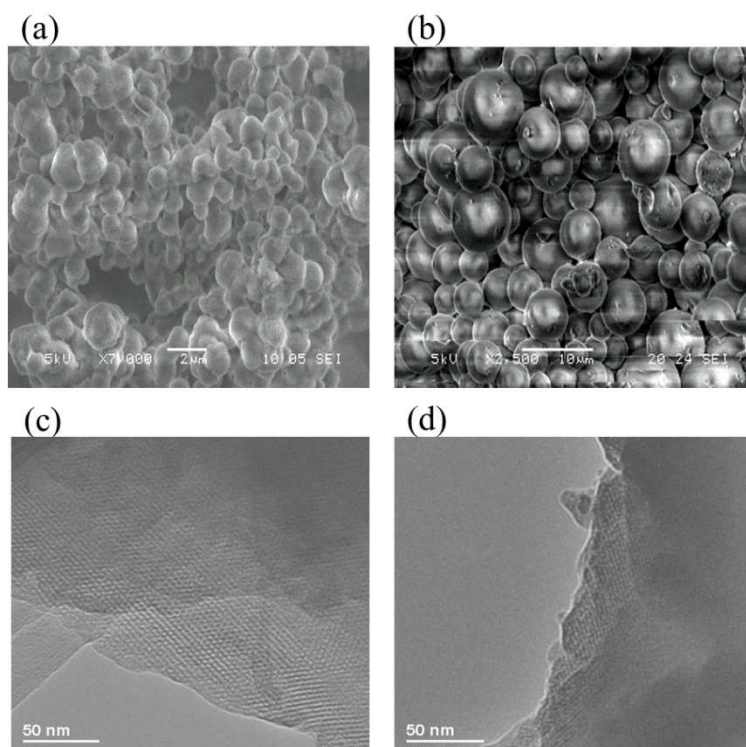


Figure 3.8. SEM images of (a) SBA-1(823) and (b) SBA-2(823) and HRTEM images of (c) SBA-1(823) and (d) SBA-2(823).

3.4. Modification of Mesoporous Silicas by Calcination

Calcination at high temperature will reduce the pore size of SBA materials and may improve adsorption ability by increasing the interaction of the silica framework with CO_2 . It may also have a strong effect on adsorption of molecules with a larger kinetic diameter than CO_2 and so may allow these materials to act as a molecular sieve.

The mesoporosity of SBA materials calcined at different temperatures was confirmed by low-angle PXRD. The PXRD patterns of SBA-1 and SBA-2 (Figure 3.9) show that the diffraction peaks shift progressively to higher angles with the increase in calcination temperature, indicating a systematic contraction of the unit cell. The d-spacing of as-prepared SBA-1 (210) diffraction peak is 33.4 Å and for SBA-1(1173) the d-spacing changes to 32.2 Å. This indicates a 3.5% contraction for the SBA-1(1173) lattice. While the SBA-2 (002) diffraction peak changes from 48.3 Å for as-prepared SBA-2, to 39.8 Å for SBA-2(1173), this corresponds to a 17.6% contraction of the pores. It can be clearly seen that the intensity of (200), (210) and (211) reflection peaks for as-prepared SBA-1 and the (002) reflection peak for as-prepared SBA-2 decrease slightly

and become broader as the calcination temperature increases. The (320), (321) and (400) reflection peaks for as-prepared SBA-1 and (110), (103) and (112) reflection peaks for as-prepared SBA-2 decrease with increasing calcination temperature. It suggests that the mesoporous structures are partly distorted or collapse during contraction of the pores.

Many parameters that describe the pore structure of mesoporous materials, for example surface area and porosity, can be determined with nitrogen adsorption. In this study N₂ adsorption was used to further investigate the contraction of the pores and structural properties of SBA-1 and SBA-2 samples after calcination (Figure 3.10). There is no N₂ adsorption observed on as-prepared SBA-1 and SBA-2 due to pore blockage by template. The capillary condensation for calcined SBA-1 samples occurs in the range of $p/p_0 = 0.2-0.3$ and for calcined SBA-2 samples in the range of $p/p_0 = 0.3-0.4$; this lower onset is characteristic for the smaller cage size of the SBA-1. The N₂ adsorption isotherms of SBA-1(823), SBA-1(973), SBA-1(1073), SBA-2(823), SBA-2(973) and SBA-2(1073) show Type IV behaviour, typical for mesoporous materials where pores are in a connected network. The SBA-2(1173) shows no N₂ adsorption, this can be associated with the collapse or closing of the silica structure. The capillary condensation of N₂ for calcined SBA-1 and SBA-2 samples is shifted to lower pressure with increasing calcination temperature, this suggests a reduction of the pore size. The larger shrinkages observed for SBA-2 compared to SBA-1 by PXRD, results in a faster decrease of N₂ uptake when calcination temperature increases. The calcination process has a strong effect on the connectivity of the SBA-1 and SBA-2 porous network.

The changes in pore size were investigated further by examination of pore properties and surface areas of as-prepared and calcined SBA materials, summarised in Table 3.1. The as-prepared SBA-1 shows smaller average pore width, lower pore volume, but higher surface area than as-prepared SBA-2, possible due to the different size of the pore entrance. The window of SBA-2 shrinks with increasing calcination temperature and the uptake of nitrogen drops more quickly than for SBA-1. The bigger pores of SBA-2 are more affected by heating than the SBA-1 pores. This was confirmed by low angle PXRD (see Figure 3.9), where SBA-1(1173) has a 3.5% contraction compared to a 17.6% contraction of the SBA-2(1173).

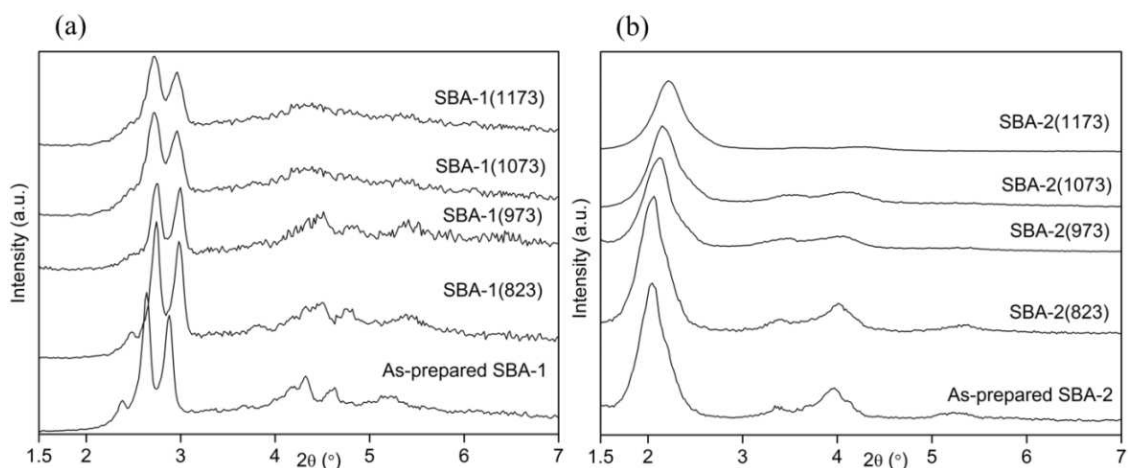


Figure 3.9. PXRD patterns of (a) SBA-1, SBA-1(823), SBA-1(973), SBA-1(1073), SBA-1(1173) and (b) SBA-2, SBA-2(823), SBA-2(973), SBA-2(1073), SBA-2(1173). The (offset) patterns have been collected at 298 K using the same operating conditions.

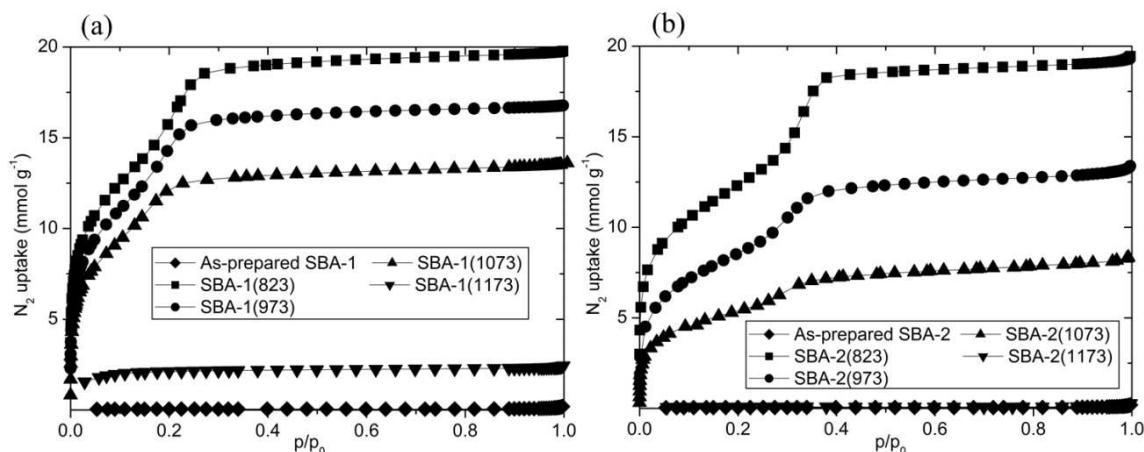


Figure 3.10. Nitrogen adsorption isotherms at 77K of (a) SBA-1, SBA-1(823), SBA-1(973), SBA-1(1073), SBA-1(1173) and (b) SBA-2, SBA-2(823), SBA-2(973), SBA-2(1073), SBA-2(1173).

Additionally, ^{29}Si MAS NMR and density measurements of as-prepared and calcined SBA-2 structures were collected to further investigate the condensation of the silicate framework (Figure 3.11). ^{29}Si MAS NMR is a powerful technique for analyzing the local environment of silicon in the mesoporous wall and indicates the polymerisation level of the silica. In this study it was used to measure the amounts of different types of silicon units, Q^2 , Q^3 and Q^4 using deconvolution of the signals (see the appendix). From the ^{29}Si MAS NMR spectrum of as-prepared SBA-2 three peaks can be attributed to: $\text{Si}(\text{OSiO})_2(\text{OH})_2$ (-90 ppm, Q^2), $\text{Si}(\text{OSiO})_3\text{OH}$ (-100 ppm, Q^3)

and $\text{Si}(\text{OSiO})_4$ (-110 ppm, Q^4). Spectra of SBA-2(823), SBA-2(973) and SBA-2(1073) show the gradual condensation of the silica framework. The number of silicon sites, Q^2 and Q^3 , decreases gradually and the silicon Q^4 site starts dominating. The density of SBA-2(823), 3.2 g cm^{-3} , is almost three times higher than density of the as-prepared sample (1.2 g cm^{-3}) because in the latter the measurement is an average of the silica framework and the template within the pores whereas in the former it is the measured density of the silica walls alone. The density changes are of the order SBA-2(823) > SBA-2(973) > SBA-2(1073) > SBA-2(1173), from 3.2 g cm^{-3} to 2.3 g cm^{-3} . This may be explained by the shrinkage of some parts of the SBA-2 framework with increasing temperature, making them inaccessible for helium adsorption. ^{29}Si MAS NMR and density measurement are in a good agreement with low-angle PXRD (see Figure 3.9) and N_2 adsorption (see Figure 3.10) showing condensation of silica framework with increasing calcination temperature in SBA materials.

Table 3.1. Structural characteristics of as-prepared and calcined SBA-1 and SBA-2.

Sample	Average pore width ^{a)} /Å	Total pore volume ^{b)} /cm ³ g ⁻¹	BET surface area ^{c)} /m ² g ⁻¹
SBA-1(as-prepared)	N/A	0.00	2.8 ± 0.1
SBA-1(823)	24 ± 1	0.68 ± 0.02	1358 ± 36
SBA-1(973)	24 ± 1	0.57 ± 0.02	1144 ± 37
SBA-1(1073)	24 ± 1	0.26 ± 0.01	897 ± 37
SBA-1(1173)	N/A	0.00	151 ± 4
SBA-2(as-prepared)	N/A	0.00	3.6 ± 0.1
SBA-2(823)	30 ± 1	0.58 ± 0.02	808 ± 14
SBA-2(973)	28 ± 1	0.45 ± 0.01	705 ± 10
SBA-2(1073)	28 ± 1	0.19 ± 0.01	348 ± 7
SBA-2(1173)	N/A	0.00	13.2 ± 0.1

a) Average pore width has been estimated from the desorption branch of the nitrogen isotherm using the BJH method

b) Total pore volume has been estimated from the nitrogen uptake at $p/p_0 = 0.9$ and liquid nitrogen density ($0.808 \text{ cm}^3 \text{ g}^{-1}$)

c) The BET surface area was estimated by using multipoint BET method

The CO_2 adsorption isotherms of SBA-1(823), SBA-1(1073), SBA-2(823) and SBA-2(1073) are linear in the entire pressure range, which indicates physisorption (Figure 3.12). The highest uptake of CO_2 at 0.1 bar is 0.20 mmol g^{-1} and 0.10 mmol g^{-1} for SBA-1 and SBA-2, respectively. Total uptake, at 0.95 bar, for SBA-1(823) and SBA-2(823) is 1.50 mmol g^{-1} and 0.90 mmol g^{-1} , respectively. Calcination at higher temperature decreases the CO_2 uptake on SBA-1(1073) to 0.80 mmol g^{-1} and

increases the uptake on SBA-2(1073) to 1.10 mmol g^{-1} . The interaction of CO_2 with the framework of SBA-1 and SBA-2 is weak. It becomes slightly stronger and CO_2 uptake higher when the pore size becomes smaller at higher calcination temperature. The CO_2 performance of SBA-1 and SBA-2 depends on the size, surface chemistry of the pores, connectivity and accessibility of the network.

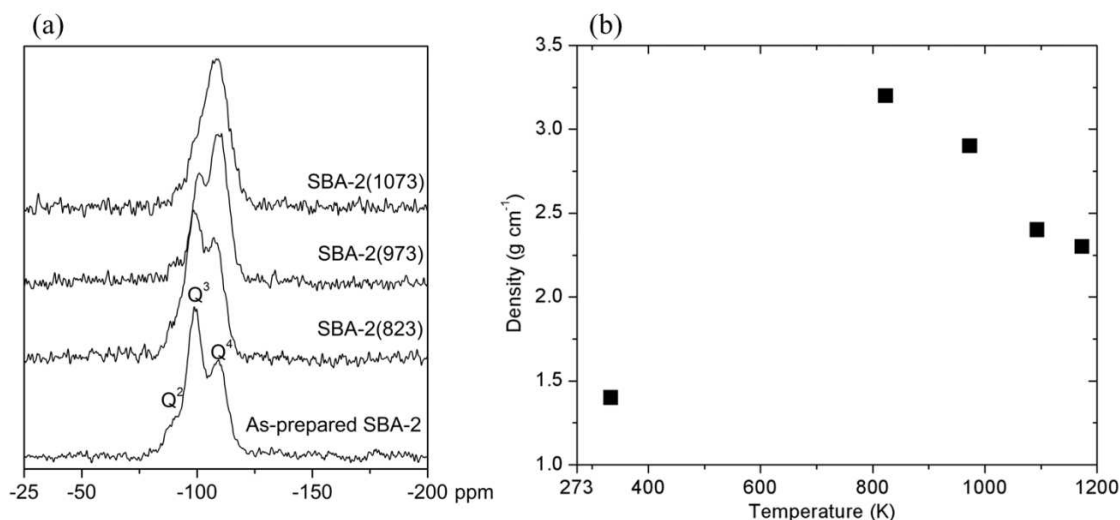


Figure 3.11. (a) ^{29}Si MAS NMR spectra of SBA-2, SBA-2(823), SBA-2(973) and SBA-2(1073) and (b) effect of calcination temperature on density of SBA-2, SBA-2(823), SBA-2(973), SBA-2(1073) and SBA-2(1173).

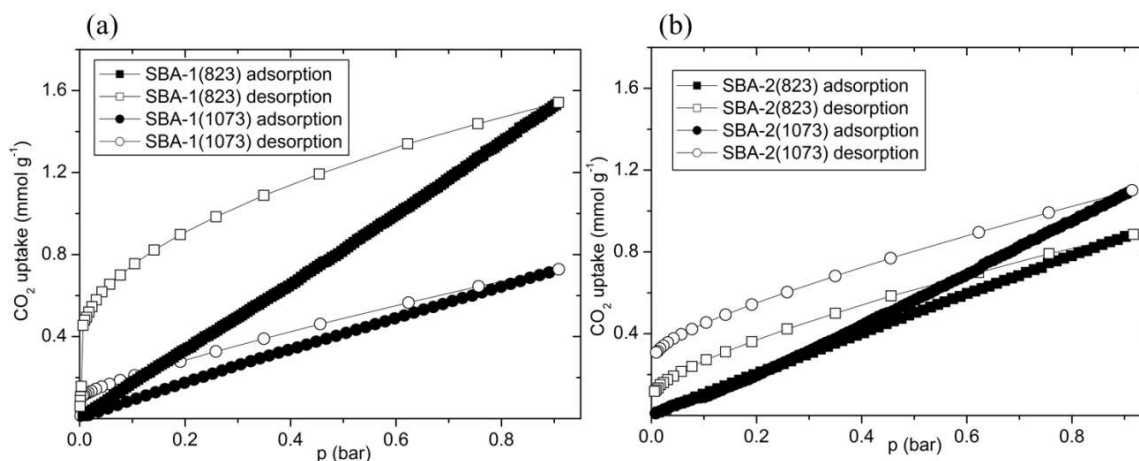


Figure 3.12. CO_2 sorption isotherms at 298 K on (a) SBA-1(823), SBA-1(1073) and (b) SBA-2(823), SBA-2(1073).

Due to their low CO_2 adsorption, SBA-1 and SBA-2 are not good candidates for CO_2 capture from flue gas at pressure 0.1 bar and temperature 298 K. Therefore, attempts to improve the CO_2 uptake by the modification of SBA-1 and SBA-2 by nitridation were made.

3.5. Functionalisation of Mesoporous Silicas by Nitridation

The hydroxyl groups on the surface of mesoporous materials are important for gas adsorption and surface modification. High concentration of surface silanol groups (SiOH) leads to ready surface modification. Functionalisation can be achieved either by post-synthesis modification or by *in situ* synthesis. One of the methods for post-synthesis modification of mesoporous silicas is nitridation, replacement of the oxygen atoms with nitrogen atoms. Nitridation is a simple and rapid way of functionalising porous materials. It may create new and strong CO₂ adsorption sites. More details on mesoporous solids and the suggested mechanism of their nitridation are given in chapter 1.

In this study, nitridation has been examined for improving CO₂ uptake at 0.1 bar and 298 K. Here, SBA-1 and SBA-2 have been functionalised by reaction with ammonia in the nitridation process for the first time. The nitridation of SBA-1 and SBA-2 was carried out at the University of Nottingham, in collaboration with Eric Masika and Prof. Robert Mokaya.

PXRD was used to assess the structural ordering of the ammonia-treated SBA materials. Comparison of the PXRD patterns of NSBA-1(1073), NSBA-1(1173), NSBA-2(973), NSBA-2(1073) and NSBA-2(1173) with the PXRD patterns of the starting materials, SBA-1(823) and SBA-2(823), is presented in Figure 3.13. The PXRD patterns of the SBA-1 and SBA-2 before and after nitridation show typical ordered mesoporous materials. NSBA-1(1073), NSBA-1(1173), NSBA-2(973), NSBA-2(1073) and NSBA-2(1173) show similar behaviour to calcined SBA-1 and SBA-2 series (see Figure 3.9). The diffraction peaks of SBA-2 shift progressively to higher angles with the increase in nitridation temperature, indicating that the unit cells have decreased in size. For NSBA-1 series three well-resolved peaks which correspond to (200), (210) and (211) reflections can be observed to broaden with nitridation. The (002) reflection peak for NSBA-2 series also decreases and becomes broader during nitridation. Reflection peaks in the region of 4–6° 2θ for both NSBA series start disappearing when the temperature is higher than 973 K. NSBA-1 and NSBA-2 nitrided above 973 K are partly distorted or collapsed.

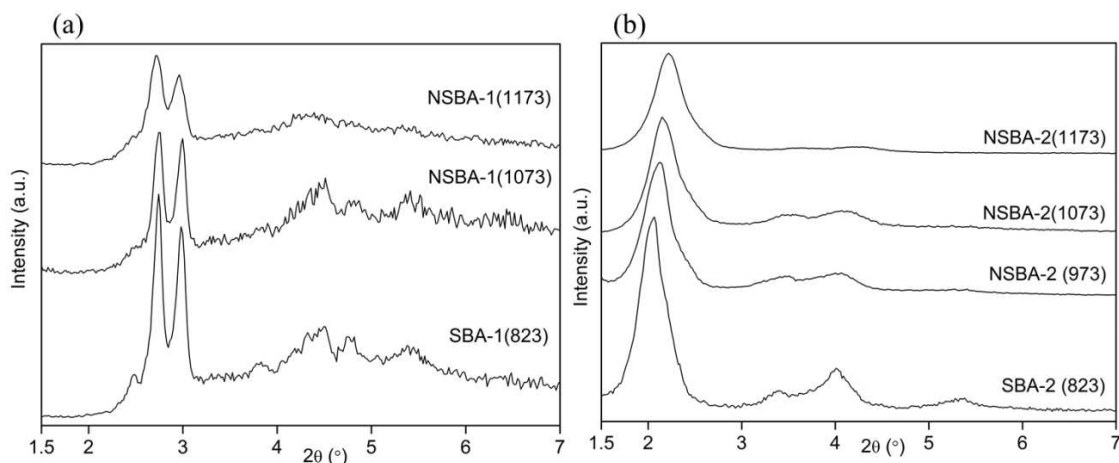


Figure 3.13. PXRD patterns of (a) SBA-1(823), NSBA-1(1073), NSBA-1(1173) and (b) SBA-2(823), NSBA-2(973), NSBA-2(1073), NSBA-2(1173). The (offset) patterns have been collected at 298 K using the same operating conditions.

Structural ordering of the NSBA materials was also investigated by HRTEM. HRTEM images of NSBA-1(1073) and NSBA-2(973) show well-ordered uniform pores (Figure 3.14).

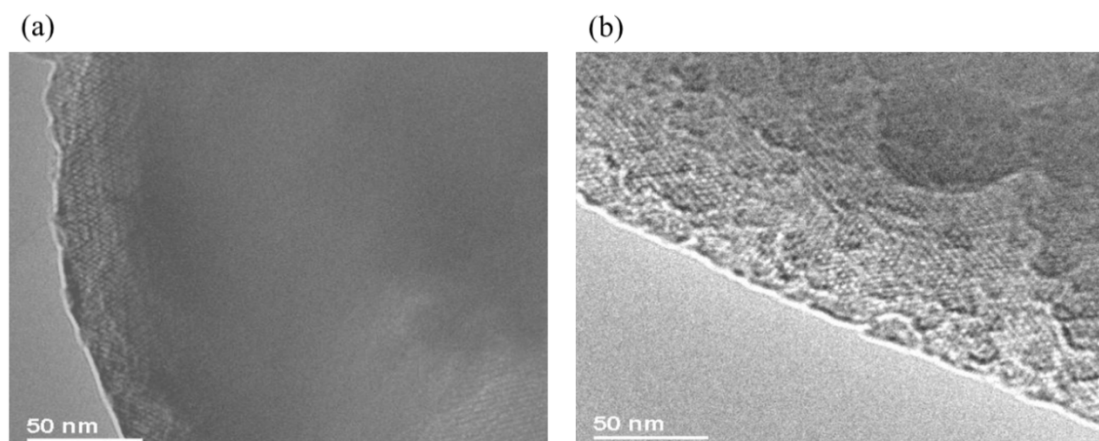


Figure 3.14. HRTEM images of (a) NSBA-1(1073) and (b) NSBA-2(973).

Incorporation of nitrogen into NSBA materials was further investigated by ^{29}Si MAS NMR. Figure 3.15 presents ^{29}Si MAS NMR spectra of SBA-1(823), NSBA-1(1073), SBA-2(823) and NSBA-2(973). From the ^{29}Si MAS NMR spectrum of SBA-1(823) and SBA-2(823) three peaks can be attributed to: $\text{Si}(\text{OSiO})_2(\text{OH})_2$ (-90 ppm, Q^2), $\text{Si}(\text{OSiO})_3\text{OH}$ (-100 ppm, Q^3) and $\text{Si}(\text{OSiO})_4$ (-110 ppm, Q^4). It can be observed that SBA-1(823) possesses more Q^4 sites than SBA-2(823), SBA-2(823) contains mainly Q^3 sites. Spectra of NSBA-1(1073) and NSBA-2(973) show the condensation of silica framework, where the ratio of Q^3/Q^4 slightly increases. New downfield peaks for

NSBA-1(1073) and NSBA-2(973), from -50 ppm to -90 ppm, can be observed. The spectra of NSBA-1(1073) and NSBA-2(973) are characterised by three peaks at -45 ppm, -55 ppm, -65 ppm and -80 ppm which can be attributed to SiN_4 , SiN_3O , SiN_2O_2 and SiNO_3 , respectively. The ^{29}Si MAS NMR spectra of NSBA-1(1073) and NSBA-2(973) imply that nitrogen has been introduced into the framework, while the silanols remain.

Nitrogen content of the NSBA series was analyzed using energy dispersive X-ray spectroscopy (EDX) and the results are shown in Table 3.2. It is clearly seen that incorporation of nitrogen increases at higher nitridation temperatures. The sample with the highest nitrogen content is NSBA-2(1173) with 9% of nitrogen. The sample with lowest nitrogen content, 3%, is NSBA-2(973). Around 1% more N is being introduced to NSBA-2(1173) than NSBA-1(1173). This can be due to the morphology, as SBA-2 has higher BET surface area and consequently more sites to introduce NH_3 . No difference in nitrogen content is observed for NSBA-1(1073) and NSBA-1(1173), and NSBA-2(1073) and NSBA-2(1173). Around 9% is the highest nitrogen content which can be introduced into SBA-1 and SBA-2 structures during nitridation under the conditions investigated here.

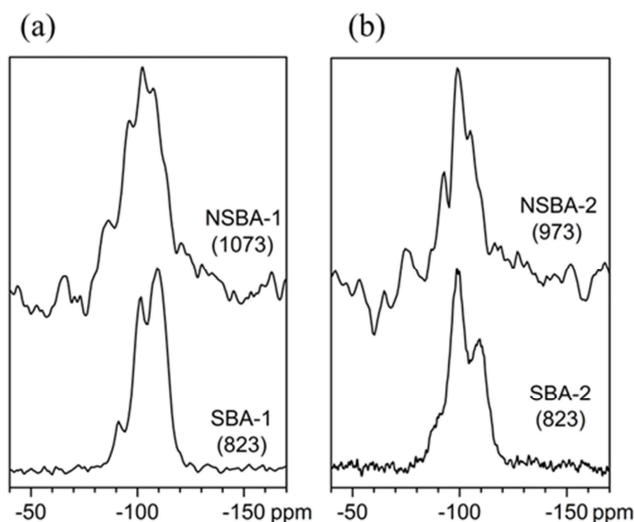


Figure 3.15. ^{29}Si MAS NMR spectra of (a) SBA-1(823), NSBA-1(1073) and (b) SBA-2(823), NSBA-2(973).

Table 3.2. EDX analysis of SBA samples before and after nitridation.

Element	Atomic %						
	SBA-1 (823)	NSBA-1 (1073)	NSBA-1 (1173)	SBA-2 (823)	NSBA-2 (973)	NSBA-2 (1073)	NSBA-2 (1173)
Si	43 ± 1	37 ± 1	37 ± 1	40 ± 1	45 ± 1	41 ± 1	41 ± 1
O	57 ± 1	55 ± 1	55 ± 1	60 ± 1	52 ± 1	50 ± 1	50 ± 1
N	N.D.	8 ± 1	8 ± 1	N.D.	3 ± 1	9 ± 1	9 ± 1

Values for nitrogen and oxygen are semi-quantitative
N.D. – not detected

Gas sorption ability and structural ordering of nitrated materials were further investigated by N₂ adsorption (Figure 3.16). The SBA-1(823) and SBA-2(823) possess large surface areas and high N₂ uptakes. NSBA-1(1173) and NSBA-2(973) are not porous to nitrogen. The nitrogen adsorption isotherms of NSBA-1(1073) and NSBA-2(973) are Type IV indicating that samples nitrated at those temperatures have mesoporous structures. The capillary condensation step, which is in the relative pressure range of $p/p_0 = 0.20$ – 0.30 for SBA-1(1073) and $p/p_0 = 0.30$ – 0.40 for SBA-2(973) (see Figure 3.10), shifts to a lower pressure range for NSBA-1(1073) ($p/p_0 = 0.15$) and NSBA-2(973) ($p/p_0 = 0.20$). It has already been proved in this study (see Figure 3.10) that high temperature of calcination reduces the size of the pores and causes contraction of the unit cell of SBA-1 and SBA-2. The nitridation has a stronger effect than calcination on the final connectivity of the SBA porous networks.

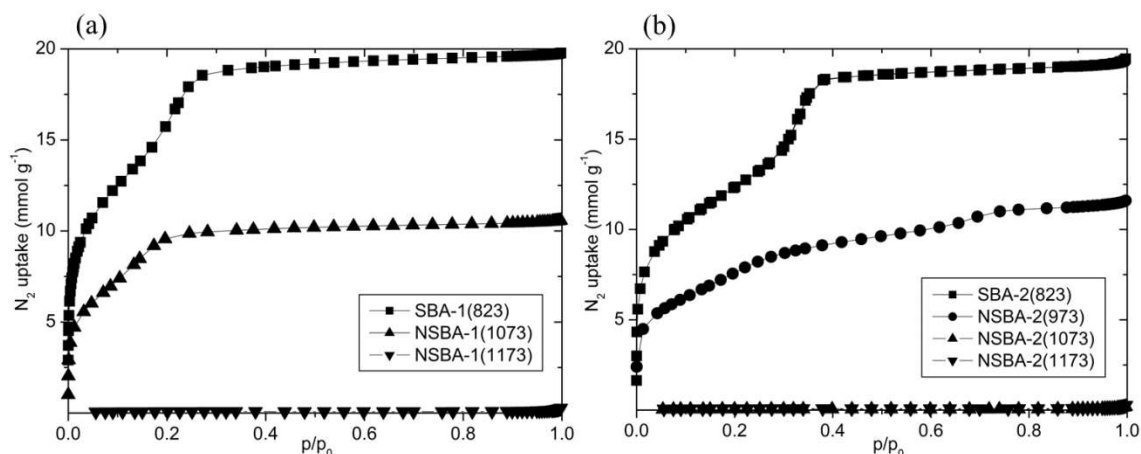


Figure 3.16. N₂ adsorption at 77 K of (a) SBA-1(823), NSBA-1(1073), NSBA-1(1173) and (b) SBA-2(823), NSBA-2(973), NSBA-2(1073), NSBA-2(1173).

Figure 3.17 shows the temperature dependence of the nitridation on nitrogen content and surface area. The introduction of nitrogen into SBA materials is found to be enhanced with an increase in nitridation temperature, but the BET surface area is

strongly reduced. The nitrogen content of 7.56% for NSBA-1(1073) is achieved and the BET surface area is $696.2 \text{ m}^2\text{g}^{-1}$. For NSBA-1(1173) *ca.* 0.5% more of nitrogen can be introduced but BET surface area drops to $0.0 \text{ m}^2\text{g}^{-1}$, indicating that the sample is no longer porous. NSBA-2 remains porous (BET = $608.6 \text{ m}^2\text{g}^{-1}$) only when the nitrogen content is 3.0%.

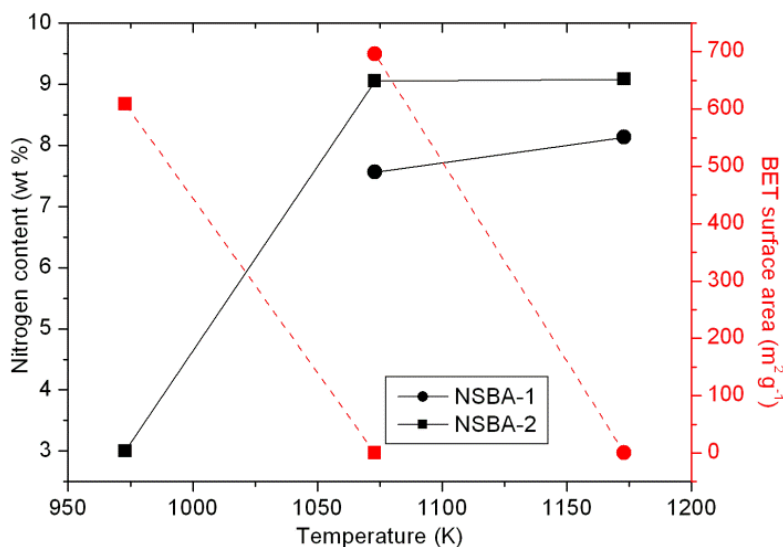


Figure 3.17. The dependence of nitrogen content (black, straight lines) and BET surface area (red, dashed lines) of SBA-1 and SBA-2 on the temperature of nitridation.

Structural changes of SBA materials before and after nitridation were further investigated (Table 3.3). With an increase of temperature from 973 K to 1173 K total pore volume and BET surface area of NSBA samples decrease, similar to what was already observed in this study for calcination temperature on SBA samples (see Figure 3.10). For NSBA-1(1073) and NSBA-2(973) which remain porous, the nitrogen content is *ca.* 7.0% for NSBA-1(1073) and 3.0% for NSBA-2(973). The total pore volume and BET surface area of NSBA-1(1073) are 31% and 23% respectively, smaller than for SBA-1(1073). For NSBA-2(973) the total pore volume and BET surface area are 15% and 14%, respectively, smaller than for SBA-2(973). High temperature plus ammonia treatment cause faster degradation of the SBA-2 mesoporous structure than of the SBA-1. The average pore size for NSBA-1(1073) is 8% smaller than for SBA-1(1073), however the average pore size of NSBA-2(973) is 3% higher than for SBA-2(973). To investigate this difference further pore size distribution (PSD) curves were prepared (Figure 3.18). The pore size distributions of SBA-1(1073),

NSBA-1(1073) and SBA-2(973) are narrow and centered at approximately 23 Å, 22 Å and 28 Å, respectively. The pore size distribution of NSBA-2(973) is characterised by two maxima, narrow at approximately 23 Å and broad at approximately 70 Å.

Table 3.3. Structural characteristics of calcined and nitrified SBA-1 and SBA-2.

Sample	Average pore width ^{a)} /Å	Total pore volume ^{b)} /cm ³ g ⁻¹	BET surface area ^{c)} /m ² g ⁻¹
SBA-1(823)	24 ± 1	0.68 ± 0.02	1358 ± 36
SBA-1(1073)	24 ± 1	0.26 ± 0.01	897 ± 37
NSBA-1(1073)	22 ± 1	0.18 ± 0.01	696 ± 15
SBA-1(1173)	N/A	0.00	151 ± 4
NSBA-1(1173)	N/A	0.00	0
SBA-2(823)	30 ± 1	0.58 ± 0.02	808 ± 14
SBA-2(973)	28 ± 1	0.45 ± 0.01	705 ± 10
NSBA-2(973)	30 ± 1	0.35 ± 0.01	609 ± 12
SBA-2(1073)	28 ± 1	0.19 ± 0.01	348 ± 7
NSBA-2(1073)	N/A	0.00	0
SBA-2(1173)	N/A	0.00	13.2 ± 0.1
NSBA-2(1173)	N/A	0.00	0

a) Average pore width has been estimated from the desorption branch of the nitrogen isotherm using the BJH method

b) Total pore volume has been estimated from the nitrogen uptake at $p/p_0 = 0.9$ and liquid nitrogen density ($0.808 \text{ cm}^3 \text{ g}^{-1}$)

c) The BET surface area was estimated by using multipoint BET method

High temperatures at which NSBA materials are prepared make them stable upon further heating. The TGA of NSBA-1(1073) and NSBA-2(973) (Figure 3.19) shows two major weight losses. The first weight loss at low temperature ($T < 400 \text{ K}$), *ca.* 8% for NSBA-1(1073) and *ca.* 12% for NSBA-2(973), is due to desorption of physisorbed water. The second weight loss from 400 K to 800 K, *ca.* 4% for NSBA-1(1073) and *ca.* 1.5% for NSBA-2(973), may be due to amine desorption from surface groups, resulting in lower nitrogen content. Therefore, it can be concluded that the structure of NSBA-1(1073) and NSBA-2(973) are stable in structure, but not composition, up to 1100 K.

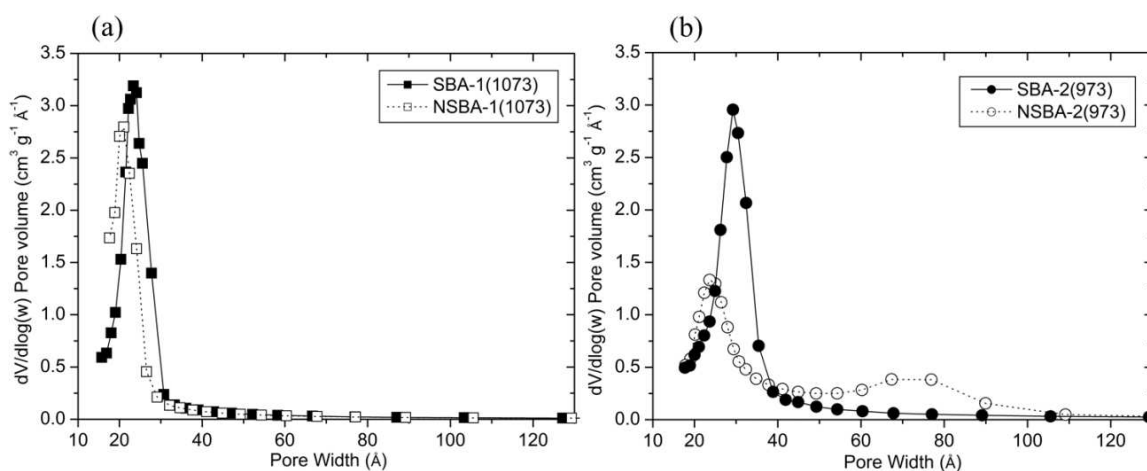


Figure 3.18. BJH pore size distribution curves of (a) SBA-1(1073), NSBA-1(1073) and (b) SBA-2(973), NSBA-2(973).

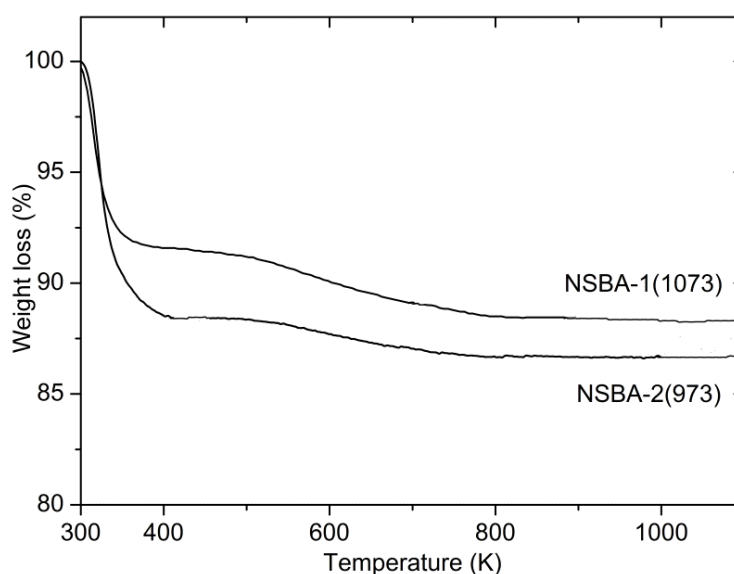


Figure 3.19. TGA curves of NSBA-1(1073) and NSBA-2(973).

Incorporation of nitrogen into porous materials slightly enhances the CO_2 adsorption performance (Figure 3.20). The uptake of CO_2 at 0.1 bar is 0.13 mmol g^{-1} and 0.10 mmol g^{-1} for NSBA-1(1073) and NSBA-2(973), respectively. The total uptake at 0.95 bar for NSBA-1(1073) and NSBA-2(973) are 0.97 mmol g^{-1} and 0.88 mmol g^{-1} , respectively. The CO_2 adsorption isotherms of calcined SBAs are linear in the entire pressure range, clearly indicating physisorption. In contrast, the CO_2 adsorption isotherms of nitrated samples show Type I behaviour with hysteresis which indicates some irreversible chemisorption with strong interactions between CO_2 molecules and nitrated groups. This indicates that higher CO_2 adsorption of NSBA-1(1073) and NSBA-2(973) is primarily attributed to the change in surface chemistry. The content of

incorporated nitrogen is double for NSBA-1(1073) compared to NSBA-2(973), but only leads to a slightly higher CO₂ adsorption. The increase in CO₂ uptake on different mesoporous silica samples after nitridation was also observed by Patil *et al.*¹⁷ Even though the nitrogen content, and therefore number of chemisorption sites, is higher for NSBA-1(1073), the higher surface area and larger pore size of NSBA-2(973) may allow better access of CO₂ to the fewer sites it possesses.

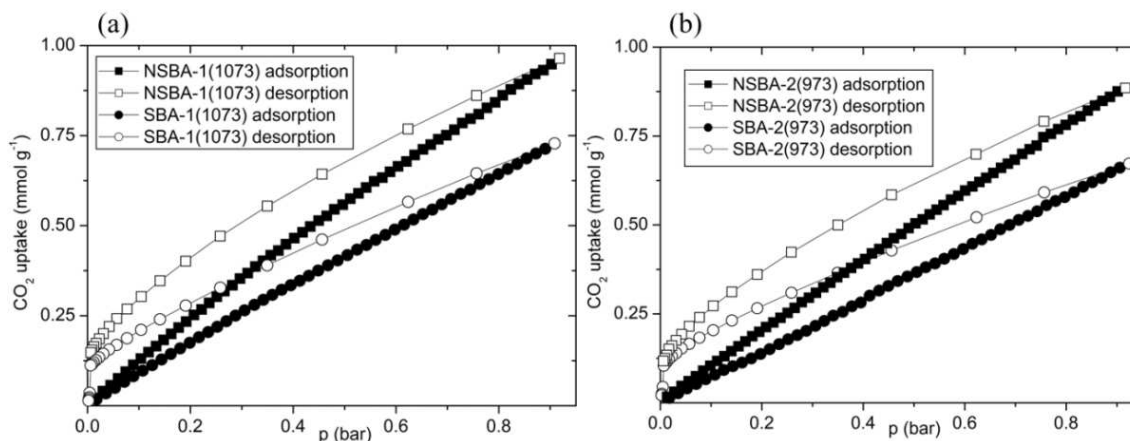


Figure 3.20. CO₂ sorption isotherms at 298 K on (a) SBA-1(1073), NSBA-1(1073) and (b) SBA-2(973), NSBA-2(973).

Dependence of CO₂ adsorption on incorporated nitrogen content and nitridation temperature was further investigated. Figure 3.21 presents CO₂ adsorption isotherms for NSBA-2(973), NSBA-2(1073) and NSBA-2(1173), where the incorporated nitrogen content is 3.0%, 9.1% and 9.1%, respectively (see Table 3.2). Introduction of more nitrogen to the silica structure has not changed the CO₂ adsorption significantly. At total pressure (0.95 bar) the CO₂ uptake for NSBA-2(973) and NSBA-2(1073) is almost the same, *ca.* 1.0 mmol g⁻¹, even if the nitrogen content is *ca.* 6% higher for NSBA-2(1073). NSBA-2(1173) adsorbs 1.12 mmol g⁻¹ at 0.95 bar. The CO₂ adsorption at 0.1 bar for NSBA-2(973) and NSBA-2(1073) is only *ca.* 14% higher than for NSBA-2(1173), due to the shape of the CO₂ isotherm. The isotherms of CO₂ adsorption on NSBA-2(973), NSBA-2(1073) and NSBA-2(1173) are Type I with a slope in the low-pressure range, which indicates physisorption with strong interactions between CO₂ molecules and nitrated groups.

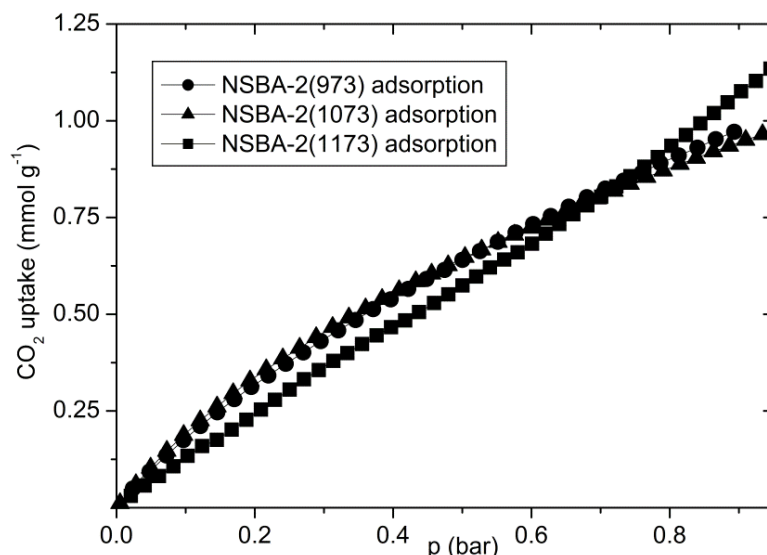


Figure 3.21. CO_2 sorption isotherms at 298 K on NSBA-2(973), NSBA-2(1073) and NSBA-2(1173).

Main conclusion of this study is that there is no nitrogen uptake for NSBA-2(1073) and NSBA-2(1173) (see Figure 3.16), therefore substitution of oxygen atoms by nitrogen atoms not only improves the CO_2 -adsorbent bonding but also increases the CO_2/N_2 selectivity.

3.6. Realistic, Atomistic Model of SBA-2 and Simulation of Synthesis

Simulations of SBA-2 structure and synthesis have been previously reported by Perez-Mendoza *et al.*¹² They represented the SBA-2 structure as a system of spherical cavities with smooth walls, and similarly smooth cylindrical connecting channels. An important limitation of their approach is the smoothness of the pore models used to represent SBA-2 since it is well-known that the pore surface of real periodic mesoporous silica (PMS) materials is rough.²² The study presented here was conducted to understand the synthesis process in more details and to create realistic, atomistic model of SBA-2.²³

Modelling of SBA-2 was carried out at the University of Edinburgh, in collaboration with Drs Carlos A. Ferreiro-Rangel and Tina Düren. SBA-2 samples, for comparison, were synthesised and characterised at the University of St Andrews.

Kinetic Monte Carlo (kMC) technique has been applied to the condensation, aggregation, deformation, and calcination stages of the synthesis of SBA-2. Density, magic angle spinning nuclear magnetic resonance (^{29}Si NMR) and nitrogen adsorption

were measured on as-prepared and calcined samples to help in the validation of the simulation method.

^{29}Si MAS NMR provides information on the connectivity of the silicon in a material and N_2 adsorption determined structural properties of SBA-2. The degree of polymerisation, Q^n , and N_2 adsorption isotherm of experimental and simulated SBA-2 are presented in Figure 3.22. It can be seen (Figure 3.22a) that the degree of polymerisation obtained for the simulated materials agree well with the percentages reported here for SBA-2 materials (*ca.* 66% Q^4 and *ca.* 30% Q^3 for samples calcined at 823 K). Although, the simulated material shows slightly higher Q^2 , Q^3 and lower Q^4 , this can be due to the fact that the simulated temperature is not a physical temperature but a close match to the experimental degree of polymerisation can be achieved. Also, the nitrogen adsorption prediction (Figure 3.22b) is in good agreement with the experimental measurement for the SBA-2 material. The model shows the shape of the Type IV isotherm and the capillary condensation at around $p/p_0 = 0.3$ as was also reported earlier in this study (see Figure 3.10b). The density of the simulated SBA-2 is very close to the experimental value measured by helium pycnometry of 3.2 g/cm^3 for SBA-2(823).

Two of the most remarkable results can be highlighted. The simulation shows that the pores of the SBA-2 are connected through windows formed during micelle aggregation because of the close packing of the spherical micelles. The simulation also highlighted that water plays an important role especially in the early stages of the silica structure formation. These processes are shown schematically in Figure 3.23. The connecting windows which arise from packing of the micelles and proximity during the aggregation stage of the synthesis promoted by regions of thinned silica network can be seen. Water molecules that accumulate in these regions contribute to the creation of the connecting window promoting silica polymerisation during the early stages of the synthesis. It was also found that water molecules make an important contribution to the roughness of the final simulated material and the strong adsorption sites are due to this surface roughness.

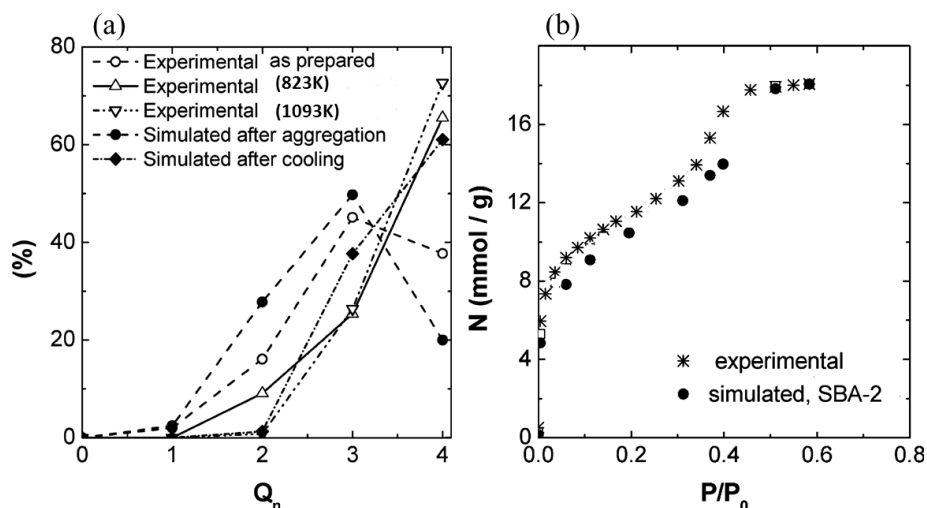


Figure 3.22. (a) Experimental degree of polymerisation, Q^n , for SBA-2, SBA-2(823) and SBA-2(1073) in comparison to the degree of polymerisation of the simulated model, and (b) N_2 adsorption isotherm of experimental and simulated SBA-2 at 77 K.²³

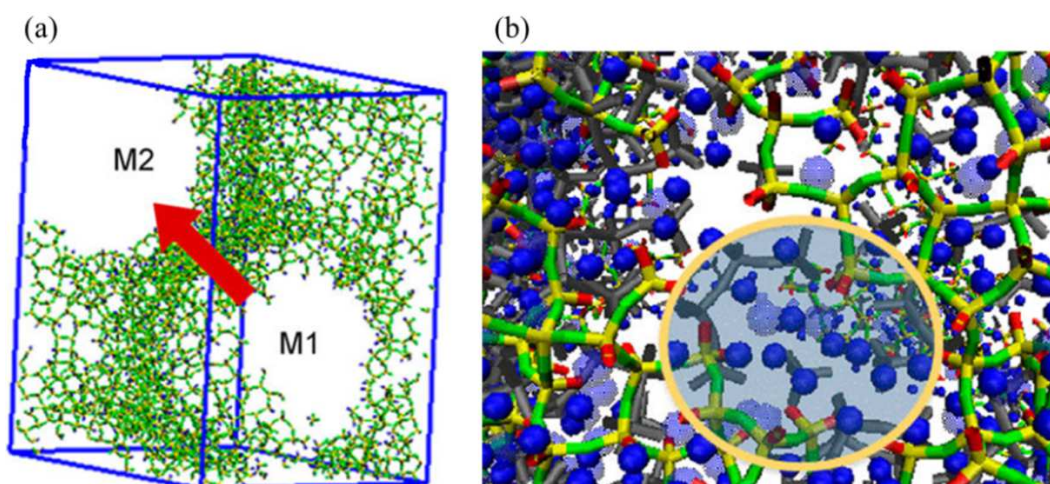


Figure 3.23. (a) SBA-2 model at the end of the aggregation stage, and (b) enlarged view of the connection between micelles (M1 and M2) in the SBA-2 model (silanol oxygens in red, bridging oxygens in green, silicon atoms in yellow, water molecules in blue).²³

3.7. Conclusions

In conclusion, due to low CO_2 adsorption (*ca.* 0.2 mmol g^{-1} at 0.1 bar) of SBA and NSBA, these materials are not good candidates for CO_2 capture and storage from flue gas at ambient temperature and pressure. They may have reasonably high uptake at high pressures and low temperatures but this was not investigated as part of this study.

It was found that the CO₂ performance of SBA-1 and SBA-2 depends on the size, surface chemistry of the pores, connectivity and accessibility of the network. SBA materials possess large pore volumes, but the silica framework does not interact strongly with CO₂. Modification of the silica framework by calcination did not improve the CO₂ uptake. The attempts to improve the CO₂ uptake by the modification of SBA materials by nitridation, by creating strong CO₂ adsorption sites, were made for the first time in this study. Around 9% is the highest nitrogen content which was introduced to SBA structures during nitridation. The nitridation has a stronger effect than calcination on the final connectivity of the SBA porous network. High temperature plus ammonia treatment cause faster degradation of the mesoporous structures. Nitridation only slightly enhanced the CO₂ uptake, nevertheless, nitrided samples show high CO₂/N₂ selectivity.

Experimental results of SBA-2 obtained during this PhD study helped to validate a realistic and atomistic model of SBA-2 and its computer-simulated synthesis. Results from this study can be applied to model the synthesis of other mesoporous silicas with different (even more complicated than SBA-2) structures by using the kinetic Monte Carlo (kMC) method.

References

1. Huo Q. S., Leon R., Petroff P. M. and Stucky G. D., *Science*, **1995**, 268, 1324-1327
2. Huo Q. S., Margolese D. I., Ciesla U., Feng P. Y., Gier T. E., Sieger P., Leon R., Petroff P. M., Schuth F. and Stucky G. D., *Nature*, **1994**, 368, 317-321
3. Anderson M. W., Egger C. C., Tiddy G. J. T., Casci J. L. and Brakke K. A., *Angew. Chem. Int. Edit.*, **2005**, 44, 3243-3248
4. Garcia-Bennett A. E., Williamson S., Wright P. A. and Shannon I. J., *J. Mater. Chem.*, **2002**, 12, 3533-3540
5. Beck J. S., Vartuli J. C., Roth W. J., Leonowicz M. E., Kresge C. T., Schmitt K. D., Chu C. T. W., Olson D. H., Sheppard E. W., McCullen S. B., Higgins J. B. and Schlenker J. L., *J. Am. Chem. Soc.*, **1992**, 114, 10834-10843
6. Kresge C. T., Leonowicz M. E., Roth W. J., Vartuli J. C. and Beck J. S., *Nature*, **1992**, 359, 710-712
7. Zhou W., *Micron*, **2000**, 31, 605-611

8. Hunter H. M. and Wright P. A., *Micropor. Mesopor. Mat.*, **2001**, *43*, 361-373
9. Hunter H. M. A., Garcia-Bennett A. E., Shannon I. J., Zhou W. Z. and Wright P. A., *J. Mater. Chem.*, **2002**, *12*, 20-23
10. Ravikovitch P. I. and Neimark A. V., *Langmuir*, **2002**, *18*, 1550-1560
11. Perez-Pariente J., Diaz I., Mohino F. and Sastre E., *Appl. Catal. A-Gen.*, **2003**, *254*, 173-188
12. Perez-Mendoza M., Gonzalez J., Wright P. A. and Seaton N. A., *Langmuir*, **2004**, *20*, 7653-7658
13. Perez-Mendoza M., Gonzalez J., Wright P. A. and Seaton N. A., *Langmuir*, **2004**, *20*, 9856-9860
14. Zapilko C. and Anwander R., *Chem. Mater.*, **2006**, *18*, 1479-1482
15. Zapilko C., Liang Y. C. and Anwander R., *Chem. Mater.*, **2007**, *19*, 3171-3176
16. Gonzalez J., *Adsorption properties of organically functionalised mesoporous solids and dynamics of adsorbed molecules in microporous organic-inorganic hybrid solids*, University of St Andrews, **2005**
17. Patil U., Fihri A., Emwas A. H. and Polshettiwar V., *Chemical Science*, **2012**, *3*, 2224-2229
18. Egger C. C., Anderson M. W., Tiddy G. J. T. and Casci J. L., *Phys. Chem. Chem. Phys.*, **2005**, *7*, 1845-1855
19. Kim M. J. and Ryoo R., *Chem. Mater.*, **1999**, *11*, 487-491
20. Chino N. and Okubo T., *Micropor. Mesopor. Mat.*, **2005**, *87*, 15-22
21. Keulen J., *Mat. Constr.*, **1973**, *6*, 181-183
22. Coasne B., Hung F. R., Pellenq R. J. M., Siperstein F. R. and Gubbins K. E., *Langmuir*, **2005**, *22*, 194-202
23. Ferreiro-Rangel C. A., Lozinska M. M., Wright P. A., Seaton N. A. and Düren T., *J. Phys. Chem. C*, **2012**, *116*, 20966-20974

4. Preparing Zeolites as Carbon Dioxide Adsorbents

Details of synthesis, ion exchange, framework modification methods, dehydration and characterisation for zeolites and silicoaluminophosphates (SAPO) materials are given in this chapter.

4.1. Synthesis

a) Synthesis of K-chabazite

Zeolite K-chabazite was synthesised from the gel composition: 2.65 K₂O: 1.0 Al₂O₃: 4.8 SiO₂ : 183 H₂O, according to a published procedure.¹ Na-Y zeolite (CF-900; 8 g; 0.70 mmol; Crosfield) was exchanged by mechanical stirring for 24 hours at 353 K with 2 M ammonium chloride solution (NH₄Cl; 99.9%; Alfa Aesar). The mixture was filtered and to the filtrate a new volume of NH₄Cl was added. The procedure was repeated five times, and the NH₄-Y was dried at 373 K overnight and heated at 823 K, to remove NH₃, leaving the protonic form of zeolite Y. H-Y was then suspended in distilled water (64 mL) and an aqueous solution of potassium hydroxide (KOH; 9 g; 72.3 mmol; 98.5%; Fisher Chemicals) was added. The mixture was stirred for 1 hour, and then was transferred into a polypropylene bottle (Figure 4.1a). The gel was heated in the oven at 368 K for 4 days and the solid product was recovered by filtration, washed with distilled water, and dried at 373 K.

b) Synthesis of K-ZK-5

Zeolite K-ZK-5 was synthesised from the gel composition: 2.7 K₂O: 0.05 Sr(NO₃)₂: 1.0 Al₂O₃: 5 SiO₂: 61 H₂O, according to a published procedure.² The starting mixture was prepared by dissolving aluminium isopropoxide (C₉H₂₁O₃Al; 1.86 g; 9.12 mmol; ≥98%; Sigma-Aldrich) in potassium hydroxide (KOH; 1.36 g; 24.2 mmol; 98.5%; Fisher Chemicals) and water (10 mL), under continuous stirring. The solution was added to Ludox AS-40 (6.77 g; 45.0 mmol of SiO₂; 40%, suspension in water; Sigma-Aldrich) and strontium nitrate (Sr(NO₃)₂; 0.099 g; 0.47 mmol; 99.5%; AnalaR) and the mixture was stirred until homogeneous. The crystallisation was carried out under static

conditions in polytetrafluoroethylene(PTFE)-lined stainless-steel autoclaves (Figure 4.1b) for 120 hours at 433 K. The product was filtered, washed with deionised water and dried at 373 K overnight.

c) Synthesis of SAPO STA-14

SAPO STA-14 was synthesised from the gel composition: 1 Al: 0.2 Si: 0.8 P: 0.108 K222: 40 H₂O, according to a published procedure.³ Aluminium hydroxide (Al(OH)₃; 0.58 g; 6.25 mmol; 50–57% of Al₂O₃; Sigma-Aldrich) was added to ortho-phosphoric acid (o-H₃PO₄; 0.58 g; 5.00 mmol; 85% in water, Prolabo) prior to the addition of fumed silica (SiO₂; 0.08 g; 1.33 mmol; 97%, Fluka). 4,7,13,16,21,24-hexaoxa-1,10-diazabicyclo-[8.8.8]-hexacosane (K222; C₁₈H₃₆N₂O₆; 0.25 g; 0.67 mmol; 97%; ABCR) was added to the gel, followed by adjustment of the pH to 7 by the addition of tetraethylammonium hydroxide solution (TEAOH; C₈H₂₁NO; 1.5 mL; 34% aqueous; Sigma-Aldrich). The gel was stirred at room temperature until homogeneous then loaded in PTFE-lined stainless steel autoclaves (Figure 4.1b) and heated at 463 K for 144 hours. After removing the autoclave from the oven and allowing it to cool, product was filtered from the reaction mixture, washed, and allowed to dry at 373 K overnight. The as-prepared SAPO STA-14 was heated at 823 K under oxygen for 12 hours to remove the template.

d) Synthesis of Na,Cs-Rho

Zeolite Na,Cs-Rho was synthesised from the gel composition: 0.31 NaOH: 0.02 Cs₂O: 1.0 Al₂O₃: 3.1 SiO₂: 0.16 (18-crown-6): 14 H₂O, according to a published procedure.⁴ The starting mixture was prepared by dissolving 1,4,7,10,13,16-hexaoxacyclooctadecane (18-crown-6; C₁₂H₂₄O₆; 1.12 g; 4.25 mmol; ; ≥99%; Sigma-Aldrich), cesium hydroxide (CsOH; 0.75 g; 5.00 mmol; 99.9%; Sigma-Aldrich) and sodium hydroxide (NaOH; 0.33 g; 8.3 mmol; 98.5%; Fisher Chemicals) in distilled water (6.7 mL). Sodium aluminate (NaAlO₂; 2.21 g; 27.0 mmol; 31% Na₂O, 38,5% Al₂O₃; BDH Chemicals Ltd.) followed by colloidal silica, Ludox AS-40 (12.5 g; 83.0 mmol of SiO₂; 40%, suspension in water; Sigma-Aldrich) was added and the mixture stirred until homogeneous. The gel formed was aged at room temperature for 24 hours in a closed polypropylene bottle (Figure 4.1a) under continuous stirring. The crystallisation was carried out under static conditions in the same closed polypropylene bottle for 8 days at

383 K. After reaction, the solid obtained was filtered, washed with distilled water then dried at 373 K overnight. The as-prepared Na,Cs-Rho was heated at 823 K under oxygen for 12 hours to remove the template.

e) Synthesis of SAPO(RHO)

SAPO(RHO) was synthesised from the gel composition: 2.0 DEA: 1.0 Al₂O₃: 0.8 P₂O₅: 0.4 TEOS: 0.2 CTAB: 100 H₂O, according to a published procedure.⁵ A homogenous solution was prepared by dissolving aluminium isopropoxide (C₉H₂₁O₃Al; 2.26 g; 11.10 mmol; ≥ 98%; Sigma-Aldrich) in orthophosphoric acid (o-H₃PO₄; 0.87 g; 8.88 mmol; 85% in water, Prolabo) and deionised water, followed dropwise addition of tetraethylorthosilicate (TEOS; C₈H₂₀O₄Si; 0.46 g; 2.20 mmol; 98%; Sigma-Aldrich). The aqueous solution of hexadecyltrimethylammonium bromide (CTAB; C₁₉H₄₂NBr; 0.40 g; 1.11 mmol; ≥ 99%; Sigma-Aldrich), together with diethylamine (DEA; C₄H₁₁N; 10 mL; 0.56 mmol; ≥ 99.5%; Sigma-Aldrich) was mixed into the gel and it was stirred at room temperature until homogeneous then loaded into a stainless-steel autoclave (Figure 4.1b). After crystallisation for 7 days, the product was washed with deionised water and dried at 433 K overnight. The as-prepared SAPO(RHO) was heated at 823 K under oxygen for 12 hours to remove the template.

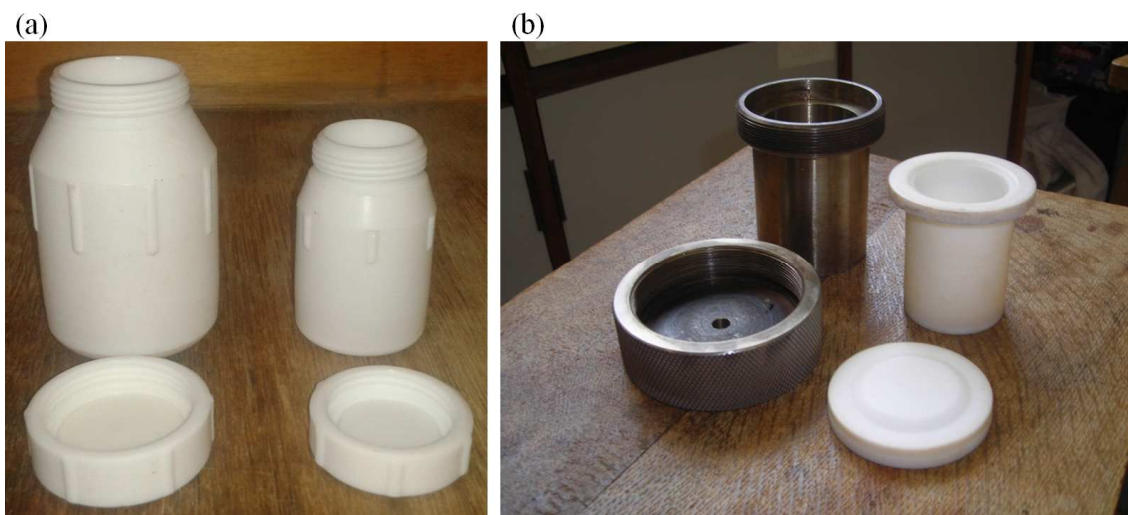


Figure 4.1. (a) Polypropylene bottles used for K-chabazite and Na,Cs-Rho synthesis and (b) a polytetrafluoroethylene(PTFE)-lined stainless-steel autoclave used for K-ZK-5, SAPO STA-14 and SAPO(RHO) synthesis.

4.2. Ion Exchange

a) Zeolites

Ion exchange of chabazite, ZK-5 and Rho was conducted according to published procedures.⁶⁻⁹ The as-prepared K-chabazite and K-ZK-5 were fully exchanged to cationic forms by repeated extended cation exchange treatments at 353 K using 4 M metal chloride solutions (99.5–99.9%; Sigma-Aldrich), where the as-prepared Na,Cs-crown ether-form of zeolite Rho was first calcined at 823 K in oxygen for 12 hours to remove all organic molecules and then fully exchanged with 10% NH₄Cl solution (99.9%; Alfa Aesar) and then with 10% metal nitrate solutions (99.5–99.9%; Sigma-Aldrich) at 353 K in a round bottom flask with condenser (Figure 4.2). The ammonium forms of chabazite, ZK-5 and Rho were heated to obtain the hydrogen form for 12 hours at 823 K in flowing oxygen. The lithium forms of chabazite, ZK-5 and Rho were prepared by lithium exchange of the sodium form until no more sodium could be exchanged. The lithium content was confirmed by subsequent repeated ion exchange with ammonium chloride, and the lithium content of the resulting solutions was measured by atomic absorption spectroscopy (AAS). Any residual trace ammonia was converted to H⁺ prior to all subsequent adsorption, structural and spectroscopic measurements by heating at 823 K prior to analysis.

It was also possible to prepare mixed K/NH₄-chabazite, Na/NH₄-chabazite, Li/NH₄-chabazite, and Ca/NH₄-chabazite and Na/NH₄-Rho, Li/NH₄-Rho, and Ca/NH₄-Rho solids (general formula (M⁺)_{x-y}(NH₄⁺)_yAl_xSi_{1-x}O₂) via careful removal of cations by subsequent controlled ion exchange at 333 K for 30 minutes. Weighed portions (0.2 g) of cationic chabazite and Rho solids were stirred with 10 mL of ammonium chloride solution, with concentrations in the range of 0.01–3.00 M NH₄Cl. The amount of K⁺, Na⁺ and Ca²⁺ remaining in the K,NH₄-forms, Na,NH₄-forms and Ca,NH₄-forms of the zeolites was determined by EDX. To determine the lithium content of the Li,NH₄-chabazite and Li,NH₄-Rho, the amount of Li⁺ ions lost to the solution during ion exchange was measured by AAS. After conversions, the zeolites were washed twice with deionised water, dried at 373 K and heated at 823 K for 12 hours, in order to remove NH₄⁺ ions and obtain the K,H-forms, Na,H-forms, Li,H-forms and Ca,H-forms.

The lithium ion exchange experiment was carried out in 50 mL round-bottom flasks heated at 333 K for 30 minutes. Weighed portions (0.20 g) of zeolites Li-chabazite and Li-Rho were stirred with 10.0 mL of ammonium chloride solution. The concentration of NH_4^+ was gradually increased to obtain the required exchange levels and was in the range of 0.2–200 mg/L NH_4^+ . The highest concentration of NH_4^+ (200 mg/L) was used to determine the total amount of Li^+ present in the zeolite. In this case ion exchange was carried out successively until no Li^+ was observed in the solution. To determine the lithium content of the partially ammonium-exchanged zeolite, the amount of Li^+ ions lost to the solution during ion exchange was calculated and subtracted from the determined total amount of lithium. All the solutions were transferred to 30.0 mL or 50.0 mL volumetric flasks and enough deionised water was added. In order to quantitatively determine Li^+ in the zeolite the AAS was used. The calibration curves were provided and were selected according to the expected concentrations of Li^+ in the solution: 50 ppm, 100 ppm and 150 ppm. Standard solutions were prepared by diluting the standard Li^+ solution with water. A blank sample containing ammonium chloride solution and water was prepared. The concentrations of Li^+ ions in the solutions are the average of three measurements (Table 4.1). After the AAS analysis, the zeolites were washed twice with deionised water, dried at 373 K and heated at 823 K for 12 hours, in order to remove NH_4^+ ions and obtain the Li,H-forms.

Table 4.1. The analytical characteristic of the ion exchange of Li-chabazite and Li-Rho (from AAS).

Sample	Concentration of Li^+ in the solution /ppm ^{a)}	Volume of the solution /mL	Mass of Li^+ in the solution /mg	Cations in the solution per unit cell	Cations per unit cell
Li-Chabazite(1)	150.0 ^{b)} ± 0.5	30	4.5 ± 0.2	8.5 ± 0.2	0
Li-Chabazite(2)	111.2 ± 0.5	30	3.3 ± 0.1	6.1 ± 0.2	2.1 ± 0.1
Li-Chabazite(3)	73.3 ± 0.5	30	2.2 ± 0.1	4.1 ± 0.2	4.3 ± 0.1
Li-Chabazite(4)	57.5 ± 0.5	30	1.7 ± 0.1	3.2 ± 0.2	5.2 ± 0.2
Li-Chabazite(5)	22.2 ± 0.5	30	0.7 ± 0.1	1.2 ± 0.1	7.2 ± 0.2
Li-Chabazite(6)	0	30	0	0	8.5 ± 0.2
Li-Rho(1)	67.5 ^{b)} ± 0.5	50	3.5 ± 0.2	9.5 ± 0.2	0
Li-Rho(2)	57.2 ± 0.5	50	2.9 ± 0.2	7.8 ± 0.2	1.3 ± 0.1
Li-Rho(3)	49.1 ± 0.5	50	2.5 ± 0.1	6.7 ± 0.2	2.4 ± 0.1
Li-Rho(4)	41.1 ± 0.5	30	1.2 ± 0.1	3.4 ± 0.2	5.8 ± 0.2
Li-Rho(5)	29.0 ± 0.5	30	0.9 ± 0.1	2.4 ± 0.1	6.8 ± 0.2
Li-Rho(6)	14.6 ± 0.5	30	0.4 ± 0.1	1.1 ± 0.1	8.4 ± 0.2
Li-Rho(7)	0	30	0	0	9.5 ± 0.2

a) average of three measurements

b) sum of three successive measurements where third measurement was 0 ppm

b) Silicoaluminophosphates (SAPOs)

Ion exchange of SAPO STA-14 and SAPO(RHO) was conducted according to a published procedure.¹⁰ Sodium acetate (CH₃COONa; 99%; Sigma-Aldrich) was dissolved in ethanol. Around 1 g of each calcined and proton-containing sample was placed in exchange solution in a flask at a reflux condition (Figure 4.2) and it was stirred in 30 mL of the exchange solution three times at 333 K, each time for 20 minutes. After exchange, samples were washed in 50 mL ethanol three times and then they were dried at 373 K overnight.

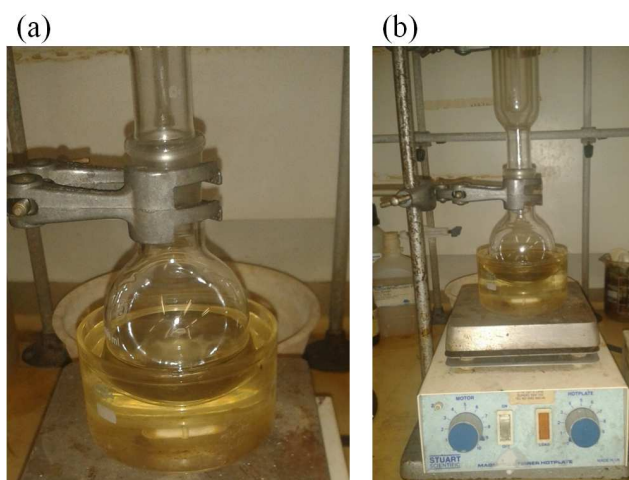


Figure 4.2. (a) Set up for ion exchange consists of round bottom flask with condenser and oil bath, and (b) set up for ion exchange on a hot plate.

c) Derivation of the unit cell composition of zeolites and silicoaluminophosphates

Unit cell composition for aluminosilicate zeolites was derived using a simplified empirical formula:

$$M_x^{n+} Al_x Si_{1-x} O_2 \cdot yX \quad (4.1)$$

where x can vary from 0–0.5, Mⁿ⁺ represents inorganic or organic cations and X represents neutral guest molecules or included species. The Si/Al ratio was obtained from ²⁹Si MAS NMR. The EDX analysis was used to confirm the amount of extra-framework cations that were exchanged and that no other unexpected elements are present after ion exchange. In silicoaluminophosphates 20% of phosphorous is replaced by silicon and the number of extra-framework cations is equal to the number of silicon cations.

4.3. Framework Modification and Dehydration

a) Dealumination of H-Rho

Calcined Na,Cs-Rho was ion exchanged five times for 1 hour with 3 M ammonium nitrate ($\text{NH}_4\text{-Cl}$; 3 g of zeolite for every set of samples in 20 mL solution) under reflux condition and washed with deionised water. $\text{NH}_4\text{-Rho}$ dried at 373 K was pelleted into 3 mm thick pellets, broken into smaller pieces and steamed in a water vapour stream in flowing nitrogen (20 mL h^{-1}) at 743 K, 773 K, 823 K for 6 hours, respectively. Two sets of steamed samples were prepared. They are denoted as ST1-H-Rho(743), ST1-H-Rho(773), ST1-H-Rho(823) for first set of steaming samples (ST1) and ST2-H-Rho(743), ST2-H-Rho(773), ST2-H-Rho(823) for second set of steaming samples (ST2). H-Rho heated at 823 K is denoted as H-Rho(823). The water was introduced by a syringe pump. ST1 was prepared with water a flow rate of 1.5 mL h^{-1} and ST2 with a water flow rate of 2 mL h^{-1} . The samples were steamed in a custom-built apparatus presented in Figure 4.3. Steamed samples were compared with the H-form of Rho which was prepared by deammoniation of $\text{NH}_4\text{-Rho}$ under shallow bed heating at 823 K for 12 hours. For the attempted removal of extra-framework aluminium from ST2-H-Rho(743) ion exchange and washing with acid were performed. The ion exchange was conducted three times for 1 hour with 1 M calcium nitrate on 0.5 g of ST-Rho in 5 mL solution under reflux at 333 K. For the acid wash, the ST2-H-Rho(743) sample was stirred in 0.5 M HCl at 298 K for 15 minutes, twice.

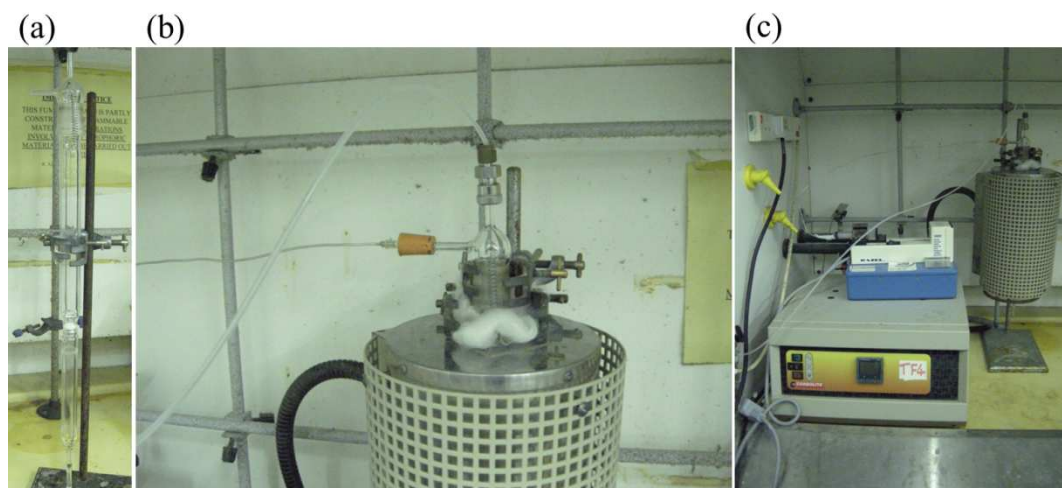


Figure 4.3. Set up for steaming of Rho zeolite which contains: (a) quartz tube with the frit in the middle, (b) quartz tube connected to the syringe pump and nitrogen cylinder and (c) tube furnace with syringe pump.

b) Nitridation of H-Y, US-Y and H-Rho

Dehydration of H-Y (framework Si/Al = 2.6), US-Y (framework Si/Al = 8.0) and H-Rho (framework Si/Al = 4.15) prior to the nitridation was performed under nitrogen flow. The temperature was slowly ramped to 383 K at a ramp rate of 0.1 K min^{-1} in the tube furnace (Figure 4.4), held at that temperature for 2 hours, then slowly ramped to 673 K at a ramp rate of 0.5 K min^{-1} , and held at that temperature for 10 hours. Following this dehydration step, samples were heated in flowing nitrogen till the temperature reached 823 K, and then switched to ammonia with high flow rate of *ca.* $2000 \text{ cm}^3 \text{ min}^{-1}$. The temperature was then raised to between 973–1123 K, left for 24 hours and the furnace was cooled down to room temperature under nitrogen flow.

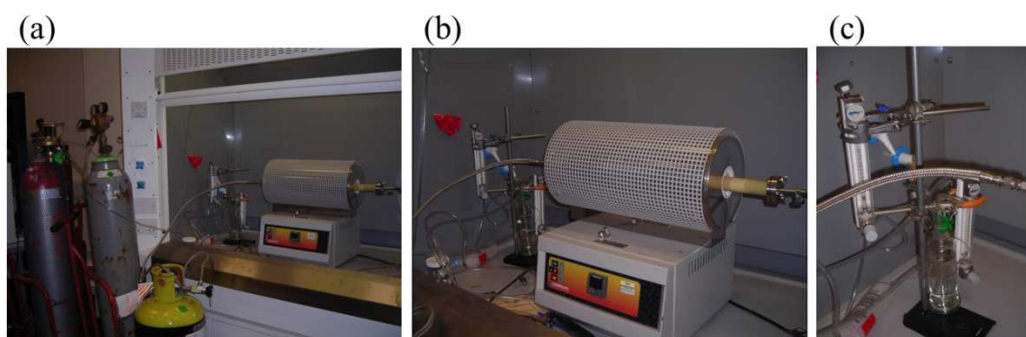


Figure 4.4. (a) Set up for nitridation, (b) tube furnace connected to gas and (c) gas flow meters.

c) Dehydration

In order to measure the structure of dehydrated zeolites the powders were loaded into 0.7 mm quartz glass capillaries (Figure 4.5a) and dehydrated at 623 K at 10^{-5} mbar on a glass line (Figure 4.5b) for 12 hours, before capillaries were flame-sealed.

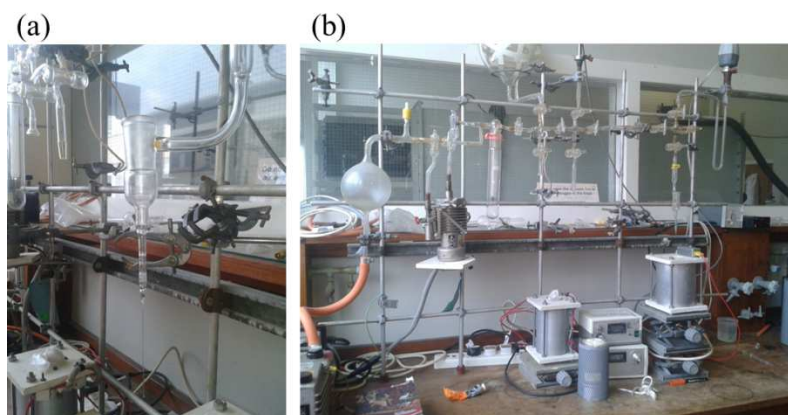


Figure 4.5. (a) Quartz glass capillary attached to the holder on a glass line and (b) glass line used for samples dehydration.

4.4. Characterisation

a) Powder X-ray diffraction (PXRD) and Rietveld refinement

Crystallinity of all as-prepared, ion exchanged, calcined and dehydrated samples was measured in Debye-Scherrer geometry on a Stoe STAD i/p diffractometer with monochromated Cu $K_{\alpha 1}$ X-rays ($\lambda = 1.54056 \text{ \AA}$). The structures of dehydrated samples were determined by Rietveld refinement against the PXRD data, using the GSAS suite of programs.¹¹ For chabazite, ZK-5, Rho and Na-SAPO(RHO), starting framework models were adapted from literature examples with the unit cell modified to that derived from the diffraction pattern.¹²⁻¹⁵ Starting cation positions were estimated from literature models and the framework atomic positions were refined with geometric constraints on Al,Si-O ($1.60 \pm 0.05 \text{ \AA}$) and O-O ($2.60 \pm 0.05 \text{ \AA}$) distances to maintain regular tetrahedral coordination. Final extra-framework cation positions and occupancies were determined by refinement of starting positions and by using difference Fourier methods to look for additional positions. The ZK-5 prepared here contains a small amount of chabazite (a polytype of ZK-5), so that the diffraction data was analysed via a two-phase refinement, using a structural model for chabazite as a starting point.¹³

In situ dehydration at 773 K under flow of He and *in situ* high pressure measurements under CO₂ at 298 K (data collected at Instituto de Tecnologia Quimica in Valencia) were performed in an Anton Parr XRK-900 reaction chamber attached to the Panalytical X'Pert PRO diffractometer with Bragg-Brentano geometry, using Cu $K_{\alpha 1}$ X-radiation (1.54056 \AA).

b) Electron microscopy (EM) with electron dispersive X-ray (EDX) analysis

Morphology of chabazite, ZK-5, Rho and SAPO(RHO) crystals was measured by field emission gun scanning electron microscopy (FEG-SEM) on a Jeol JSM-6700F electron microscope. Jeol JEM 2011 high resolution transmission electron microscopy (HRTEM) operating at 200 keV was used to investigate the structures of dehydrated chabazite. Electron dispersive X-ray (EDX) analysis on all samples was performed in a JEOL JSM 5600 SEM, with an Oxford INCA Energy 200 EDX analyser. The EDX area scans were performed over three different regions and averaged.

c) Solid-state ^{27}Al , ^{29}Si MAS NMR and ^{27}Al MQ MAS NMR

Solid-state ^{27}Al and ^{29}Si MAS NMR spectra were performed on selected samples using a Varian VNMRs spectrometer operating at 79.44 MHz for ^{29}Si and 104.20 MHz for ^{27}Al in collaboration with the University of Durham. Deconvolution of the ^{29}Si MAS NMR spectrum of the as-prepared chabazite, ZK-5 and Na,Cs-Rho, in which all aluminium occupies tetrahedral sites, was used to determine the framework Si/Al ratio of zeolites and used to calibrate the Si/Al ratios determined via EDX. The framework Si/Al ratio (for all zeolites in this study which have only one tetrahedral site) was determined using equation:

$$\frac{\text{Si}}{\text{Al}} = \frac{\sum_{n=0}^4 I_{n\text{Al}}}{\sum_{n=0}^4 0.25nI_{n\text{Al}}} \quad (4.2)$$

where $I_{n\text{Al}}$ denotes the intensity of the ^{29}Si peak corresponding to a $\text{Si}[n\text{Al},(4-n)\text{Si}]$ environment. A two-dimensional ^{27}Al MQ MAS NMR spectrum of steamed Rho sample (ST2-H-Rho(743)) was obtained using a pulse sequence consisting of two-pulses (of duration 2.8 and 1.0 μs at an RF field equivalent to 105 kHz) and a z-filter (at an RF field equivalent to 15 kHz). 4000 repetitions were acquired for each of 32 increments in t_1 . The recycle delay was 0.2 and the spinning rate was 12 kHz. Spectral referencing is with respect to external 1 M aqueous AlCl_3 . The spectrum is plotted after shearing and the indirectly detected, “isotropic”, axis is scaled by a factor of 12/31.

d) Thermogravimetric analysis (TGA)

Thermogravimetry of all samples was performed using a Netzsch TG 209 instrument with a heating rate of 3 K min^{-1} up to 973 K in flowing air, in order to determine the temperature at which water, template or ammonia (in the case of NH_4 -forms) were evolved.

e) In situ infra-red spectroscopy (IR)

In situ IR spectra of chabazite and Rho samples with and without adsorbed CO_2 were measured at room temperature using self-supporting wafers (ca. 30 mg, 2 cm^2) placed in a pyrex cell with KBr windows. The infra-red cell was connected to a vacuum line for evacuation, dehydration and CO_2 adsorption (Figure 4.6a). The wafers were heated at 673 K for 4 hours to ensure full dehydration and CO_2 (> 99.9995%; supercritical fluid

chromatography, SFC, grade; British Oxygen Company, BOC) was admitted to give a range of equilibrium. Samples were measured using a Nicolet Magna instrument (deuterated triglycine sulphate, DTGS, detector, 4 cm^{-1} resolution, Figure 4.6b).

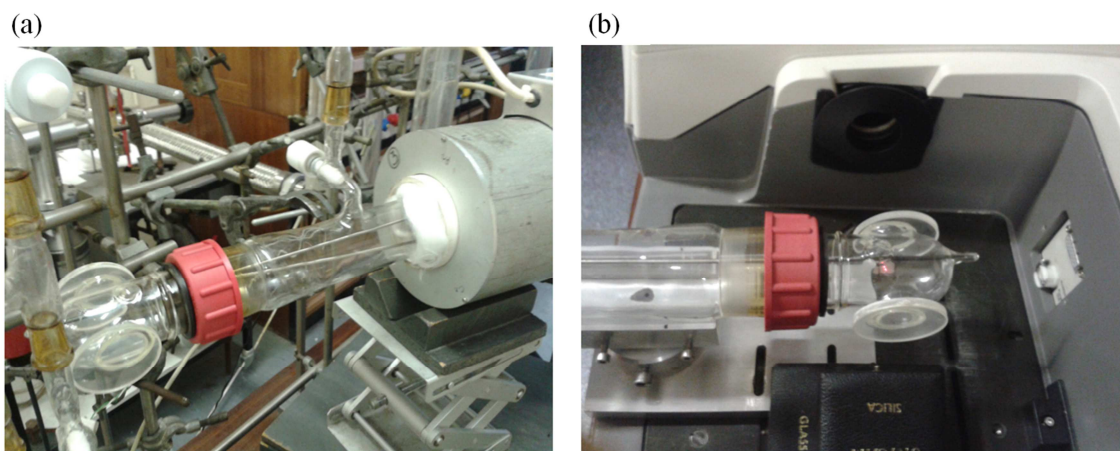


Figure 4.6. (a) Pyrex cell with KBr windows and self-supporting wafers with the sample placed inside the tube oven which is connected to the glass line and (b) pyrex cell placed in a Nicolet Magna instrument for measurement.

f) N_2 , CO_2 and C_2H_6 adsorption

N_2 adsorption isotherms were measured volumetrically at 77 K using a Micromeritics Tristar II 3020. CO_2 adsorption isotherms were measured volumetrically starting at lower pressures using a Micromeritics 2020 porosimeter. This was typically performed from 0–1 bar at 298 K, although for Na-Rho isotherms up to 0.14 bar were also collected sequentially on the same sample at 273 K, 298 K and 308 K. Prior to N_2 and CO_2 adsorption/desorption isotherms being measured, the samples were degassed under high vacuum at temperatures chosen from examination of the TGA plots that would result in the removal of all physically bound water. The temperature of 623 K was used for all samples except NH_4 -Rho, which is known to undergo partial deammoniation at this temperature. For NH_4 -Rho, 500 K was chosen as a compromise temperature to remove most of the physisorbed water whilst resulting in minor amounts of deammoniation. During measurement of the CO_2 adsorption isotherms each measurement on the adsorption and desorption branches was allowed up to 2.5 hours to reach equilibrium, if this time was required. Ethane adsorption isotherms were measured volumetrically at 293 K using a custom-built glass line. High pressure isotherms (up to 10 bar, data collected at Instituto de Tecnologia Quimica in Valencia) of CO_2 and CH_4 were measured at 283 K, 298 K, 303 K and 333 K on an IGA-3

gravimetric instrument from Hiden Isochema Ltd equipped with a thermostatic bath FP50-HE from Julabo. The hypothetical CO₂/CH₄ equilibrium selectivity factor (α) was calculated using equation:

$$\alpha = \frac{Q_{CO_2}}{Q_{CH_4}} \quad (4.3)$$

where QCO₂ and QCH₄ are the equilibrium molar uptakes of CO₂ and CH₄ at given pressure taken from the corresponding single component isotherms.

g) Zero Length Column (ZLC) method

For all M,H-forms of chabazite and Rho the reversible capacity for CO₂ adsorption at 0.1 bar CO₂ and at 308 K was estimated by the Zero Length Column (ZLC) method (data collected at the University of Edinburgh).^{16,17} The technique is based on following the desorption curve of a sample previously saturated with a mixture of 10% of CO₂ (sorbate) in He (carrier). When equilibrium between the gas phase and the adsorbed phase is reached the flow is switched to pure He (purge) and the outlet gas phase concentration from the column is monitored. An on-line quadrupole mass spectrometer (Ametek Benchtop) is connected to the ZLC to monitor the outlet gas concentration. The apparatus is provided with drying columns to ensure pre-dried gases entering the system. A very small amount of material (10 mg) is required to fill a ZLC. Before each experiment the samples were dehydrated overnight at 623 K under a flow of pure He. The calculations of the CO₂ capacities are based on the dry weight of the sample. To ensure that full saturation was reached preliminary ZLC experiments were run increasing the exposure time to the sorbate: the sample was fully equilibrated when the CO₂ capacity obtained did not change with the exposure time.

h) In situ synchrotron X-ray diffraction

For the fully-exchanged Na-chabazite and Na-Rho the structural response to CO₂ adsorption was measured by *in situ* synchrotron X-ray diffraction performed at beamline I-11 at the Diamond Light Source.¹⁸ This was achieved using a custom-built gas handling line.¹⁹ Samples were loaded into a 0.7 mm quartz glass capillary to a depth of around 1 cm and a quartz wool plug was packed above this to prevent loss of powder upon evacuation and dehydration. The capillary was attached to a gas dosing line attached to a goniometer head, which was permitted to rock by 20° in the beam

to improve powder averaging during diffraction. The samples were dehydrated under evacuation (10^{-5} mbar) using an Oxford Cryocool blowing hot air at 500 K for 2 hours. Series of diffraction patterns, each of 2 minutes and over the 2θ range 2–140°, were collected at 298 K before and after dehydration, and also after dosing with 0.1 bar, 0.2 bar or 1 bar of CO₂, each time after 15 minutes equilibration. Subsequently, diffraction patterns were measured during evacuation of the sample at 298 K, as carbon dioxide was removed. For the dehydrated zeolite and that on which CO₂ was adsorbed at 0.1 and 0.2 bar, five patterns were summed and the data binned to 0.005° 2θ . For other patterns, the data in individual patterns was binned to 0.005° 2θ . Full Rietveld refinement was then performed for Na-chabazite and Na-Rho after dehydration, in equilibrium with 0.1 bar, 0.2 bar or 1 bar of CO₂, and after prolonged evacuation, in each case to determine the framework zeolite structure and the location and site occupancy of sodium cations and any CO₂ molecules. CO₂ adsorption sites were located by difference Fourier mapping. The starting framework model used was that refined against the synchrotron PXRD data collected immediately prior to the CO₂ loading. The occupancy and location of the cations and the identified CO₂ positions were then refined against the data with constraints applied to maintain a linear CO₂ geometry and chemically reasonable bond lengths.

References

1. Ridha F. N., Yang Y. and Webley P. A., *Micropor. Mesopor. Mat.*, **2009**, *117*, 497-507
2. Verduijn J. P., US Patent **1991**
3. Castro M., Warrender S. J., Wright P. A., Apperley D. C., Belmabkhout Y., Pirngruber G., Min H. K., Park M. B. and Hong S. B., *J. Phys. Chem. C*, **2009**, *113*, 15731-15741
4. Chatelain T., Patarin J., Fousson E., Soulard M., Guth J. L. and Schulz P., *Microporous Mater.*, **1995**, *4*, 231-238
5. Su X., Tian P., Li J. Z., Zhang Y., Meng S. H., He Y. L., Fan D. and Liu Z. M., *Micropor. Mesopor. Mat.*, **2011**, *144*, 113-119
6. Zhang J., Singh R. and Webley P. A., *Micropor. Mesopor. Mat.*, **2008**, *111*, 478-487
7. Dyer A. and Enamy H., *Zeolites*, **1981**, *1*, 66-68

8. Lee Y., Reisner B. A., Hanson J. C., Jones G. A., Parise J. B., Corbin D. R., Toby B. H., Freitag A. and Larese J. Z., *J. Phys. Chem. B*, **2001**, *105*, 7188-7199
9. Langmi H. W., Book D., Walton A., Johnson S. R., Al-Mamouri M. M., Speight J. D., Edwards P. P., Harris I. R. and Anderson P. A., *J. Alloys Compd.*, **2005**, *404-406*, 637-642
10. Hong M., Li S., Funke H. F., Falconer J. L. and Noble R. D., *Micropor. Mesopor. Mat.*, **2007**, *106*, 140-146
11. Larson A. C. and Von Dreele R. B., '*General Structure Analysis System (GSAS)*', Los Alamos National Laboratory, USA, **1994**
12. Lievens J. L., Verduijn J. P. and Mortier W. J., *Zeolites*, **1992**, *12*, 690-697
13. Cartlidge S. and Meier W. M., *Zeolites*, **1984**, *4*, 218-225
14. Tian P., Su X. O., Wang Y. X., Xia Q. H., Zhang Y., Fan D., Meng S. H. and Liu Z. M., *Chem. Mater.*, **2011**, *23*, 1406-1413
15. Corbin D. R., Abrams L., Jones G. A., Eddy M. M., Harrison W. T. A., Stucky G. D. and Cox D. E., *J. Am. Chem. Soc.*, **1990**, *112*, 4821-4830
16. Eic M. and Ruthven D. M., *Zeolites*, **1988**, *8*, 472-479
17. Brandani S., Hufton J. and Ruthven D., *Zeolites*, **1995**, *15*, 624-631
18. Thompson S. P., Parker J. E., Potter J., Hill T. P., Birt A., Cobb T. M., Yuan F. and Tang C. C., *Rev. Sci. Instrum.*, **2009**, *80*
19. Parker J. E., Potter J., Thompson S. P., Lennie A. R. and Tang C. C., *Mater. Sci. Forum*, **2012**, *706-709*, 1707-1712

5. Zeolite Chabazite: Structural Investigation of an Established Carbon Dioxide Adsorbent

5.1. Introduction

In 1963 Smith^{1,2} first reported the crystal structure of a naturally-occurring zeolite chabazite (topology type CHA). The framework structure of chabazite is built up from double six-membered rings (D6Rs) linked by single four-membered rings (S4R). This results in a structure containing ‘chabazite’ cages (CHA-cages), the pore spaces of which are connected to six other such cages via non-planar single eight-membered rings (S8R, Figure 5.1a).

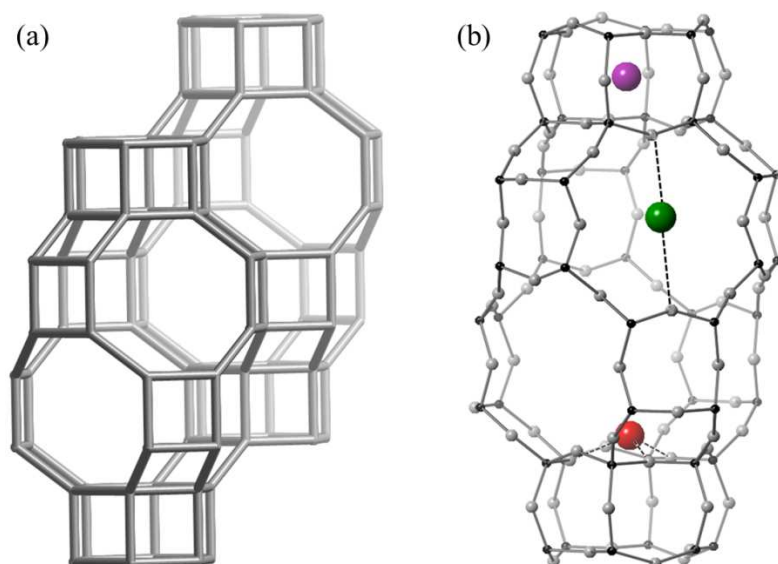


Figure 5.1. (a) Illustration of the chabazite topology showing the interconnection of cages through single eight-membered ring windows linked together by tilted single four-membered rings and (b) representation of the extra-framework cation positions in chabazite: the double six ring site (D6R; purple), the single six-membered ring site (S6R; red) and the single eight-membered ring window site (S8R; green).

Si/Al ratio controls the charge-balancing cation concentration and consequently their siting in zeolites. Cation distribution in extra-framework sites is an important structural parameter for generating adsorption sites and strong adsorption interactions.³ In small-

pore zeolites with high cation contents, cage access is usually considered to be controlled by the size of the cation and the degree of occupancy of the window.⁴ Previous studies have characterised the cation sites in dehydrated and hydrated forms of chabazite and the occupancy of these sites was determined for K^+ , Na^+ , Li^+ and Ca^{2+} .⁵⁻⁹ Three cation positions for dehydrated chabazite have been observed: one at the centre of the double six-membered ring (D6R site, coordinates (0,0,0)), one at the single six-membered ring site (S6R site, coordinates (0,0,x), $x \approx 0.2$) and one at the single eight-membered ring window site (S8R site, coordinates (1/2,1/2,0)) in the CHA-cage, depending on cation size and charge (Figure 5.1b and Table 5.1).^{5,6,8,9} Ca^{2+} cations in dehydrated chabazite prefer to occupy the single six-membered ring sites with additional Ca^{2+} cations in the centre of D6R.⁶ For Li^+ cations in Li-chabazite the primary cationic site is at the S6R site, as determined using neutron powder diffraction and nuclear magnetic resonance spectroscopy by Smith *et al.*^{8,9} In Na-chabazite, at low sodium content, Na^+ cations occupy a site in the S8R windows, where at high Na content (70% and higher), sodium cations also reside at the S6R sites.^{8,9} The preferred lithium and sodium positions in chabazite were confirmed by the study on mixed Li,Na-chabazite, where Li^+ cations prefer coordination at the S6R windows, while sodium cations are located at the S8R sites.⁸ Smith *et al.*⁹ showed that for mixed, dehydrated Na,K-chabazite the K^+ cations reside primarily at the S8R window site in the presence of Na^+ cations, which occupy S6R sites, as confirmed by Ugliengo *et al.*¹⁰ and Ridha *et al.*¹¹ In K-chabazite with high K content ($Si/Al < 3$) the second cationic site for K is close to the S6R.^{11,12} For dehydrated Na-chabazite with high sodium content ($Si/Al < 3$) the reduction of the rhombohedral $R\bar{3}m$ symmetry to monoclinic $C2/m$ symmetry (Figure 5.2) has been observed. This results from elliptical distortion of most eight-membered rings to accommodate the Na^+ cations and the extra Na^+ cations are displaced to positions close to the S6R sites.⁵

Table 5.1. Positions of extra-framework cations in dehydrated chabazite ('+' indicates presence and '-' indicates absence of cations in a cationic site).

Sample	D6R site	S6R site	S8R site	Reference
K-chabazite	–	+	+	⁹ and this work
Na-chabazite	–	+	+	^{5,8,9,13} and this work
Li-chabazite	–	+	–	^{8,9,13} and this work
Ca-chabazite	+	+	–	^{6,14} and this work

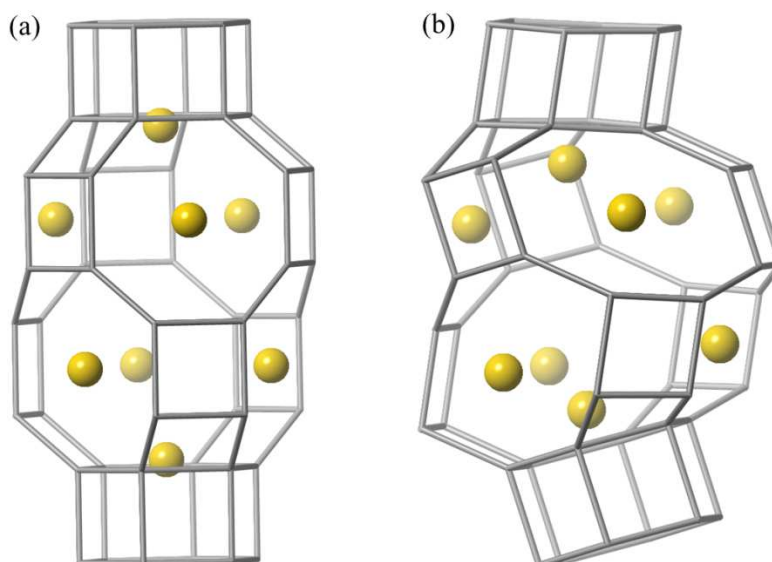


Figure 5.2. Structures of Na-chabazite with (a) rhombohedral $R\bar{3}m$ symmetry and (b) monoclinic $C2/m$ symmetry, with extra-framework Na^+ cations (yellow spheres) present.⁵

Early research on natural chabazite was focused on its geological, mineralogical and geochemical characteristics.¹⁵ Natural chabazite however is variable in chemical composition which affects its performance in applications. Synthetic chabazite therefore has many advantages and it now has many applications (for example ion exchange, adsorption and catalysis).^{11,16-18} A considerable number of adsorption and separation studies of gases (for example CO_2 , CH_4 and N_2)^{12,18,19} on different ion exchanged forms of chabazite have been reported. Chabazite has relatively small cages that facilitate strong interactions with adsorbed molecules, even at the highest levels of pore filling. Larger and more polar molecules interact strongly with zeolites having smaller univalent cations, or divalent cations (which have larger density charge than monovalent cations of similar size).²⁰

At the beginning of these studies, there was no combined structure/adsorption data on chabazite materials, although there was CO_2 adsorption data on a range of Li-, Na-, K- and Ca-chabazite structures.^{11,18,21,22} The group of Webley^{11,18,21,22} reported the adsorption of CO_2 on Li-, Na- Ca-chabazite and K-chabazite, indicating that uptakes of between 4 mmol g^{-1} and 5 mmol g^{-1} were obtained at 303 K and 0.1 bar, with the highest values obtained for Li-chabazite due to the high electrostatic interactions of CO_2 with the small Li^+ cations. Hudson *et al.*²³ reported CO_2 adsorption on

Cu-SSZ-13 (a high Si/Al chabazite) to be selective, although with lower uptake, and attribute the selectivity to the favorable interaction with the D8R of the framework rather than with the extra-framework Cu^{2+} cations. It has been also proved that chabazite is one of relatively few zeolitic materials that retains high CO_2 loading capacity at elevated temperatures, *ca.* 523 K (the benchmark zeolite 13X retains CO_2 loading capacity only to 393 K).²⁴ Shang *et al.*²⁵ reported a successful ‘encapsulation mechanism’ for K-chabazite (Si/Al = 2.2) for N_2 and CH_4 storage where gas molecules are included at elevated temperatures and pressures into pores of zeolite which are normally not accessible under ambient conditions.¹² Singh *et al.*¹⁹ showed that K-chabazite (Si/Al = 2.4) possesses higher O_2/Ar selectivity than Ca- and Li-chabazite and attribute this to pore blockage by a K^+ cation located in or near the S8R windows. Furthermore, the presence of the larger K^+ cation in the pores imparts the advantage of increasing the selectivity over N_2 , which is both larger and interacts more weakly than CO_2 , and so is less readily taken up.¹²

Within the period of the thesis, some additional adsorption studies and limited structural work on chabazite was performed. Yang *et al.*²⁶ measured the pore size effect and the metal cation effect on the adsorption of CO_2 , CH_4 , and N_2 in small pore zeolites (CHA, Si/Al = 2.63, KFI and LEV). They observed that the Na-forms produced the best results for selective adsorption of CO_2/N_2 (187 for Na-chabazite) and CO_2/CH_4 (42 for Na-chabazite), followed by the Li-forms ($\text{CO}_2/\text{N}_2 = 154$ and $\text{CO}_2/\text{CH}_4 = 32$ for Li-chabazite), whereas the K-forms gave high CH_4/N_2 (14.5 for K-chabazite) and CO_2/N_2 (352 for K-chabazite) selectivity and Ca-forms were not very selective ($\text{CO}_2/\text{CH}_4 = 51$, $\text{CO}_2/\text{N}_2 = 127$ and $\text{CH}_4/\text{N}_2 = 1.6$ for Ca-chabazite), calculated from pure component adsorption isotherms. According to this work the selectivity arises due to the size of the channels and size of extra-framework cations, but very recent work of Shang *et al.*¹² showed that not only are these two features important, but also important is the position of the cation in the structure. They proposed a ‘molecular trapdoor’ mechanism through which high selectivity for particular guest molecules (CO_2 over CH_4 , and CO over N_2) is achieved in chabazite. The S8R are large enough for CH_4 , N_2 and CO_2 to pass through, but their access is blocked by the presence of Cs^+ or K^+ cations occupying the position in the centre of the S8R window and they have to move for adsorbate molecules to be able to enter the CHA-cages. The ‘molecular trapdoor’

mechanism can be achieved only for zeolites with high cation contents (low Si/Al ratio) when the cations occupying the entrance to the cages do not move permanently to other cationic positions during adsorption. The 'molecular trapdoor' adsorbents are of interest for either pre-combustion purification or post-combustion separation – we have described a similarly interesting effect for zeolite Rho (see chapter 7).

In this study chabazite (Si/Al = 3), prepared from a zeolite Y precursor, is of interest for its cation dependent CO₂ adsorption properties. Chabazites with different extra-framework cations (H⁺, K⁺, Na⁺, Li⁺ and Ca²⁺) were prepared and modified for applications in carbon dioxide adsorption at ambient temperature and pressure. K-chabazite and Na-chabazite structures with adsorbed CO₂ have been determined from *in situ* powder X-ray diffraction, via structure refinement of K-chabazite and Na-chabazite during CO₂ adsorption at high pressure (using *in situ* laboratory powder X-ray diffraction and *in situ* powder synchrotron X-ray diffraction, respectively). The adsorption behaviour of all chabazite materials, including Li,H-, K,H- and Na,H-forms with different degrees of cation exchange, has been discussed with reference to the crystal structures of the dehydrated forms. Additionally, dehydrated structures of K-, Na- and Li-chabazite were investigated by high resolution transmission electron microscopy (HRTEM).

5.2. Characterisation of Different Cationic Forms of Chabazite

As-prepared K-chabazite and its ion exchanged forms were characterised by a combination of physico-chemical techniques.

Phase identification, the crystallinity and the phase purity of K-, H-, Na-, Li-, and Ca-chabazite were determined by PXRD. The PXRD pattern of K-chabazite (Figure 5.3a) shows many well-resolved and sharp diffraction peaks in the region of $2\theta = 7.0\text{--}65.0^\circ$. No reflections other than those due to K-chabazite are visible and the sample exhibits high crystallinity. All of the reflections are associated with $R\bar{3}m$ trigonal symmetry with the unit cell parameters $a = b = 13.8177(5)$ Å, $c = 15.0741(0)$ Å and $\alpha = \beta = 90^\circ$, $\gamma = 120^\circ$. The PXRD patterns of Na-, Li- and Ca-chabazite (Figure 5.3b) indicate no significant changes in crystalline structure due to ion exchange. However the H-form partially loses its crystallinity.

SEM was carried out to determine the morphology of as-prepared and exchanged chabazite. The SEM images of K-chabazite and Na-chabazite are presented in Figure 5.4. The SEM micrographs indicate that K-chabazite and Na-chabazite appear as agglomerates of small crystals and no amorphous phase is visible. The size of the crystals of K-chabazite and Na-chabazite is similar, between 0.4 μm and 0.5 μm . The SEM micrographs demonstrate that ion exchange does not affect the shape and size of the crystals. The unit cell compositions of all chabazite samples were estimated from a combination of EDX analysis and MAS NMR spectroscopy.

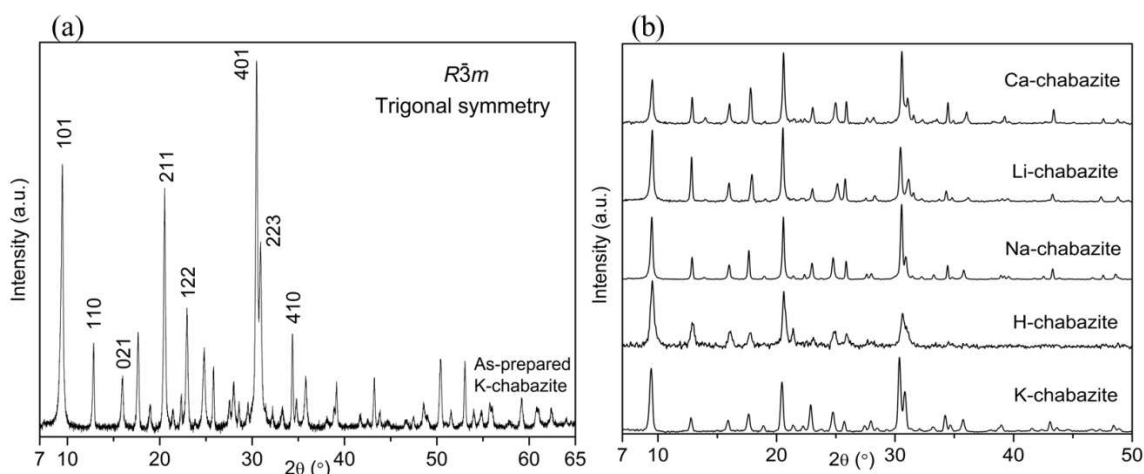


Figure 5.3. PXRD patterns of (a) K-chabazite indexed according to the trigonal $R\bar{3}m$ symmetry and (b) comparison of K-chabazite with H-, Na-, Li- and Ca-chabazite. The (offset) patterns have been collected at 298 K using the same operating conditions.

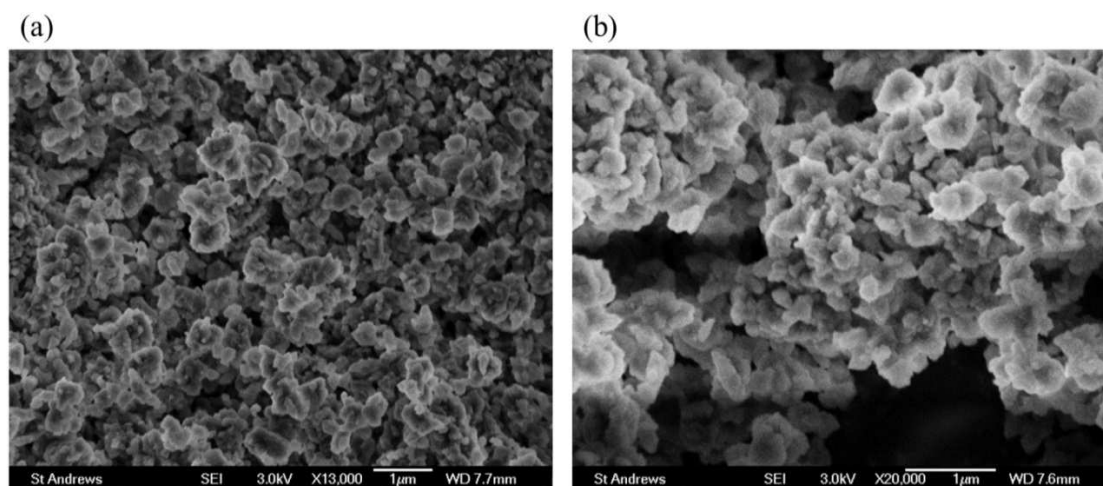


Figure 5.4. SEM micrographs of (a) as-prepared K-chabazite and (b) ion exchanged Na-chabazite.

EDX spectroscopy confirms that the ion exchange of K^+ for Na^+ , Li^+ and Ca^{2+} in chabazite occurred. Figure 5.5 shows the peaks of the framework elements, O, Si and Al, and extra-framework cations, K^+ , Na^+ , Li^+ and Ca^{2+} , which are present in the structure of chabazite. No other elements are observed.

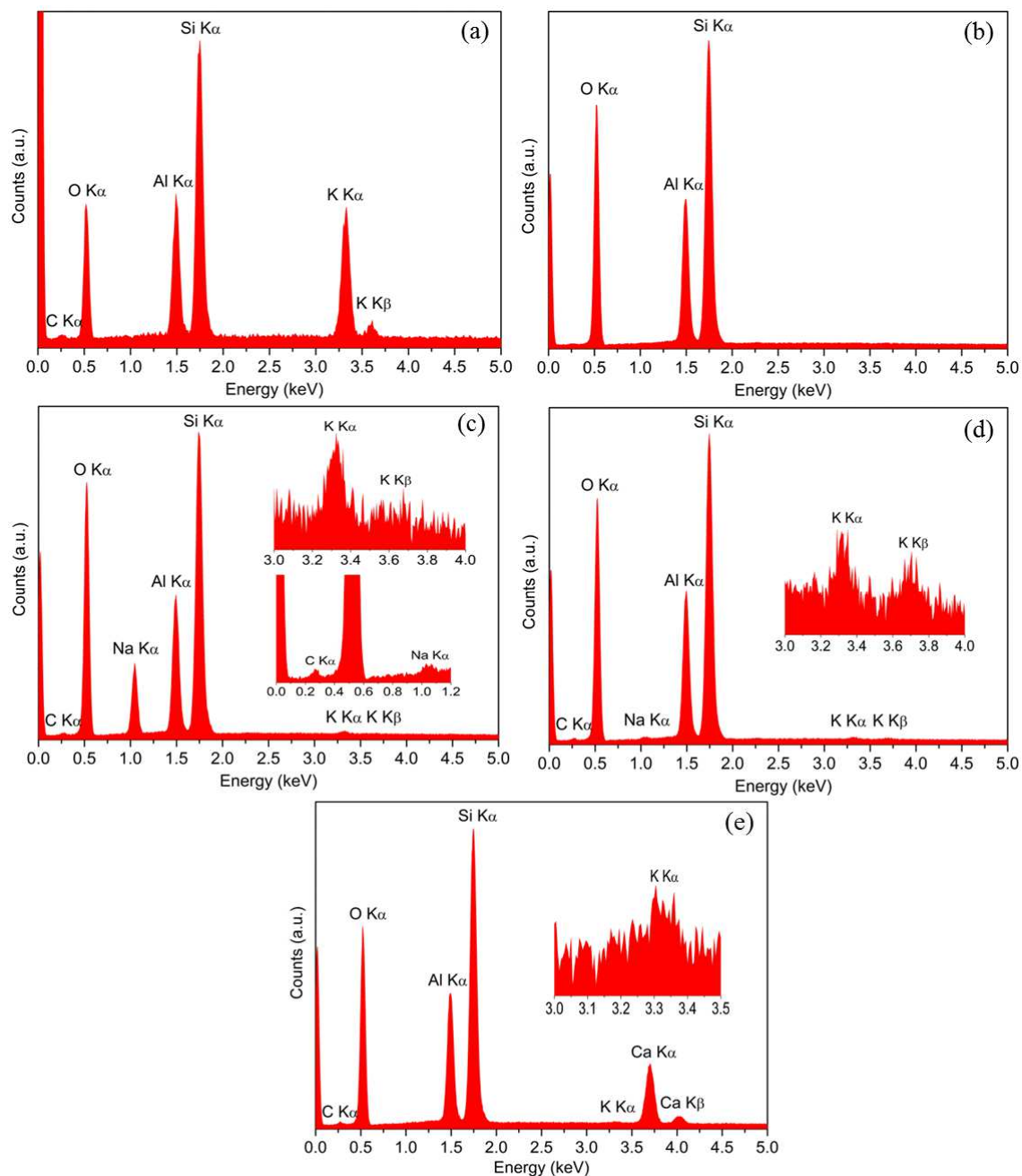


Figure 5.5. EDX spectra of (a) K-chabazite, (b) H-chabazite, (c) Na-chabazite, (d) Li-chabazite and (e) Ca-chabazite. The insets show magnified images of less visible peaks.

From the ^{29}Si MAS NMR spectrum of the as-prepared K-chabazite (Figure 5.6a) four sharp and strong peaks can be attributed to: Si(3Al) (-93 ppm), Si(2Al) (-98 ppm), Si(1Al) (-103 ppm) and Si(0Al) (-108 ppm). ^{27}Al MAS NMR spectrum (Figure 5.6b) reveals only the tetraordinated framework Al at 57 ppm. The framework Si/Al ratio is 3.0 determined by ^{29}Si MAS NMR spectroscopy using equation 4.2 in chapter 4 and deconvolution of the signals (see the appendix). The Si/Al ratio obtained from NMR is in good agreement with Si/Al ratio obtained from EDX analysis. The compositions calculated accordingly for chabazite materials are given in Table 5.2. The formula for the derivation of the unit cell composition is given in chapter 4.

Table 5.2. EDX analysis of zeolite chabazite before and after ion exchange.

Sample	O	Atomic %				Na	Li	Ca	Unit cell formula of dehydrated sample
		Si	Al	K					
K-chabazite	63 ± 1	22 ± 1	7 ± 1	8 ± 1	N.D.	N.D.	N.D.	$\text{K}_9\text{Al}_9\text{Si}_{27}\text{O}_{72}$	
H-chabazite	71 ± 1	21 ± 1	8 ± 1	N.D.	N.D.	N.D.	N.D.	$\text{H}_9\text{Al}_9\text{Si}_{27}\text{O}_{72}$	
Na-chabazite	64 ± 1	22 ± 1	7 ± 1	0.2	7 ± 1	N.D.	N.D.	$\text{Na}_{8.8}\text{K}_{0.2}\text{Al}_9\text{Si}_{27}\text{O}_{72}$	
Li-chabazite	71 ± 1	21 ± 1	8 ± 1	0.2	0.3	N.D.	N.D.	$\text{Li}_{8.5}\text{Na}_{0.3}\text{K}_{0.2}\text{Al}_9\text{Si}_{27}\text{O}_{72}$	
Ca-chabazite	68 ± 1	21 ± 1	7 ± 1	0.2	N.D.	N.D.	4 ± 1	$\text{Ca}_{4.4}\text{K}_{0.2}\text{Al}_9\text{Si}_{27}\text{O}_{72}$	

Values for oxygen are semi-quantitative
N.D. – not detected

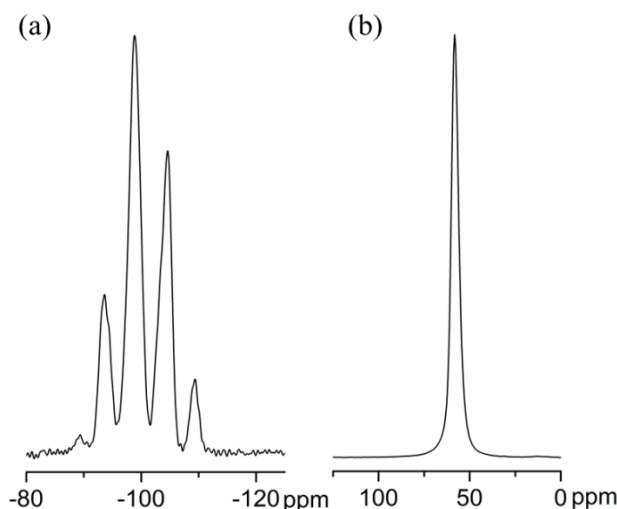


Figure 5.6. (a) ^{29}Si MAS NMR and (b) ^{27}Al MAS NMR spectra of as-prepared K-chabazite.

From TGA (Figure 5.7a) K- and Na-chabazite show one dehydration step, corresponding to *ca.* 20 % weight loss, which may be explained as a consequence of the removal of physisorbed water molecules at low temperatures, between 300 K and 400 K. The TGA curves of Li- and Ca-chabazite show two dehydration steps. Li^+ and Ca^{2+} cations bind water molecules very strongly. The step of *ca.* 3 % weight loss for Li^+

and *ca.* 5 % for Ca^{2+} from 400 K to 700 K is due to the desorption of water chemisorbed on the cations. The high charge density of cations (for example Li^+ and Ca^{2+}) may result in problems with water removal during the activation process, since a sample which is not completely dry may adsorb less CO_2 . The activation temperature is crucial especially for samples containing Li^+ cations. However, the TGA curve of H-chabazite does not show a plateau at high temperatures, instead it decreases at a constant rate. This is in a good agreement with PXRD results (see Figure 5.3b) which confirmed that H-chabazite is not very stable and heating at high temperatures causes further degradation of the structure, possibly via dehydroxylation.

Nitrogen adsorption isotherms of H-, Na-, Li- and Ca-chabazite samples show Type I behaviour (Figure 5.7b), which is characteristic for adsorbents having a microporous structure. The sequence of N_2 adsorption uptake for chabazite samples is Li-chabazite > Na-chabazite > Ca-chabazite > H-chabazite > K-chabazite. Li-chabazite possesses the highest N_2 uptake of 8 mmol g^{-1} at $p/p_0 = 0.9$. The N_2 uptakes of Na- and Ca-chabazite are similar, 6.5 mmol g^{-1} at $p/p_0 = 0.9$. H-chabazite shows a low uptake of N_2 , 3 mmol g^{-1} at $p/p_0 = 0.9$. H-, Na-, Li- and Ca-chabazite demonstrate access of the porous structures to N_2 molecules. There is a very low N_2 uptake on as-prepared K-chabazite, what suggests that its S8R window sites are blocked by K^+ cations and N_2 molecules were unable to enter (see structure solution, below).

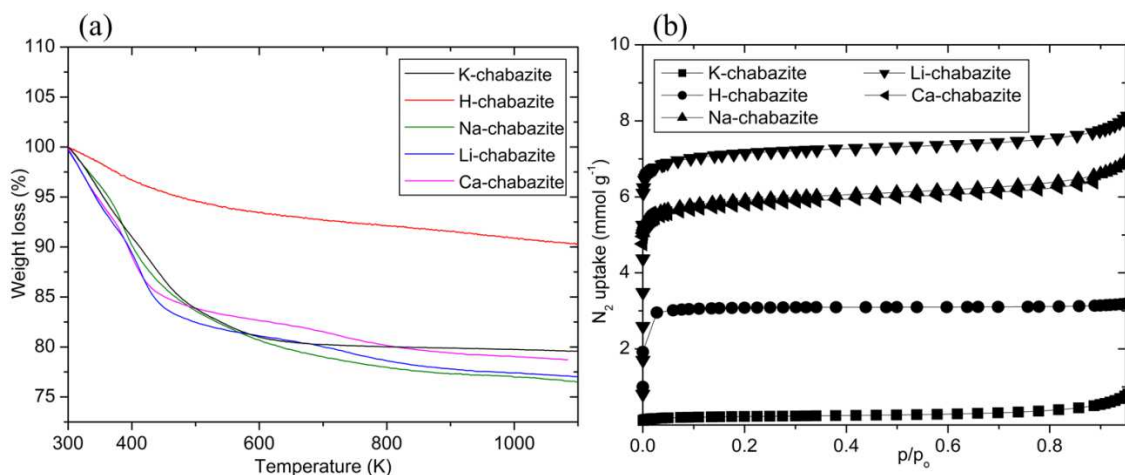


Figure 5.7. (a) TGA curves and (b) N_2 adsorption isotherms at 77 K of K-, H-, Na-, Li- and Ca-chabazite.

5.3. Structural Studies of K-, Na-, Li- and Ca-Chabazite

The structural changes of chabazite structures upon dehydration were investigated by Rietveld analysis (as described in the experimental section) and TEM studies. Final observed, calculated and difference Rietveld plots for the laboratory powder data, collected at 298 K, of K-chabazite, Li-chabazite and Ca-chabazite are shown in Figure 5.8. Crystallographic details from Rietveld analysis of dehydrated K-chabazite, Na-chabazite and Ca-chabazite samples are given in the appendix.

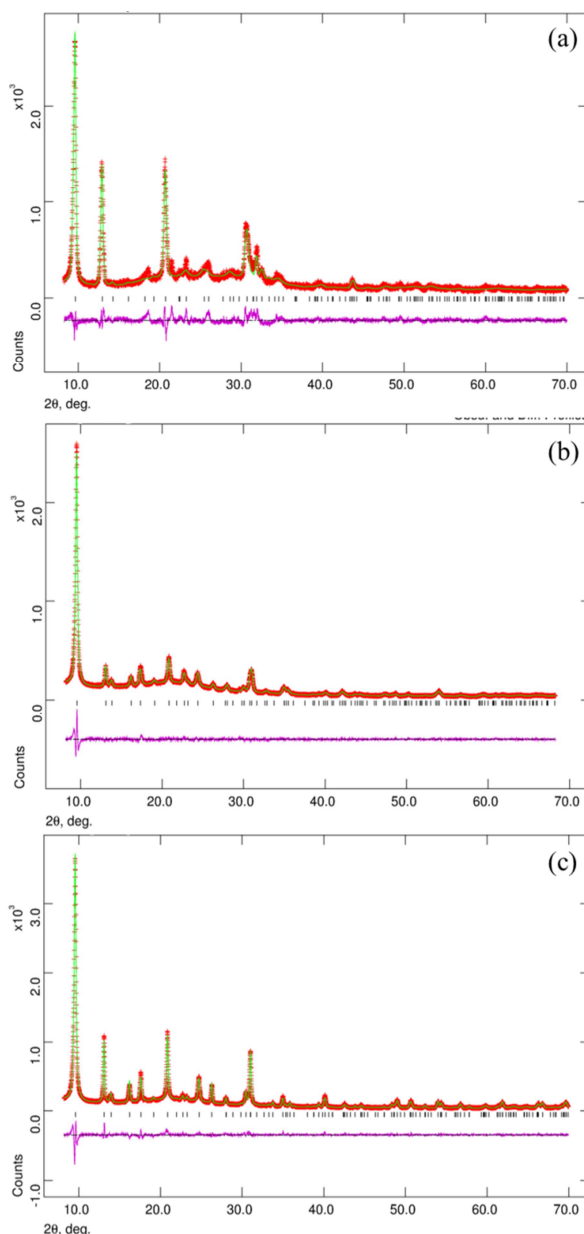


Figure 5.8. Final observed, calculated and difference Rietveld plots for the powder data refinement of dehydrated (a) K-chabazite, (b) Li-chabazite and (c) Ca-chabazite.

Figure 5.9 presents the PXRD patterns of hydrated, dehydrated and rehydrated K-, Na-, Li- and Ca-chabazite samples. For all chabazite samples in the hydrated form the structure adopts the rhombohedral symmetry with space group $R\bar{3}m$. Upon dehydration K-, Li-, and Ca-chabazite remain in this symmetry, while dehydration of Na-chabazite resulted in a transformation to a mixture of two symmetries, thought to be rhombohedral $R\bar{3}m$ symmetry and monoclinic $C2/m$ symmetry. Identification of a monoclinic phase was conducted via refinement using a literature $C2/m$ starting model as well as a $R\bar{3}m$ starting model. The best fit was achieved by two-phase refinement. For K-chabazite and Na-chabazite the structural effects observed upon dehydration are reversible (Figure 5.9a,b).

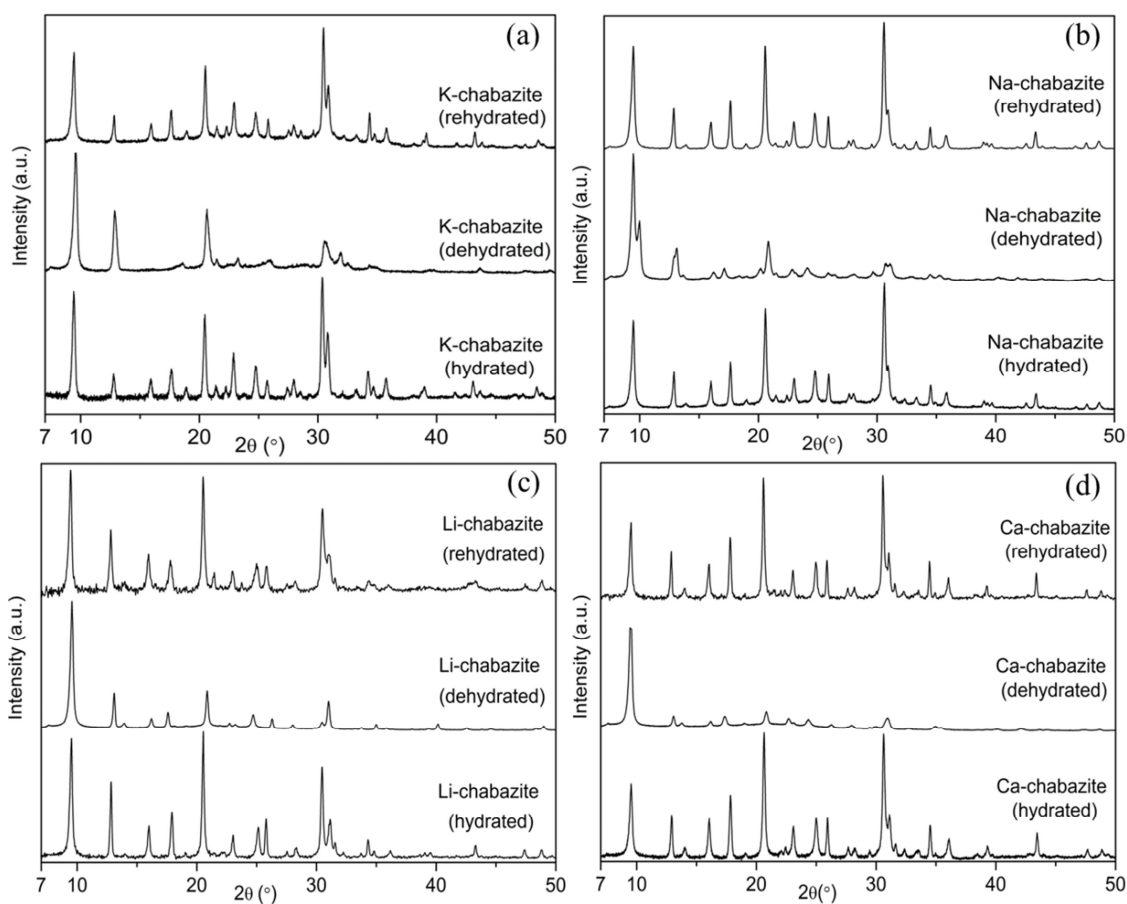


Figure 5.9. PXRD patterns of hydrated, dehydrated and re-hydrated (a) K-chabazite, (b) Na-chabazite, (c) Li-chabazite and (d) Ca-chabazite samples. The (offset) patterns have been collected at 298 K using the same operating conditions.

Rietveld refinement gives the structures of K-, Li- and Ca-chabazite which are shown in Figure 5.10. Refined unit cell parameters, cation locations and occupancies in K-, Li-

and Ca-chabazite, obtained by Rietveld analysis of laboratory X-ray data collected at 298 K are given in Table 5.3.

In dehydrated K-chabazite the cation movements, upon dehydration, provoke significant distortion in the framework leading to a significant reduction in the c dimension, $c = 14.666(5)$ Å, compared to the other forms, where $c = 15.1909(6)$ Å for Li-chabazite and $c = 15.4113(14)$ Å for Ca-chabazite. The structure retains rhombohedral symmetry, $R\bar{3}m$, but the PXRD pattern contains only broadened reflections. Using Rietveld analysis it was possible to refine the structure and find the K^+ cations, despite the broad lines from PXRD (see Figure 5.9a). The K^+ cations are located at a site close to the plane of the S8R windows (Figure 5.10a). It has been found that the S8R sites are fully occupied by K^+ cations, giving 9 K^+ per unit cell and 3 K^+ per CHA-cage (Table 5.3), including that all of the entrances to the CHA-cage are blocked, as was also previously suggested by no uptake of N_2 at 77 K (see Figure 5.7b). The presence of large K^+ cations in the S8R site makes the window significantly bigger than for chabazite with no cations occupying this site (for example Ca-chabazite, Figure 5.11). The K–O distances in the S8R sites are 2.95(1) Å, consistent with those reported in the literature.^{7,9}

Structure of Li-chabazite was determined by Rietveld analysis, taking into account the residual K^+ and Na^+ in this material. The low atomic number of lithium makes determination of the lithium sites difficult. In Li-chabazite the S6R sites are fully occupied by Li^+ cations, which gives 6 Li^+ per unit cell (Figure 5.10b and Table 5.3). This is unlikely to be an accurate value due to the low electron density associated with Li^+ but a previous structural analysis by neutron diffraction of a dehydrated mixed Li,Na,-chabazite indicated that the S6R site is the preferred position for the small Li^+ (residual Li^+ cations were found in S4R site).⁸ No other sites than S6R for Li^+ cations could be found in the structure prepared for this study and most of the Li^+ cations required for charge balance are located in S6R site. There is also some scattering, assigned as K^+ and Na^+ , in the S8R, the presence of which was confirmed by EDX (see Figure 5.5d and Table 5.2). The Li–O distances in the S6R sites are 2.09(1) Å.

Calcium cation positions in dehydrated Ca-chabazite are located at a site close to the plane of the S6R site and in the middle of the D6R site (Figure 5.10c and Table 5.3). It has been found that the occupancy of the S6R sites is 59%, giving 3.5 Ca^{2+} per unit cell

and 1.1 Ca²⁺ per CHA-cage and the D6R sites have an occupancy of 33% that gives 1 Ca²⁺ per unit cell and 0.33 Ca²⁺ per CHA-cage. The residual 0.2 K⁺ per unit cell detected by EDX (see Figure 5.5e and Table 5.2), and should occupy the S8R site, could not be localised due to the very low occupancy. The Ca–O distances in the D6R sites are 2.73(2) Å and in the S6R sites are 2.38(1) Å, consistent with those reported in the literature.⁶

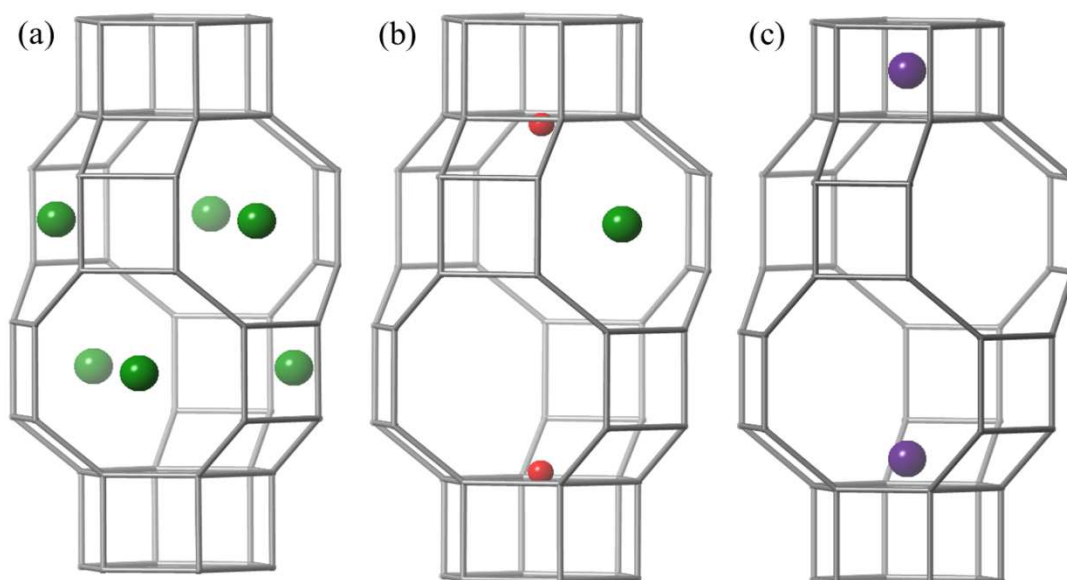


Figure 5.10. Possible cation distributions in one CHA-cage of dehydrated (a) K-chabazite (K – larger, green spheres), (b) Li-chabazite (K – larger, green spheres; Li – smaller, red spheres) and (c) Ca-chabazite (Ca – larger, purple spheres), determined from Rietveld analysis of laboratory X-ray powder diffraction data collected at 298 K.

Table 5.3. Refined unit cell parameters, cation locations and occupancies in K-chabazite, Li-chabazite, Ca-chabazite and Na,H-chabazite(7.8 Na⁺), obtained by Rietveld analysis of laboratory X-ray data collected at 298 K.

Sample	Unit cell parameters /Å	Space group	S8R site occupancy		S6R site occupancy		D6R site occupancy	
			Frac. Occup.	Cations/unit cell	Frac. Occup.	Cations/unit cell	Frac. Occup.	Cations/unit cell
K-chabazite	a,b= 13.7285(14) c= 14.666(5)	$R\bar{3}m$	1.00	9.00	N.D.	N.D.	N.D.	N.D.
Li-chabazite	a,b= 13.60126(3) c= 15.1909(6)	$R\bar{3}m$	0.05(1)	0.45(7)	0.79(1)	4.74(2)	N.D.	N.D.
Ca-chabazite	a,b= 13.6099(7) c= 15.4113(14)	$R\bar{3}m$	N.D.	N.D.	0.59(3)	3.12(3)	0.33(2)	1.00
Na,H-chabazite (7.8Na ⁺)	a,b=13.4427(12) c= 15.5434(19)	$R\bar{3}m$	0.30(1)	3.00	0.80(2)	4.82(6)	N.D.	N.D.
N.D. – not detected								

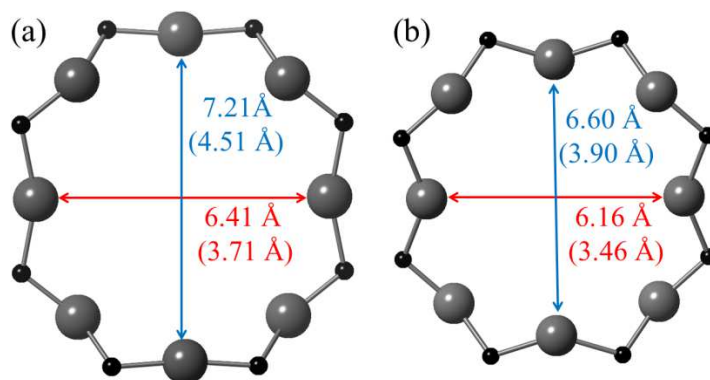


Figure 5.11. Free dimensions of single eight-membered ring window in (a) K-chabazite and (b) Ca-chabazite. In the brackets, the distance minus twice the ionic radius of O^{2-} , 1.35 Å.

For dehydrated Na-chabazite a different response of the structure was observed compared with that for dehydrated K-chabazite, resulting in a change of the space group from the rhombohedral $R\bar{3}m$ to the mixture of two phases: rhombohedral $R\bar{3}m$ and monoclinic $C2/m$, suggested by Le Bail analysis (Figure 5.12).

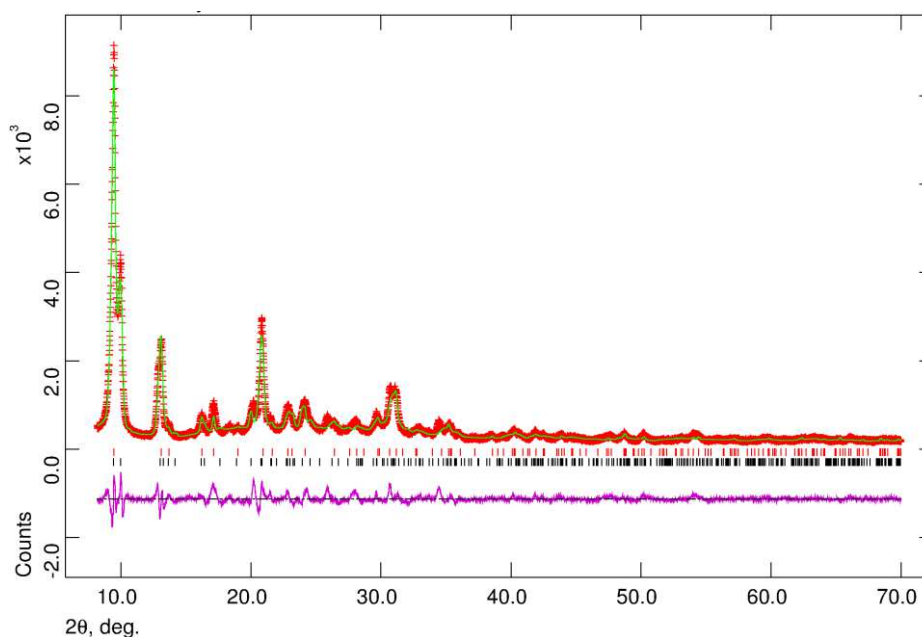


Figure 5.12. Final observed, calculated and difference Le Bail plot for the powder data analysis of Na-chabazite.

This type of phase mixture for Na-chabazite has not been previously reported. In 1977 Mortier *et al.*⁶ observed that upon dehydration of a chabazite with unit cell composition $Na_{11.4}Al_{11.4}Si_{24.6}O_{72} \cdot nH_2O$, the rhombohedral $R\bar{3}m$ symmetry of Na-chabazite undergoes reduction to monoclinic $C2/m$ symmetry (see Figure 5.2). The reduction

results from elliptical distortion of most S8Rs. The largest deformation occurs at the S4R bridges between D6Rs due to the lack of coordinated water molecules. Furthermore, the distortion appears to increase with increasing number of cations.

In order to investigate this phenomenon more closely, a sample of Na-chabazite with less Na^+ was prepared. The PXRD patterns of a Na,H-chabazite sample with compositions $\text{Na}_{7.8}\text{H}_1\text{K}_{0.2}\text{Al}_9\text{Si}_{27}\text{O}_{72}$ is presented in Figure 5.13. It can be seen that removal of cations from Na-chabazite causes the sample to maintain rhombohedral $R\bar{3}m$ symmetry upon dehydration. It is thought that Na-chabazite prepared in this study possesses a transitional structure composition, possibly not completely uniform throughout the crystals, where the number of Na^+ cations does not allow for a complete change of the rhombohedral $R\bar{3}m$ symmetry to monoclinic $C2/m$ symmetry but remains as a mixture of these two phases.

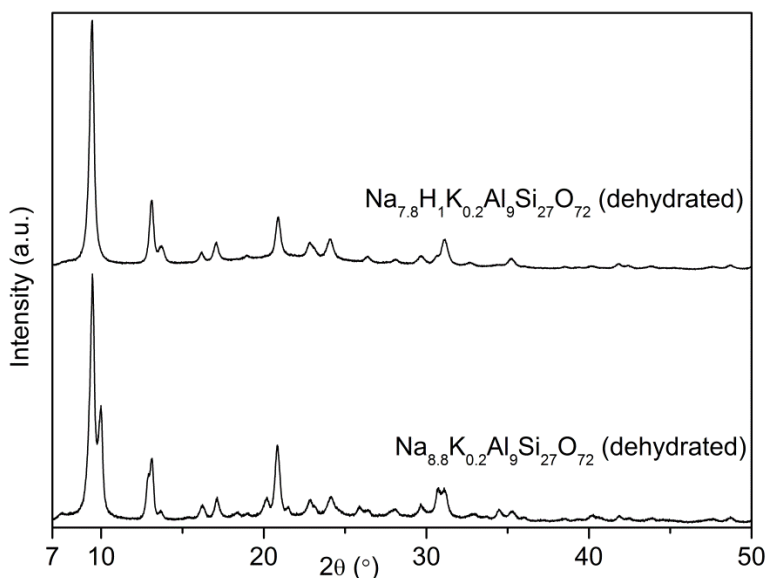


Figure 5.13. PXRD patterns of Na-chabazite and Na,H-chabazite samples. The (offset) patterns have been collected at 298 K using the same operating conditions.

Due to the presence of two phases and the associated overlapping reflections, the structure refinement and location of Na^+ cations in dehydrated Na-chabazite were impossible to obtain. Instead, Rietveld analysis on $\text{Na}_{7.8}\text{H}_1\text{K}_{0.2}\text{Al}_9\text{Si}_{27}\text{O}_{72}$ (Na,H-chabazite) was conducted. Crystallographic details from Rietveld analysis of dehydrated Na,H-chabazite samples are given in the appendix. Final observed, calculated and difference Rietveld plots for the powder data refinement and possible cation distributions in one CHA-cage of dehydrated Na,H-chabazite ($\text{Na}_{7.8}\text{H}_1\text{K}_{0.2}\text{Al}_9\text{Si}_{27}\text{O}_{72}$)

are presented in Figure 5.14. All of the reflections are associated with $R\bar{3}m$ trigonal symmetry and the unit cell parameters are $a = b = 13.4427(12) \text{ \AA}$, $c = 15.5434(19) \text{ \AA}$ and $\alpha = \beta = 90^\circ$, $\gamma = 120^\circ$. The Na^+ cation positions are located at the sites close to the plane of the S8R window and close to the plane of the S6R. It has been found that the S8R sites are 1/3 occupied by Na^+ cations, giving 3 Na^+ per unit cell and 1 Na^+ per CHA-cage in this site. The S6R sites are 80% occupied, giving 4.8 Na^+ per unit cell and 1.6 Na^+ per CHA-cage. Na–O distances in the S8R sites are $2.95(1) \text{ \AA}$ and in the S6R are $2.38(1) \text{ \AA}$ (see Table 5.3).

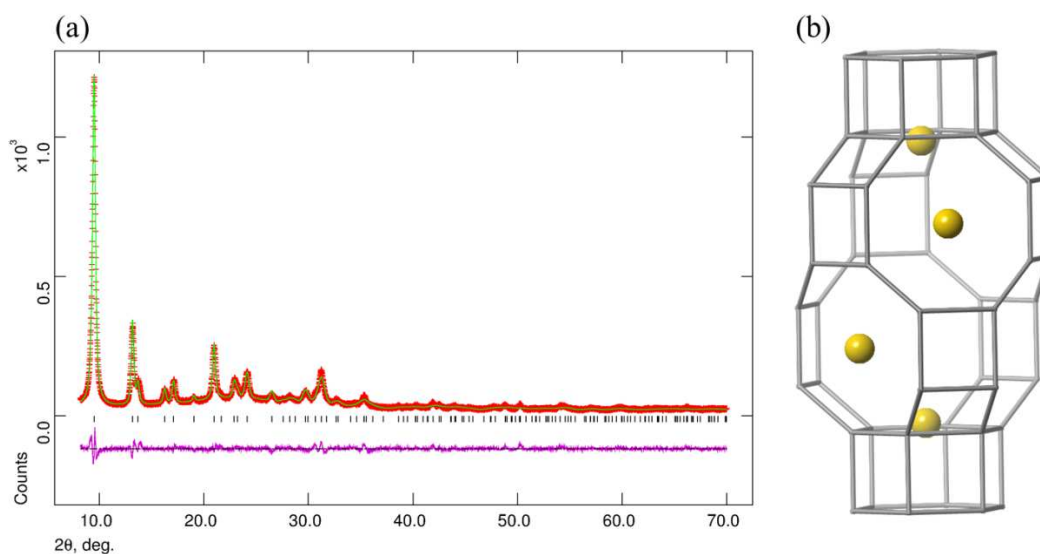


Figure 5.14. (a) Final observed, calculated and difference Rietveld plots for the powder data refinement and (b) possible cation distributions in one CHA-cage of dehydrated Na,H-chabazite ($\text{Na}_{7.8}\text{H}_1\text{K}_{0.2}\text{Al}_9\text{Si}_{27}\text{O}_{72}$), determined from Rietveld refinement of laboratory X-ray powder diffraction data.

Transmission electron microscopy was used to further investigate the structure of dehydrated Li-, K- and Na-chabazite. Selected area electron diffraction patterns corresponding to dehydrated Li-chabazite, K-chabazite and Na-chabazite were recorded (Figure 5.15). For the Li-chabazite and K-chabazite the patterns are consistent with the unit cell of the crystal structures determined by Rietveld refinement of the PXRD patterns and could be indexed as $[1\bar{1}2]$ zone axis patterns. The Na-chabazite pattern is consistent with the rhombohedral $R\bar{3}m$ unit cell determined for 7.8 Na^+ per unit cell. The sharp electron diffraction spots (especially for K-chabazite) in the patterns are characteristic of high crystallinity, indicating that the broadness of the diffraction peaks observed by PXRD is most likely due to the small domain size. Additional background

spots are visible due to the difficulty of isolating single crystals or domains of chabazite due to their small size.

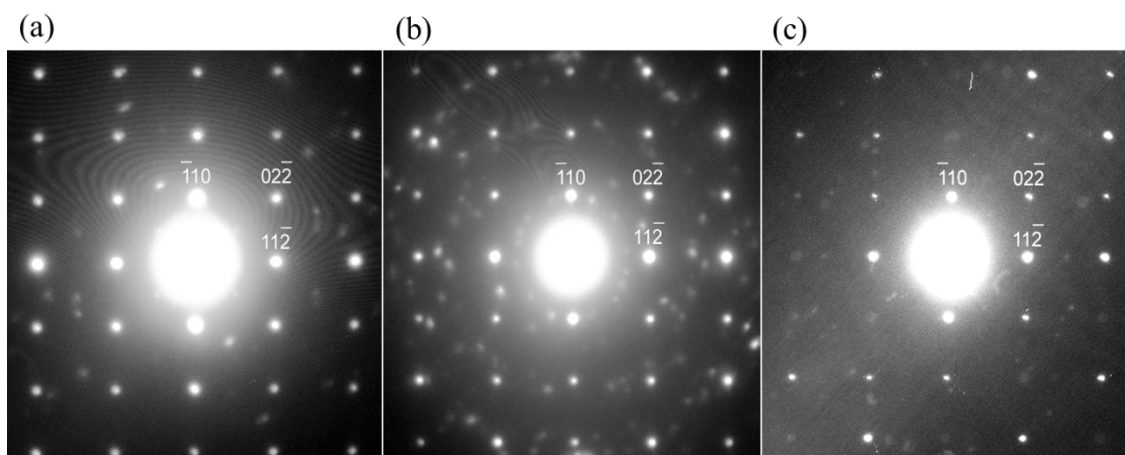


Figure 5.15. Selected area electron diffraction patterns of dehydrated (a) Li-chabazite, (b) K-chabazite and (c) Na-chabazite parallel to the $[1\bar{1}2]$ axis (micrographs taken by Dr. David Miller).

5.4. Carbon Dioxide Adsorption Study of Cationic Forms of Chabazite

Role of structure and cation type on CO_2 adsorption was investigated by: (i) CO_2 adsorption at 298 K and up to 1 bar pressure on K-, H-, Na-, Li- and Ca-chabazite, (ii) *in situ* IR spectroscopy of CO_2 adsorption on K-, Na-, Li- and Ca-chabazite, (iii) N_2 and CO_2 adsorption on partially-exchanged K,H-, Na,H-, Li,H-, Ca,H-chabazite, (iv) *in situ* synchrotron PXRD studies of CO_2 adsorption on Na-chabazite, (v) high pressure CO_2 adsorption and CO_2/CH_4 selectivity. Together, these experiments should give a clear description of CO_2 adsorption on chabazite.

(i) CO_2 adsorption at 298 K and up to 1 bar pressure on K-, H-, Na-, Li- and Ca-chabazite

CO_2 adsorption isotherms of K-, H-, Li- and Ca-chabazite samples show Type I behaviour, characteristic for adsorbents having a microporous structure (Figure 5.16), indicating strong interactions between CO_2 molecules and the chabazite structure. The CO_2 uptake at 298 K and at 1 bar for chabazite samples is of the order H-chabazite (1.4 mmol g^{-1}) < K-chabazite (3.8 mmol g^{-1}) < Ca-chabazite, Na-chabazite, Li-chabazite (all 5–5.1 mmol g^{-1}).

Low uptake on H-chabazite at 1 bar (Figure 5.16a) is due to loss of crystallinity and pore volume as shown by N₂ adsorption at 77 K (see Figure 5.7b).

K-chabazite shows a lower CO₂ uptake at 1 bar (Figure 5.16b) than the Ca-, Na- and Li-chabazite, which is probably due to the larger size (and lower charge density) of the K⁺ cations. That the material adsorbs CO₂ so readily when it takes up no N₂ at 77 K indicates that the K⁺ cations are mobile and can move from their positions in the S8Rs.

Na-chabazite CO₂ isotherms at 298 K show an interesting shape which has not previously been reported for this material (Figure 5.16c). The adsorption isotherm shows a step at 0.3 bar and subsequent hysteresis upon desorption, in a more typical Type I isotherm shape. The causes for this non-Type I behaviour are discussed later.

Among the cationic forms the highest uptake of CO₂ at 298 K and 0.1 bar is for the Li-form, due to the strong interactions between Li⁺ cations and CO₂ molecules. This uptake increases to 5.1 mmol g⁻¹ by 0.9 bar and is fully reversible (Figure 5.16d). From the refinement (see Figure 5.10b) it can be seen that Li⁺ cations occupy S6R positions so they are all accessible for CO₂ adsorption.

CO₂ uptake at 298 K and 0.1 bar on Ca-chabazite is 3.7 mmol g⁻¹. This uptake increases to 4.9 mmol g⁻¹ by 0.9 bar, and it is fully reversible with small hysteresis in the low pressure range (Figure 5.16e). The Rietveld refinement reveals that Ca²⁺ cations occupy S6R and D6R sites (see Figure 5.10c). Since Ca²⁺ cations are divalent, and so have a high charge density, not only is there a half of the concentration but also Ca²⁺ cations in the D6R site are strictly inaccessible for adsorption, so only the cations in S6R sites are available to interact with CO₂.

Low-pressure sections of the isotherms, up to 0.0035 bar, are shown in Figure 5.16f. Larger and more polar molecules will interact more strongly with zeolites having a large cation charge density (small ionic radius), where divalent cations generally have larger charge density than monovalent cations of similar size.²⁰ The charge density for extra-framework cations in chabazite increases in the sequence of K⁺ < Na⁺ < Ca²⁺ < Li⁺, resulting in the highest CO₂ uptake at low pressures for Li-chabazite which decreases for Ca-chabazite, Na-chabazite and K-chabazite respectively, consistent with previous reports.^{11,21}

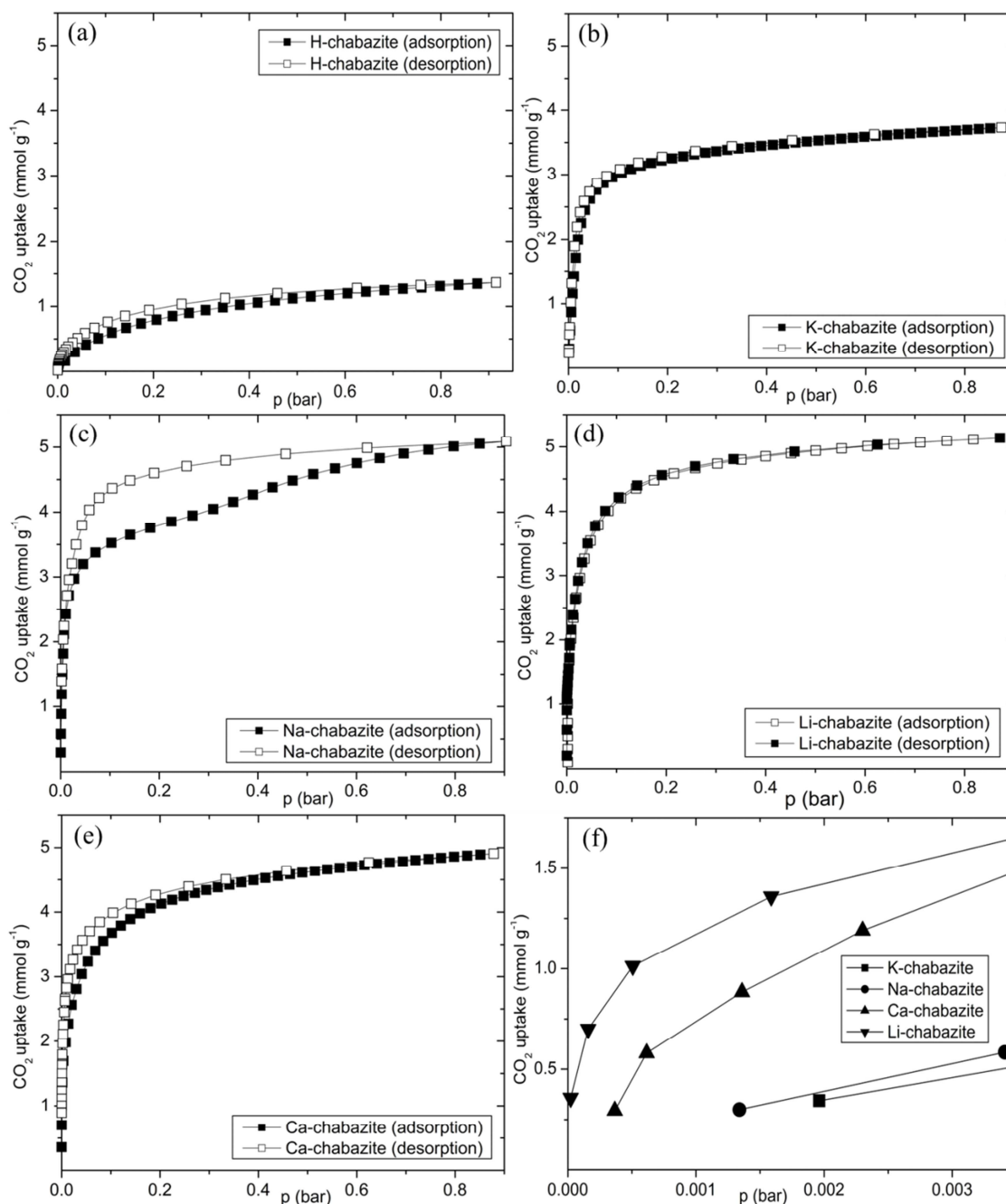


Figure 5.16. CO₂ sorption isotherms at 298 K for (a) H-chabazite, (b) K-chabazite, (c) Na-chabazite, (d) Li-chabazite, (e) Ca-chabazite and (f) the low pressure sections of the isotherms.

Further examination of Na-chabazite involved the measurement of CO₂ adsorption on the Na,H-chabazite samples with composition Na_{7.8}H₁K_{0.2}Al₉Si₂₇O₇₂. The CO₂ isotherms of Na,H-chabazite exhibit a much smaller hysteresis than Na-chabazite (Figure 5.17a). It was previously proved that this composition of Na,H-chabazite is no longer a mixture of two phases, but possess rhombohedral $R\bar{3}m$ symmetry (see

Figure 5.13). The observed stepped isotherm hysteresis of Na-chabazite must result from the presence of two phases, each of which has different uptake, and likely opening of monoclinic form (see Figure 5.16c). The sequential CO₂ adsorption isotherms on Na-chabazite, when the sample after first adsorption was left at the instrument for further two adsorptions, without degassing between, show smaller hysteresis. The gradual decrease of the hysteresis may be caused by the incomplete closing of the monoclinic form upon desorption of CO₂ (Figure 5.17b).

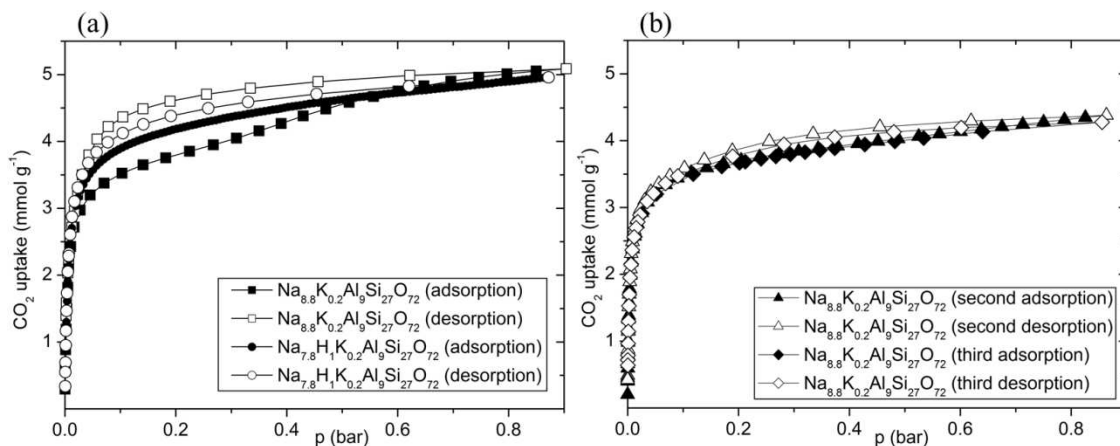


Figure 5.17. (a) CO₂ sorption isotherms at 298 K of Na-chabazite and Na,H-chabazite showing smaller hysteresis for samples with less Na⁺ cations and (b) sequential second and third CO₂ adsorption isotherms at 298 K on Na-chabazite showing the gradual decrease of the hysteresis.

(ii) *In situ* IR spectroscopy of CO₂ adsorption on K-, Na-, Li- and Ca-chabazite

In situ IR spectroscopy of CO₂ adsorbed on chabazite can be interpreted in conjunction with the adsorption isotherms and the structural information. The infra-red spectra were recorded in a range of CO₂ pressure from traces to 860 mbar and are presented in Figure 5.18. The infra-red spectra of CO₂ adsorbed on chabazite samples show a strong band at 2358 cm⁻¹ due to the ν₃ asymmetric stretching vibration of adsorbed CO₂. A similar band has been reported for CO₂ adsorbed in other zeolites.^{27,28} As the CO₂ coverage is increased in chabazite, the ν₃ band broadens and becomes too intense to monitor.

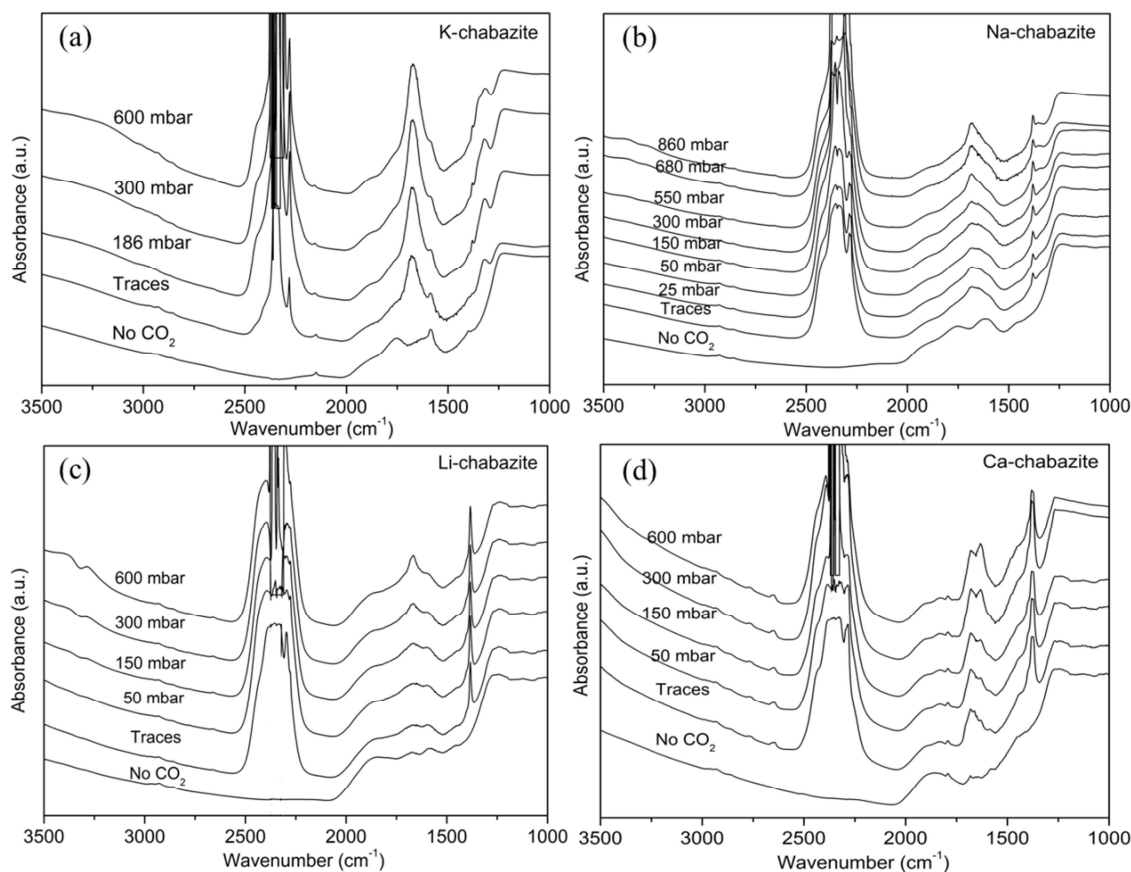


Figure 5.18. $3550 - 1200 \text{ cm}^{-1}$ range of the infra-red spectra of CO_2 adsorbed on (a) K-chabazite, (b) Na-chabazite, (c) Li-chabazite and (d) Ca-chabazite showing the development of the ν_3 asymmetric stretch of CO_2 , measured as CO_2 is dosed at different equilibrium pressures.

Second important band is the ν_1 symmetric stretching vibration corresponding to interaction of CO_2 with cations which may be observed as a weak band at 1378 cm^{-1} (Figure 5.19). This vibration is infrared forbidden for the gas phase molecule (at 1388 cm^{-1}), but becomes weakly allowed when the symmetry is lowered due to interaction with zeolite cations. This band is very weak for K-chabazite and Na-chabazite and very sharp and intense for Li-chabazite and Ca-chabazite for which the cations have high charge density. For all chabazite samples only one ν_1 vibration is observed, increasing in intensity with increasing surface coverage, which may indicate a single CO_2 adsorption site. Furthermore, structural refinement of K-chabazite and Li-chabazite suggested that in the dehydrated forms there is only one cationic site. For all the samples an additional band may be seen at 1635 cm^{-1} , increasing in intensity with increasing surface coverage. Bands in this region have been previously reported as

an adsorbed carbonate or bicarbonate when CO_2 is adsorbed in alkali metal zeolites, particularly in the presence of adsorbed water.^{28,29} From these comparisons it may be assumed that small amounts of carbonate and/or bicarbonate species are formed when CO_2 is adsorbed in chabazite samples.

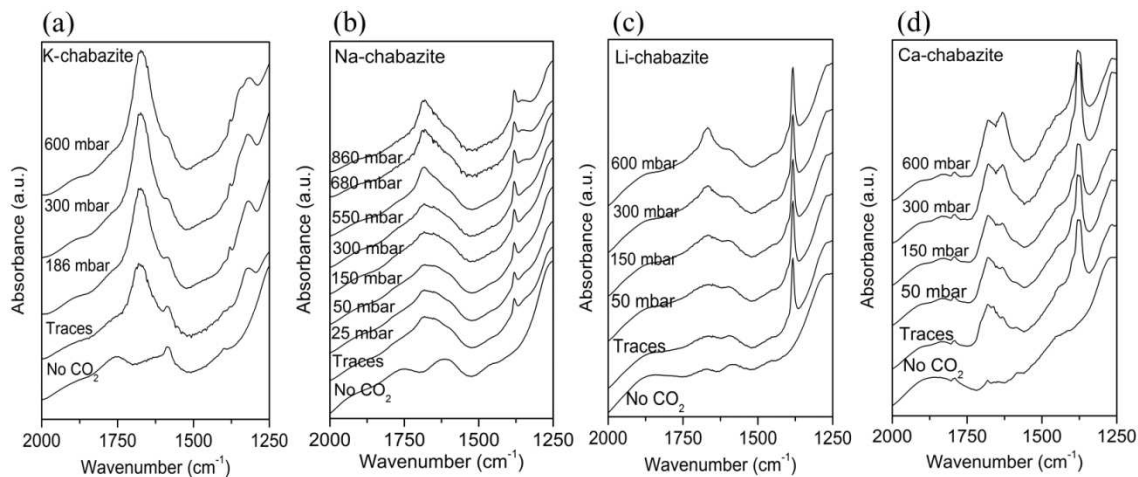


Figure 5.19. 2000 -1250 cm^{-1} range of the infra-red spectra of CO_2 adsorbed on (a) K-chabazite, (b) Na-chabazite, (c) Li-chabazite and (d) Ca-chabazite showing the development of the ν_1 symmetric stretch of CO_2 reacting with cations, measured as CO_2 is dosed at different equilibrium pressures.

(iii) N_2 and CO_2 adsorption on partially-exchanged K,H-, Na,H-, Li,H- and Ca,H-chabazite

Nitrogen and CO_2 adsorption was measured on samples with different cation contents. The preparation of M,H-chabazite samples is described in chapter 4. The uptakes of N_2 at 77 K ($p/p_0 = 0.1$) and CO_2 at 300 K ($p = 0.1$ bar) as a function of cation-content in chabazite are presented in Figure 5.20. Table 5.4 contains EDX data for the K,H-chabazite, Na,H-chabazite and Ca,H-chabazite samples. For the AAS data for Li,H-chabazite see Table 4.1 in chapter 4.

Reversible CO_2 uptake was measured at 298 K and at 0.1 bar using the ZLC method at the University of Edinburgh in collaboration with Enzo Mangano and Prof. Stefano Brandani. PXRD was conducted to check the crystallinity of samples after removal of the cations and the results are presented in Figure 5.21.

There is one favourable site for K^+ cations in chabazite structure which is S8R (see Figure 5.10a). All of the K^+ cations occupy this window site which is also

an entrance to CHA-cage that results in low N₂ uptake on as-prepared K-chabazite at 77 K (*ca.* 0.1 mmol g⁻¹). However, the CO₂ uptake at 0.1 bar is 2.7 mmol g⁻¹. Admission of CO₂ molecules into the CHA-cage is only possible if the K⁺ cations migrate away from the S8R sites. Also, the CO₂ interacts more strongly with K⁺ than does N₂, resulting in easier access to the CHA-cage. The N₂ adsorption stays very low above 4.5 K⁺ per unit cell. Below 4.5 K⁺ per unit cell N₂ adsorption starts increasing and again decreasing below 3 K⁺ per unit cell. Increase of the N₂ adsorption can be caused by ‘opening’ of the window sites to the CHA-cage by removing K⁺ cations. K,H-chabazite shows very low crystallinity (Figure 5.21a) when less than 4.5 K⁺ per unit is present, resulting in low N₂ adsorption for these materials. CO₂ uptake at 0.1 bar increases with increasing cation content as the number of strong CO₂:cation interactions increases. The formula for the derivation of the unit cell composition is given in chapter 4.

Table 5.4. EDX analysis of M,H-chabazite samples before and after ion exchange.

Sample	O	Si	Atomic %		Na	Ca
			Al	K		
K ₉ Al ₉ Si ₂₇ O ₇₂	63 ± 1	21 ± 1	7 ± 1	8 ± 1	N.D.	N.D.
K ₆ H ₃ Al ₉ Si ₂₇ O ₇₂	66 ± 1	21 ± 1	7 ± 1	5 ± 1	N.D.	N.D.
K _{4.5} H _{4.5} Al ₉ Si ₂₇ O ₇₂	68 ± 1	21 ± 1	7 ± 1	3 ± 0.5	N.D.	N.D.
K ₃ H ₆ Al ₉ Si ₂₇ O ₇₂	69 ± 1	21 ± 1	7 ± 1	2 ± 0.5	N.D.	N.D.
K _{1.5} H _{7.5} Al ₉ Si ₂₇ O ₇₂	70 ± 1	21 ± 1	7 ± 1	1 ± 0.5	N.D.	N.D.
Na _{8.8} K _{0.2} Al ₉ Si ₂₇ O ₇₂	64 ± 1	22 ± 1	7 ± 1	0.2	7 ± 1	N.D.
Na _{6.5} H _{2.3} K _{0.2} Al ₉ Si ₂₇ O ₇₂	65 ± 1	21 ± 1	7 ± 1	0.2	5 ± 1	N.D.
Na ₅ H _{3.8} K _{0.2} Al ₉ Si ₂₇ O ₇₂	66 ± 1	21 ± 1	7 ± 1	0.2	4 ± 0.5	N.D.
Na ₃ H _{5.8} K _{0.2} Al ₉ Si ₂₇ O ₇₂	68 ± 1	21 ± 1	7 ± 1	0.2	3 ± 0.5	N.D.
Na ₁ H _{7.8} K _{0.2} Al ₉ Si ₂₇ O ₇₂	67 ± 1	23 ± 1	8 ± 1	0.2	1 ± 0.5	N.D.
Ca _{4.4} K _{0.2} Al ₉ Si ₂₇ O ₇₂	68 ± 1	21 ± 1	7 ± 1	0.2	N.D.	4 ± 0.5
Ca ₃ H _{2.8} K _{0.2} Al ₉ Si ₂₇ O ₇₂	65 ± 1	23 ± 1	7 ± 1	0.2	N.D.	3 ± 0.5
Ca _{2.5} H _{3.8} K _{0.2} Al ₉ Si ₂₇ O ₇₂	68 ± 1	21 ± 1	7 ± 1	0.2	N.D.	2 ± 0.5
Ca _{1.5} H _{5.8} K _{0.2} Al ₉ Si ₂₇ O ₇₂	69 ± 1	21 ± 1	7 ± 1	0.2	N.D.	1 ± 0.5
Ca ₁ H _{6.8} K _{0.2} Al ₉ Si ₂₇ O ₇₂	69 ± 1	21 ± 1	7 ± 1	0.2	N.D.	1 ± 0.5

Values for oxygen are semi-quantitative

N.D. – not detected

Na-chabazite is porous to N₂ because Na⁺ cations do not occupy all of the S8R sites. For this material, both N₂ and CO₂ adsorption curves show a similar trend. The uptake of N₂ and CO₂ decreases with decreasing Na⁺ cation content (Figure 5.21b). The decrease of N₂ uptake is due to the loss of crystallinity (Figure 5.21b). The CO₂ adsorption on Na-chabazite will be investigated further below.

It was not possible to analyse CO₂ adsorption for Li-chabazite via ZLC due to problems with water during measurement on the ZLC. Li⁺ cations possess high charge density and adsorb water very strongly. Even the very low levels of water present in the ZLC system were sufficient for significant water uptake. Fully exchanged Li-chabazite exhibits a very high uptake of CO₂ (see Figure 5.16d). N₂ uptake drops with decreasing of number of Li⁺ cations which, similarly to Na-chabazite, is due to the loss of crystallinity (Figure 5.20c and Figure 5.21c).

N₂ uptake on Ca-chabazite increases when around 2 Ca²⁺ are removed and decreases sharply when more than 2 Ca²⁺ are removed (Figure 5.20d). Removal of the Ca²⁺ cations can create more space for N₂ adsorption. Crystallinity of Ca-chabazite starts decreasing below 2 Ca²⁺ per unit cell and the N₂ uptake becomes lower. CO₂ adsorption curves show similar behaviour to those on K-chabazite and Na-chabazite, where materials with less cations show less CO₂ uptake 0.1 bar.

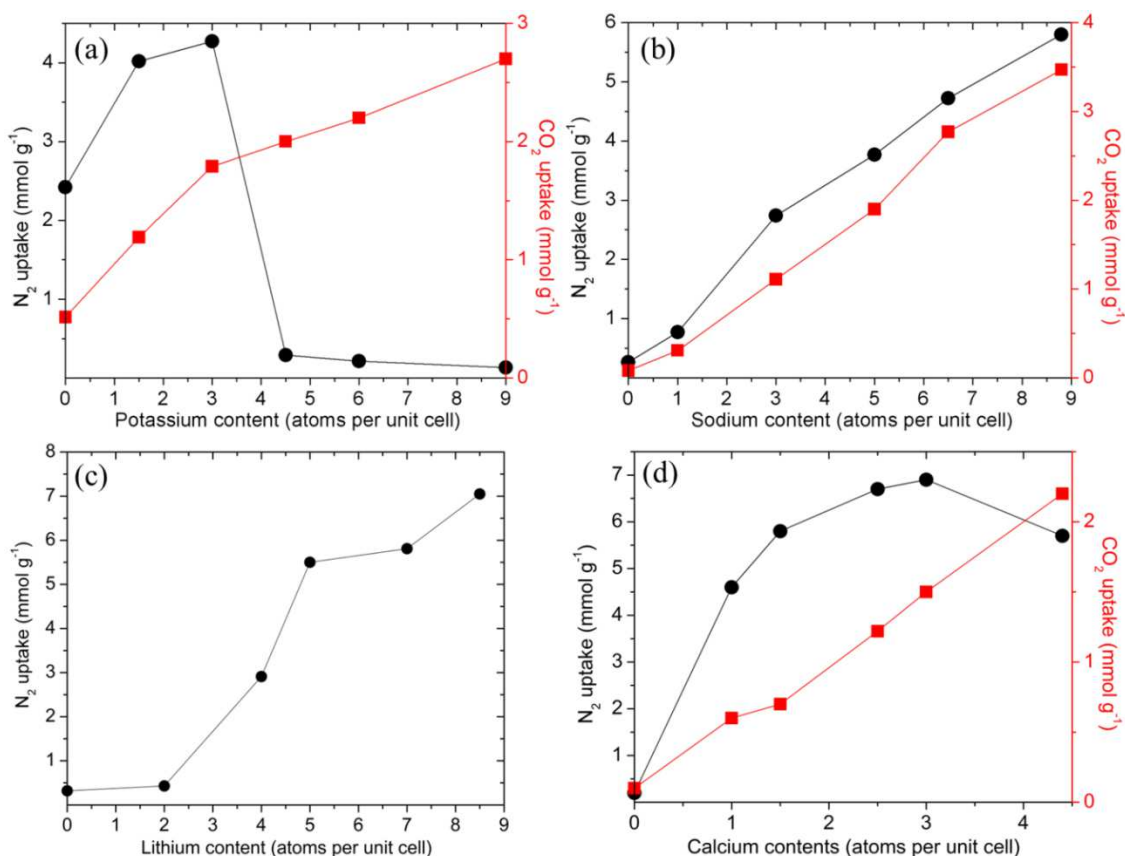


Figure 5.20. Uptake of N₂ at 77 K ($p/p_0 = 0.1$) and CO₂ at 298 K ($p = 0.1$ bar) as a function of (a) K-content in K-chabazite, (b) Na-content in Na-chabazite, (c) Li-content in Li-chabazite (only N₂) and (d) Ca-content in Ca-chabazite.

It can be clearly seen that CO₂ adsorption depends strongly on the concentration of extra-framework cations. Removal of cations causes fast decrease of CO₂ uptake. Also, introduction of protons makes the chabazite framework unstable and a decrease in the crystallinity can be observed.

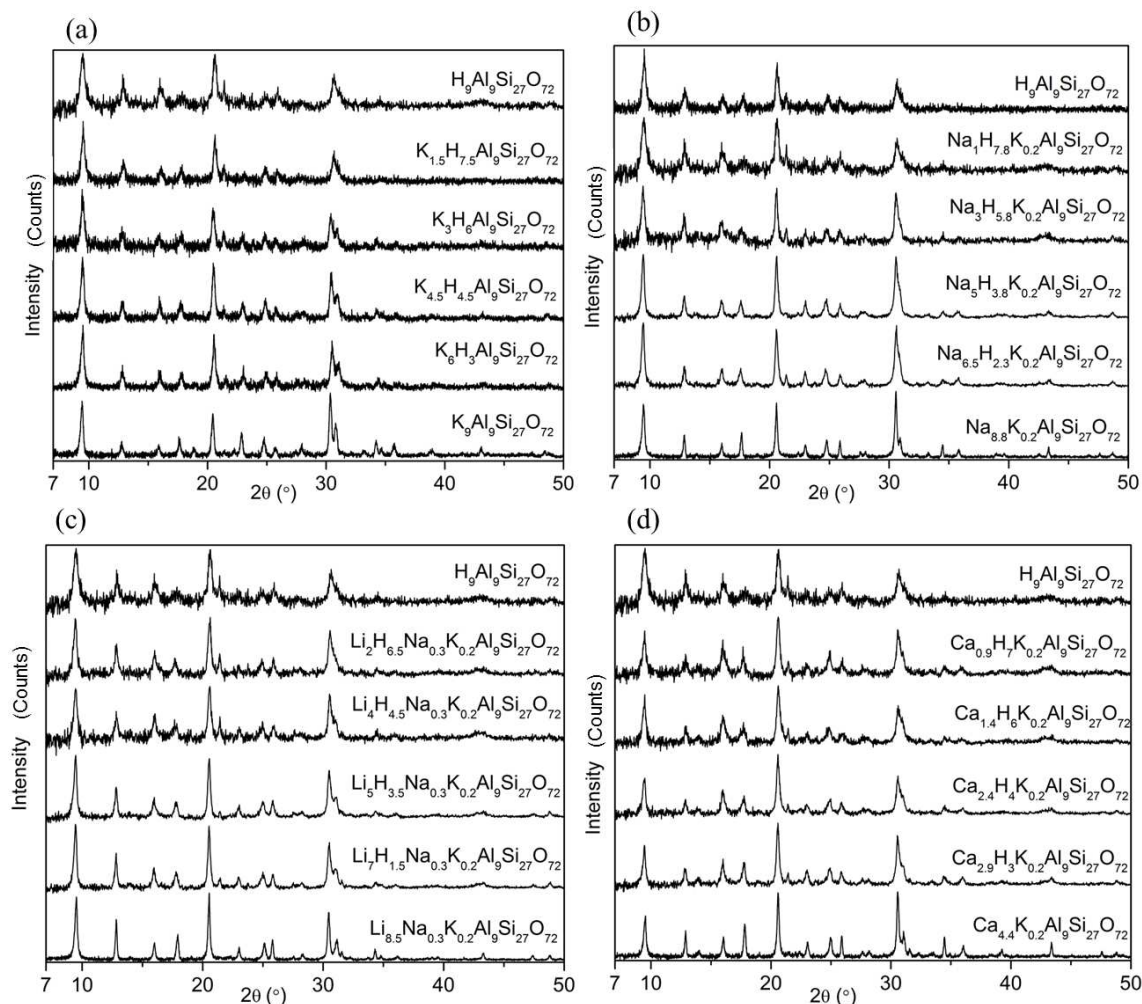


Figure 5.21. PXRD patterns of (a) K,H-chabazite, (b) Na,H-chabazite, (c) Li,H-chabazite and (d) Ca,H-chabazite series. The (offset) patterns have been collected at 298 K using the same operating conditions.

(iv) *In situ* synchrotron PXRD studies of CO₂ adsorption on Na-chabazite

As described above, fully exchanged Na-chabazite showed non-Type I adsorption behaviour that had not previously been reported. This was therefore examined in more detail.

For the fully-exchanged Na-chabazite the structural response to CO₂ adsorption was measured by *in situ* synchrotron PXRD performed at beamline I-11 at the Diamond

Light Source. The experimental details for *in situ* synchrotron PXRD are given in chapter 4.

Synchrotron PXRD patterns of the as-prepared, dehydrated (where no changes to the structure were observed upon further dehydration), in equilibrium with 1 bar of CO₂ and after CO₂ desorption Na-chabazite samples are presented in Figure 5.22a. It can be seen that none of the samples show the second set of peaks indicating the presence of the monoclinic phase observed in the laboratory, $C2/m$ (see Figure 5.2), and the samples retain rhombohedral $R\bar{3}m$ symmetry. The samples were heated for short periods to very high temperatures and it is very unlikely that any water would still be present in the structure. After CO₂ is adsorbed onto dehydrated Na-chabazite more reflections are visible and existing reflections sharpen slightly. The changes are reversible when CO₂ is desorbed from the structure.

To investigate the presence or absence of the monoclinic phase further, the influence of heating time on the dehydration was measured in the laboratory. Na-chabazite was dehydrated at 623 K on a glass line for 2 hours, 6 hours and 20 hours. Six hours is the amount of time used for dehydration\degassing the sample before CO₂ adsorption measurement and 2 hours is the time used in the Diamond experiment. The PXRD patterns of the samples dehydrated for different periods of time are presented in Figure 5.22b. It can be concluded that 2 hours dehydration is not enough time for the phase transformation and the sample remains in rhombohedral $R\bar{3}m$ symmetry. Two hours is probably long enough for the sample to be dehydrated but is not long enough for Na⁺ cations to move to cause the transformation of the structure. Dehydration for 6 hours and 20 hours gives the same amount of the monoclinic phase. It is possible that different parts of the sample possess slightly different composition and that only the Na rich regions undergo the cation driven distortion. Dehydration for 6 hours in the adsorption experiment allows the sample to transform to the mixture of phases and results in the step in the CO₂ adsorption isotherm (see Figure 5.16c). Additionally, experiments in which a higher temperature was used, 773 K, for a short time (2 hours) also did not result in any of the structure converting to monoclinic.

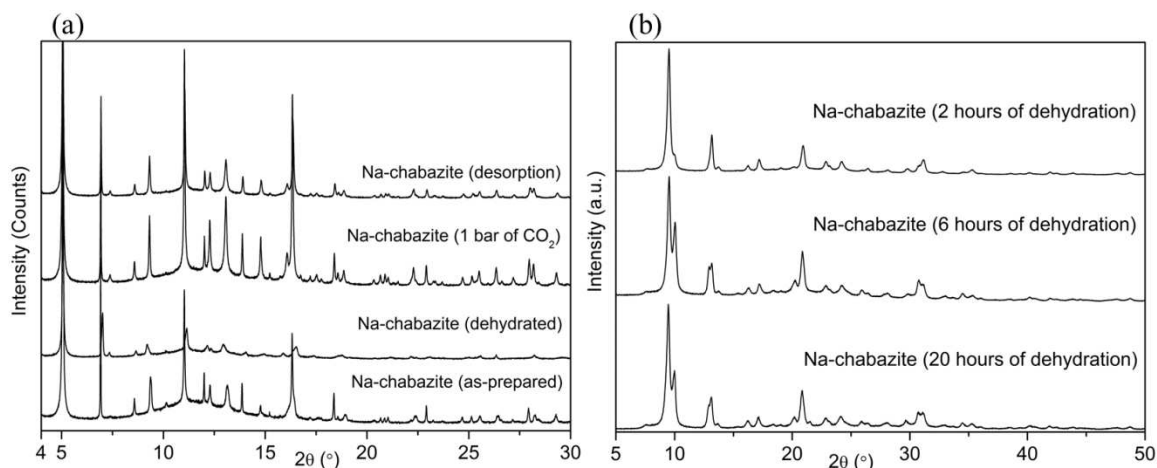


Figure 5.22. (a) Synchrotron PXRD patterns of as-prepared, dehydrated and with 1 bar of CO_2 adsorbed Na-chabazite where no second phase (C2/m) is observed and (b) laboratory PXRD patterns of Na-chabazite dehydrated at different temperatures. The (offset) patterns have been collected at 298 K using the same operating conditions.

Rietveld refinement was performed for Na-chabazite dehydrated and in equilibrium with 1 bar of CO_2 . The occupancies of the cation sites in Na-chabazite with and without CO_2 are given in Table 5.5, with full crystallographic details supplied in the appendix. Final observed, calculated and difference Rietveld plots for the synchrotron PXRD refinement of dehydrated and in equilibrium with 1 bar CO_2 Na-chabazite are given in Figure 5.23.

In dehydrated Na-chabazite, with $R\bar{3}m$ symmetry, Na^+ cations occupy two sites: S8R and S6R. There are 4.8 Na^+ per unit cell (1.6 Na^+ per CHA-cage) in S8R sites and 4.5 Na^+ per unit cell (1.3 Na^+ per CHA-cage) in S6R sites (Table 5.5 and Figure 5.24a). Not all of the S8R sites are occupied by Na^+ cations, which makes fully exchanged Na-chabazite porous to nitrogen (see Figure 5.7b and Figure 5.20b). After CO_2 adsorption all of the cations retain their positions. It was difficult to locate CO_2 molecules at 1 bar pressure adsorbed on Na-chabazite but strong electron density in the middle of the CHA-cage is clearly visible (Figure 5.24b). Difference Fourier analysis together with constrained refinement locates three refined sites for CO_2 molecules in the Na-chabazite structure: one is found close to the S6Rs, while the second site is in the middle of the S8Rs (Figure 5.24c). Before CO_2 adsorption, the Na–O distances are 2.40(1) Å for the Na^+ cations in S6R sites and 3.60(1) Å for the Na^+

cations in S8R sites. After CO₂ adsorption, the Na–O distances are 2.42(1) Å for the Na⁺ cations in S6R sites and 3.53(2) Å for the Na⁺ cations in S8R sites. The O–O distance between O atoms in S8R sites and the closest O atom from CO₂ is 2.53(1) Å.

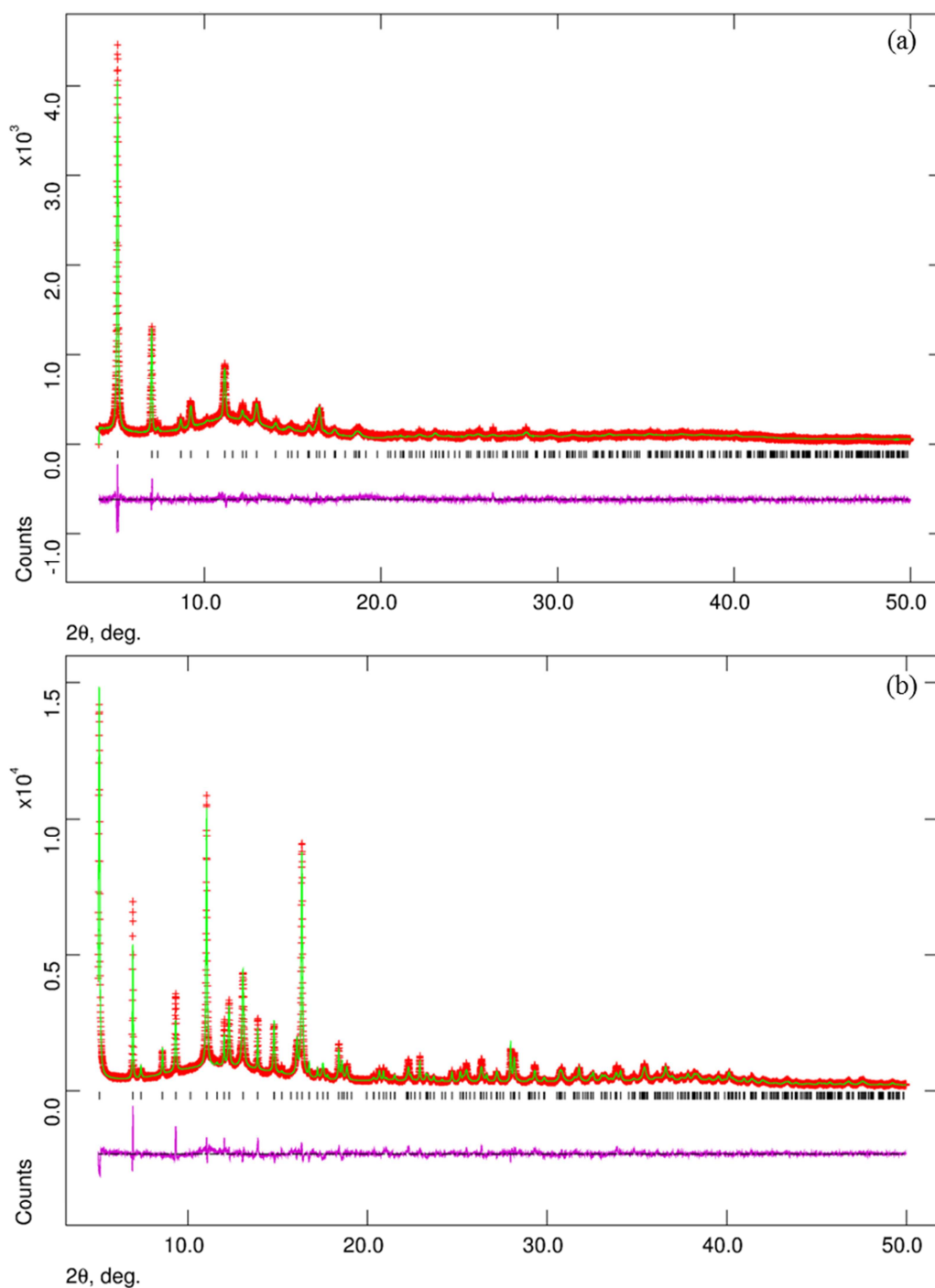


Figure 5.23. Final observed, calculated and difference Rietveld plots from in situ synchrotron powder data refinement of Na-chabazite (a) dehydrated and (b) in equilibrium with 1 bar of CO₂, collected at 298 K.

Table 5.5. Unit cell parameters, space group and cation site occupancies in dehydrated Na-chabazite and in equilibrium with 1 bar of CO₂, as determined by Rietveld refinement from synchrotron PXRD collected at 298 K.

Sample	Unit cell parameters /Å	Space group	S8R site occupancy		S6R site occupancy		D6R site occupancy	
			Frac. Occup.	Cations/unit cell	Frac. Occup.	Cations/unit cell	Frac. Occup.	Cations/unit cell
Na-chabazite	a,b=13.5537(9) c= 15.4529(17)	R $\bar{3}m$	0.50(4)	4.75(2)	0.81(2)	4.86(1)	N.D.	N.D.
Na-chabazite (1 bar)	a,b=13.69108(3) c= 15.2838(5)	R $\bar{3}m$	0.59(5)	5.31(3)	0.49(1)	2.94(1)	N.D.	N.D.

N.D. – not detected

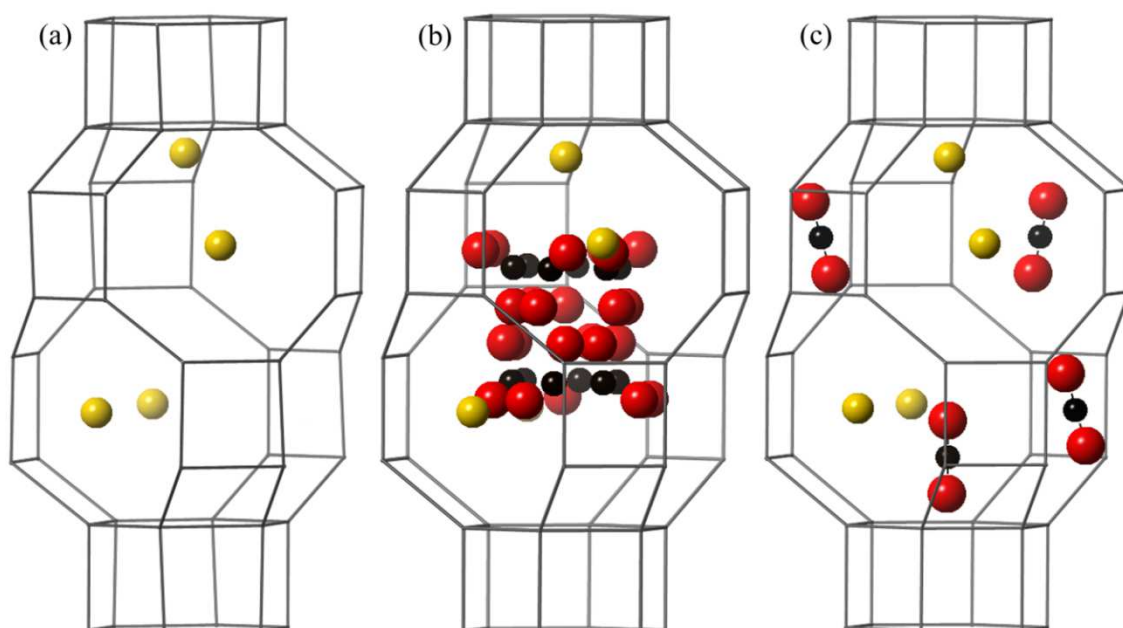


Figure 5.24. Possible arrangements of Na⁺ cations and CO₂ molecules within a CHA-cage of Na-chabazite at 298 K based on: (a) the refined dehydrated structure, (b) the refined dehydrated structure in equilibrium with 1 bar of CO₂ and (c) possible arrangements of cations and CO₂ (Na – yellow spheres; O – red spheres; C – black spheres).

(iv) High pressure CO₂ adsorption and CO₂/CH₄ selectivity of K-chabazite

In collaboration with Instituto de Tecnologia Quimica in Valencia *in situ* PXRD during CO₂ adsorption up to 5 bar and high pressure adsorption isotherms for CO₂ and CH₄ were collected. It can be observed that after CO₂ is adsorbed on dehydrated K-chabazite more reflections start being visible and existing reflections sharpen up (Figure 5.25) as was previously observed for Na-chabazite (see Figure 5.22a), indicating that changes

occur for the K-chabazite structure during CO₂ adsorption. The changes are reversible when CO₂ is desorbed from the structure.

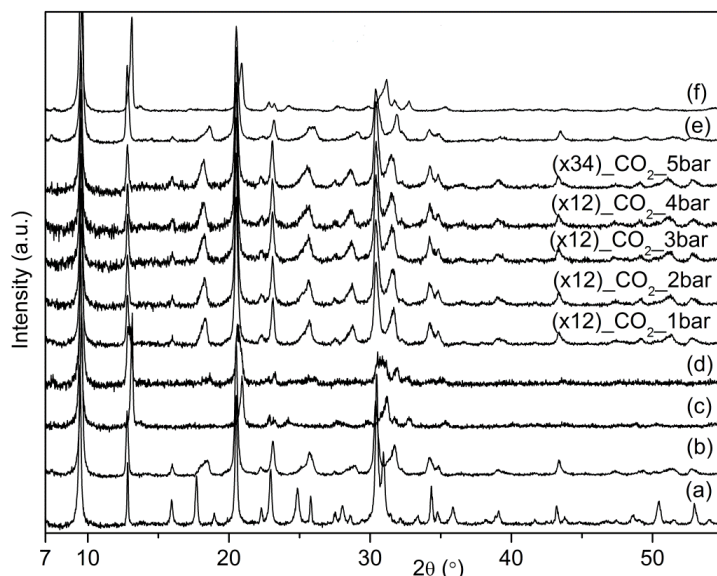


Figure 5.25. *In situ* PXRD of K-chabazite during CO₂ adsorption up to 5 bar. (a) Sample in air (including water molecules from the ambient moisture), (b) and (e) samples dehydrated at 298 K under He flow for 2 hours, (c), (d) and (f) samples dehydrated at 573 K under He flow for 2 hours and cooled down to RT. The "xnn" before the "CO₂_pressure" indicates the number of patterns combined (1 pattern = 2 hours). Data collected at Instituto de Tecnologia Quimica in Valencia at 298 K.

Rietveld analysis was performed on K-chabazite in equilibrium with 1 bar and 5 bar of CO₂ to investigate the changes that occurred in the PXRD patterns. Final observed, calculated and difference Rietveld plots for the laboratory powder data of K-chabazite in equilibrium with 1 bar and 5 bar of CO₂ are shown in Figure 5.26. Refined unit cell parameters, cation locations and occupancies in dehydrated K-chabazite and K-chabazite in equilibrium with 1 bar and 5 bar of CO₂ are given in Table 5.6. Crystallographic details from Rietveld analysis of K-chabazite in equilibrium with 1 bar and 5 bar of CO₂ are given in the appendix.

Possible arrangements of K⁺ cations and CO₂ molecules within a CHA-cage of K-chabazite at 298 K and in equilibrium with 1 bar and 5 bar of CO₂ are given in Figure 5.27. It was difficult to localise CO₂ molecules from PXRD laboratory data but strong electron density in the middle of CHA-cage was clearly visible. In dehydrated

K-chabazite, K^+ cations are found to occupy all S8R window sites (see Figure 5.10a). Since all S8R windows are occupied by K^+ cations some of them must move to allow CO_2 adsorption as it was shown recently by Shang *et al.*¹² The Rietveld refinement reveals that 1 K^+ per unit cell when 1 bar of CO_2 is adsorbed and 2 K^+ per unit cell when 5 bar of CO_2 is adsorbed move to the S6R site (Table 5.6). This was not observed for Na-chabazite where Na^+ cations do not occupy all S8R sites (see Figure 5.24a). This process must not be energetically very difficult to reverse because no hysteresis during CO_2 adsorption can be visible (see Figure 5.16a). It was calculated from the high pressure CO_2 adsorption isotherm (Figure 5.28) that around 9 molecules of CO_2 should be adsorbed from 1 to 5 bar, giving 3 CO_2 molecules per CHA-cage. Before CO_2 adsorption, the K–O distances are 3.08(5) Å for the K^+ cations in S8R sites. After CO_2 adsorption, the K–O distances are 3.16(1) Å for the K^+ cations in S6R sites and 3.18(2) Å for the K^+ cations in S8R sites. The K–O distances between K^+ cations in S6R sites and the closest O atom from CO_2 is 3.55(5) Å.

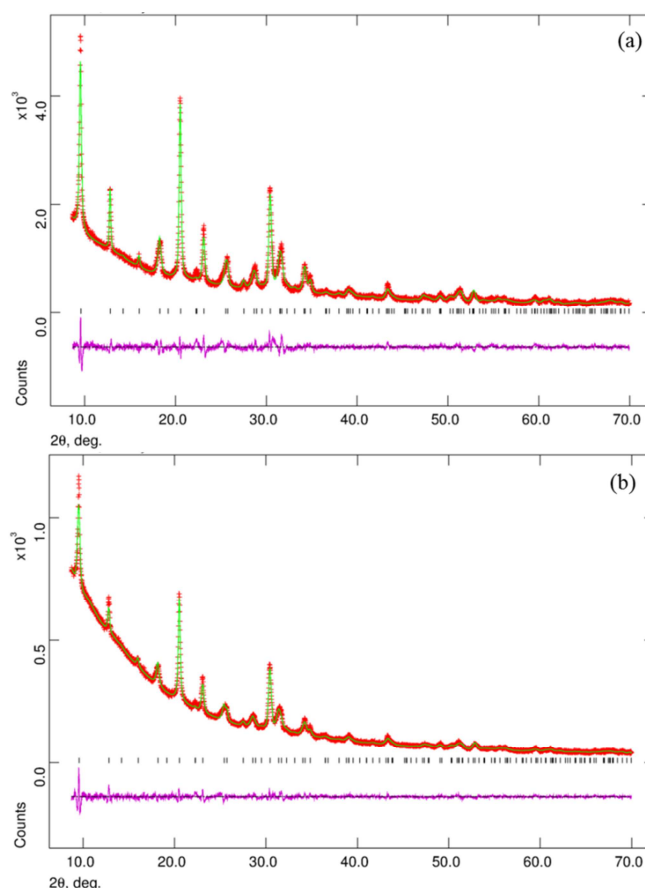


Figure 5.26. Final observed, calculated and difference Rietveld plots from the powder data refinement of (a) K-chabazite in equilibrium with 1 bar of CO_2 and (b) K-chabazite in equilibrium with 5 bar of CO_2 .

Table 5.6. Refined unit cell parameters, cation locations and occupancies in dehydrated K-chabazite and in equilibrium with 1 bar and with 5 bar of CO₂, obtained by Rietveld analysis of laboratory X-ray data collected at 298 K.

Sample	Unit cell parameters /Å	Space group	S8R		S6R	
			Frac. Occup.	Cations/unit cell	Frac. Occup.	Cations/unit cell
K-chabazite	$a, b = 13.7285(14)$ $c = 14.666(5)$	$R\bar{3}m$	1.00	9.00	N.D.	N.D.
K-chabazite (1bar)	$a, b = 13.8646(12)$ $c = 14.6090(25)$	$R\bar{3}m$	0.56(5)	5.04(1)	0.67(4)	4.02(1)
K-chabazite (5bar)	$a, b = 13.8584(14)$ $c = 14.6747(27)$	$R\bar{3}m$	0.45(3)	4.05(2)	0.83(2)	4.98(3)

N.D. – not detected

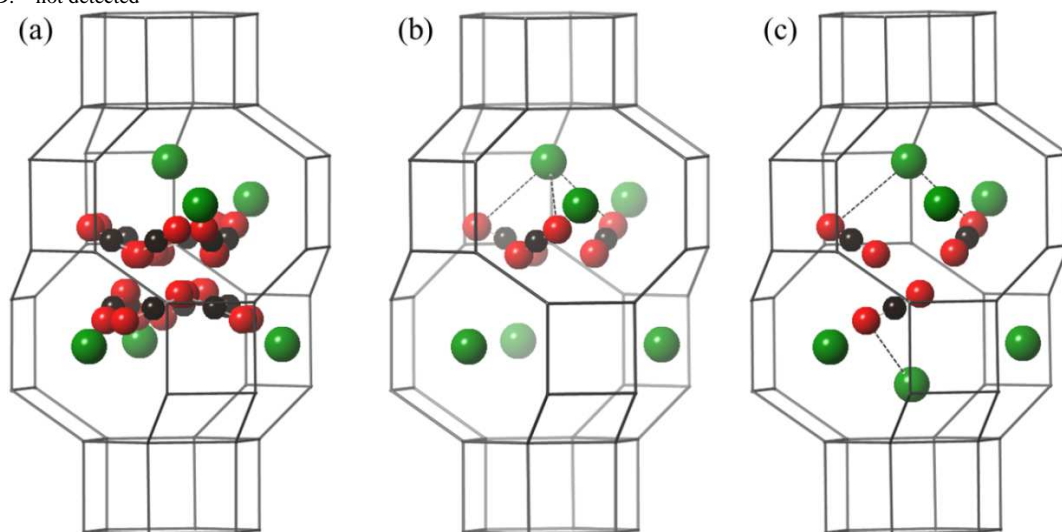


Figure 5.27. Possible arrangements of K⁺ cations and CO₂ molecules within an CHA-cage of K-chabazite at 298 K (a) based on the refined structure in equilibrium with 1 bar of CO₂ and (b), (c) two possible arrangements of cations and CO₂ at 'full occupancy' (K – green spheres; O – red spheres; C – black spheres).

Carbon dioxide and CH₄ adsorption isotherms obtained for K-chabazite (Figure 5.28a) show that CO₂ is adsorbed in a larger amount than CH₄. The α factor is plotted against pressure in Figure 5.28b. The CO₂/CH₄ equilibrium selectivity factor (α) was calculated from single component isotherms using equation 4.3 from chapter 4. The selectivities from 6 to 2 are obtained at pressure ranges of 0–8 bar which are close to those obtained for zeolites already used in industry for the CO₂/CH₄ separation process.^{30,31} This selectivity for CO₂ over CH₄ arises because the CH₄ interacts more weakly with cations

but the data shows that the K^+ cations can move to allow both CO_2 and CH_4 to be adsorbed at 298 K.

Observation made on selectivity of K-chabazite can be put in the content of recent work on chabazite by the group of Webley.¹² They show that whereas K-chabazite with Si/Al ratio of 3.0 (as in this work) does not give higher selectivity in CO_2/CH_4 or CO_2/N_2 separations, than expected from the difference in interaction energies of these molecules with the extra-framework cations, it is observed that K- and Cs-chabazite with lower Si/Al ratios and consequently higher cation contents show very high CO_2/N_2 and CO_2/CH_4 selectivities. When there is more than 9 K^+ per unit cell (Si/Al < 3.0) any residual cations will start occupying S6R and K^+ from S8R will not be able to move and they will act as ‘trapdoors’, this will still allow the passage of CO_2 molecules into chabazite whilst the larger size (4 Å) and lower interaction of hydrocarbons results in their exclusion.

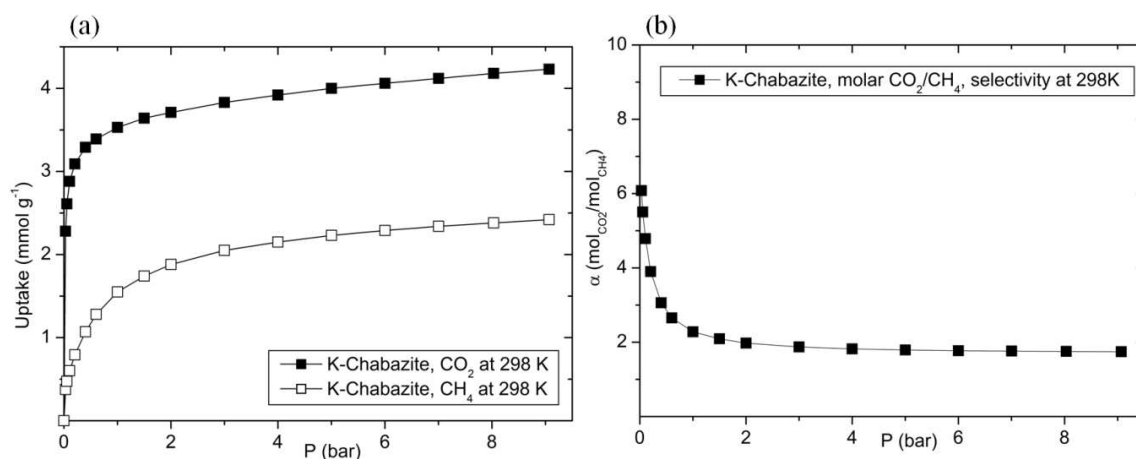


Figure 5.28. (a) CO_2 and CH_4 adsorption isotherms of K-chabazite at 298 K, and (b) CO_2/CH_4 equilibrium selectivity factor according to gravimetric measurements. Data collected at Instituto de Tecnologia Quimica in Valencia.

5.5. Conclusions

Chabazite is well known as a good CO_2 adsorbent. It was chosen for this study due to its small pore size that facilitates strong interactions with adsorbed molecules and easily exchangeable extra-framework cations, some of which reside in the S8R sites and can affect the accessibility of the CHA-cage.

H-chabazite possesses low crystallinity due to the acid hydrolysis of the framework, and it does not show strong adsorption of CO₂ at conditions relevant to carbon capture from flue gases. Adsorption is of Type I with no hysteresis.

Highest values of CO₂ adsorption for the zeolite chabazite are observed on the lithium form. Li⁺ cations are expected to occupy S6R sites in the CHA-cage, and so leave window sites free of cations. As a result the CO₂ adsorption isotherm at 298 K does not show hysteresis and all the Li⁺ cations in the S6R sites are accessible for CO₂ adsorption.

Only minor distortions of the framework geometry occur upon dehydration for Ca-chabazite resulting in a small hysteresis for CO₂ adsorption isotherm, in contrast with the results found for chabazites exchanged with monovalent cations in this study. Similar to Li-chabazite, in Ca-chabazite cations do not occupy S8R sites but they are found in S6R and D6R sites. The cations in the D6R site are strictly inaccessible for adsorption, so only the cations in S6R sites are available to interact with CO₂, which results in slightly lower CO₂ uptake on this material compared to Li-chabazite.

CO₂ adsorption isotherm at 298 K of K-chabazite shows reasonably good uptake with no hysteresis but the PXRD pattern of this material reveals that upon dehydration the structure undergoes structural changes that result in broad reflections. Notably there is a considerable (*ca.* 5 %) reduction in the *c* axis, and K⁺ cations fully occupy S8R sites. The changes are reversible upon re-hydration. When CO₂ is adsorbed peaks begin to sharpen. The refinement on dehydrated K-chabazite with CO₂ adsorbed reveals that 1 K⁺ per unit cell (for 1 bar of CO₂) or 2 K⁺ per unit cell (for 5 bar of CO₂) move and stay in S6R sites, indicating that ‘solvation’ by adsorbed CO₂ molecules permits local cation migration. This cation migration must, also be possible in the presence of CH₄ at 298 K, as shown by adsorption isotherms, but is not possible at 77 K for N₂. Shang *et al.*¹² talked of gating temperature for each chabazite-adsorbate system, below which cation relocation from S8R site is not possible, even momentarily, so adsorption does not occur. They also show that for low silica chabazites (where there is more than 9 K⁺ per unit cell, Si/Al < 3) residual cations start occupying the S6R sites which restricts motion of the S8R potassium cations and so hinders uptake, so the zeolite windows act

as molecular specific ‘trapdoors’. For these low silica chabazites, CO₂ uptake is permitted while lower interaction of hydrocarbons and N₂ results in their exclusion.

This ‘trapdoor effect’ is discussed further in relation to our studies of zeolite Rho described in chapter 7.

In contrast to the Li-, Ca- and K-chabazite, which retain their rhombohedral $R\bar{3}m$ symmetry upon dehydration, the dehydration of Na-chabazite results in a transformation to a mixture of rhombohedral $R\bar{3}m$ symmetry and monoclinic $C2/m$ symmetry and the CO₂ adsorption isotherm at 298 K shows a step and marked hysteresis. These changes to the Na-chabazite structure are also observed as a second set of diffraction peaks and the broadening of existing reflections and they are reversible upon re-hydration. The phase mixture for Na-chabazite observed in this study has not been reported previously. The monoclinic phase is not observed for Na-chabazite with a lower concentration of Na⁺ cations and CO₂ adsorption isotherms on Na,H-chabazite sample show no step or hysteresis. It may be assumed that Na-chabazite prepared in this study possesses a special structure composition where the number of Na⁺ cations does not allow for a complete change of the rhombohedral $R\bar{3}m$ symmetry to monoclinic $C2/m$ symmetry but remains as a mixture of these two phases. Attempts were made to characterise the structure of Na-chabazite during CO₂ adsorption by *in situ* synchrotron PXRD. Due to the time limit of dehydration under vacuum the Na-chabazite structure transformation during dehydration was not observed. However this dehydration time was probably long enough for the sample to dehydrate, this allowed a model of CO₂ adsorbed on Na-chabazite with rhombohedral $R\bar{3}m$ symmetry to be prepared, which does not exist previously in the literature. Similar to K-chabazite, when the CO₂ is adsorbed diffraction peaks sharpen. In Na-chabazite, Na⁺ cations occupy S8R sites and S6R sites. In contrast to K-chabazite, not all of S8R sites are blocked by Na⁺ cations and there is no need for their displacement. The CO₂ molecules occupy three positions: in the middle of CHA-cage, in the centre of S8R and close to the centre of S6R.

Adsorption characteristics of chabazites are strongly dependent upon their cation composition. The cage access is controlled by the size of the cation and the degree of occupancy of the window sites. The results gathered in this study broaden

the knowledge of chabazite structure by *in situ* CO₂ adsorption and electron diffraction studies.

References

1. Smith J. V., Rinaldi F. and Dent Glasser L. S., *Acta Cryst.*, **1963**, *16*, 45-63
2. Smith J. V., *Acta Cryst.*, **1962**, *15*
3. Coe C. G. and Gaffiney T. R., 4 943 304, US Patent, **1990**
4. De Baerdemaeker T. and De Vos D., *Nat. Chem.*, **2013**, *5*, 89-90
5. Mortier W. J., Pluth J. J. and Smith J. V., *Mater. Res. Bull.*, **1977**, *12*, 241-249
6. Mortier W. J., Pluth J. J. and Smith J. V., *Mater. Res. Bull.*, **1977**, *12*, 97-102
7. Alberti A., Galli E., Vezzalini G., Passaglia E. and Zanazzi P. F., *Zeolites*, **1982**, *2*, 303-309
8. Smith L. J., Eckert H. and Cheetham A. K., *J. Am. Chem. Soc.*, **2000**, *122*, 1700-1708
9. Smith L. J., Eckert H. and Cheetham A. K., *Chem. Mater.*, **2001**, *13*, 385-391
10. Ugliengo P., Busco C., Civalleri B. and Zicovich-Wilson C. M., *Mol. Phys.*, **2005**, *103*, 2559-2571
11. Ridha F. N., Yang Y. and Webley P. A., *Micropor. Mesopor. Mat.*, **2009**, *117*, 497-507
12. Shang J., Li G., Singh R., Gu Q., Nairn K. M., Bastow T. J., Medhekar N., Doherty C. M., Hill A. J., Liu J. Z. and Webley P. A., *J. Am. Chem. Soc.*, **2012**, *134*, 19246-19253
13. Civalleri B., Ferrari A. M., Llunell M., Orlando R., Mérawa M. and Ugliengo P., *Chem. Mater.*, **2003**, *15*, 3996-4004
14. Grey T., Gale J., Nicholson D. and Peterson B., *Micropor. Mesopor. Mat.*, **1999**, *31*, 45-59
15. Gundogdu M. N., Yalcin H., Temel A. and Clauer N., *Miner. Deposita*, **1996**, *31*, 492-513
16. Zamzow M. J. and Murphy J. E., *Separ. Sci. Technol.*, **1992**, *27*, 1969-1984
17. Coronas J. and Santamaria J., *Catal. Today*, **1999**, *51*, 377-389
18. Zhang J., Singh R. and Webley P. A., *Micropor. Mesopor. Mat.*, **2008**, *111*, 478-487
19. Singh R. K. and Webley P., *Adsorption*, **2005**, *11*, 173-177

20. Auerbach S. M., Carrado K. A. and Dutta P. K., *'Handbook of Zeolite Science and Technology - Aussie Zeolite'*, Marcel Dekker, Inc., USA, **2003**
21. Ridha F. N. and Webley P. A., *Sep. Purif. Technol.*, **2009**, 67, 336-343
22. Ridha F. N. and Webley P. A., *Micropor. Mesopor. Mat.*, **2010**, 132, 22-30
23. Hudson M. R., Queen W. L., Mason J. A., Fickel D. W., Lobo R. F. and Brown C. M., *J. Am. Chem. Soc.*, **2012**, 134, 1970-1973
24. Singh R., Ram Reddy M. K., Wilson S., Joshi K., Diniz da Costa J. C. and Webley P., *Energy Procedia*, **2009**, 1, 623-630
25. Shang J., Li G., Singh R., Xiao P., Liu J. Z. and Webley P. A., *J. Phys. Chem. C*, **2010**, 114, 22025-22031
26. Yang J., Zhao Q., Xu H., Li L., Dong J. and Li J., *J. Chem. Eng. Data*, **2012**, 57, 3701-3709
27. Garrone E., Bonelli B., Lamberti C., Civalieri B., Rocchia M., Roy P. and Arean C. O., *J. Chem. Phys.*, **2002**, 117, 10274-10282
28. Galhotra P., Navea J. G., Larsen S. C. and Grassian V. H., *Energ. Environ. Sci.*, **2009**, 2, 401-409
29. Siporin S. E., McClaine B. C. and Davis R. J., *Langmuir*, **2003**, 19, 4707-4713
30. Delgado J. A., Uguina M. A., Gómez J. M. and Ortega L., *Sep. Purif. Technol.*, **2006**, 48, 223-228
31. Cavenati S., Grande C. A. and Rodrigues A. E., *J. Chem. Eng. Data*, **2004**, 49, 1095-1101

6. ZK-5: Zeolite with High Carbon Dioxide Uptake at Ambient Temperature and Pressure

6.1. Introduction

Zeolite ZK-5 (topology type KFI) was first synthesised by Kerr¹ and its structure was determined by Meier and Kokotailo.² In recent years, alternative methods of synthesising ZK-5 have been published that allow some control of the Si/Al ratio and crystal size.³⁻⁵ ZK-5 is a polytype of chabazite, being also built up from double six-membered rings (D6Rs) linked via single four-membered rings (S4Rs, Figure 6.1).

Its framework structure has body-centred cubic symmetry, and every α -cage is linked to six other α -cages via paulingite cages (Figure 6.1b). The α -cage/paulingite cage connections comprise planar eight-membered ring windows with 4.0 Å diameter. Paulingite cages are interconnected via eight-membered ring windows which are non-planar and have smaller free diameters. Like chabazite, the ZK-5 framework has a low framework density (15 T/1000 Å³) and a high pore volume for small molecules. Studies have recently shown that ZK-5 can be prepared in cationic forms that have excellent CO₂ uptake and working capacity, in excess of that of benchmark zeolite 13X.⁶⁻⁸

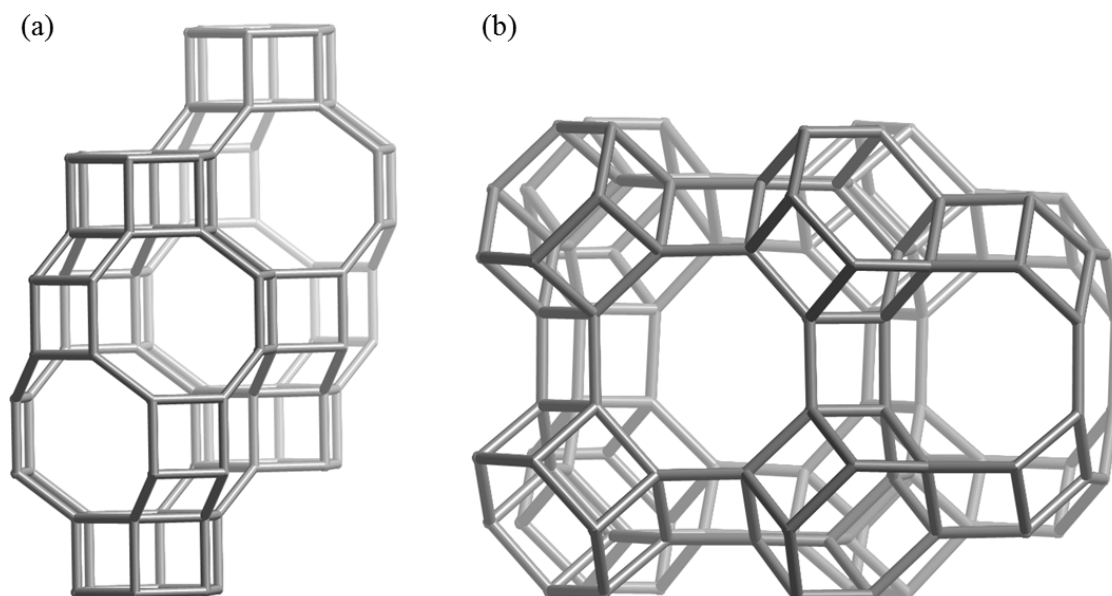


Figure 6.1. Structure of (a) chabazite and its polytype (b) ZK-5 built up from double six-membered rings (D6Rs) linked via single four-membered rings (S4Rs).

Extra-framework cation positions of K^+ , Na^+ and Li^+ in ZK-5 determined in previous studies^{2,5,7,8} have been located mainly in two sites: the first one in single eight-membered ring (S8R site, coordinates (0, 1/4, 1/2)) of the *pau* cages between α -cages and the second is in single six-membered ring (S6R site, coordinates (x,x,x), $x \approx 0.15$) of the α -cages. These sites are illustrated in Figure 6.2. Sodium and potassium cations in ZK-5 occupy part of the S6R sites in the α -cages and all the S8R sites of the *pau* cages.^{2,5,7,8} Lithium cations occupy sites near the S6R of the hexagonal prisms.^{7,8}

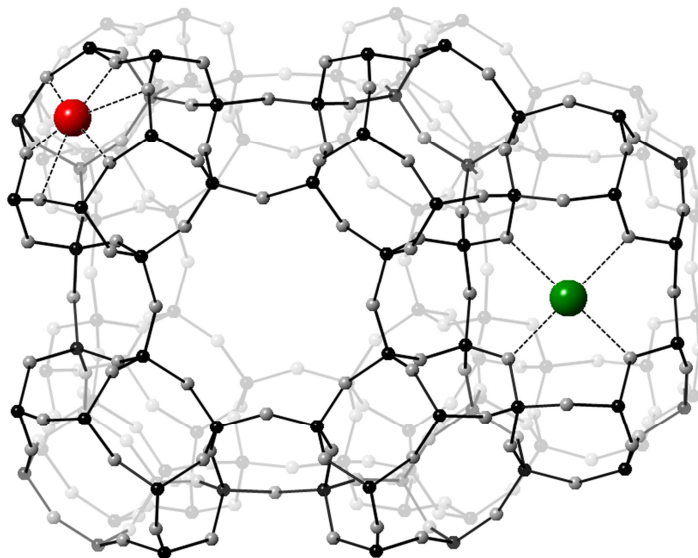


Figure 6.2. Representation of the extra-framework cation positions close to the single six-membered ring windows (S6R, red) and close to the single eight-membered ring windows in *pau* cage (S8R, green).

In this study, different cations (K^+ , H^+ , Na^+ and Li^+) have been introduced into the ZK-5 structure and their influence on CO_2 adsorption has been measured. The location of the cations in the dehydrated ZK-5 has been determined where possible by Rietveld refinement and the selectivity of CO_2 over ethane measured on K- and Na-ZK-5. For comparison, SAPO STA-14 (St Andrews material 14), a silicaluminophosphate with the same topology as ZK-5, has been prepared and ion exchanged with sodium.

6.2. Characterisation of Different Cationic Forms of ZK-5

K-ZK-5 was prepared by hydrothermal synthesis and ion exchanged as described in chapter 4. All ZK-5 forms were characterised by a combination of physico-chemical techniques.

PXRD was used to identify the crystallinity of the as-prepared hydrated K-ZK-5 and to investigate the changes of zeolite structure caused by the ion exchange with different cations. The PXRD pattern of K-ZK-5 presented in Figure 6.3a shows well-resolved and sharp diffraction peaks in the region of $2\theta = 5.0\text{--}50.0^\circ$. It can be also seen that the as-prepared K-ZK-5 contains small amounts of impurities identified as chabazite. The ZK-5 reflections of the as-prepared hydrated sample are associated with $Im\bar{3}m$ cubic symmetry with the unit cell parameter $a = 18.7067(2)$ Å. The PXRD pattern of K-ZK-5 is compared with the patterns of hydrated H-, Na- and Li-ZK-5 in Figure 6.3b. The changes in intensities and 2θ values of the reflections caused by introducing different cations to the zeolite structure can be observed. The impurities coming from chabazite are visible for all ion exchanged samples.

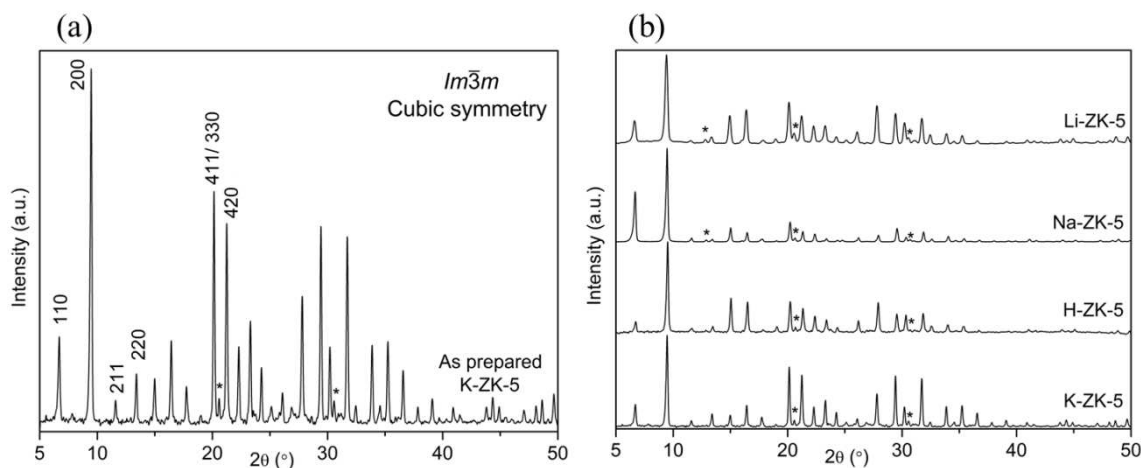


Figure 6.3. PXRD patterns of (a) K-ZK-5 indexed according to the cubic symmetry and (b) the comparison of K-ZK-5 with H-, Na- and Li-ZK-5. '*' indicates chabazite impurities. The (offset) patterns have been collected at 298 K using the same operating conditions.

Size and shape of ZK-5 crystals before and after ion exchange were characterised by SEM and the secondary electron micrographs of K-ZK-5 and Na-ZK-5 are presented in Figure 6.4. It is apparent that the ion exchange does not influence the shape and size of the crystals. Both samples consist of *ca.* 1.4 μm cubes.

Unit cell compositions of all ZK-5 samples were estimated from a combination of EDX analysis and MAS NMR spectroscopy. The EDX analysis (Table 6.1 and Figure 6.5) confirms that K^+ can be ion exchanged by NH_4^+ , Na^+ , and Li^+ in ZK-5. The NH_4 -form gives the H-form upon heating at 823 K. All ion exchanged samples contain a small

amount of residual K^+ , which could not be removed even after many hours of ion exchange. No other elements apart from the framework O, Si, Al, and extra-framework cations are visible in the EDX spectra. The Si/Al ratio was measured as 4.2.

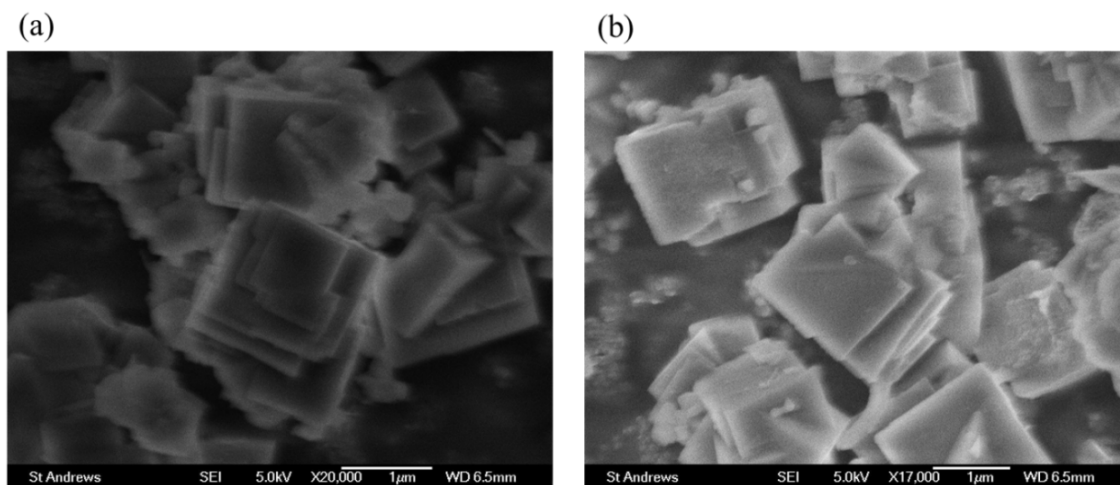


Figure 6.4. SEM micrographs of (a) as-prepared K-ZK-5 and (b) ion exchanged Na-ZK-5.

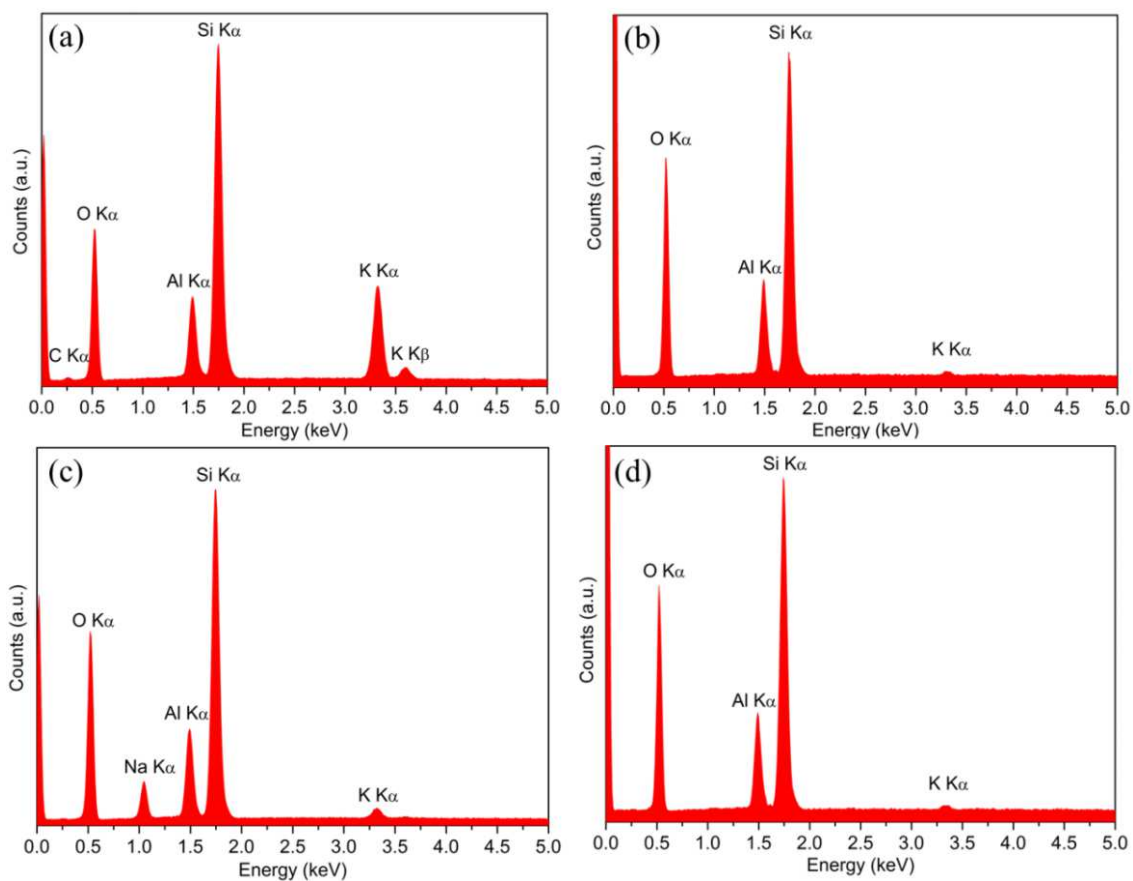


Figure 6.5. EDX spectra of (a) K-ZK-5, (b) H-ZK-5, (c) Na-ZK-5 and (d) Li-ZK-5.

From the ^{29}Si MAS NMR spectrum of the as-prepared K-ZK-5 (Figure 6.6a) three sharp and strong peaks can be attributed to: Si(2Al) (-98.17 ppm), Si(1Al) (-103.13 ppm) and Si(0Al) (-107.89 ppm). ^{27}Al MAS NMR spectrum (Figure 6.6b) reveals only the tetraordinated framework Al at 57 ppm. The framework Si/Al molar ratio is 4.16 determined by ^{29}Si MAS NMR spectroscopy using equation 4.2 in chapter 4 and the deconvolution of the signals (see the appendix). The Si/Al ratio obtained from NMR is in a good agreement with Si/Al ratio obtained from EDX analysis. The ^{29}Si MAS NMR value was taken as the more accurate, and compositions calculated accordingly for ZK-5 materials are given in Table 6.1. The formula for the derivation of the unit cell composition is given in chapter 4.

Table 6.1. EDX analysis of ZK-5 before and after ion exchange.

Sample	O	Atomic %					Unit cell formula of dehydrated sample
		Si	Al	Na	Li	K	
K-ZK-5	70 ± 1	20 ± 1	5 ± 1	N.D.	N.D.	5 ± 1	$\text{K}_{18.6}\text{Al}_{18.6}\text{Si}_{77.4}\text{O}_{192}$
H-ZK-5	75 ± 1	20 ± 1	5 ± 1	N.D.	N.D.	N.D.	$\text{H}_{18.6}\text{Al}_{18.6}\text{Si}_{77.4}\text{O}_{192}$
Na-ZK-5	70 ± 1	21 ± 1	5 ± 1	4 ± 1	N.D.	0.6	$\text{Na}_{16.6}\text{K}_2\text{Al}_{18.6}\text{Si}_{77.4}\text{O}_{192}$
Li-ZK-5	75 ± 1	20 ± 1	5 ± 1	N.D.	N.D.	0.2	$\text{Li}_{17.8}\text{K}_{0.8}\text{Al}_{18.6}\text{Si}_{77.4}\text{O}_{192}$

Values for oxygen are semi-quantitative

N.D. – not detected

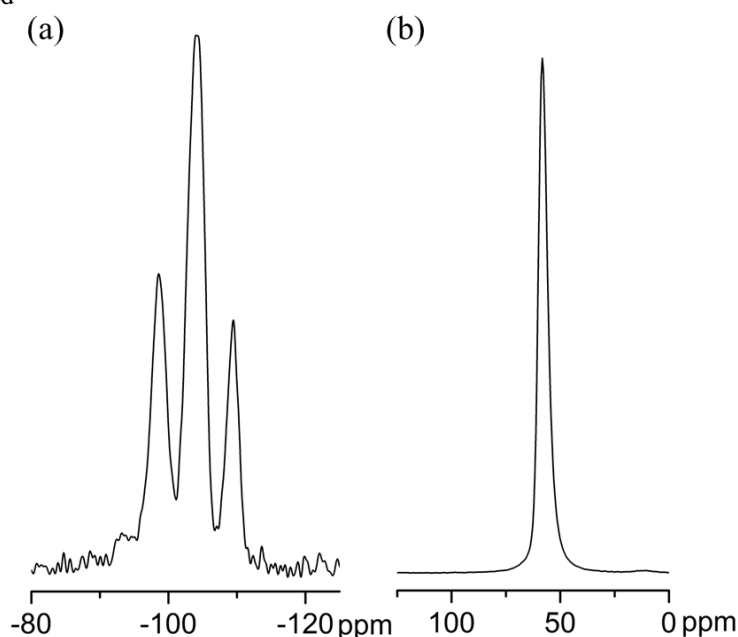


Figure 6.6. (a) ^{29}Si MAS NMR and (b) ^{27}Al MAS NMR spectra of as-prepared K-ZK-5.

From TGA (Figure 6.7a), K-, H- and Na-ZK-5 show one dehydration step, *ca.* 15% weight loss for K- and Na-ZK-5, and *ca.* 12% weight loss for H-ZK-5, which corresponds to the removal of weakly physisorbed water molecules from 300 K to

400 K. The TGA curve of Li-ZK-5 shows two dehydration steps. The first weight loss between 300 K and 400 K of *ca.* 17% is due to the desorption of physisorbed water and the second steps of *ca.* 5% weight loss from 400 K to 500 K due to chemisorbed water desorption.

Adsorption isotherms of N₂ at 77 K on K-, H-, Na- and Li-ZK-5 are presented in Figure 6.7b. N₂ adsorption isotherms of all ZK-5 samples show Type I behaviour, characteristic for adsorbents having a microporous structure. The sequence of N₂ adsorption uptake for ZK-5 samples is H-ZK-5 > Li-ZK-5 > Na-ZK-5 > K-ZK-5. H-ZK-5 shows the highest porosity to N₂ of 7.5 mmol g⁻¹ at p/p₀ = 0.9. The N₂ uptakes of Li- and Na-ZK-5 are similar, 6.0 mmol g⁻¹ at p/p₀ = 0.9. H-, Na- and Li-ZK-5 demonstrate easy access of the porous structures to N₂ molecules, this would be expected from the small dimensions of H⁺, Na⁺ and Li⁺ and it suggests that none of the cations in ZK-5 block the entrances to the α -cage. However, K-ZK-5, where the dimensions of K⁺ are the largest of all cations, shows lower uptake of N₂ (3.5 mmol g⁻¹).

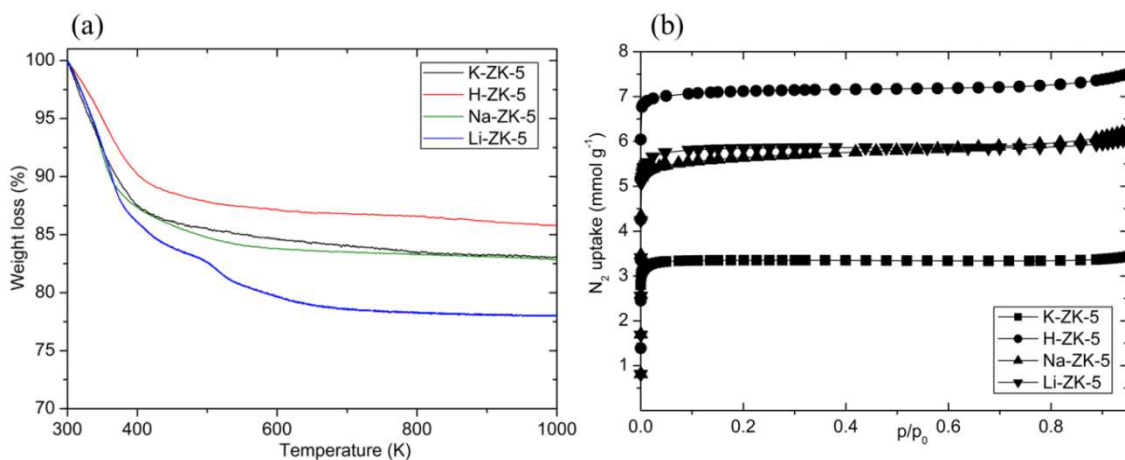


Figure 6.7. (a) TGA curves and (b) N₂ adsorption isotherms at 77 K of K-ZK-5, H-ZK-5, Na-ZK-5 and Li-ZK-5.

6.3. Structural Studies of K-, Na-, and Li-ZK-5

Figure 6.8 presents a comparison of the PXRD patterns of hydrated and dehydrated K-, Na- and Li-ZK-5 samples, measured at 298 K. For all ZK-5 samples in the hydrated form the structure adopts a cubic symmetry with space group $Im\bar{3}m$. ZK-5 does not show flexibility upon dehydration and acts as a good example of a rigid, small pore

structure with permanent porosity to N_2 . The chabazite impurities are also visible for all dehydrated samples. The relative intensities of these impurity peaks appear greater for the dehydrated samples. They are most apparent in the K-ZK-5 where the impurity reflections at $2\theta = 13^\circ$ and 21° become clearly visible.

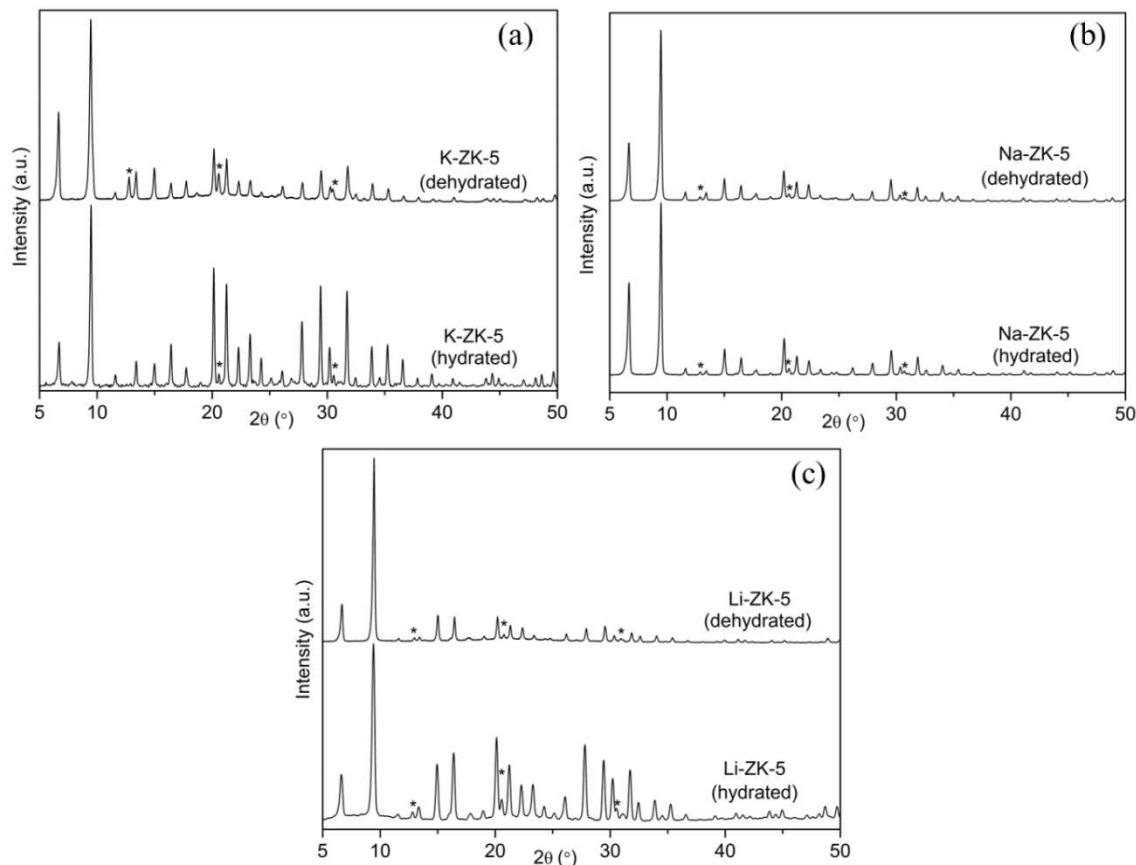


Figure 6.8. Comparison of PXRD patterns of hydrated and dehydrated (a) K-ZK-5, (b) Na-ZK-5 and (c) Li-ZK-5 samples. The (offset) patterns have been collected at 298 K using the same operating conditions.

Structures of K-, Na- and Li-ZK-5 were determined by Rietveld refinement (as described in chapter 4), taking into account the residual K^+ in the Li- and Na-ZK-5 and also the presence of chabazite impurity. The diffraction data was analysed via a two-phase refinement, including a structural model for chabazite.⁹ Rietveld plots for all ZK-5 samples are presented in Figure 6.9. Crystallographic details for these refinements are given in Table 6.2 and in the appendix. The O–O distance is calculated from the distance between the O atom centres minus double the van der Waals ionic radius of O^{2-} , 1.35 Å.

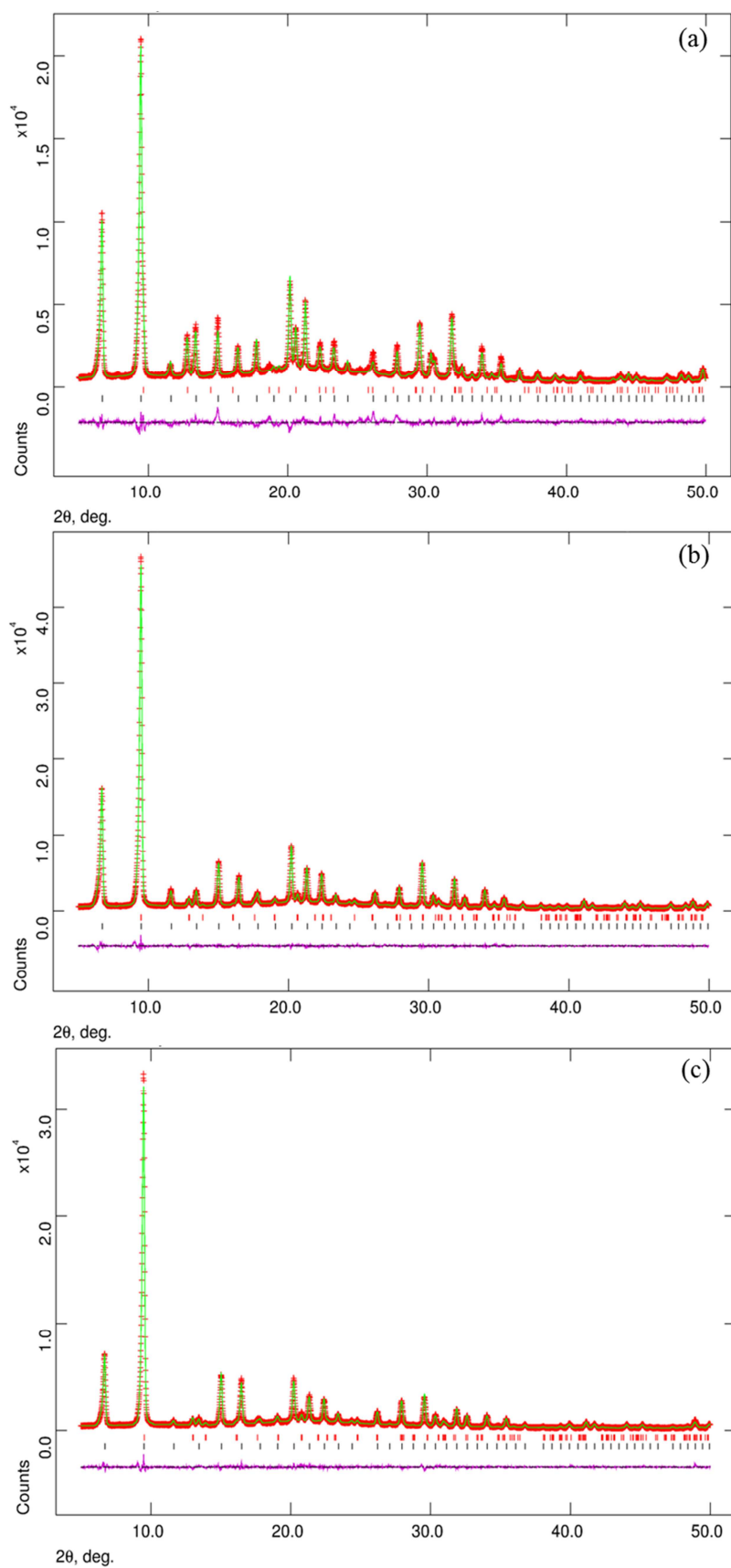


Figure 6.9. Final observed, calculated and difference Rietveld plots for the powder data refinement of (a) K-ZK-5, (b) Na-ZK-5 and (c) Li-ZK-5.

Rietveld refinement of dehydrated samples reveals that the unit cell parameter a , varies in the sequence Li-ZK-5 < Na-ZK-5 < K-ZK-5. The minimum O–O distance across the circular windows changes from 3.67 Å for K-ZK-5 to 4.00 Å for Na-ZK-5 and 3.90 Å for Li-ZK-5. The most occupied site in K-ZK-5 and Na-ZK-5 is S8R (12 K⁺ per unit cell and 8 Na⁺ per unit cell, respectively) and in Li-ZK-5 it is S6R (16 Li⁺ per unit cell).

Figure 6.10 shows a possible arrangement of cations in a single α -cage and associated *pau* cages for K-ZK-5, Na-ZK-5 and Li-ZK-5. Around 20% for K-ZK-5, and 10% for Na-ZK-5 and Li-ZK-5 of the samples were found to be chabazite. Due to the large amount of the second phase in K-ZK-5 a full structure refinement was not possible. However, two extra-framework cation sites were located for K⁺ cations and they are consistent with those described for this material in the literature.¹⁰ The S8R sites contain 12 K⁺ per unit cell and the S6R sites *ca.* 4 K⁺ per unit cell. The K–O distances in the S8R sites are 2.72(5) Å, and for the S6R are 2.90(1) Å. The same extra-framework cation sites have been found for Na-ZK-5. Both sites, S8R and S6R, are occupied by *ca.* 8 Na⁺ per unit cell. There is an extra scattering in the S8R sites assigned as 2 K⁺ per unit cell. The Na–O distances in the S8R sites are 2.67(1) Å, and for the S6R are 2.35(1) Å. In Li-ZK-5 there is only one cation site, the S6R, which is fully occupied by Li cations (16 Li⁺ per unit cell), and, similar to Na-ZK-5, there is some scattering in the S8R sites corresponding to 1 K⁺ cation per unit cell. The Li–O distances in the S6R sites are 2.09(1) Å, and the K–O distance is 2.89(1) Å. For all ZK-5 samples the S8R sites in the windows connecting the α -cage with the *pau* cage are unoccupied, allowing the free migration of N₂ into the structure.

Table 6.2. Space group, minimum O–O distance of S8R windows and cation site occupancies in dehydrated zeolite ZK-5 as determined by Rietveld refinement from laboratory powder X-ray diffraction collected at 298 K.

Sample	Unit cell parameter /Å	Space group	O–O /Å	S8R		S6R	
				Frac. Occup.	Cations/unit cell	Frac. Occup.	Cations/unit cell
K-ZK-5	18.6552(5)	$Im\bar{3}m$	3.67	0.85 K	12.0 K	0.24 K	3.68 K
Na-ZK-5	18.6142(2)	$Im\bar{3}m$	4.00	0.166(1) K 0.636(5) Na	1.99(2) K 7.63(5) Na	0.536(4) Na	8.57(6) Na
Li-ZK-5	18.5985(3)	$Im\bar{3}m$	3.90	0.089(5) K	1.08(1) K	1.0 Li	16 Li

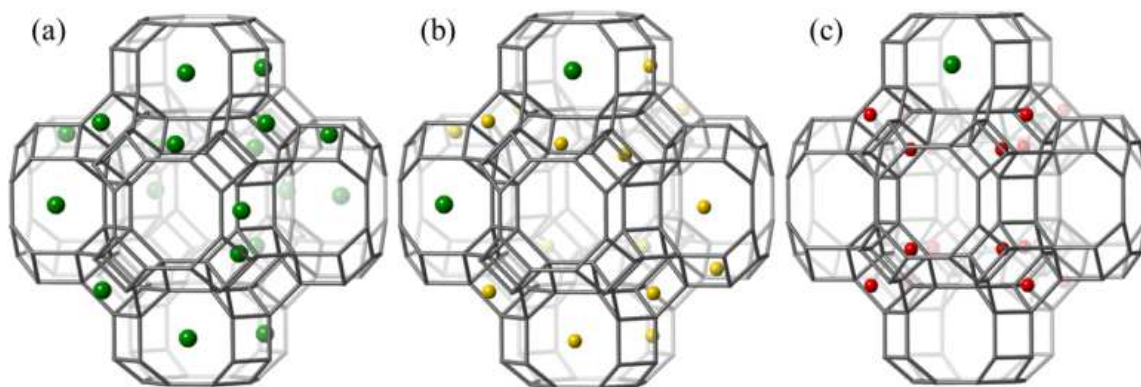


Figure 6.10. Possible cation distributions in one α -cage and surrounding *pau* cages of dehydrated (a) K-ZK-5 (larger, green spheres, K), (b) Na-ZK-5 (larger, green spheres, K; smaller, yellow spheres, Na) and (c) Li-ZK-5 (larger, green spheres, K; smaller, red spheres, Li), determined from Rietveld analysis of laboratory X-ray powder diffraction data collected at 298 K.

6.4. Carbon Dioxide Adsorption Study of K-, H-, Na- and Li-ZK-5

To examine the properties of the ZK-5 structure for adsorption, CO₂ isotherms were collected at 298 K on the K-, H-, Na- and Li-forms of ZK-5 and they are presented in Figure 6.11. All isotherms are fully reversible. The shape of the CO₂ isotherms corresponds to Type I behaviour, characteristic for adsorbents having a microporous structure. These isotherms for cationic forms of ZK-5 indicate physisorption with strong interactions between CO₂ molecules and the ZK-5 structure. The sequence of CO₂ uptake at 298 K on this materials is of the order H-ZK-5 < K-ZK-5 < Na-ZK-5 < Li-ZK-5.

All ZK-5 materials have permanent porosity for N₂ (see Figure 6.7b) and for CO₂ adsorption isotherms no hysteresis was observed. The framework structure of ZK-5 contains α -cages which are linked via larger *pau* cages which enable easy gas penetration into the ZK-5 structure. H-ZK-5, similar to H-chabazite, shows the lowest CO₂ uptake at 298 K and 0.1 bar, 0.6 mmol g⁻¹. This uptake increases to 2 mmol g⁻¹ by 0.9 bar. The highest uptake at 0.1 bar and 298 K was obtained for the Li-ZK-5, 4.7 mmol g⁻¹, comparable to values reported for its polytype chabazite.^{11,12} K- and Na-ZK-5 also show high uptakes at 0.1 bar and 298 K, 2.8 mmol g⁻¹ and 4.2 mmol g⁻¹, respectively. In K-ZK-5 and Na-ZK-5 the K⁺ and Na⁺ cations occupy sites either within S8R sites in the *pau* cages, where they do not block access between α -cages, or in S6R

sites within the α -cages. Therefore, all Na^+ and K^+ cations are accessible and the uptake at low CO_2 pressure is higher for the cations with the higher charge density. In Li-ZK-5 most of the Li^+ cations occupy S6R sites. More detailed adsorption data on cationic forms of ZK-5 ($\text{Si}/\text{Al} = 4.7$) published very recently confirm the levels of CO_2 uptake described here.⁶ CO_2 adsorption isotherms are fully reversible for all ZK-5 samples, an observation that becomes particularly noteworthy in comparison to observation on Rho made in the next chapter.

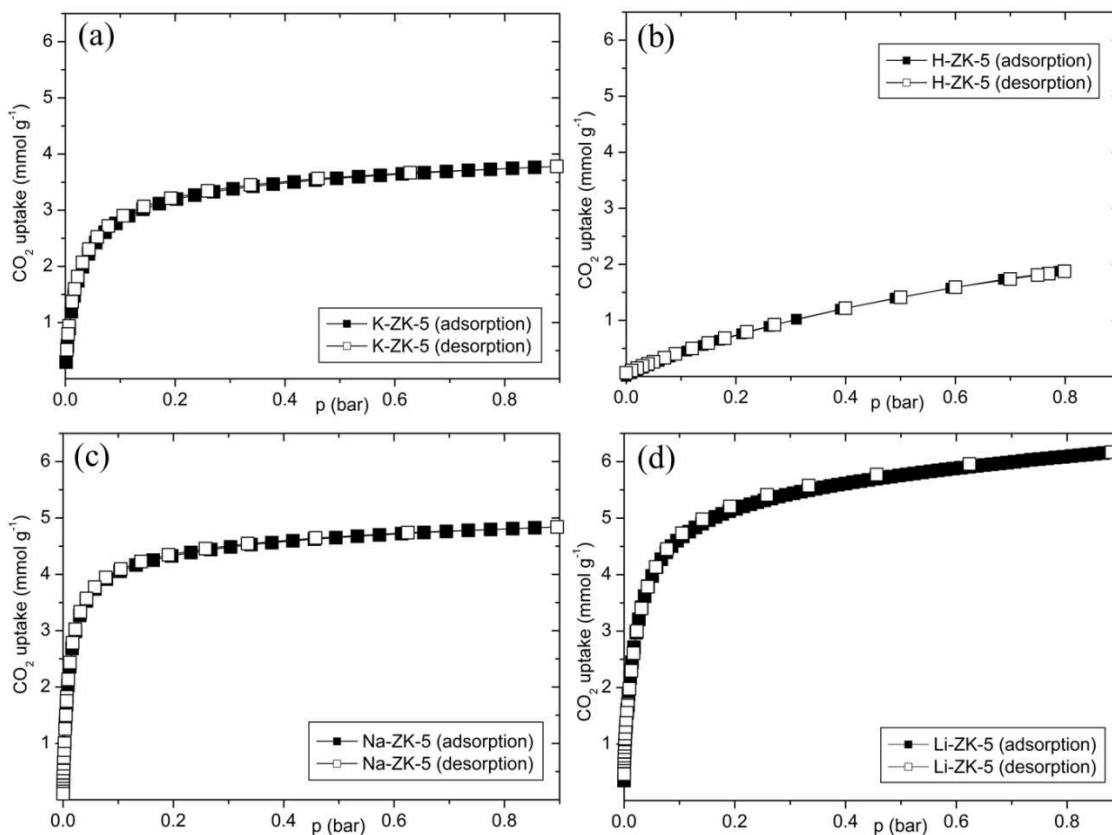


Figure 6.11. CO_2 sorption isotherms at 298 K of (a) K-ZK-5, (b) H-ZK-5, (c) Na-ZK-5 and (d) Li-ZK-5.

The uptakes on the K-, Na- and Li-forms of ZK-5 are high at full CO_2 pressure range, but the selectivity to CO_2 over small hydrocarbons is low. Ethane adsorption at 298 K on K-ZK-5 and Na-ZK-5 (Figure 6.12) shows that both are adsorbed in appreciable amounts. Clearly, Na^+ and K^+ cations do not block ethane uptake. The uptake on K-ZK-5 is lower than on Na-ZK-5 due to the size of K^+ cations.

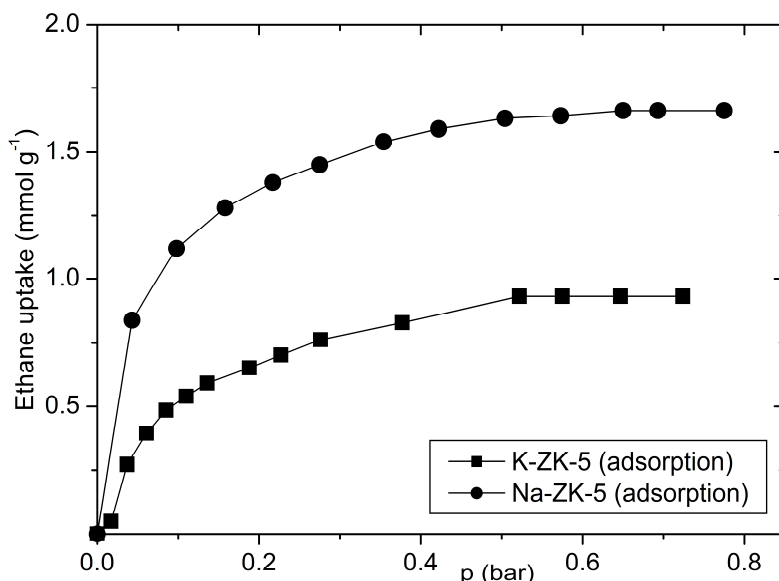


Figure 6.12. Ethane adsorption on K-ZK-5 and Na-ZK-5 at 298 K.

6.5. Comparison of ZK-5 (KFI) with SAPO STA-14 (KFI)

Comparison of chemico-physical and adsorption properties of ZK-5 with SAPO STA-14 was conducted. SAPO STA-14 has the same structure type, KFI, as the zeolite ZK-5 (see Figure 6.1b) and it was first synthesised by the St Andrews group via a co-templating approach.¹³ The synthesis of SAPO STA-14 involves the combined use of the azaoxacryptand-4,7,13,16,21,24-hexaoxa-1,10-diazabicyclo[8.8.8]-hexacosane (K222) and tetraethylamine cation (TEA^+) to template its large α -cages and small *pau* cages, respectively. SAPO STA-14 is of interest because it is stable to template removal, giving a solid with a pore volume of *ca.* $0.30 \text{ cm}^3 \text{ g}^{-1}$.¹⁴ Additionally, SAPO Na-STA-14 was compared with Na-ZK-5. The SAPO STA-14 for this study was prepared by hydrothermal synthesis and ion exchanged as described in chapter 4. More general information about SAPO materials can be found in chapter 1. For convenience, from now on SAPO STA-14 will be referred simply STA-14 (H-STA-14 for as-prepared form and Na-STA-14 for ion exchanged form).

PXRD was used to identify the crystallinity of the as-prepared hydrated H-STA-14 and to investigate the changes of zeolite structure caused by removing the template and the ion exchange with sodium. The PXRD pattern of the as-prepared hydrated H-STA-14 sample shows well-resolved and sharp diffraction peaks in the region of $2\theta = 5.0\text{--}50.0^\circ$ (Figure 6.13). The H-STA-14 reflections of the as-prepared hydrated

sample are associated with cubic $Pn\bar{3}n$ symmetry with the unit cell parameter $a = 18.7340(1) \text{ \AA}$.

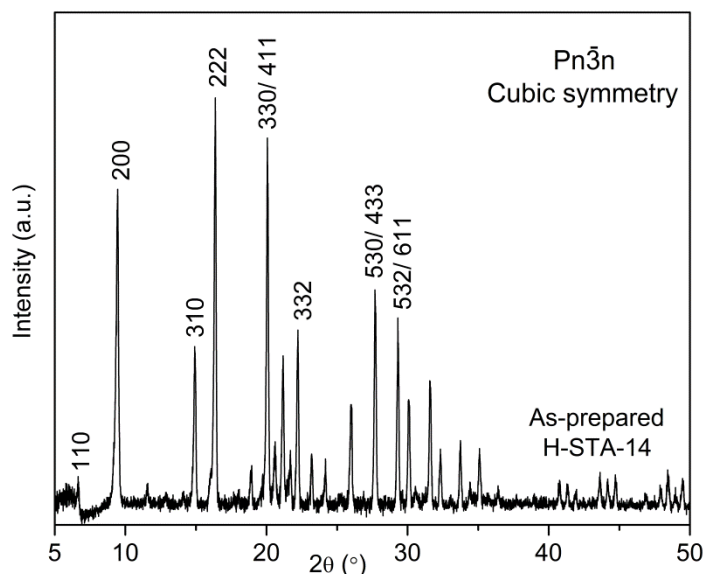


Figure 6.13. PXRD pattern of as prepared H-STA-14 indexed according to the cubic $Pn\bar{3}n$ symmetry.

The most effective temperature for template removal for H-STA-14 was determined by TGA (Figure 6.14a). The first weight loss, *ca.* 4 wt % between 300 K and 500 K, is attributed to desorption of physisorbed water molecules. The second weight loss, *ca.* 15 wt% between 550 K and 750 K, is caused by the decomposition of the azaoxacryptand 4,7,13,16,21,24-hexaoxa-1,10-diazabicyclo-[8.8.8]-hexacosane (K222) template from large α -cages. The third weight loss, *ca.* 6 wt% in the range of 750–900 K, is due to decomposition of TEA^+ from small *pau* cages. The TGA suggests that the lowest temperature at which the surfactants are completely removed is 923 K. The H-STA-14 was found to be stable to template removal without loss of crystallinity (Figure 6.14b).

Protons in heated H-STA-14 were exchanged for Na^+ cations. The degree of ion exchange was measured using X-ray energy dispersive spectroscopy (EDX). The EDX confirms that H^+ cations were exchanged for Na^+ cations in STA-14. No other elements apart from the framework O, Si, Al, P and extra-framework Na^+ cations are visible in the EDX spectra (Figure 6.15). The EDX analysis of the STA-14 (after template removal) gives an estimated unit cell composition of $\text{H}_{12}\text{Si}_{12}\text{Al}_{36}\text{P}_{48}\text{O}_{192}$ and $\text{Na}_{12}\text{Si}_{12}\text{Al}_{36}\text{P}_{48}\text{O}_{192}$ for the ion exchanged sample (Table 6.3). EDX analysis gives Si/Al

ratios of 0.30 for both samples. The formula for the derivation of the unit cell composition is given in chapter 4.

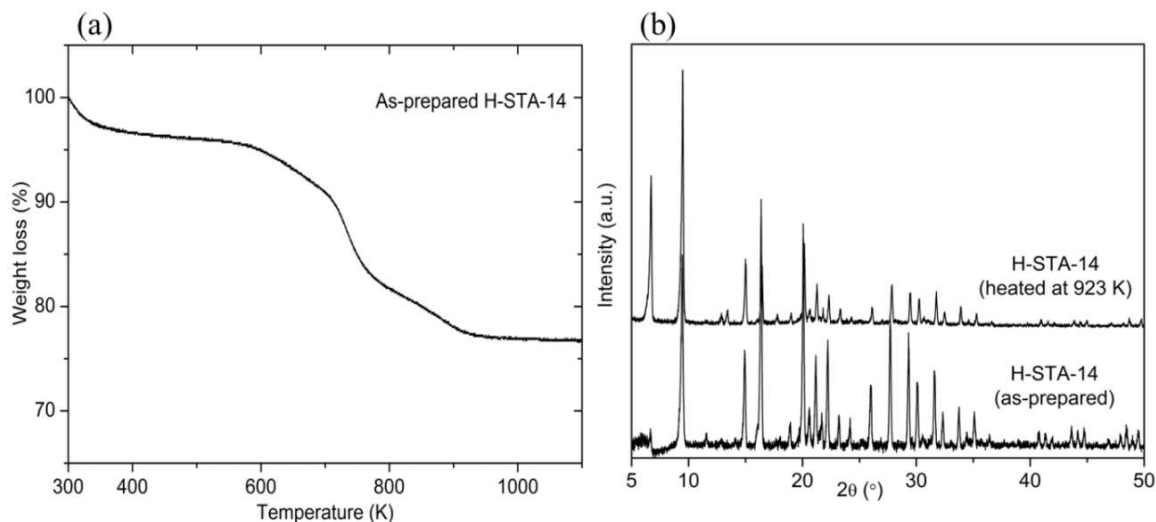


Figure 6.14. (a) TGA curve of as-prepared H-STA-14 and (b) PXRD patterns of as-prepared and heated H-STA-14. The (offset) patterns have been collected at 298 K using the same operating conditions.

The crystallinity of ion exchanged Na-STA-14 samples was measured using PXRD and its porosity was monitored by N₂ adsorption at 77 K. The PXRD pattern of Na-STA-14 compared to heated H-STA-14 (Figure 6.16a) reveal that the ion exchanged sample suffers loss in crystallinity. This loss in crystallinity and introduction of Na⁺ cations to the structure of Na-STA-14 upon ion exchange results in a decrease in N₂ uptake: 2 mmol g⁻¹ for this sample against a value of 8.5 mmol g⁻¹ for H-STA-14 at p/p₀ = 0.9 (Figure 6.16b). It may be concluded that STA-14 is most stable and crystalline in the H-form. Similar observation has been previously reported for SAPO-34 which showed a significant crystallinity loss after conventional ion exchange by copper with a dramatic decrease of N₂ uptake.¹⁵

Table 6.3. EDX analysis of STA-14 before and after ion exchange.

Sample	Atomic %					Unit cell formula of dehydrated samples
	O	P	Si	Al	Na	
H-STA-14	72 ± 1	11 ± 1	3 ± 0.5	14 ± 1	N.D.	H ₁₂ Si ₁₂ Al ₄₈ P ₃₆ O ₁₉₂
Na-STA-14	69 ± 1	11 ± 1	3 ± 0.5	14 ± 1	3 ± 0.5	Na ₁₂ Si ₁₂ Al ₄₈ P ₃₆ O ₁₉₂

Values for oxygen are semi-quantitative

N.D. – not detected

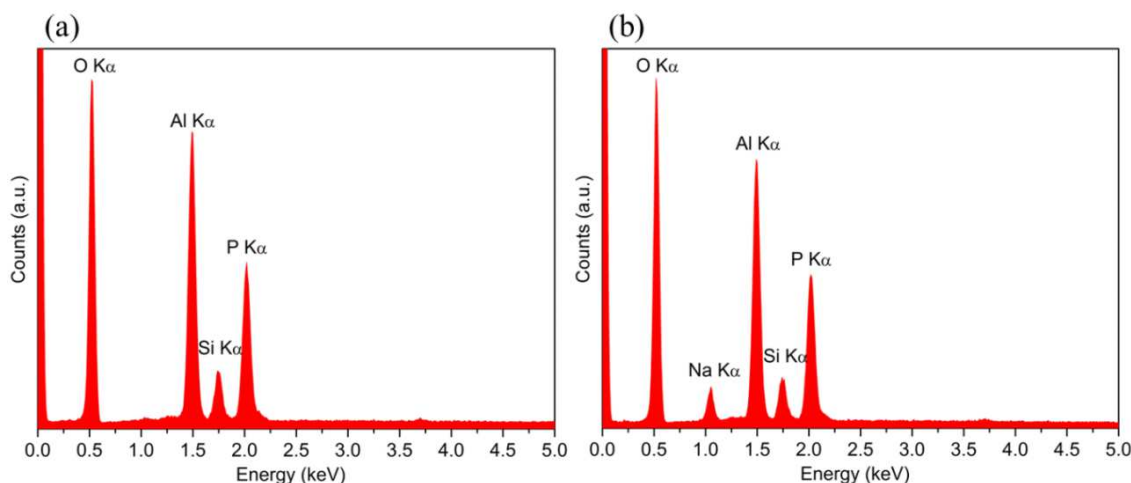


Figure 6.15. EDX spectra of (a) heated H-STA-14 and (b) Na-STA-14.

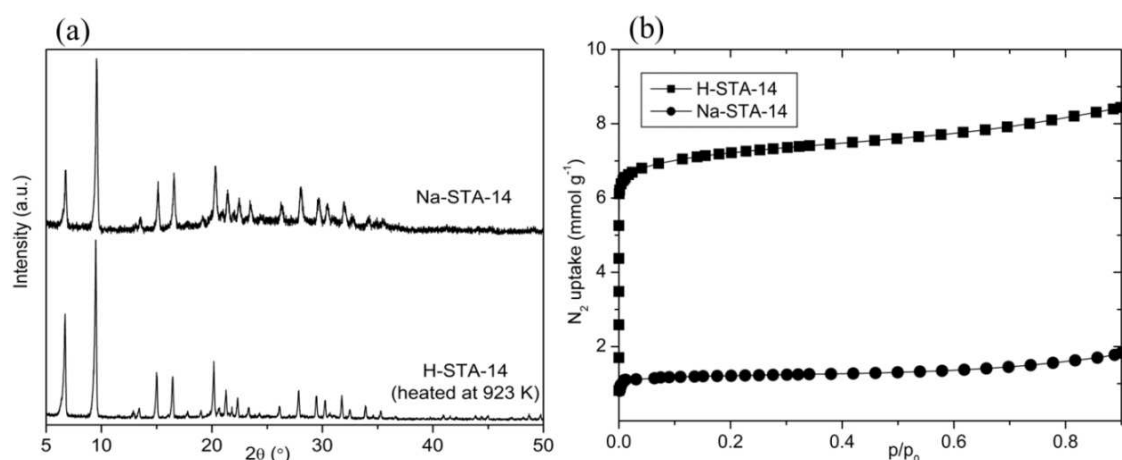


Figure 6.16. (a) PXRD patterns and (b) N_2 adsorption isotherms of heated H-STA-14, and ion exchanged Na-STA-14. The (offset) patterns have been collected at 298 K using the same operating conditions.

CO_2 isotherms were collected at 298 K for heated H-STA-14 and Na-STA-14 (Figure 6.17). The CO_2 isotherms of H-STA-14 and Na-STA-14 correspond to Type I behaviour and they show that H-STA-14 and Na-STA-14 adsorb 2.7 mmol g^{-1} and 2.5 mmol g^{-1} of CO_2 at 0.9 bar and 0.75 mmol g^{-1} and 1.0 mmol g^{-1} at 0.1 bar, respectively. The CO_2 uptake on H-STA-14 is slightly higher than uptake on H-ZK-5 (2.0 mmol g^{-1} at 0.9 bar), which may be due to the higher crystallinity of as-prepared H-STA-14 and presence of (unstable) H-chabazite impurity in H-ZK-5. The CO_2 uptake on Na-STA-14 is lower than on Na-ZK-5 (4.4 mmol g^{-1} at 0.9 bar), due to the lower number of Na^+ cations in Na-STA-14 structure and the loss of crystallinity during ion exchange.

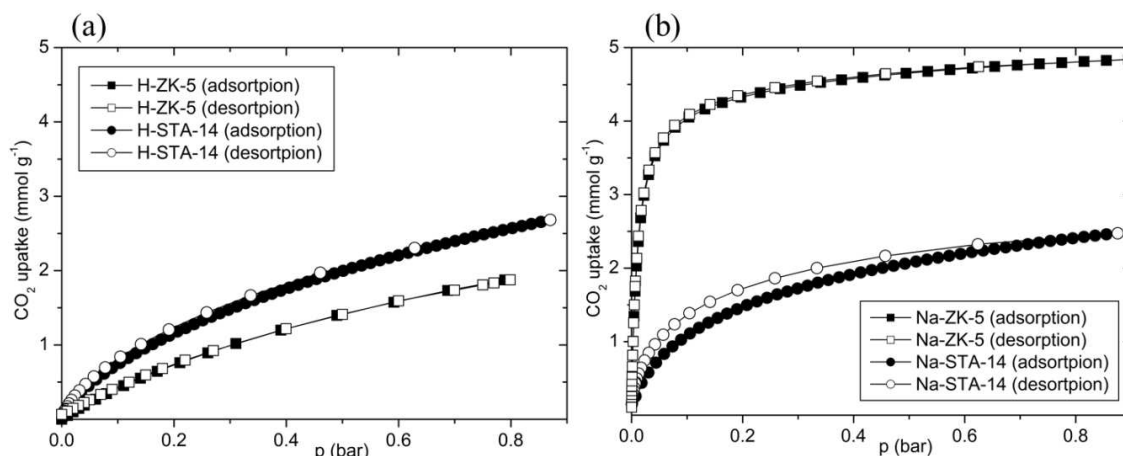


Figure 6.17. CO₂ sorption isotherms at 298 K of (a) heated H-ZK-5 and H-ZK-5, and (b) Na-ZK-5 and Na-ZK-5.

6.6. Conclusions

Cation sites were found for K-ZK-5 and Li-ZK-5 in S6Rs and S8Rs and for Na-ZK-5 in S8Rs (plus residual K⁺ in S6Rs). None of the cations occupy the entrances to α - and pau cages. The highest CO₂ uptake at 298 K and 0.1 bar in this study was obtained for Li-ZK-5 (4.7 mmol g⁻¹). K- and Na-forms also show high uptakes at these conditions, 2.8 mmol g⁻¹ and 4.2 mmol g⁻¹, respectively. ZK-5 does not show flexibility upon dehydration and its CO₂ isotherms are fully reversible, so it serves as a good example of a zeolite with a rigid, highly porous small pore structure. None of these materials studied are selective for CO₂ over small hydrocarbons, because of the absence of cations in the entrances to the cages. For comparison SAPO STA-14 (KFI) was prepared. H-ZK-5 acts similarly to H-ZK-5. Both of them show high nitrogen uptake at $p/p_0 = 0.9$ and 77 K (*ca.* 8 mmol g⁻¹) but low CO₂ at 0.1 bar and 298 K (*ca.* 0.8 mmol g⁻¹). Ion exchange of H⁺ in STA-14 with Na⁺ results in loss of crystallinity and Na-ZK-5 showed much lower CO₂ uptake than Na-ZK-5.

References

1. Kerr G. T., *Science*, **1963**, *140*, 1412
2. Meier W. M. and Kokotailo G. T., *Z. Kristallogr.*, **1965**, *121*, 211
3. Shubaeva M. A. and Zhdanov S. P., *B. Acad. Sci. Ussr Ch+*, **1987**, *36*, 15-18
4. Chatelain T., Patarin J., Farré R., Pétigny O. and Schulz P., *Zeolites*, **1996**, *17*, 328-333

5. Lievens J. L., Verduijn J. P. and Mortier W. J., *Zeolites*, **1992**, *12*, 690-697
6. Liu Q. L., Pham T., Porosoff M. D. and Lobo R. F., *ChemSusChem*, **2012**, *5*, 2237-2242
7. Lozinska M. M., Mangano E., Mowat J. P. S., Shepherd A. M., Howe R. F., Thompson S. P., Parker J. E., Brandani S. and Wright P. A., *J. Am. Chem. Soc.*, **2012**, *134*, 17628-17642
8. Remy T., Peter S. A., Van Tendeloo L., Van der Perre S., Lorgouilloux Y., Kirschhock C. E. A., Baron G. V. and Denayer J. F. M., *Langmuir*, **2013**
9. Cartlidge S. and Meier W. M., *Zeolites*, **1984**, *4*, 218-225
10. Parise J. B., Shannon R. D., Prince E. and Cox D. E., *Z. Kristall.*, **1983**, *165*, 175-190
11. Ridha F. N. and Webley P. A., *Sep. Purif. Technol.*, **2009**, *67*, 336-343
12. Ridha F. N. and Webley P. A., *Micropor. Mesopor. Mat.*, **2010**, *132*, 22-30
13. Castro M., Garcia R., Warrender S. J., Slawin A. M. Z., Wright P. A., Cox P. A., Fecant A., Mellot-Draznieks C. and Bats N., *Chem. Commun.*, **2007**, *0*, 3470-3472
14. Castro M., Warrender S. J., Wright P. A., Apperley D. C., Belmabkhout Y., Pirngruber G., Min H. K., Park M. B. and Hong S. B., *J. Phys. Chem. C*, **2009**, *113*, 15731-15741
15. Frache A., Palella B. I., Cadoni M., Pirone R., Pastore H. O. and Marchese L., *Top. Catal.*, **2003**, *22*, 53-57

7. Zeolite Rho: Potential Material for Selective Gas Capture

7.1. Introduction

Zeolite Rho (topology type RHO) was first synthesised by Robson *et al.*¹ without using a template and with a Si/Al ratio of around 3.0. In 1995 Chatelain *et al.*² synthesised zeolite Rho with a Si/Al ratio as high as 4.5 by using 18-crown-6 ether as an organic template. The framework of zeolite Rho is composed of a body-centered cubic arrangement of α -cages linked via double eight-membered rings (D8Rs, Figure 7.1a).

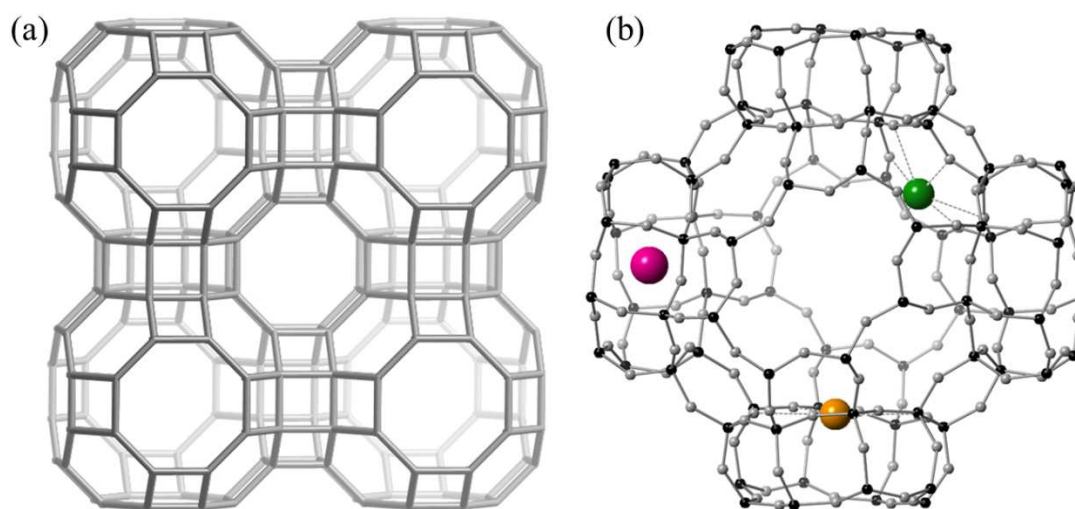


Figure 7.1. Framework structure of zeolite Rho in $Im\bar{3}m$ symmetry, showing an α -cage surrounded by six double 8-membered rings (D8Rs) that act as windows and (b) generalised structure of zeolite Rho in $I\bar{4}3m$ symmetry, showing the position of extra-framework cations in sites of: type I, double eight-membered ring, D8R site, purple spheres; type II, single eight-membered ring, S8R site, orange spheres; and type III, single six-membered ring, S6R site, green sphere.

It is well known that upon dehydration the Rho framework displays considerable flexibility.³⁻⁶ The hydrated forms of Rho adopt $Im\bar{3}m$ symmetry. Dehydrated H-Rho remains with $Im\bar{3}m$ symmetry whereas for all cation exchanged Rho materials dehydration resulted in transformation to the $I\bar{4}3m$ form (Figure 7.2) where the structure adjusts to coordinate cations better.

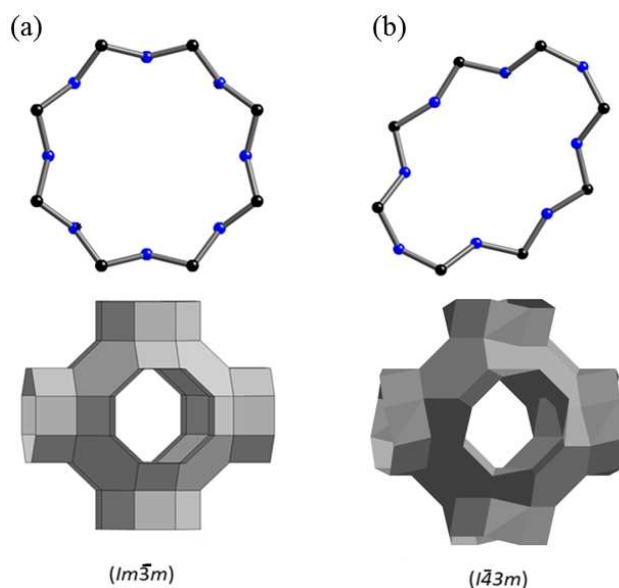


Figure 7.2. Shape of S8R and α -cage for cationic forms of Rho (a) before and (b) after dehydration.

In previous studies, cation positions in the zeolite Rho framework were located within the centre of the double eight-membered rings (D8R site, coordinates $(\frac{1}{2}, 0, 0)$ denoted as site I here), at a site close to the plane of the eight-membered rings (S8R site, coordinates $(x, 0, 0)$, $x \approx 0.4$, denoted as site II) or at a site close to six-membered rings in the α -cage (S6R site, coordinates, (x, x, x) , $x \approx 0.3$, denoted as site III), depending on cation size and charge (see Figure 7.1b and Table 7.1).^{3,4,7,8} It was found that the double eight-membered ring entrances to the Rho zeolite are preferential sites for K^+ , Ca^{2+} and NH_4^+ cations.^{3,4,7} Johnson *et al.*⁸ reported that in dehydrated Na,Cs-Rho the framework is distorted with Cs^+ cations occupying D8R and Na^+ cations in S8R sites. Lithium exchange of this material produces a more distorted framework which causes greater shrinkage of the unit cell and Li^+ cations are found in S6R sites. In zeolite Rho with high cation content residual Na^+ or Cs^+ cations also occupy S6R sites.

Table 7.1. Positions of extra-framework cations in dehydrated Rho ('+' indicates presence and '-' indicates absence of cations in a cationic site).

Sample	Site I (D8R)	Site II (S8R)	Site III (S6R)	Reference
Cs-Rho	+	-	+	⁸ and this work
Na-Rho	-	+	+	⁸ and this work
NH_4 -Rho	+	+	-	⁹ and this work
Li-Rho	-	-	+	⁸ and this work
K-Rho	+	+	-	⁷ and this work
Ca-Rho	+	-	-	^{3,4} and this work

Together with the variability in cation siting this offers an opportunity to introduce a high degree of selectivity by controlling the type, size, occupancy and position of extra-framework cations. Zeolite Rho has previously been investigated for CO₂/N₂, CO₂/CH₄ and O₂/N₂ separations.¹⁰⁻¹² Araki *et al.*,¹⁰ in their work, compared the single component adsorption of CO₂ and N₂ at room temperature on Na,Cs-Rho, Na-X and SAPO-34. Zeolite Na,Cs-Rho showed the highest ratio of CO₂ adsorbed to N₂ adsorbed, 54.1, whereas for zeolite Na-X it was only 15.7 and for SAPO-34 13.8. They suggested that the high CO₂/N₂ adsorption ratio is the result of the differences in pore size, where Na-X and SAPO-34 possess pore diameters bigger than the kinetic diameter of N₂ and in zeolite Na,Cs-Rho the pore size is big enough to admit CO₂ molecules, but does not admit N₂ molecules. In this study we will show that it is the position in the Rho framework of the extra-framework cations and their mobility rather than pore size that is very important for selective adsorption of small gas molecules. Very recently, work on zeolite Na,Cs-Rho by Palomino *et al.*¹¹ showed very high CO₂/CH₄ selectivity at less than 1 bar and also non-Type I adsorption behaviour for CO₂ above 1 bar, interpreted in terms of the structural flexibility of the Rho structure. *In situ* X-ray diffraction showed that at pressures of around 1 bar the framework structure undergoes the transformation from $I\bar{4}3m$ to $Im\bar{3}m$ that has been previously observed for zeolite Rho upon hydration, in which both the pore volume and the window size increases and the selectivity decreases. Elsewhere zeolite Li-Rho was proposed as an oxygen selective adsorbent in the separation of oxygen and nitrogen in a pressure swing adsorption (PSA) process due to the significant distortion of the framework upon dehydration that results in a reduced size of the windows.¹² Only a very general explanation was suggested for the complex behaviour of zeolite Rho, which is expected to result in part from the extra-framework cation distribution and strong cation-dependent structural flexibility of its structure.^{4,12-14}

In this study, zeolite Rho has been chosen as a potential sorbent for CO₂ capture because of its chemical, thermal and hydrothermal stability, high pore volume (0.36 cm³g⁻¹, which is the highest of small pore materials, see later), moderately polar character (Si/Al \approx 4) and readily exchangeable extra-framework cations.

Measurements of CO₂ adsorption on zeolite H-Rho and Rho samples fully exchanged with a range of cations (NH₄⁺, Na⁺, Li⁺, K⁺, Cs⁺, Ca²⁺) prepared by exhaustive ion

exchange are presented. The presence of cations (other than protons) is observed to prevent the uptake of N₂ at 77 K but allow CO₂ uptake at 298 K. CO₂ adsorption isotherms reveal a range of behaviour, including strong deviation from Type I adsorption and hysteresis. The CO₂ adsorption on zeolite Rho is found to be a complex function of cation type and loading. According to these measurements, and also because sodium is inexpensive, Na-Rho possesses the most potential among Rho zeolites as an adsorbent for the selective uptake of CO₂ at reasonable rates and with accessible uptake capacity at low partial pressures and ambient temperatures. Consequently, the mechanism of CO₂ adsorption and desorption on Na-Rho under conditions relevant to carbon capture from flue gases is studied in greater depth by a combination of *in situ* powder synchrotron PXRD and IR spectroscopy. Furthermore, H-Rho was for the first time ultra-stabilised and nitrated in this study and its subsequent performance in CO₂ adsorption has been measured.

Zeolite Rho data were also compared with similar measurements performed on a silicoaluminophosphate material, SAPO(RHO). SAPO(RHO) has the same topology type, RHO, as the zeolite Rho where structure is built of α -cages linked via double eight-membered rings (see Figure 7.1a). The general properties of SAPO materials are described in chapter 1. SAPO(RHO) is of particular interest because it is a solid with a high pore volume of around 0.36 cm³g⁻¹, similar to zeolite Rho.

Adsorption behaviour of all Rho and SAPO(RHO) materials has been discussed by reference to the crystal structures of the dehydrated forms. Additionally, high pressure adsorption of CO₂ and CH₄ and theoretical selectivity of CO₂/CH₄ was measured for Na-, Cs-, K- and Ca-Rho and related to structural changes for Cs-Rho.

7.2. Characterisation of Different Cationic Forms of Rho

Na,Cs-Rho was prepared by hydrothermal synthesis, calcined and ion exchanged as described in chapter 4. All Rho forms were characterised by a combination of physico-chemical techniques.

PXRD was used to identify the crystallinity and the phase purity of Na,Cs-, NH₄-, H-, Na-, Cs-, Li-, K- and Ca-Rho. The PXRD pattern of Na,Cs-Rho (containing 18-crown-6, Figure 7.3a) shows well-resolved and sharp diffraction peaks in the region of 5.0–

50.0° 2 θ . No reflections other than those due to the Na,Cs-Rho topology are visible and the sample exhibits high crystallinity. All of the reflections are associated with $Im\bar{3}m$ cubic symmetry with the unit cell parameters $a = 15.2252(1)$ Å. The PXRD pattern of Na,Cs-Rho was compared with PXRD patterns of NH₄-, H-, Na-, Cs-, Li-, K- and Ca-Rho in Figure 7.3b. No changes in crystallinity after ion exchange are visible.

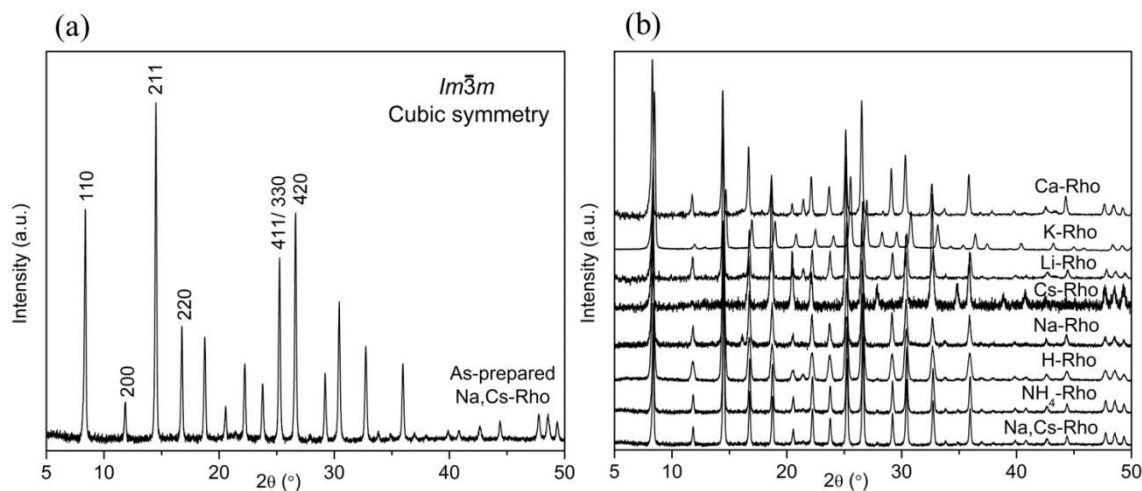


Figure 7.3. PXRD patterns of (a) Na,Cs-Rho indexed according to the cubic symmetry and (b) the comparison of Na,Cs-Rho with NH₄-, H-, Na-, Cs-, Li-, K- and Ca-Rho. The (offset) patterns have been collected at 298 K using the same operating conditions.

Morphology of Na,Cs- and Na-Rho samples was investigated by SEM analysis. The SEM micrograph of Na,Cs-Rho (Figure 7.4a) indicates that the synthesis gives 1–2 μm particles built up from smaller crystallites around 0.1 μm in size. The ion exchange does not modify the shape and size of the crystals, as confirmed by the SEM micrograph of ion exchanged Na-Rho (Figure 7.4b). No amorphous phase was observed for either sample.

Unit cell compositions of all Rho samples were estimated from a combination of EDX analysis and MAS NMR spectroscopy. From the ²⁹Si MAS NMR spectra of Rho three sharp and strong peaks can be attributed to: Si(2Al) (–97 ppm), Si(1Al) (–103 ppm) and Si(0Al) (–109 ppm) (Figure 7.5a). ²⁷Al MAS NMR spectra reveal the tetraordinated framework Al at 57 ppm (Figure 7.5b). No extra-framework Al is visible which confirms that the exhaustive cation exchange at high temperature (353 K) does not cause changes to the zeolite framework.

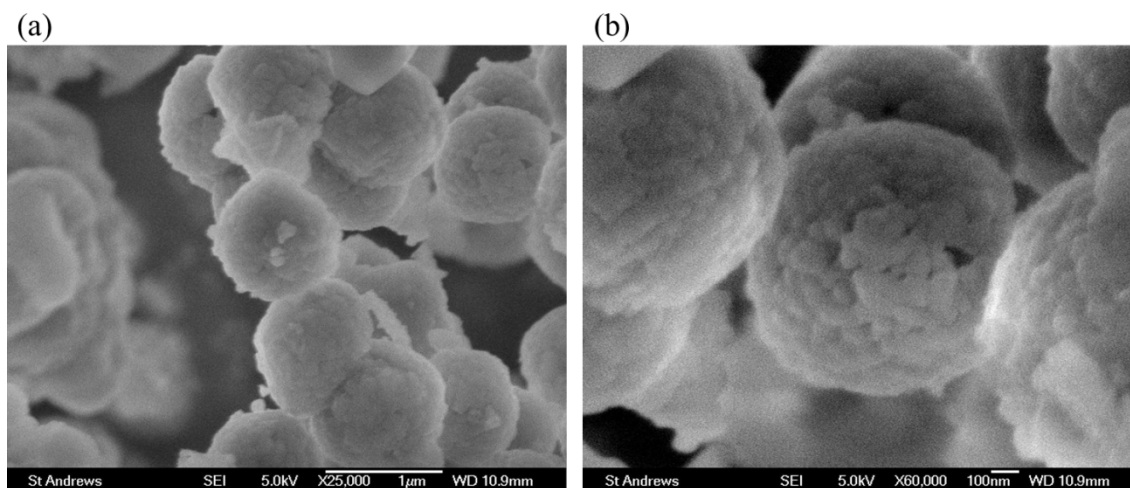


Figure 7.4. SEM micrographs of (a) as-prepared Na,Cs-Rho and (b) ion exchanged Na-Rho.

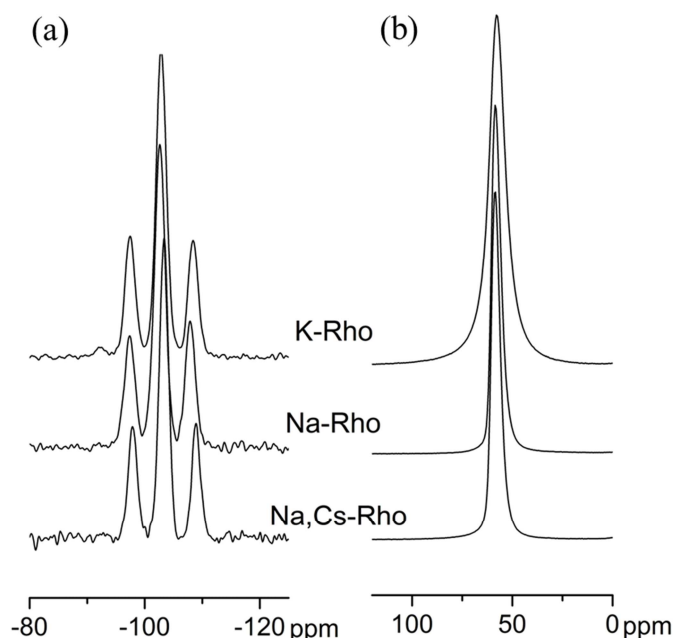


Figure 7.5. (a) ^{29}Si MAS NMR and (b) ^{27}Al MAS NMR spectra of as-prepared Na,Cs-Rho and ion exchanged Na- and K-Rho.

EDX spectroscopy confirms that the ion exchange of Na^+ and Cs^+ for NH_4^+ , Na^+ , Cs^+ , Li^+ , K^+ and Ca^{2+} in Rho occurs (Table 7.1). No other elements than the framework O, Si and Al, and extra-framework cations are visible in the EDX spectra presented in Figure 7.6. The Si/Al ratio measured in the as-prepared zeolite Rho was obtained by EDX as 4.0 and by deconvolution of the ^{29}Si MAS NMR spectrum as 3.9, using equation 4.2 (see the appendix). The NMR value was taken as the more accurate, and

compositions calculated accordingly for all Rho materials. Full details of the composition of cation exchanged zeolites are given in Table 7.2. The formula for the derivation of the unit cell composition is given in chapter 4.

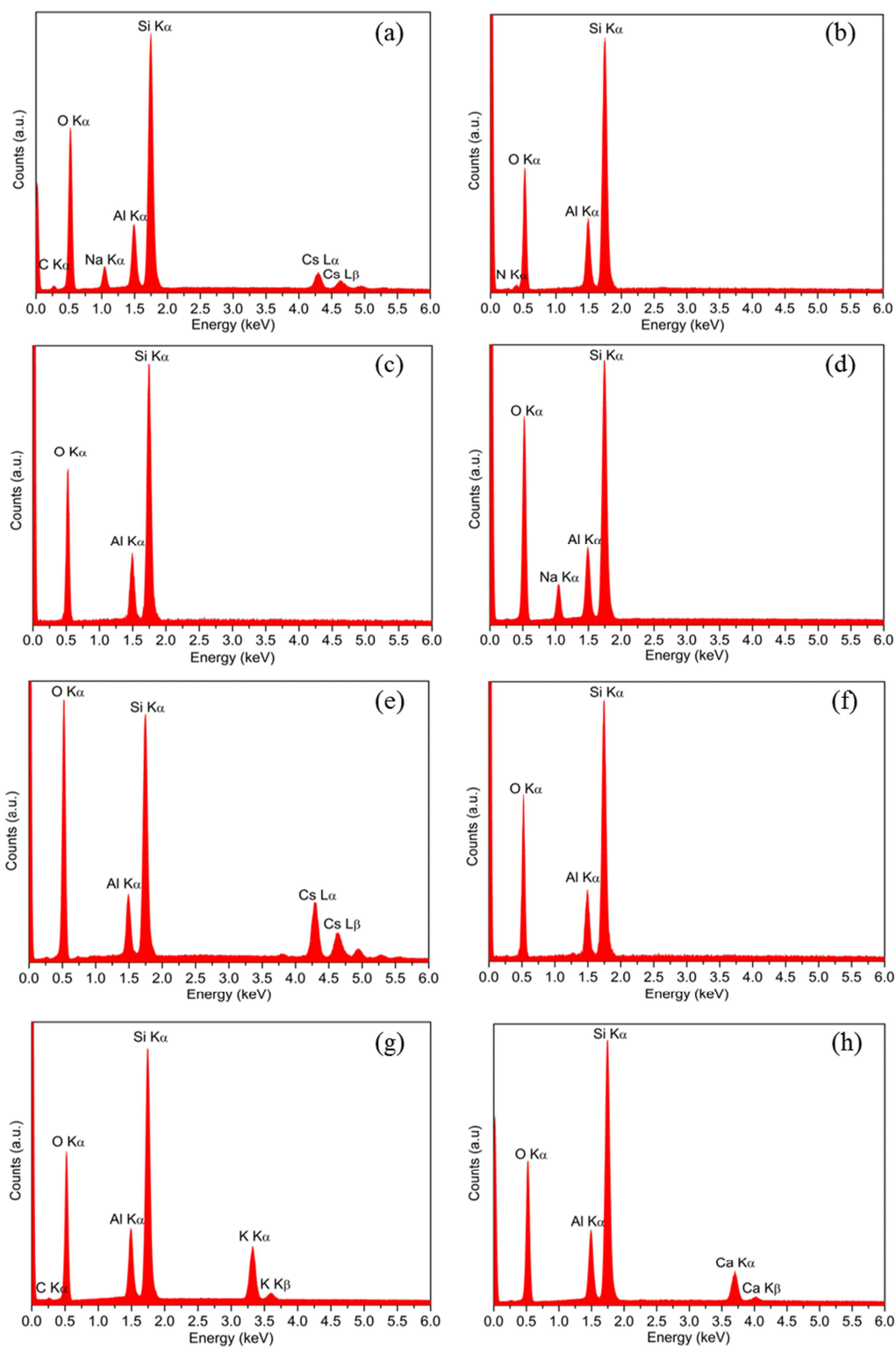


Figure 7.6. EDX spectra of (a) Na,Cs-Rho, (b) NH_4 -Rho, (c) H-Rho, (d) Na-Rho, (e) Cs-Rho, (f) Li-Rho, (g) K-Rho and (h) Ca-Rho.

Table 7.2. EDX analysis of zeolite Rho before and after ion exchange.

Sample	Atomic %								Unit cell formula of dehydrated sample
	O	Si	Al	Na	Cs	K	Ca	N	
Na,Cs-Rho	68 ± 1	21 ± 1	5 ± 1	4 ± 0.5	2 ± 0.5	N.D.	N.D.	N.D.	Na _{6,8} Cs _{3,0} Al _{9,8} Si _{38,2} O ₉₆
NH ₄ -Rho	64 ± 1	24 ± 1	6 ± 1	N.D.	N.D.	N.D.	N.D.	6 ± 1	(NH ₄) _{9,8} Al _{9,8} Si _{38,2} O ₉₆
H-Rho	68 ± 1	26 ± 1	6 ± 1	N.D.	N.D.	N.D.	N.D.	N.D.	(AlO _x H _y) _{0,6} H _{9,3-δ} Al _{9,3} Si _{38,7} O ₉₆
Na-Rho	68 ± 1	22 ± 1	5 ± 1	5 ± 1	N.D.	N.D.	N.D.	N.D.	Na _{9,8} Al _{9,8} Si _{38,2} O ₉₆
Cs-Rho	67 ± 1	20 ± 1	5 ± 1	N.D.	7 ± 1	N.D.	N.D.	N.D.	Cs _{9,8} Al _{9,8} Si _{38,2} O ₉₆
Li-Rho	73 ± 1	21 ± 1	5 ± 1	N.D.	N.D.	N.D.	N.D.	N.D.	Li _{9,8} Al _{9,8} Si _{38,2} O ₉₆
K-Rho	67 ± 1	21 ± 1	5 ± 1	N.D.	N.D.	6 ± 1	N.D.	N.D.	K _{9,8} Al _{9,8} Si _{38,2} O ₉₆
Ca-Rho	72 ± 1	20 ± 1	5 ± 1	N.D.	N.D.	N.D.	3 ± 0.5	N.D.	Ca _{4,9} Al _{9,8} Si _{38,2} O ₉₆

Values for oxygen are semi-quantitative
N.D. – not detected

From TGA, all Rho materials show a dehydration step, corresponding to *ca.* 15% weight loss, which may be explained as a consequence of the removal of physisorbed water molecules between 300 K and 400 K. Additionally, the TGA curves of Na,Cs-, NH₄-, Li- and Ca-Rho show additional weight loss steps. As prepared Na,Cs-Rho contains template (18-crown-6) in the pores which has to be removed for ion exchange and to make the material porous. The second weight loss is *ca.* 7 % between 400 K and 800 K and it is due to the decomposition of the template. The TGA of Na,Cs-Rho suggests that the lowest temperature at which the template is completely removed is 800 K, therefore Na,Cs-Rho was calcined at 823 K before ion exchange. The second weight loss at 400–800 K for NH₄-Rho, *ca.* 5%, is due to ammonia desorption. Li⁺ and Ca²⁺ cations bind water molecules very strongly. The second steps of *ca.* 5% weight loss for Li-Rho and *ca.* 3% for Ca-Rho from 400 K to 550 K are due to the chemisorbed water desorption.

Adsorption isotherms of N₂ collected at 77 K on Na,Cs-, NH₄-, H-, Na-, Cs-, Li-, K- and Ca-Rho are presented in Figure 7.7b. The N₂ adsorption isotherm of H-Rho shows Type I behaviour, characteristic for adsorbents having a microporous structure. There is no significant N₂ adsorption on cationic samples.

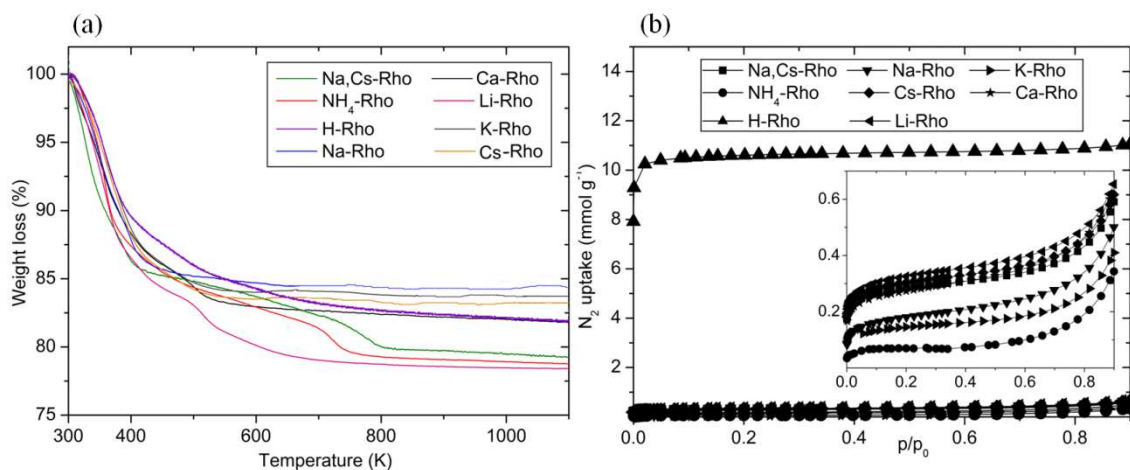


Figure 7.7. (a) TGA curves and (b) N₂ adsorption isotherms at 77 K of Na,Cs-, NH₄-, H-, Na-, Cs-, Li-, K- and Ca-Rho.

7.3. Functionalisation of H-Rho by Dealumination and Nitridation

Attempts were made to modify the framework composition of zeolite H-Rho by dealumination and nitridation and the effect of each of these processes on CO₂ adsorption was measured. During dealumination the hydrothermal treatment of the NH₄-Rho results in migration of tetrahedrally-coordinated framework Al to extra-framework positions and recrystallisation of the framework with a higher Si/Al ratio. Extra-framework aluminium sites may act as a new CO₂ adsorption sites and they may enhance CO₂ uptake, while a higher Si/Al ratio would make zeolites more hydrophilic which may be an advantage in terms of CO₂ adsorption from flue gas. Nitridation involves the replacement of the oxygen atoms with nitrogen atoms in the zeolitic structure. It is a simple and fast way of functionalising porous materials. Nitridation involves the reaction of ammonia with the zeolite framework and may result in new sites such as: NH₄⁺, NH₃ adsorbed on Lewis acid sites, -NH₂, >NH and >N-. The mechanism for the dealumination and nitridation of zeolites is described in more detail in chapters 1 and 4. In this study, dealumination and nitridation were of interest for improving CO₂ uptake of zeolite Rho at 0.1 bar and 298 K.

Dealumination process was conducted according to a published procedure¹⁵ and it is described in chapter 4. The dealuminated zeolite samples were characterised using PXRD, N₂ adsorption, ²⁹Si MAS NMR and ²⁷Al MAS NMR, EDX spectroscopy, TGA and CO₂ adsorption.

PXRD patterns were recorded before and after the dealumination treatment using different water flow rates in order to determine the effect of the treatment on the Rho structure (Figure 7.8). The steamed samples obtained in both sets remain very crystalline. For both series of samples the peaks shift slightly to higher 2θ values indicating smaller d-spacings and reduced unit cell parameters as a result of dealumination. For the first set of steaming samples (ST1), where the water flow rate was lower (1.5 mL h^{-1}), the PXRD patterns of all the dealuminated samples are identical. For second set of steaming samples (ST2), where the water flow rate was higher (2 mL h^{-1}), the X-ray intensities of Rho zeolite decrease with increasing steaming temperature which may indicate larger structural changes than for ST1 samples.

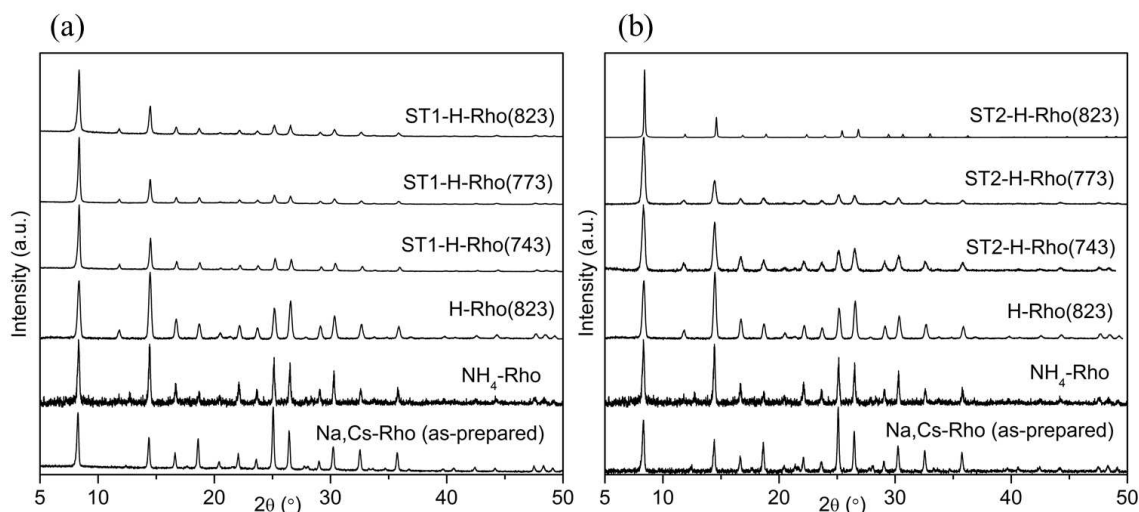


Figure 7.8. PXRD patterns of Na,Cs-Rho, NH_4 -Rho, H-Rho with (a) ST1 (first steamed set of samples with low water flow) and (b) ST2 (second steamed set of samples with high water flow). The (offset) patterns have been collected at 298 K using the same operating conditions.

Si/Al ratio of samples before and after dealumination was measured using EDX analysis and ^{29}Si MAS NMR spectroscopy (Table 7.3). According to the EDX analysis the bulk Si/Al ratio was not affected, because the Al atoms that are taken out of the framework remain in the zeolite in the form of extra-framework aluminium species. However, the framework Si/Al ratio can be measured by ^{29}Si MAS NMR and it can be seen that the frameworks are dealuminated. The framework Si/Al ratio increases from 4.15 to 7.08 for ST1 and from 4.15 to 9.41 for ST2, indicating that the higher water flow rate causes more effective dealumination. The Si/Al ratio was measured by deconvolution of the

^{29}Si MAS NMR spectra (see the appendix) and calculated using equation 4.2. There is only a small change in the framework Si/Al ratio for both sets with increasing steaming temperature which may suggest that a steaming temperature higher than 743 K does not have a major impact on the removal of Al from the Rho framework. The only effect of higher steaming temperatures was to reduce the pore volume; this can be observed later in Figure 7.9.

Table 7.3. Si/Al ratio for Na,Cs-Rho, H-Rho and steamed samples measured with EDX analysis and ^{29}Si MAS NMR (ST1 – first steamed set of samples at low water flow and ST2 – second steamed set of samples at high water flow).

Sample	Si/Al EDX	Si/Al ^{29}Si MAS NMR (ST1)	Si/Al ^{29}Si MAS NMR (ST2)
Na,Cs-Rho	4.07	3.90	3.90
H-Rho(823)	4.00	4.15	4.15
ST-H-Rho(743)	3.95	6.33	9.39
ST-H-Rho(773)	3.94	6.63	9.40
ST-H-Rho(823)	3.93	7.08	9.41

Steam treatment of the zeolite leads to a lower N_2 uptakes, but there is no change in the appearance of the isotherms which show the Type I behaviour characteristic of microporous materials. ST1 samples do not show any changes in pore volume with increasing steaming temperature. ST1-H-Rho(773) and ST1-H-Rho(823) (Figure 7.9a) show better porosity to nitrogen than ST2-H-Rho(773) and ST2-H-Rho(823) (Figure 7.9b). This may be due to the presence of less extra-framework aluminium in ST1 samples which results in less pore blockage. Sample ST2-H-Rho(743) retains a very high porosity to nitrogen after steaming. One possible explanation is that this sample was less affected by steaming because of the low steaming temperature and the possibility of faster and less invasive dealumination when a faster water flow was applied. It also remains the most crystalline of all the samples, as evidenced in its PXRD pattern (see Figure 7.8b).

Due to their higher degree of dealumination and better porosity, the properties of ST2 materials were further investigated.

TGA of ST2 samples reveals that dealumination Rho adsorbs less water (Figure 7.10). The low silica H-Rho shows the strongest interaction of water with the zeolitic

framework, 15% weight loss, which drops to *ca.* 7% for steamed zeolite Rho. Lower hydrophilic character would be useful during CO₂ adsorption in the presence of water.

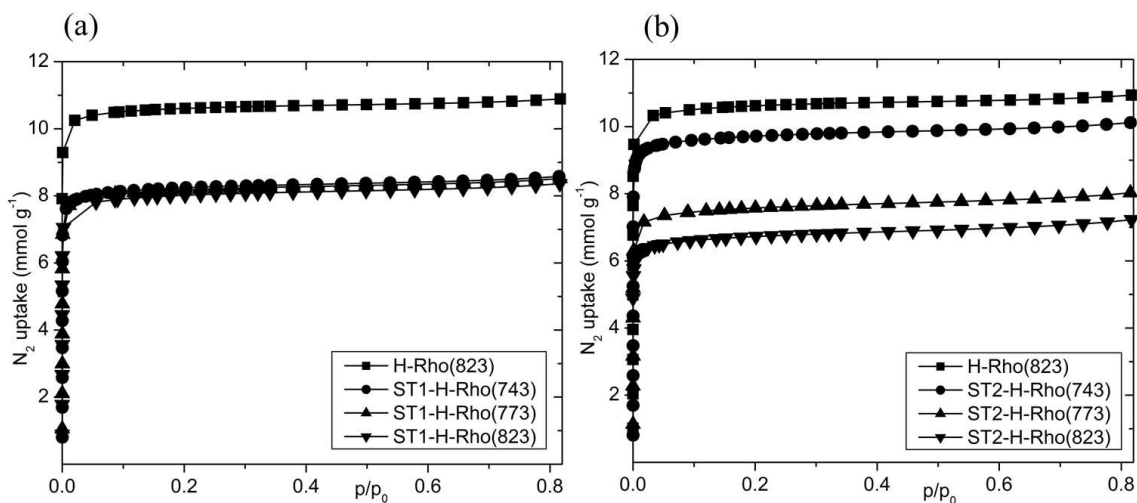


Figure 7.9. N₂ adsorption isotherms at 77 K of H-Rho and steamed Rho samples (a) ST1 (first steamed set of samples) and (b) ST2 (second steamed set of samples).

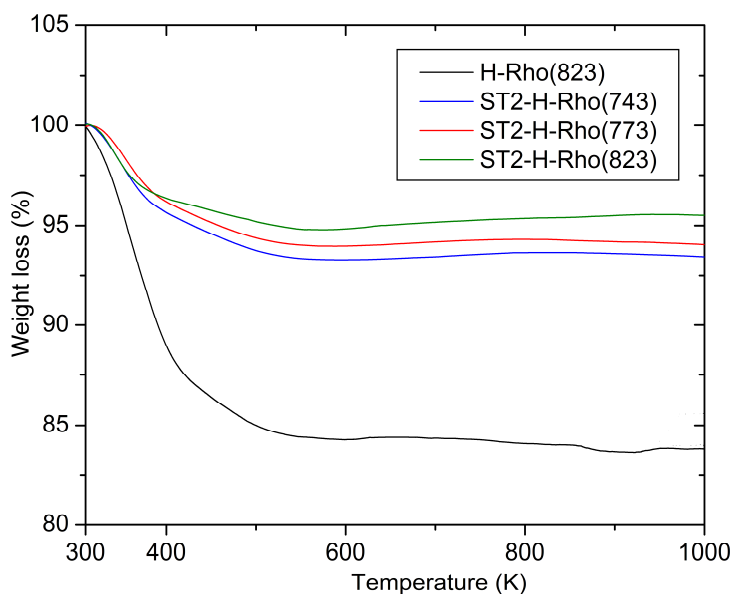


Figure 7.10. TGA curves of H-Rho and ST2 (second steamed set of samples at high water flow).

For samples from the second set the coordination geometry of the extra-framework Al was investigated in more detail by a combination of ²⁹Si MAS NMR, ²⁷Al MAS NMR and MQ MAS NMR (Figure 7.11). The Si/Al ratio for Na,Cs-Rho from ²⁹Si MAS NMR is 3.9 and the ²⁷Al MAS NMR spectrum confirms that the framework Al is in tetrahedral coordination, showing a single resonance at about 60 ppm (see

Figure 7.5). For H-Rho the ^{29}Si MAS NMR has increased slightly, to 4.15, and ^{27}Al MAS NMR indicates the presence of a small amount of octahedrally-coordinated and therefore presumably extra-framework aluminium species corresponding to a loss of 0.5 Al^{3+} per unit cell from the framework (Figure 7.11a). For ST2-H-Rho(743), ST2-H-Rho(773) and ST2-H-Rho(823) the framework Si/Al ratio remains constant (within the limits of accuracy) at 9.4 (see Table 7.3). For these samples, aluminium removed from the framework is observed to move to extra-framework sites that can be 4-fold, 5-fold or 6-fold coordinated, behaviour very similar to that reported for Al^{3+} cations in dealuminated zeolite Y.¹⁶ This indicates a framework Al content of 4.6 per unit cell, and therefore a loss of 5.4 Al per unit cell during dealumination. Charge balance for the framework Al^{3+} is attributed to protons. Additionally, ^{27}Al MQ MAS NMR of sample ST2-H-Rho(743) (Figure 7.11b) increases the resolution of different sites and reveals four different resonances which may correspond to: octahedral Al in extra-framework positions (1), five-coordinate Al in extra-framework positions (2), tetrahedral framework Al (3) and Al in a distorted tetrahedral extra-framework environment (4).

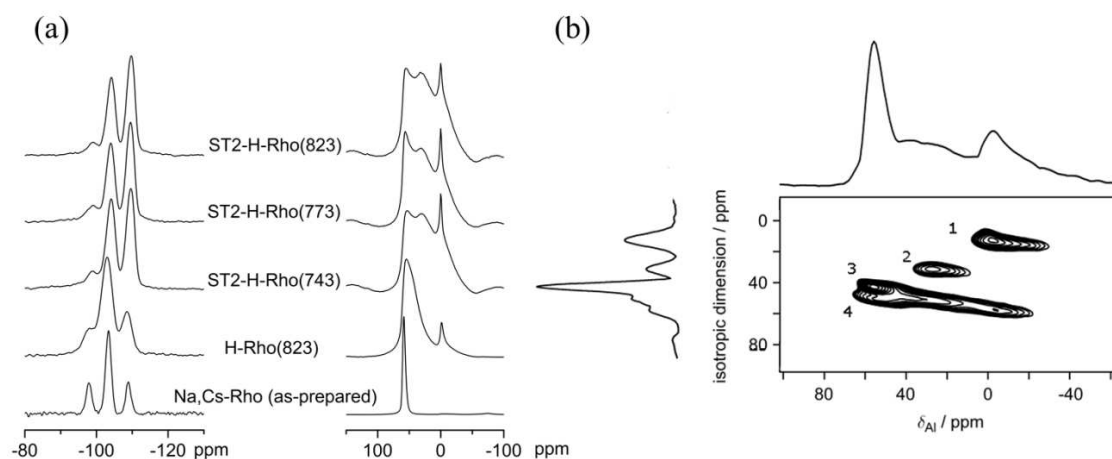


Figure 7.11. (a) ^{29}Si MAS NMR (left) and ^{27}Al MAS NMR (right) of Na,Cs-Rho, H-Rho, ST2-H-Rho(743), ST2-H-Rho(773) and ST2-H-Rho(823) (ST2 – second steamed set of samples at high water flow). (b) $3Q$ ^{27}Al MAS NMR of ST2-H-Rho(743) showing: 1 – octahedral Al in extra-framework positions, 2 – five-coordinate Al in extra-framework positions, 3 – tetrahedral framework Al, 4 – Al in a distorted tetrahedral extra-framework environment.

Although the N_2 uptake of ST2-H-Rho(743) at 0.1 bar at 77 K (9.6 mmol g^{-1}) was close to that of the H-Rho(823), the CO_2 adsorption at 0.1 bar and 298 K is 1.8 mmol g^{-1}

for H-Rho and 0.9 mmol g^{-1} for ST2-H-Rho(743) indicating that there is a weaker interaction between CO_2 and ST2-H-Rho(743) (Figure 7.12). CO_2 uptake at 0.1 bar for ST2-H-Rho(773) and ST2-H-Rho(823) is 0.8 mmol g^{-1} and 0.7 mmol g^{-1} , respectively. That there is no strong interaction with the extra-framework aluminium species indicates that the trivalent Al^{3+} cations must be shielded by associated hydroxide and/or oxide species, either within the cages, or in their own non-porous alumina phase. The observed weaker interaction is attributed to the lower framework charge in the dealuminated framework.

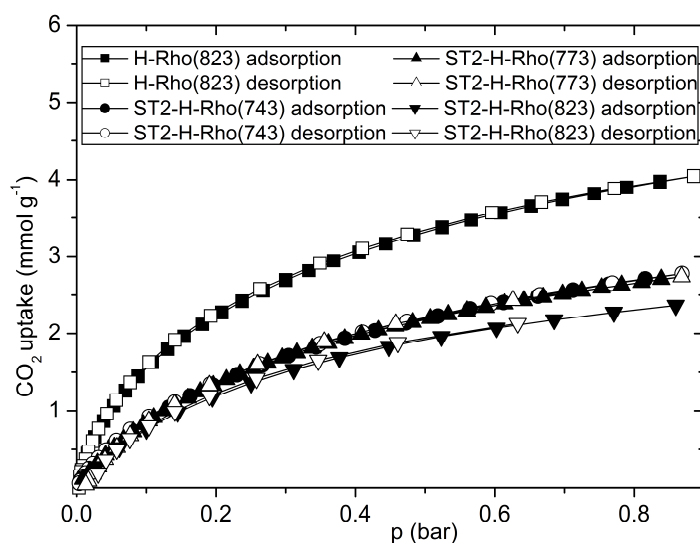


Figure 7.12. CO_2 sorption isotherms at 298 K for H-Rho and ST2 (second steamed set of samples).

It has been shown that dealumination results in frameworks with greater thermal stability and hydrophobicity but it does not enhance the CO_2 adsorption properties at low pressure. With regard to the advantages of this process an attempt was made to remove extra-framework aluminium by ion exchange and HCl treatment which may increase the CO_2 uptake. The experimental procedure is described in chapter 4. Results show it is not possible to exchange or remove the extra-framework aluminium. The EDX analysis of ST2-H-Rho(743) shows small change in Si/Al ratio and only *ca.* 0.20% of calcium was introduced. Samples after HCl treatment were no longer crystalline (Figure 7.13).

In addition, nitridation was conducted to create new CO_2 adsorption sites which may enhance CO_2 uptake. The nitridation of H-Rho was carried out at the University of Nottingham, in collaboration with Eric Masika and Prof. Robert Mokaya. Nitridation

was conducted according to published procedure¹⁷ and is described in chapters 1 and 4.

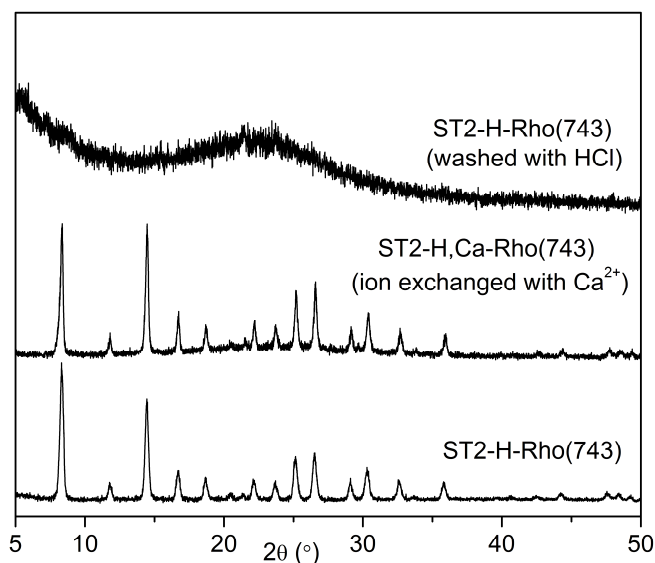


Figure 7.13. PXRD patterns of ST2-H-Rho(743) (ST2 – second steamed set of samples at high water flow) before and after ion exchange with Ca^{2+} and HCl wash. The (offset) patterns have been collected at 298 K using the same operating conditions.

H-form of zeolite Y, with Si/Al ratio 2.6, and ultrastable zeolite Y, with Si/Al ratio 8.0, were used to optimise nitridation conditions before the process was applied to H-Rho. The Si/Al ratio was measured by deconvolution of the ^{29}Si MAS NMR spectra (see the appendix) and calculated using equation 4.2. H-Y was nitrided at two temperatures: 1073 K and 1123 K and US-Y at 1073 K. Figure 7.14 shows PXRD patterns of H-Y and US-Y before and after nitridation. It may be seen that the H-Y nitrided at 1073 K stays partially crystalline; however when nitridation temperature is increased to 1123 K the structure becomes amorphous. US-Y remains crystalline after nitridation at 1073 K. It may be assumed that samples with higher Si/Al ratio will stay more crystalline after nitridation, that was also observed for these materials by Srasra *et al.*¹⁸

EDX analysis (Table 7.4 and Figure 7.15) indicates that 10% in H-Y and 13% in US-Y of oxygen atoms have been substituted for nitrogen which is similar to results previously published for these materials.¹⁸

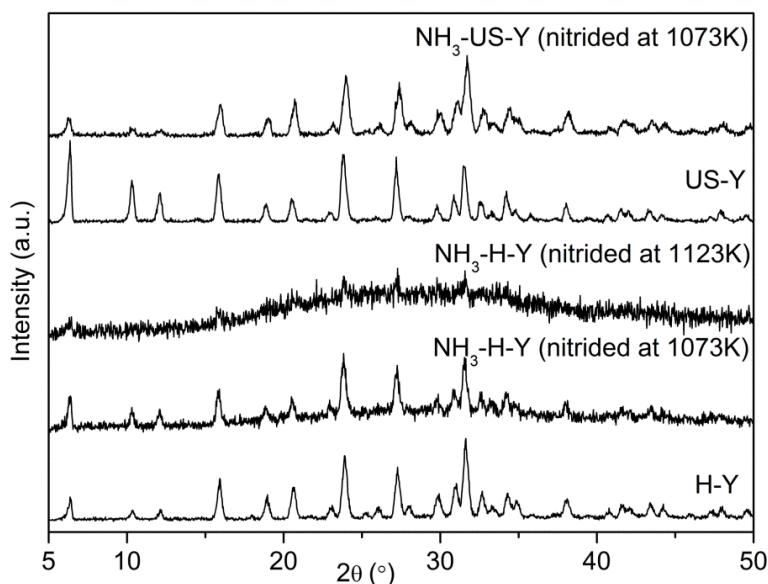


Figure 7.14. PXRD patterns of H-Y and US-Y before and after nitridation at 1073 K and 1123 K. The (offset) patterns have been collected at 298 K using the same operating conditions.

Table 7.4. EDX analysis of zeolite Y and US-Y before and after nitridation.

Sample	Atomic %			
	O	Si	Al	N
H-Y	72 ± 1	20 ± 1	8 ± 1	N.D.
NH ₃ -HY(1073K)	63 ± 1	20 ± 1	8 ± 1	9 ± 1
US-Y	64 ± 1	27 ± 1	9 ± 1	N.D.
NH ₃ -US-Y(1073K)	57 ± 1	27 ± 1	9 ± 1	7 ± 1

Values for oxygen and nitrogen are semi-quantitative

N.D. – not detected

Even if nitridation of H-Y and US-Y was successful it did not enhance CO₂ uptake significantly (Figure 7.16). The CO₂ uptake at 0.1 bar for H-Y after nitridation decreases from 2.4 mmol g⁻¹ to 0.7 mmol g⁻¹ and for US-Y increases from 2.0 mmol g⁻¹ to 2.4 mmol g⁻¹. The reason for lower CO₂ adsorption of H-Y after nitridation can be due to the poor crystallinity of the sample after nitridation (see Figure 7.14). The structure could partially collapse and block the CO₂ entrance.

It was found to be impossible to nitride H-Rho. After the sample was observed to become amorphous at 1073 K, the temperature was decreased to 973 K but the sample also did not remain crystalline at this temperature (Figure 7.17).

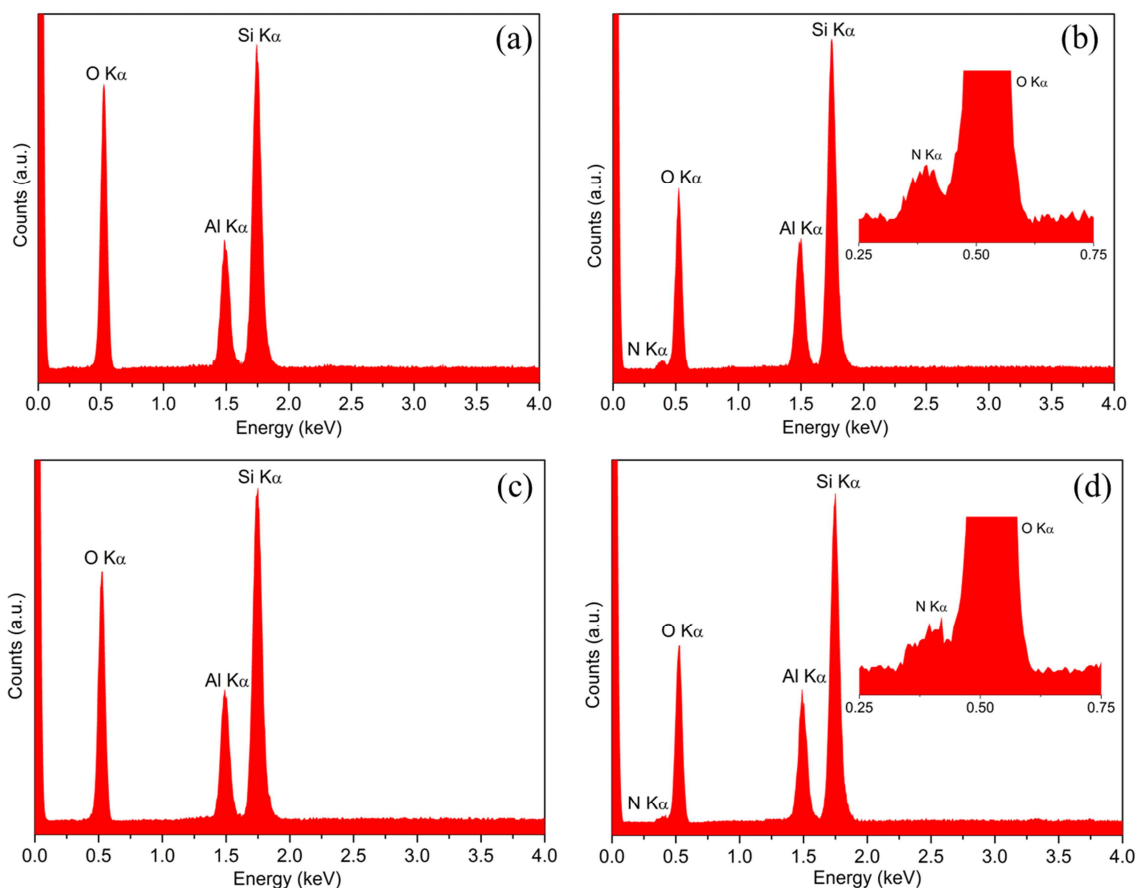


Figure 7.15. EDX spectra of (a) H-Y, (b) $\text{NH}_3\text{-HY}$, (c) US-Y and (d) $\text{NH}_3\text{-US-Y}$.

The insets show magnified images of nitrogen peak.

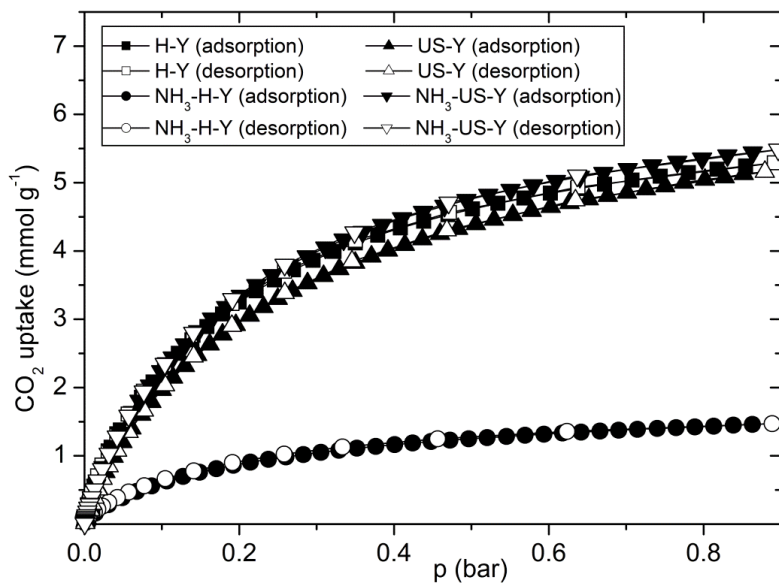


Figure 7.16. CO_2 sorption isotherms at 298 K for H-Y and US-Y before and after nitridation.

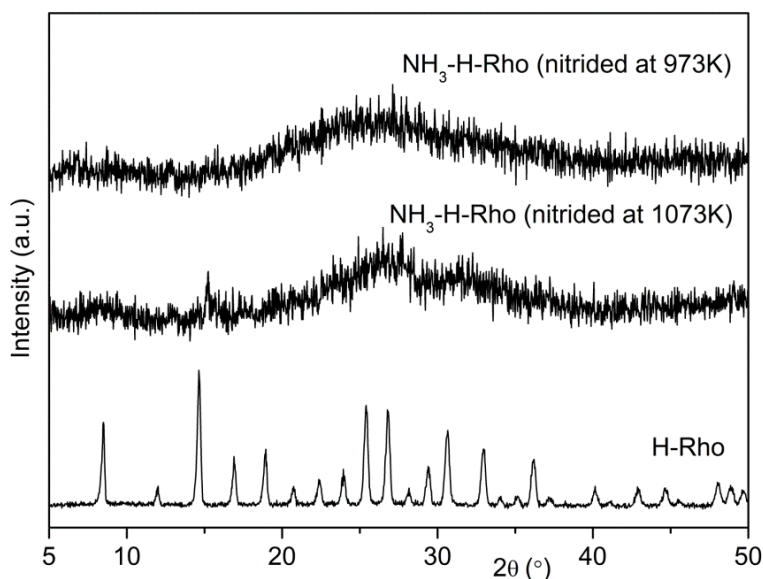


Figure 7.17. PXRD patterns of H-Rho before and after nitridation at 973 K and 1073 K. The (offset) patterns have been collected at 298 K using the same operating conditions.

7.4. Structural Studies of Na,Cs-, NH₄-, H-, Na-, Cs-, Li-, K- and Ca-Rho

For each of the Rho materials, PXRD patterns of the dehydrated samples were measured at 298 K and the structures were refined by Rietveld analysis as described in chapter 4. The PXRD profiles of dehydrated samples are presented in Figure 7.18 and the Rietveld plots for all Rho samples are presented in Figure 7.19.

Crystallographic details are given in Table 7.5, including the minimum O–O distance across the elliptical (or circular) windows delimited by S8Rs and calculated from the distance between the O atom centres, minus twice the van der Waals ionic radius of O²⁻, 1.35 Å, the occupancy of the cation sites, defined as types I, II and III as described above: further crystallographic details are supplied in the appendix. Figure 7.20 shows a possible arrangement of cations in a single α -cage and D8Rs site for Na,Cs-Rho, NH₄-Rho, H-Rho, Na-Rho, Cs-Rho, Li-Rho, K-Rho and Ca-Rho.

Rietveld refinement on dehydrated samples reveals that the unit cell parameter a increases in the order Ca-Rho < Li-Rho < Na-Rho < Na,Cs-Rho < Cs-Rho < K-Rho < NH₄-Rho < H-Rho. The minimum O–O distance across the elliptical (or circular) windows increases from 1.90 Å for Li-Rho to 3.88 Å for H-Rho, which remains in $Im\bar{3}m$ symmetry upon dehydration.

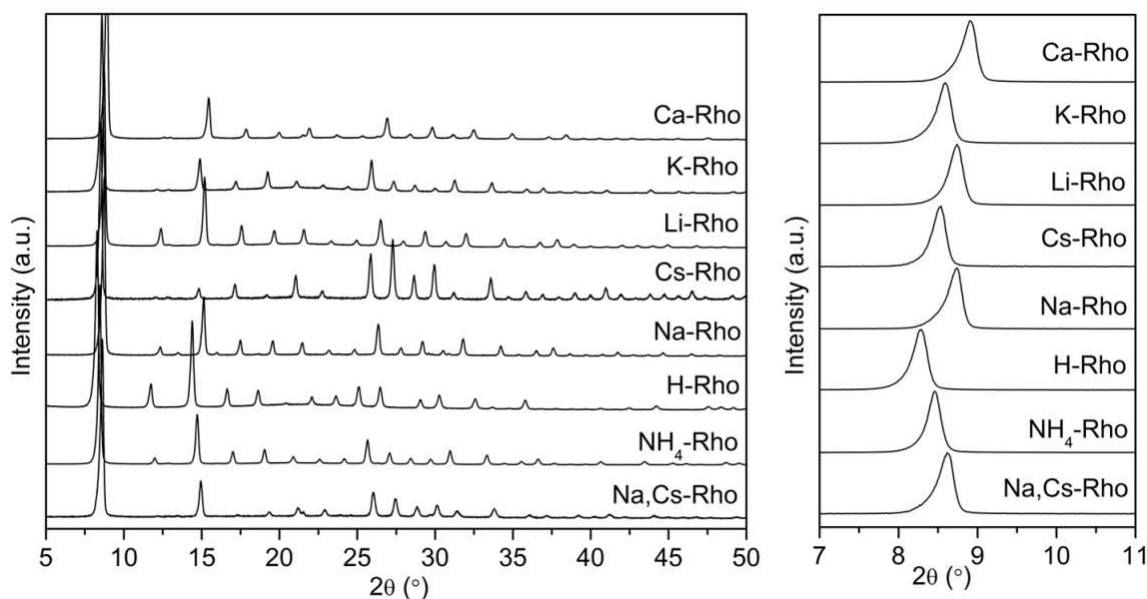


Figure 7.18. PXRD plots of dehydrated Rho samples with a magnified view of the first reflection peak. The (offset) patterns have been collected at 298 K using the same operating conditions.

In dehydrated Na,Cs-Rho (Figure 7.20a) around 3 out of 6 D8R sites (type I) are occupied by Cs^+ while Na^+ cations occupy sites of type II near the S8Rs in other windows of the large α -cages, around 3 Na^+ per unit cell, and sites of type III near S6Rs in α -cage, around 3 Na^+ per unit cell.

Available structural data on ammonium forms of Rho (Figure 7.20b) by neutron and X-ray diffraction indicate that at high ammonium contents (12 per unit cell) the cations occupy S8R sites (type II) upon dehydration, whereas for partially deammoniated samples, with 6 NH_4^+ per unit cell, the cations occupy D8R sites (type I).^{9,19} For the sample measured here it is likely that NH_4^+ cations occupy both D8R (*ca.* 2 NH_4^+ per unit cell) and S6R sites (*ca.* 8 NH_4^+ per unit cell).

Low atomic number of hydrogen makes determination of the hydrogen atoms impossible but the structure upon dehydration has $Im\bar{3}m$ symmetry (Figure 7.20c) with the biggest unit cell parameters and O–O distance of all the Rho samples studied.

In Na-Rho (Figure 7.20d) the cations occupy S8R (type II, around 6 Na^+ per unit cell) sites as well as some S6R (type III, around 3 Na^+ per unit cell) sites, so that each window has a cation at site II, assuming that two Na^+ cations will favour being

distributed over two D8R windows rather than occupying two sites in one and none in another.

D8R sites (type I) are fully occupied by Cs^+ cations in dehydrated Cs-Rho (6 Cs^+ per unit cell, Figure 7.20e). Caesium cations also occupy S6R (type III, around 3 Cs^+ per unit cell) sites within the α -cages.

For Li-Rho (Figure 7.20f), the low atomic number of lithium makes determination of the lithium site occupancies difficult, but significant scattering was measured at the S6R sites (type III), corresponding to between 5 and 6 Li^+ cations. This is unlikely to be an accurate value due to the low electron density of Li^+ but a previous structural analysis by neutron diffraction of a dehydrated mixed Li,Na,Cs-aluminosilicate zeolite indicated that the S6R site is the preferred position for the small Li^+ cation.¹² It is therefore probable that most of the Li^+ cations required for charge balance are located in this site and not in the window sites. The O–O distances are the smallest of all the Rho samples (1.9 Å).

In K-Rho (Figure 7.20g) K^+ cations are found to occupy window sites of both S8R (type II, around 7 K^+ per unit cell) and D8R (type I, around 2 K^+ per unit cell) sites so that there will be at least one and in some case two K^+ cations per S8R window.

Small divalent Ca^{2+} cations in dehydrated Ca-Rho (Figure 7.20h) pull the D8R closed (the second smallest O–O distance after Li-Rho and the smallest unit cell parameter), and fills most of the D8R (type I) window sites (5 out of 6).

Although cation rearrangement is possible upon CO_2 uptake, as observed by Palomino *et al.*¹¹ in Na,Cs-Rho, these framework structures and cation positions are a good starting point for understanding the adsorptive properties of Rho as the solid is first put in contact with CO_2 .

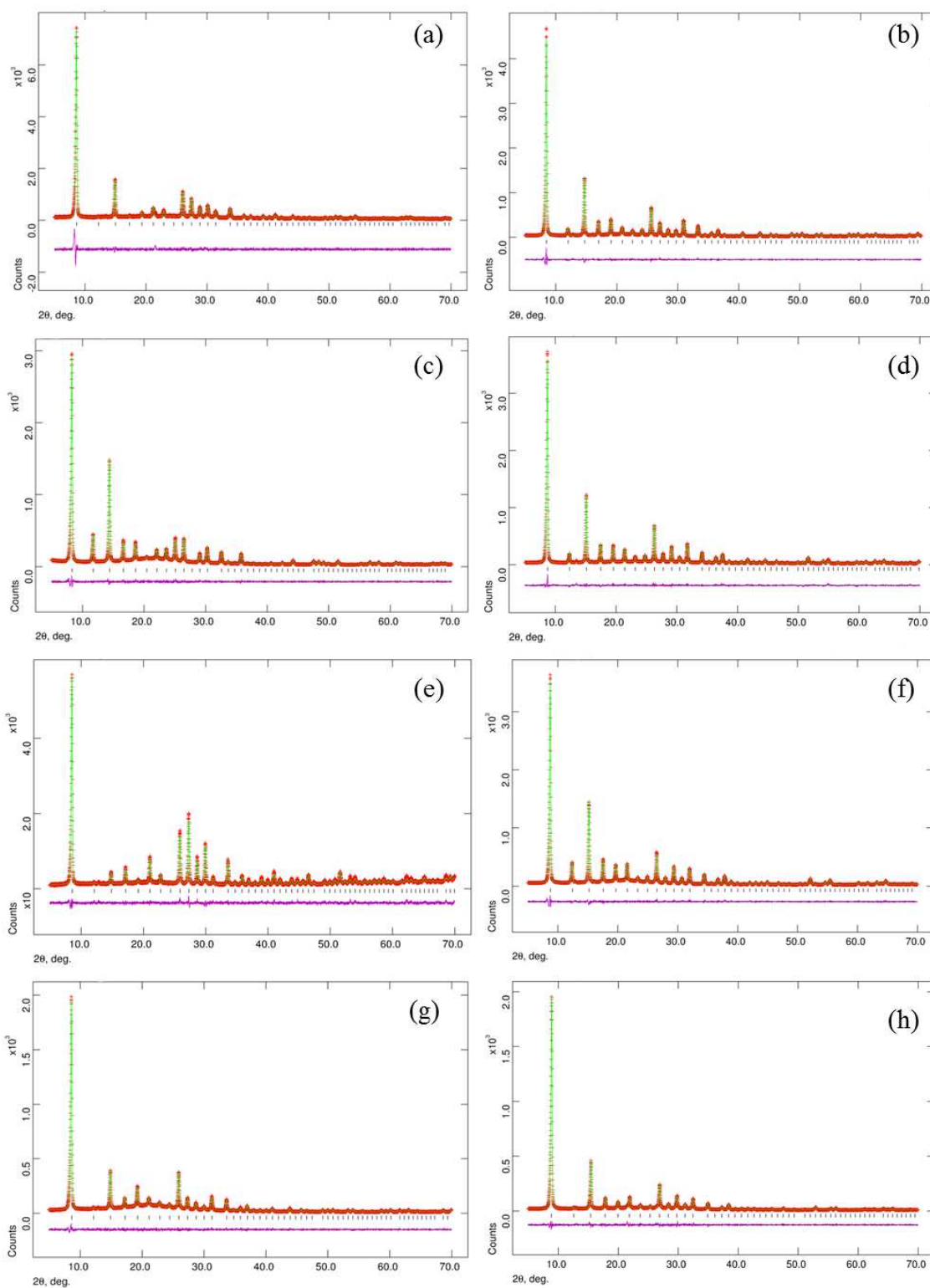


Figure 7.19. Rietveld plots of laboratory PXR profiles (at 298 K) of dehydrated (a) Na,Cs-Rho, (b) NH_4 -Rho, (c) H-Rho, (d) Na-Rho, (e) Cs-Rho, (f) Li-Rho, (g) K-Rho and (h) Ca-Rho.

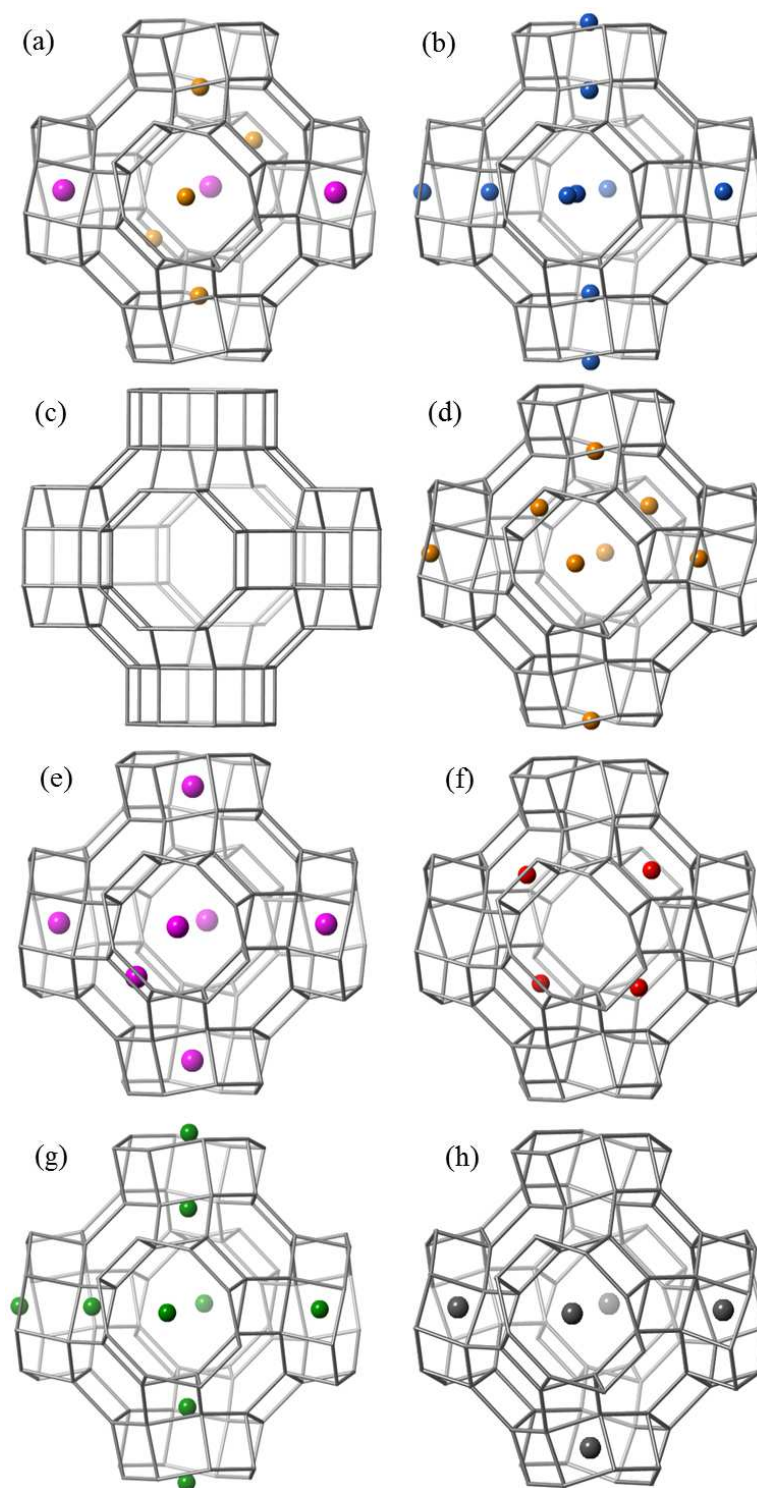


Figure 7.20. Possible cation distributions in one α -cage and associated D8R windows of dehydrated (a) Na,Cs-Rho (larger spheres, Cs; smaller spheres, Na), (b) NH₄-Rho (N only represented), (c) H-Rho, (d) Na-Rho, (e) Cs-Rho, (f) Li-Rho, (g) K-Rho and (h) Ca-Rho.

Table 7.5. Space group, minimum O–O distance of S8R windows and cation site occupancies in dehydrated zeolite Rho (Site I, D8R; Site II, S8R; Site III, S6R) as determined by Rietveld refinement from laboratory powder X-ray diffraction collected at 298 K.

Sample	Unit cell parameter /Å	Space group	O–O /Å	Site I		Site II		Site III	
				Frac. Occup.	Cations/unit cell	Frac. Occup.	Cations/unit cell	Frac. Occup.	Cations/unit cell
Na,Cs-Rho	14.5307(4)	$I\bar{4}3m$	2.69	0.426(2)	2.55(2)	0.252(1)	3.02(13)	0.317(2)	2.54(14)
NH ₄ -Rho	14.7018(2)	$I\bar{4}3m$	2.85	0.323(6)	1.93(4)	0.677(6)	8.12(7)	-	-
H-Rho	15.0352(2)	$Im\bar{3}m$	3.88	-	-	-	-	-	-
Na-Rho	14.3771(2)	$I\bar{4}3m$	2.26	-	-	0.539(7)	6.47(8)	0.372(1)	2.98(9)
Cs-Rho	14.5947(3)	$I\bar{4}3m$	2.85	1.00	6.00	-	-	0.424(3)	3.39(2)
Li-Rho	14.2448(2)	$I\bar{4}3m$	1.90	-	-	-	-	1.00	8.00
K-Rho	14.5951(2)	$I\bar{4}3m$	2.72	0.343(4)	2.06(2)	0.571(3)	6.85(4)	-	-
Ca-Rho	14.0462(1)	$I\bar{4}3m$	1.94	0.772(8)	4.63(2)	-	-	-	-

7.5. CO₂ Adsorption Related to Structure for Na,Cs-, Na- and Cs-Rho

CO₂ adsorption isotherms for Na,Cs-Rho, Na-Rho and Cs-Rho are presented in Figure 7.21. The shape of the Na,Cs-Rho and Na-Rho CO₂ isotherms correspond to Type I, which is characteristic for adsorbents having a microporous structure. The sequence of CO₂ uptake at 298 K on this materials is Cs-Rho < Na,Cs-Rho < Na-Rho.

Na,Cs-Rho showed no N₂ adsorption at 77 K (Figure 6.7b), but appreciable CO₂ uptake at 298 K, with significant hysteresis. That CO₂ is adsorbed must indicate that either the Cs or the Na⁺ cations (or both) must be able to move to permit diffusion. The *in situ* PXRD structural studies of Palomino *et al.*¹¹ indicated that above 1 bar at 298 K the structure changes symmetry to $Im\bar{3}m$ and that at 5 bar Cs⁺ is displaced from its position in D8R site to occupy a position at S8R site. The adsorption data here confirms that some cations must move sufficiently far away from their S8R site to permit the CO₂ molecules to enter the cage.

To determine the relative mobility of Cs⁺ and Na⁺ in these window sites the pure Na and Cs⁺ cation forms were prepared and the structures of the dehydrated cationic forms were measured by Rietveld refinement of laboratory X-ray data (see Table 7.5). In each case, the dehydrated form distorts to $I\bar{4}3m$ symmetry, with $a = 14.3771(2)$ Å and O–O distance 2.26 Å for Na-Rho and 14.5947(3) Å and 2.85 Å for Cs-Rho, respectively. Adsorption isotherms at 298 K up to 1 bar show the Cs⁺ form adsorbs only low amounts of CO₂ (0.6 mmol g⁻¹ at 1 bar), whereas the Na-form adsorbs CO₂ strongly, even at low

partial pressures (3.2 mmol g^{-1} at 0.1 bar), even though the window size in Na-Rho (neglecting cations) is smaller than that in Cs-Rho. Na-Rho adsorption and desorption isotherms show relatively little hysteresis at most of the pressures under these conditions of measurement, although more careful examination showed significant hysteresis at low pressures (Figure 7.22).

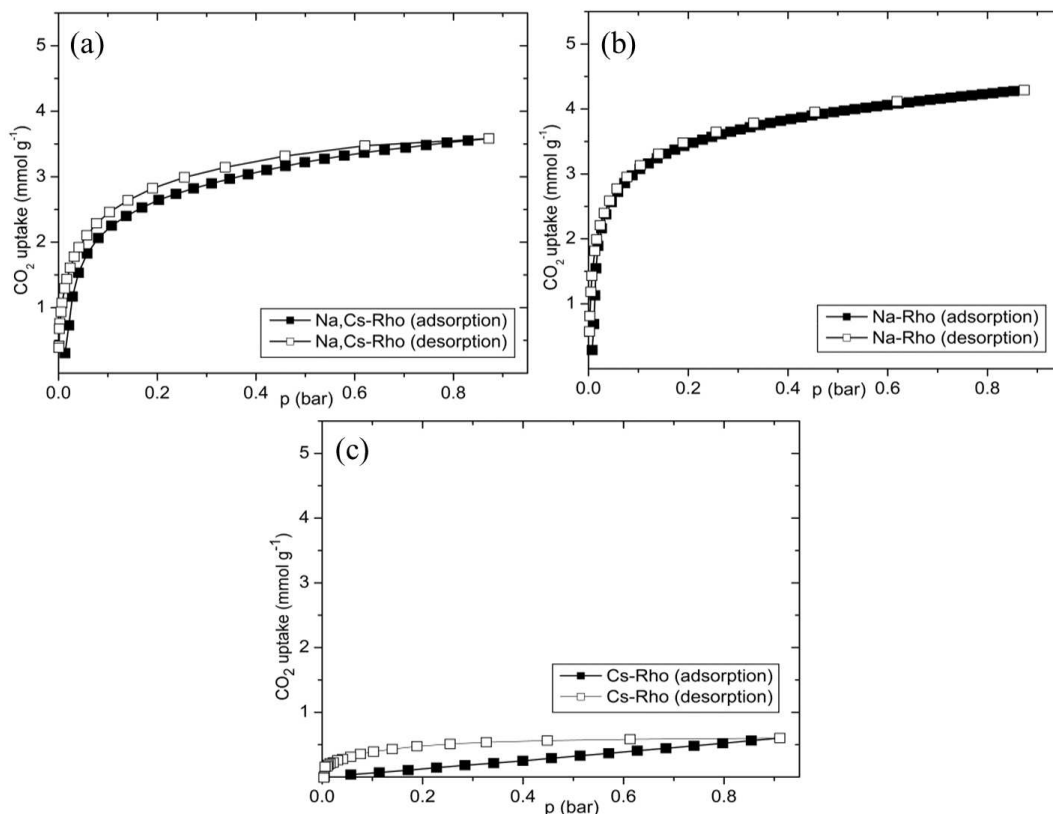


Figure 7.21. CO₂ sorption isotherms at 298 K for (a) Na,Cs-Rho, (b) Na-Rho and (c) Cs-Rho.

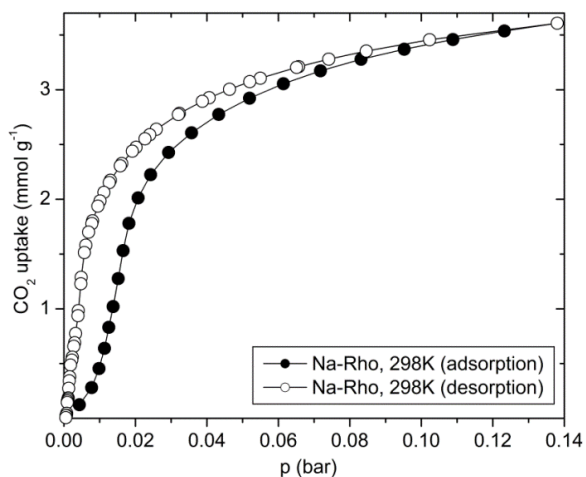


Figure 7.22. CO₂ sorption isotherm up to 140 mbar for Na-Rho at 298 K.

These results suggest that at pressures less than 1 bar the Cs⁺ cations in the D8R sites block the windows and that diffusion of CO₂ into and through Na,Cs-Rho must occur largely through the S8R windows occupied by Na⁺ cations. The mechanisms of CO₂ adsorption on Na-Rho at low pressure and adsorption on fully exchanged Cs-Rho at high pressure are further investigated in sections 7.9 and 7.10, respectively.

7.6. CO₂ Adsorption Related to Structure for H-, NH₄-, Li-, K- and Ca-Rho

Additional cation forms of zeolite Rho were prepared to determine the effect of these cations on CO₂ adsorption on zeolite Rho. The CO₂ isotherms of H-, NH₄-, Li-, K- and Ca-Rho are presented in Figure 7.23.

CO₂ isotherm for H-, NH₄- and K-Rho exhibits non-Type I behaviour. The shape of CO₂ isotherms of Li-Rho corresponds to Type I, which is characteristic for adsorbents having a microporous structure. The sequence of CO₂ uptake at 298 K and at 1 bar on these materials is Ca-Rho < NH₄-Rho < K-Rho < Li-Rho.

H-Rho possesses a pore volume of 0.36 cm³g⁻¹ (10.5 mmol(N₂) g⁻¹). The CO₂ isotherm is Type I and the uptake of CO₂ at 298 K and 0.1 bar is relatively low, 1.7 mmol g⁻¹ (Figure 7.23a). This uptake increases to 3.5 mmol g⁻¹ by 0.9 bar, and is fully reversible. The structure of dehydrated H-Rho was confirmed to have *Im* $\bar{3}m$ symmetry with $a = 15.0369(5)$ Å, where the circular 8-membered rings have an opening large enough to admit both N₂ and CO₂. Notably, the H-Rho CO₂ isotherm is very different from that reported by Araki *et al.*¹⁰ for the so-called H-Rho of their work. The difference arises because at the lower ion exchange temperature not all of the Cs⁺ cations are exchanged by ammonium and their non-Type I isotherm shape probably results from a structural change occurring as P_{CO2} increases, controlled by the presence of the residual Cs⁺ cations in D8R sites. To support this observation sample with 4 Cs⁺ per unit cell was prepared. The CO₂ adsorption measurement on Cs,H-Rho is presented in Figure 7.24 and it shows similar behaviour to the sample reported by Araki *et al.*¹⁰

N₂ uptake on NH₄-Rho at 77 K is very low, 0.32 mmol g⁻¹ at p/p₀ = 0.9. For CO₂ the adsorption and desorption branches of NH₄-Rho show relatively little hysteresis and the uptake at 0.1 bar is 0.8 mmol g⁻¹ (Figure 7.23b). The uptake indicates that the ammonium ions must be able to move from their position within the D8R windows

to allow diffusion through the windows. The low CO₂ uptake at 0.1 bar may be due to the weaker electrostatic interaction between the CO₂ and the NH₄⁺ cations than that with the smaller Na⁺ or Li⁺ cations.

There is very low N₂ uptake at 77 K for Li-Rho, 0.67 mmol g⁻¹ at p/p₀ = 0.9. This is due to the window size where Li⁺ cations do not occupy window sites, but even at room temperature the narrowest O–O window opening is only 1.90 Å. In Li-Rho the strong distortion away from *Im* $\bar{3}m$ results as the S6Rs distort to afford the small Li⁺ cations better coordination in type III sites (S6R). CO₂ adsorption onto Li-Rho gave very high uptakes, even at low partial pressures, 3.5 mmol g⁻¹ at 0.1 bar (see Figure 7.23c). Most of the Li⁺ cations are in the S6R sites, leaving the window sites empty. The CO₂ is small enough to pass through the open windows of the dehydrated Li-Rho structure, even though the crystallographic distance is apparently too small (1.9 Å), suggesting that the framework is flexible locally at 298 K.

By comparison with Na-Rho and NH₄-Rho, adsorption and desorption isotherms on the K-form of zeolite Rho show much more marked non-Type I behaviour and hysteresis (see Figure 7.23d), even with equilibration times of 2 hours. Nevertheless, high uptake at 1 bar is achieved, 4.5 mmol g⁻¹. The N₂ uptake on K-Rho is 0.40 mmol g⁻¹ at p/p₀ = 0.9. Since all K⁺ cations in K-Rho occupy sites either in the D8R position (type I) or in S8R sites (type II) on either face of the window, the K⁺ cations must move to allow CO₂ uptake. The observed hysteresis results from the need for the movement of K⁺ cations to allow passage of the CO₂ molecules: this must be energetically more difficult than movement of the Na⁺ cations, possibly because they must move from D8R sites rather than S8R sites and the K⁺ cations are coordinated to more O atoms. To further confirm that it is the displacement of the K⁺ cation that inhibits the CO₂ adsorption, rather than a molecular sieving effect due to distortion of the S8R away from circular, comparison of the minimum ring distance (see Table 7.5) in the Na- and K-Rho indicates that this is smaller for the Na-Rho than for the K-Rho, but hysteresis is greater for the K-Rho. As previously discussed, for the Li-Rho the distance is smaller still, but no hysteresis is observed because Li⁺ cations are not present in the window sites.

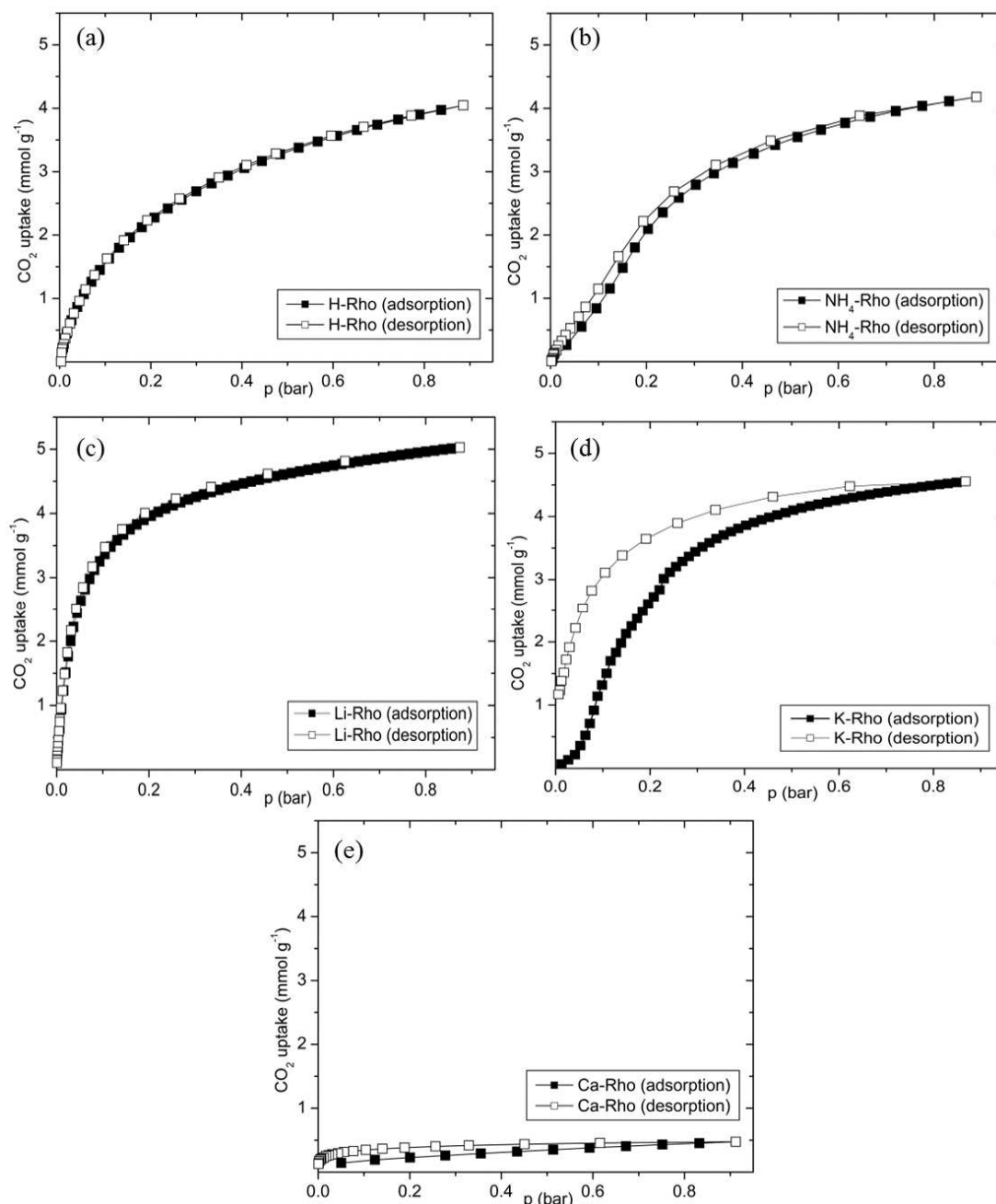


Figure 7.23. CO_2 sorption isotherms at 298 K of (a) H-Rho, (b) NH_4 -Rho, (c) Li-Rho, (d) K-Rho and (e) Ca-Rho.

Fully-exchanged Ca-Rho was also examined. It adsorbs 0.55 mmol g^{-1} of N_2 at 77 K and $p/p_0 = 0.9$ (see Figure 7.7b) and very small amount of CO_2 at 298 K, 0.5 mmol g^{-1} at 0.9 bar (see Figure 7.23e). The Ca^{2+} cations induce a very strong reduction in size of the Rho unit cell as the framework distorts to give tetrahedral coordination of the Ca^{2+} : the unit cell parameter is the smallest for all Rho samples ($a = 14.0462(1) \text{ \AA}$) and the O–O distance is only 1.94 \AA . The very low CO_2 uptake in the fully-exchanged Ca-Rho suggests that the Ca^{2+} cations cannot easily move from

D8R (which has a high occupancy of 5 Ca^{2+} per unit cell) to allow CO_2 to pass at the temperatures and CO_2 pressures of the adsorption because the structure possess the combination of very small openings (similar to Li-Rho) and Ca^{2+} cations blocking the D8R windows (similar to Cs-Rho or K-Rho).

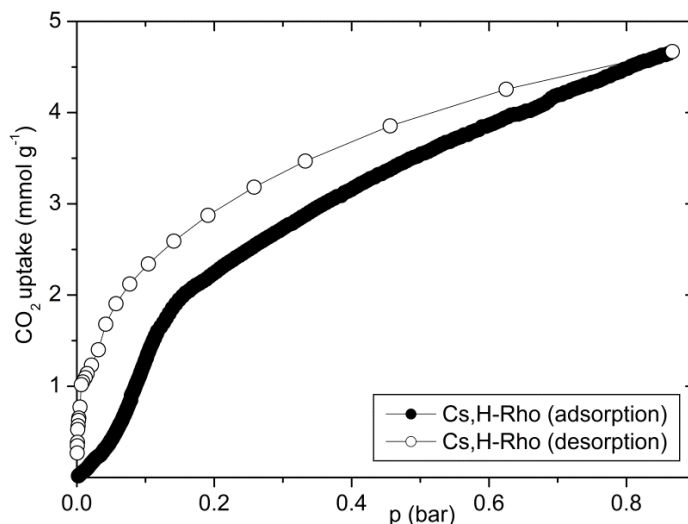


Figure 7.24. CO_2 sorption isotherm at 298 K of Cs,H-Rho sample with 4 Cs^+ per unit cell.

Results obtained in this section confirm that the cations play a very important role in determining the CO_2 adsorption and gas-separation properties of zeolite Rho. CO_2 uptake and selectivity depend heavily on the size, charge density, and distribution of cations in the Rho structure.

7.7. N_2 and CO_2 Adsorption on Na,H-Rho, Li,H-Rho and Ca,H-Rho

To investigate further the effect of cations on sorption onto Na-Rho, Li-Rho and Ca-Rho, N_2 and CO_2 uptake was measured on samples with different Na^+ , Li^+ and Ca^{2+} contents. Different amounts of cations were replaced by NH_4^+ by ion exchange, and subsequently calcined to give M,H-forms. The preparation of M,H-Rho samples is described in chapter 4.

PXRD was conducted to check the crystallinity of samples after removal of the cations. It can be seen that all ion exchanged samples remain crystalline during removal of cations and replacement by protons (Figure 7.25).

Table 7.6 contains EDX analysis data of the Na,H-Rho and Ca,H-Rho series. For the AAS data for Li,H-Rho series see Table 4.1 in chapter 4. N₂ adsorption at 77 K was measured at the University of St. Andrews and reversible CO₂ uptake at 298 K and 0.1 bar, measured by ZLC at the University of Edinburgh in collaboration with Enzo Mangano and Prof. Stefano Brandani. Examination of the N₂ capacity at 77 K and p/p₀ = 0.1 and CO₂ at 298 K and 0.1 bar of a series of Na,H-Rho, Li,H-Rho and Ca,H-Rho materials of different cation contents is presented in Figure 7.26. The formula for the derivation of the unit cell composition is given in chapter 4.

Table 7.6. EDX analysis of H,M-Rho samples before and after cation removal.

Sample	Atomic %				
	O	Si	Al	Na	Ca
Na _{9,8} Al _{9,8} Si _{38,2} O ₉₆	69 ± 1	21 ± 1	5 ± 1	5 ± 1	N.D.
Na _{8,3} H _{1,5} Al _{9,8} Si _{38,2} O ₉₆	69 ± 1	21 ± 1	5 ± 1	5 ± 1	N.D.
Na ₇ H _{2,8} Al _{9,8} Si _{38,2} O ₉₆	70 ± 1	21 ± 1	5 ± 1	4 ± 1	N.D.
Na _{5,8} H ₄ Al _{9,8} Si _{38,2} O ₉₆	71 ± 1	21 ± 1	5 ± 1	3 ± 0.5	N.D.
Na _{4,3} H _{5,5} Al _{9,8} Si _{38,2} O ₉₆	72 ± 1	21 ± 1	5 ± 1	2 ± 0.5	N.D.
Na _{3,2} H _{6,6} Al _{9,8} Si _{38,2} O ₉₆	73 ± 1	21 ± 1	5 ± 1	1 ± 0.5	N.D.
Na _{2,2} H _{7,6} Al _{9,8} Si _{38,2} O ₉₆	73 ± 1	21 ± 1	5 ± 1	1 ± 0.5	N.D.
Ca _{4,9} Al _{9,8} Si _{38,2} O ₉₆	72 ± 1	20 ± 1	5 ± 1	N.D.	3 ± 0.5
Ca ₄ H _{1,8} Al _{9,8} Si _{38,2} O ₉₆	73 ± 1	20 ± 1	5 ± 1	N.D.	2 ± 0.5
Ca ₂ H _{5,8} Al _{9,8} Si _{38,2} O ₉₆	74 ± 1	20 ± 1	5 ± 1	N.D.	1 ± 0.5

Values for oxygen are semi-quantitative

N.D. – not detected

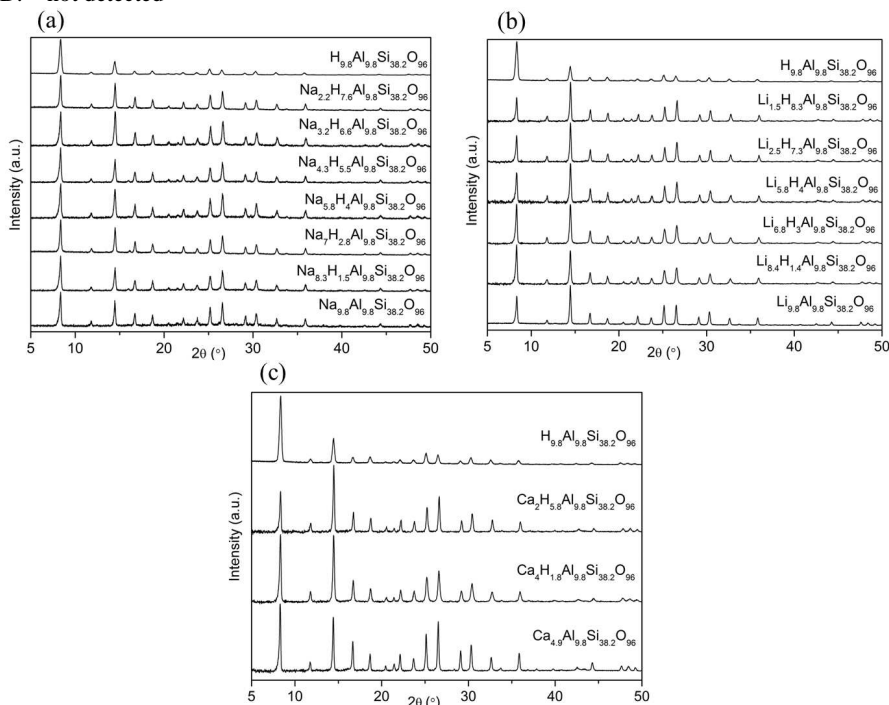


Figure 7.25. PXRD patterns of (a) Na,H-Rho, (b) Li,H-Rho and (c) Ca,H-Rho. The (offset) patterns have been collected at 298 K using the same operating conditions.

For Na,H-Rho it is shown that for more than 4 Na⁺ per unit cell the permanent porosity to N₂ at 77 K is reduced to 0.17 mmol g⁻¹ from 10.4 mmol g⁻¹ at p/p₀ = 0.1. Furthermore, when reversible CO₂ adsorption measurements are made on Na,H-Rho with a variable Na⁺ content, there is only a small increase in CO₂ uptake at 0.1 bar as the number of Na⁺ cations is increased up to 4, but at 6 cations per unit cell and above the CO₂ uptake increases as the sodium content increases. These observations are partially explained by reference to the structural analyses of a Na,H-Rho containing 4.9 Na⁺ per unit cell, for which the Rietveld plot and structure are presented in Figure 7.27a. The unit cell parameter decreases from 14.3771(2) Å for Na-Rho to 14.3447(2) Å for Na,H-Rho(50%Na) and the O–O distance drops to 2.21 Å (Na,H-Rho(50%Na)) from 2.26 Å (Na-Rho). Furthermore, at this level of 5 Na⁺ per unit cell, the Na⁺ cations occupy almost all of the windows, distributed over D8R and S8R sites. It is likely that cations are not mobile at 77 K so that there are no easy routes for N₂ through the pore space. They are mobile at 298 K in the presence of CO₂, permitting uptake. At higher Na⁺ contents the S6R sites become occupied and the presence of additional cations in these S6R sites results in the creation of additional energetic sites for CO₂ adsorption.

N₂ adsorption was also measured on samples with different Li⁺ contents. Adsorption of N₂ at 77 K decreased steadily above 2 Li⁺ per unit cell, from 10.4 mmol g⁻¹ to 0.30 mmol g⁻¹. Rietveld refinement (Figure 7.27) was conducted for the sample with 5 Li⁺ per unit cell to investigate the changes to the structure that occur when it is half occupied and has high porosity to nitrogen (8 mmol g⁻¹). At room temperature the O–O distance (taking ionic radii into account) increases from 1.90 Å (Li-Rho) to 2.24 Å (Li,H-Rho(50%Li)) together with the unit cell parameter which changes from 14.2448(2) Å (Li-Rho) to 14.4239(5) Å (Li,H-Rho(50%Li)) (Table 7.7). Therefore, as Li⁺ cations are located mainly at the S6R sites the increase in uptake is due to the increase of the window size that results from the reduced framework distortion.

N₂ and CO₂ adsorption curves were also prepared for Ca,H-Rho (Figure 7.26c). The N₂ uptake as a function of Ca²⁺ unit cell content shows similar behaviour to that described above for Li-Rho with the difference that Ca²⁺ cations occupy the D8R site (type I) and the total number of Ca²⁺ in the unit cell is half that of Li⁺. Both Li-Rho and Ca-Rho, possess a very small window size in the strongly distorted structures (see Table 7.5). In Ca-Rho the distortion is caused by the position of cations in D8R. The small divalent

Ca^{2+} cations pull the D8R closed, and fill most of the window sites (5 out of 6). It is therefore very difficult for CO_2 to enter when structure is fully occupied. When cations are removed the CO_2 uptake is only slightly higher than the CO_2 uptake on H-Rho (1.3 mmol g^{-1} at 0.1 bar). The CO_2 uptake may increase when the pressure of CO_2 increases, therefore the CO_2 adsorption at high pressure for fully exchanged Ca-Rho was investigated further (section 7.10).

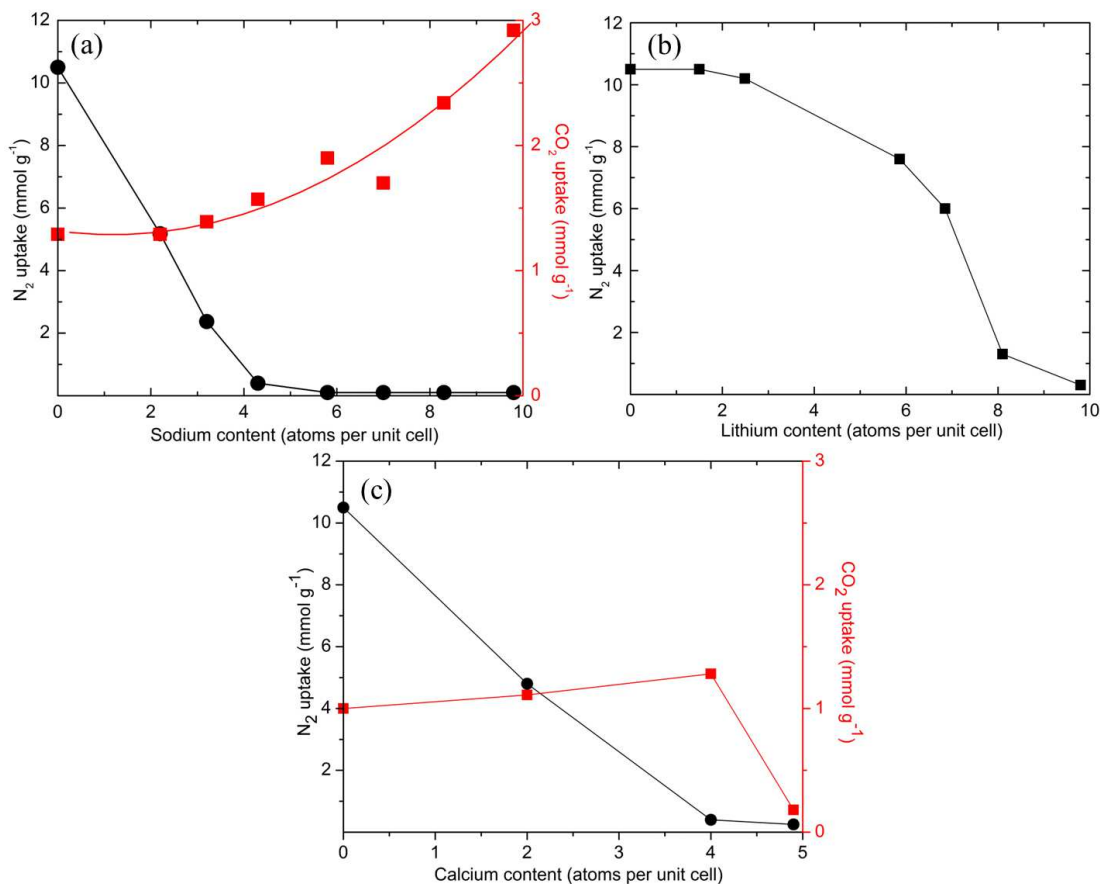


Figure 7.26. Uptake of N_2 at 77 K and $p/p_0 = 0.1$, and CO_2 at 298 K and 0.1 bar as a function of (a) Na-content of zeolite Na-Rho, (b) Li-content of zeolite Li-Rho (only N_2) and (c) Ca-content of zeolite Ca-Rho.

Table 7.7. Space group, minimum O–O distance of S8R windows and cation site occupancies in dehydrated zeolite Rho and M,H-Rho.

Sample	Unit cell parameter /Å	Space group	O–O /Å	Site I		Site II		Site III	
				Frac. Occup.	Cations/unit cell	Frac. Occup.	Cations/unit cell	Frac. Occup.	Cations/unit cell
Na-Rho	14.3771(2)	$I\bar{4}3m$	2.26	-	-	0.539(7)	6.47(8)	0.372(1)	2.98(9)
Na,H-Rho (50%Na)	14.3447(2)	$I\bar{4}3m$	2.21	0.269(6)	1.61(4)	0.241(3)	2.89(4)	-	-
Li-Rho	14.2448(2)	$I\bar{4}3m$	1.90	-	-	-	-	1.00	8.00
Li,H-Rho (50%Li)	14.4239(5)	$I\bar{4}3m$	2.24	-	-	-	-	0.65(3)	5.20(24)
Ca-Rho	14.05577(2)	$I\bar{4}3m$	1.94	0.772(8)	4.63(2)	-	-	-	-

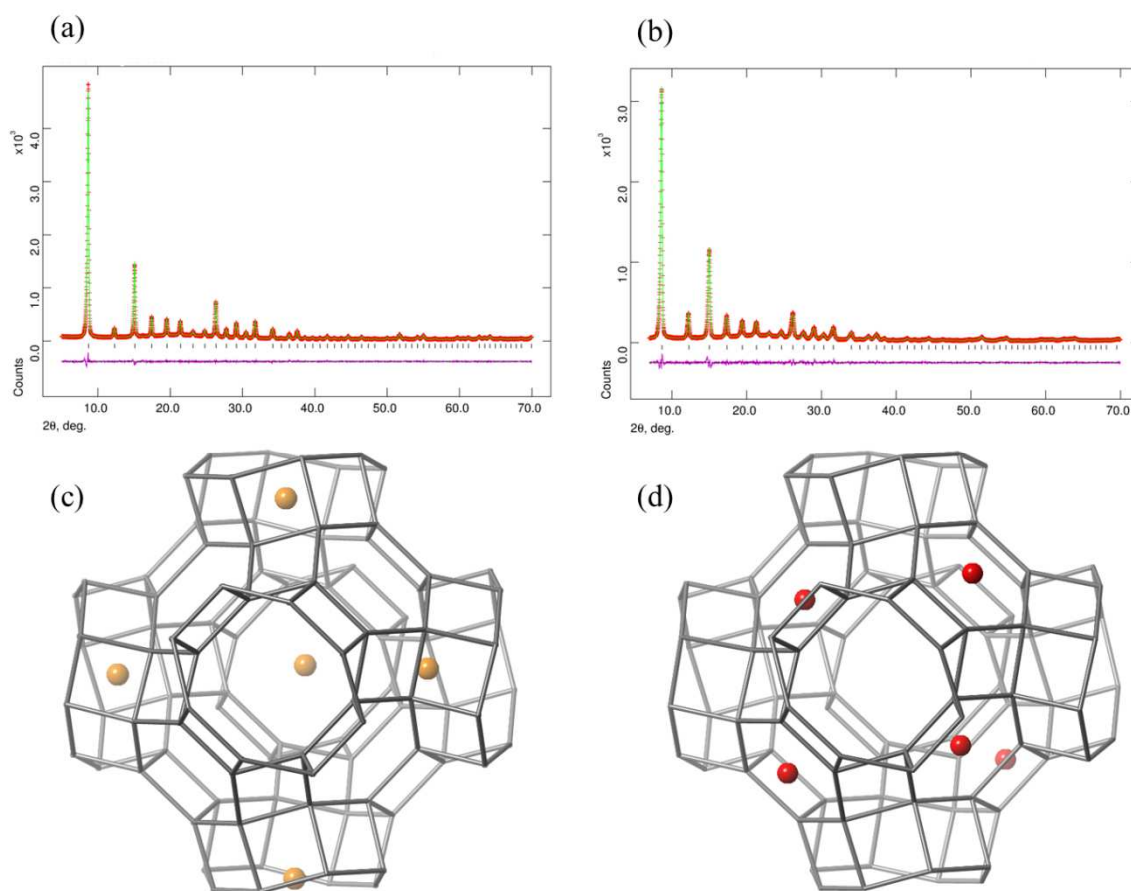


Figure 7.27. Final observed, calculated and difference Rietveld plots for the powder data refinement and possible cation distributions in one α -cage of (a) dehydrated Na,H-Rho(50%Na) and (b) dehydrated Li,H-Rho(50%Li), determined from Rietveld refinement of laboratory X-ray powder diffraction data.

7.8. *In Situ* IR Spectroscopy of CO₂ Adsorption

To better characterise and understand the interactions of CO₂ with the framework and extra-framework cations, in-situ infra-red (IR) absorption spectroscopy measurements were performed on fully exchanged Rho samples at different equilibrium CO₂ pressures.

Full range (3550 -1000 cm⁻¹) of the infra-red spectra of CO₂ adsorbed on Na,Cs-Rho, Na-Rho, Li-Rho, K-Rho and Ca-Rho at CO₂ pressure from 0.25 to 150 mbar are presented in Figure 7.28. The infrared spectra of CO₂ adsorbed onto ion exchanged Rho zeolites at low coverages show a single strong band at around 2358 cm⁻¹ due to the ν_3 asymmetric stretching vibration of adsorbed CO₂. A similar shift has been previously reported¹⁹ and it attributes to interaction of CO₂ with the cations. As the CO₂ coverage is increased in Rho, the ν_3 band broadens and becomes too intense to monitor.

Direct evidence for a CO₂:cation interaction comes from observation of the ν_1 symmetric stretching vibration of adsorbed CO₂ in Rho as a weak band at 1378 cm⁻¹ (Figure 7.29). This vibration is infra-red forbidden for the gas phase molecule (at 1388 cm⁻¹), but becomes weakly allowed when the symmetry is lowered due to interaction with zeolite cations. In the case of Na,Cs-Rho, only the 1378 cm⁻¹ band was observed, increasing in intensity with increasing surface coverage. The 1378 cm⁻¹ band is also very visible when the CO₂ is adsorbed on Na-Rho. As the CO₂ coverage is increased in Na-Rho, an additional band appears in the ν_1 region at 1416 cm⁻¹. In light of the structural evidence for two different CO₂ adsorption sites in Na-Rho (see Table 7.7 and Figure 7.20), this band may be assigned to the ν_1 mode of a second form of adsorbed CO₂, occupying sites at higher coverage. As the extinction coefficient for this mode of adsorbed CO₂ will depend strongly on the local symmetry at the adsorption site, it is not possible to quantify from the infrared data the relative amounts of the two species. In the case of Li-Rho, the ν_1 region shows two distinct bands at all CO₂ coverages (1374 cm⁻¹ and 1382 cm⁻¹). Although this might be taken as evidence for the existence of two different CO₂ adsorption sites, an additional band was also seen to appear in parallel at 1635 cm⁻¹, which was not seen with any of the other Rho zeolites (Figure 7.30). Many authors report bands in this region due to adsorbed carbonate or bicarbonate when CO₂ is adsorbed in alkali metal zeolites, particularly in the presence of adsorbed water. It may be due to the small amounts of carbonate and/or

bicarbonate species that are formed when CO_2 is adsorbed in Li-Rho, which tends to be very hydrophilic (see Figure 7.7a).

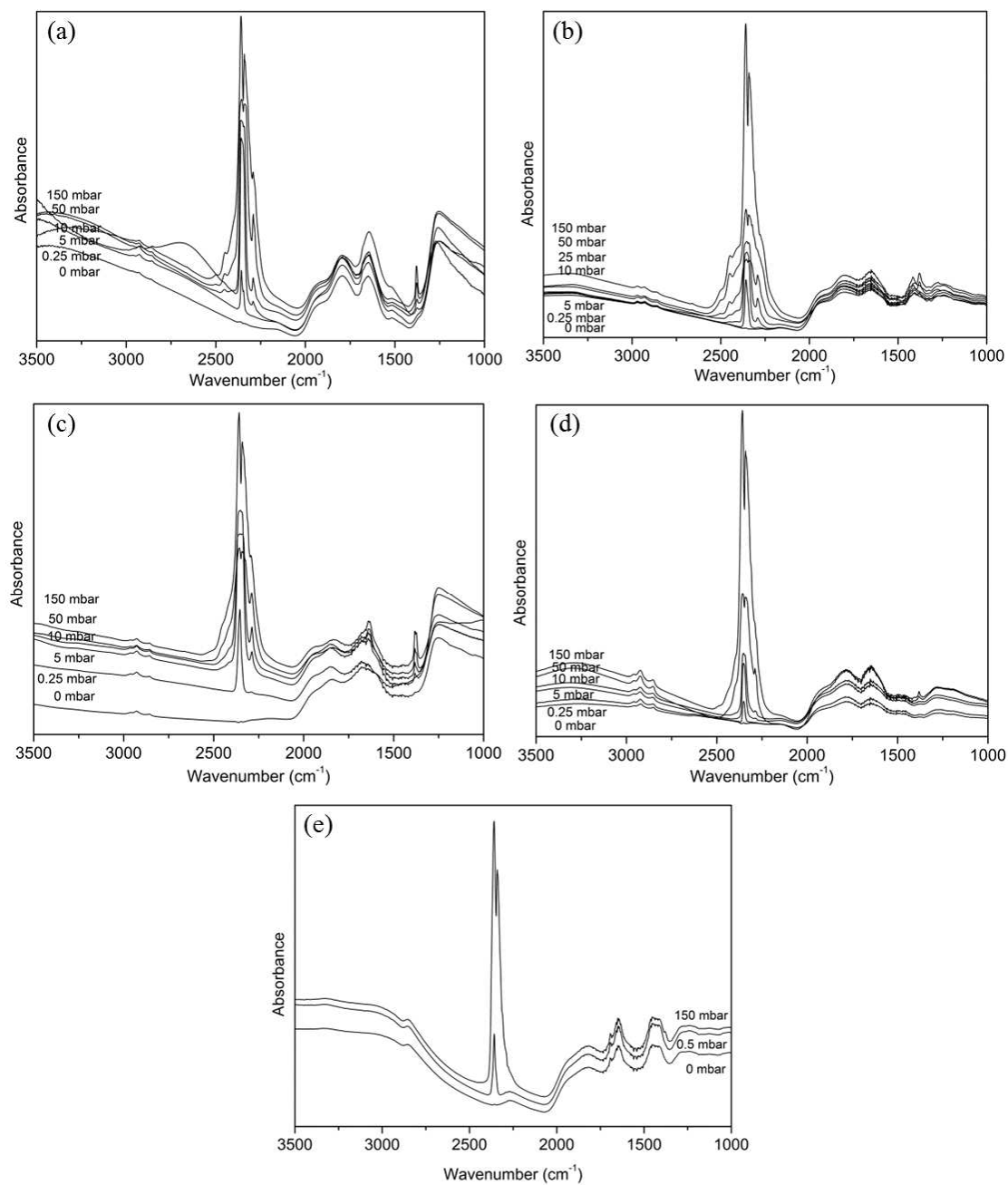


Figure 7.28. 3550 -1000 cm^{-1} range of the infra-red spectra of CO_2 adsorbed on (a) Na,Cs-Rho, (b) Na-Rho, (c) Li-Rho, (d) K-Rho and (e) Ca-Rho, measured as CO_2 is dosed at different equilibrium pressures.

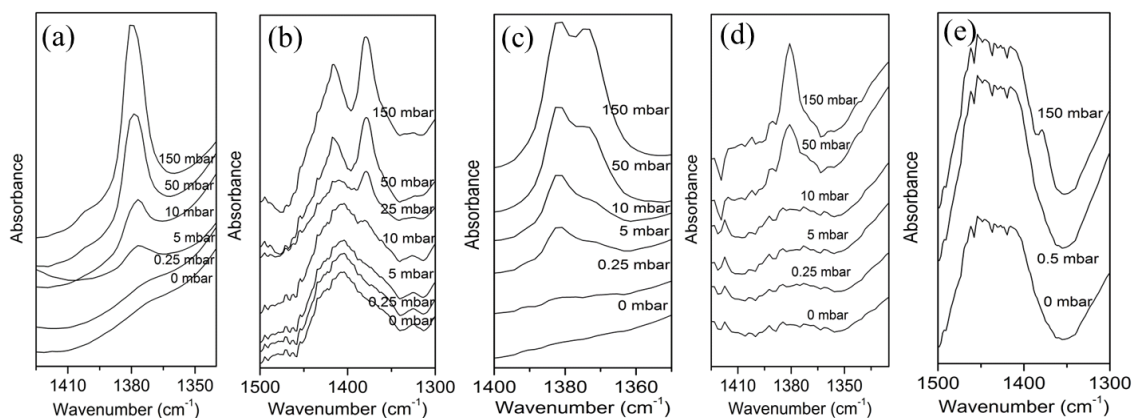


Figure 7.29. 1500 -1300 cm^{-1} range of the infra-red spectra of CO_2 adsorbed on (a) Na,Cs-Rho, (b) Na-Rho, (c) Li-Rho, (d) K-Rho and (e) Ca-Rho showing the development of the ν_1 symmetric stretch of CO_2 reacting with cations, measured as CO_2 is dosed at different equilibrium pressures.

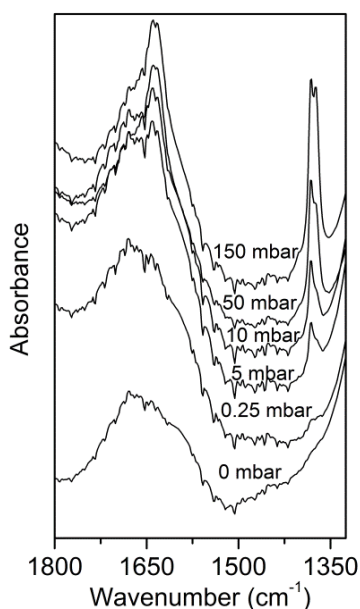


Figure 7.30. Expanded region of part of the IR spectrum of CO_2 adsorbed on Li-Rho, measured as CO_2 is dosed at different equilibrium pressures.

Additionally, in the ν_3 region, CO_2 adsorption in Li-Rho initially gave a band at 2355 cm^{-1} (Figure 7.31c), shifted from the frequency obtained with Na-Rho and Na,Cs-Rho. The higher frequency bands assigned to combination modes are present at approximately the same frequencies as in Na-Rho, Na,Cs-Rho and K-Rho (Figure 7.31a,b,d). Notably, the bands due to adsorbed CO_2 in Li-Rho are already well developed at a pressure of 0.25 mbar, more so than with the other zeolites, consistent with the different shapes of the adsorption isotherms (see Figure 7.23c). For K-Rho

also, a single band was observed in the ν_1 region (Figure 7.31d), although this band only became evident at pressures higher than those seen with other cationic Rho forms. The infra-red spectrum of Ca-Rho shows only one very weak band in the ν_1 region at 150 mbar pressure (Figure 7.31e). This may be explained by the CO_2 adsorption isotherm that shows there is not much CO_2 adsorbed on Ca-Rho even at 1000 mbar.

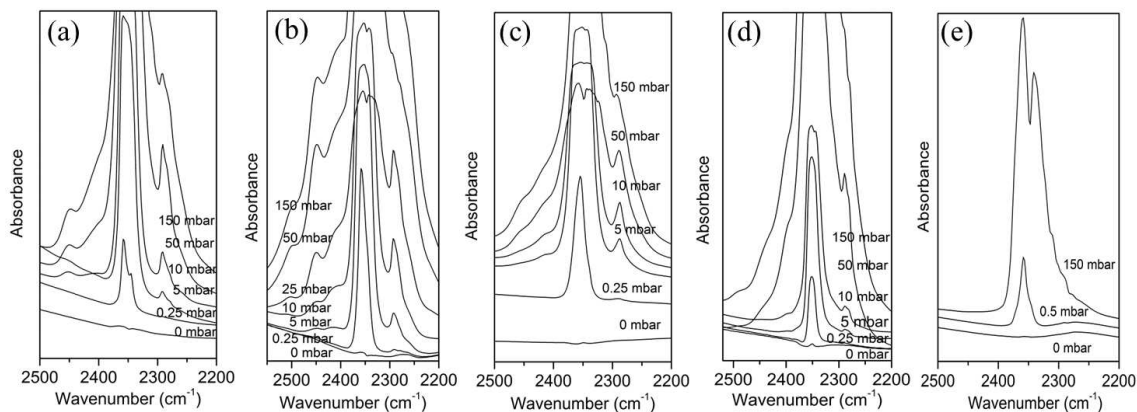


Figure 7.31. 2500-2200 cm^{-1} range of the infra-red spectra of CO_2 adsorbed on (a) Na,Cs-Rho, (b) Na-Rho, (c) Li-Rho, (d) K-Rho and (e) Ca-Rho showing the development of the ν_3 asymmetric stretch of CO_2 , measured as CO_2 is dosed at different equilibrium pressures.

7.9. A Detailed Examination of CO_2 Adsorption on Sodium Rho

Presence of mobile sodium cations in window sites ‘blocking’ or restricting access of CO_2 may suggest that the adsorption capacity of CO_2 on Na-Rho will not be as high as that on Li-Rho. However, Na-Rho shows an appreciable uptake at 0.1 bar, 298 K (at 3.2 mmol g^{-1} this is the same as that observed for Na-13X under the same conditions, see chapter 1). Furthermore, adsorption of CO_2 is more rapid on Na-Rho than on Na,Cs- or K-Rho, and so is more likely to be useful in processes requiring successive adsorption and desorption cycles. Finally, sodium is the least expensive and possesses the lowest affinity for water of the cations studied here. For these reasons, the mechanism of CO_2 adsorption on Na-Rho was studied in more detail. The additional studies included: (i) measurement of high resolution, low p_{CO_2} adsorption/desorption isotherms on Na-Rho at different temperatures; (ii) *in situ* synchrotron X-ray diffraction during CO_2 adsorption and desorption on Na-Rho and (iii) adsorption of ethane on H-Rho and Na-Rho. Together, the results obtained above for

Na-Rho and these experiments give an atomistic and quantitative description of the mechanism by which CO_2 is adsorbed and desorbed from zeolite Na-Rho.

(i) Variable temperature CO_2 adsorption/desorption isotherms

CO_2 sorption isotherms at 273 K, 298 K and 308 K (measured up to 140 mbar) for Na-Rho show strong deviation from Type I behaviour at low pressure, and strong hysteresis in the desorption branch (Figure 7.32). The CO_2 adsorption behaviour of Na-Rho lies intermediate between Li-Rho which shows a Type I isotherm with very little hysteresis (see Figure 7.23d) and K-Rho, which shows more strongly pronounced deviation (see Figure 7.23e). Hysteresis and non-Type I isotherms suggest that there is a structural change and/or dynamic effects during the adsorption. The increase in uptake as temperature decreases suggests that thermodynamic rather than kinetic factors predominate.

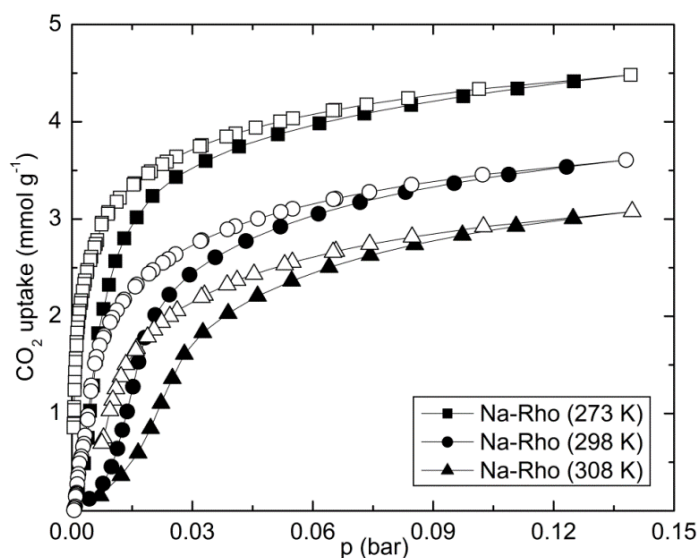


Figure 7.32. CO_2 isotherms up to 140 mbar for Na-Rho at 273 K, 298 K, 308 K. Adsorption, closed symbols; desorption, open symbols.

(ii) *In situ* PXRD studies of CO_2 adsorption

To investigate possible structural changes upon CO_2 adsorption onto Na-Rho, structural studies during the adsorption and desorption process were performed *in situ* by synchrotron PXRD. X-ray diffraction patterns were first collected on hydrated Na-Rho, and then dehydrated Na-Rho patterns were collected before and after admitting CO_2 to the gas cell at equilibrium P_{CO_2} values of 0.1 bar, 0.2 bar, (on desorption loop)

0.045 bar and after evacuation, these are presented in Figure 7.33. The experimental for *in situ* synchrotron PXRD is described in chapter 4.

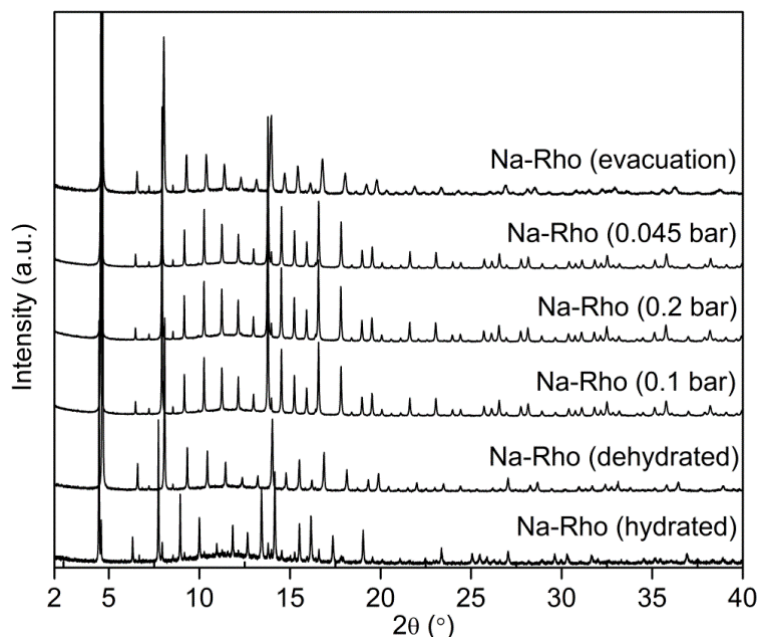


Figure 7.33. Synchrotron X-ray powder diffractions of hydrated Na-Rho, dehydrated, dehydrated Na-Rho with 0.1 bar equilibrium pressure of CO₂, 0.2 bar equilibrium pressure of CO₂, (on desorption loop) 0.045 bar of CO₂, after evacuation for ca. 20 minutes. The (offset) patterns have been collected at 298 K using the same operating conditions.

Occupancy of the cation sites, defined as types I, II and III, are given in Table 7.8, with full details of the atomic coordinates supplied in the appendix. Rietveld refinement plots of dehydrated Rho samples with and without CO₂ are given in Figure 7.34.

Hydrated Na-Rho solid has $Im\bar{3}m$ symmetry, $a = 14.9573(1)$ Å, and in the dehydrated state has $I\bar{4}3m$ symmetry, with $a = 14.4136(3)$ Å. As observed from the laboratory data, sodium cations occupy S8R sites (one cation per window between cages) with two Na⁺ cations in S6R sites in each α -cage (around 1 per two sites). Upon adsorption of CO₂ at 0.1 bar, the unit cell increases to $a = 14.6281(7)$ Å, but the symmetry remains as $I\bar{4}3m$. The expected uptake at 0.1 bar on the adsorption branch of the isotherm is 3.07 mmol g⁻¹, corresponding to 9.8 molecules of CO₂ per unit cell. Difference Fourier analysis together with constrained refinement locates two sites for CO₂ molecules in the Na-Rho structure at this point on the isotherm, one of which resides partly in the D8R and the other in the large α -cage. Careful examination of the refined positions of the

CO₂ molecules, together with those of the Na⁺ cations (all of which are at partial occupancy) at 0.1 bar suggested a likely configuration for CO₂ at the two sites as presented in Figure 7.35. In the first location (A) the CO₂ molecule adopts end-on coordination with one Na⁺ cation in the S8R, with a Na–O distance of 2.88(2) Å, through the D8R cage windows to project into the α -cage, where its other O atom is 4 Å from Na⁺ cations. In the second location (B) the CO₂ molecule adopts end-on coordination with one α -cage Na⁺ cation, with a Na–O distance of 2.58(1) Å, with the second O atom at its closest 4.5 Å from a second α -cage Na⁺ cation.

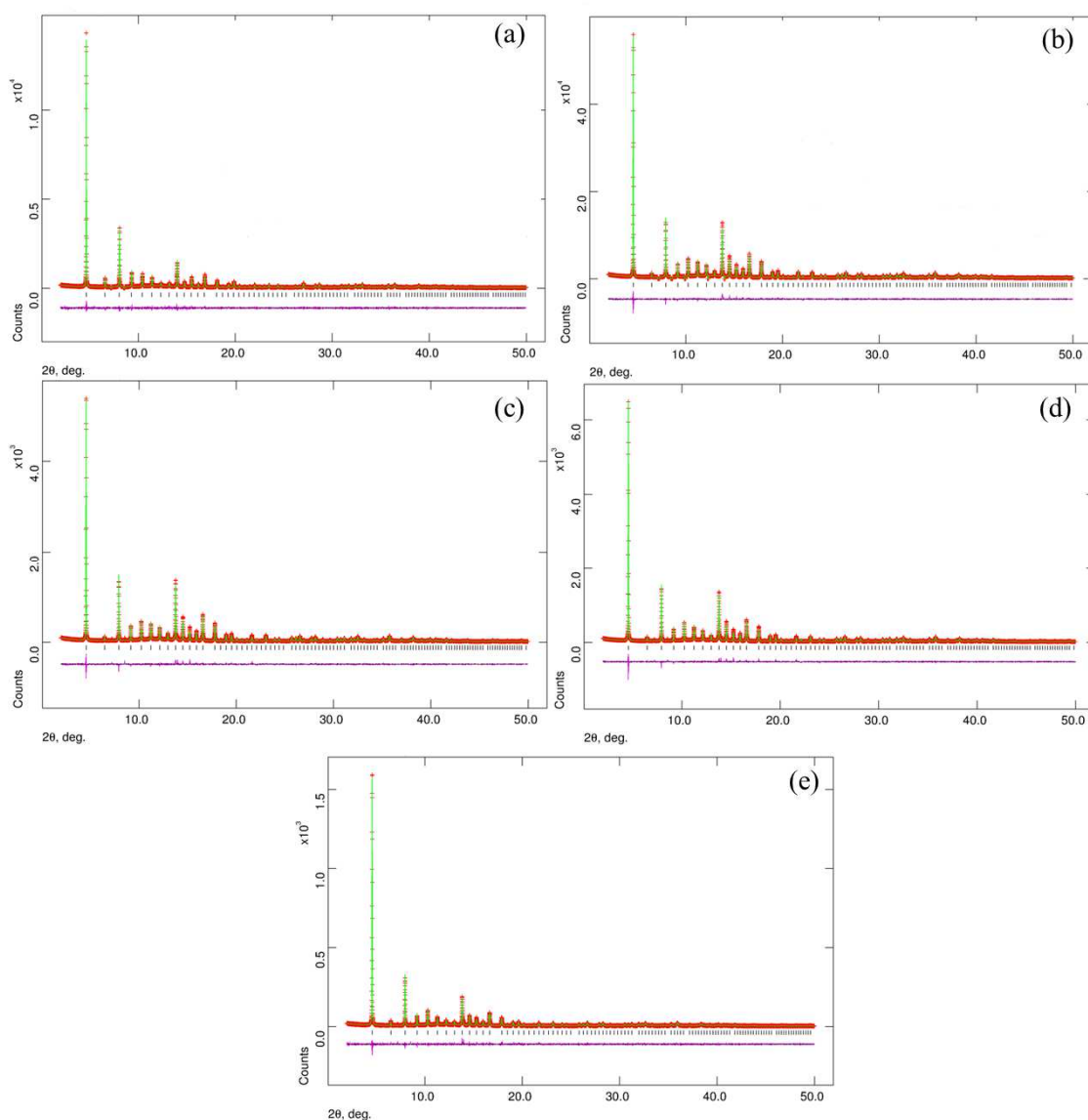


Figure 7.34. Rietveld plots of in situ synchrotron PXRD profiles of (a) dehydrated Na-Rho with (b) 0.1 bar equilibrium pressure of CO₂, (c) 0.2 bar equilibrium pressure of CO₂, (d) (on desorption loop) 0.045 bar CO₂ and (e) after evacuation for 20 minutes, collected at 298 K.

Table 7.8. Space group, minimum O–O distance of S8R windows and cation site occupancies in dehydrated zeolite Na-Rho (Site I, D8R; Site II, S8R; Site III, S6R) as determined by Rietveld refinement from laboratory powder X-ray diffraction collected at 298 K.

Sample	Unit cell parameter /Å	Space group	O–O /Å	Site I		Site II		Site III	
				Frac. Occup.	Cations/unit cell	Frac. Occup.	Cations/unit cell	Frac. Occup.	Cations/unit cell
Na-Rho	14.4134(10)	$I\bar{4}3m$	2.17	-	-	0.5	6.0	0.389(8)	3.11(8)
Na-Rho (0.1bar)	14.62823(6)	$I\bar{4}3m$	2.78	-	-	0.5	6.0	0.4	3.2
Na-Rho (0.2 bar)	14.63480(6)	$I\bar{4}3m$	2.69	-	-	0.5	6.0	0.4	3.2
Na-Rho (0.045bar)	14.62190(6)	$I\bar{4}3m$	2.77	-	-	0.5	6.0	0.4	3.2
Na-Rho (evac)	14.5633(12)	$I\bar{4}3m$	2.65	-	-	0.5	6.0	0.4	3.2

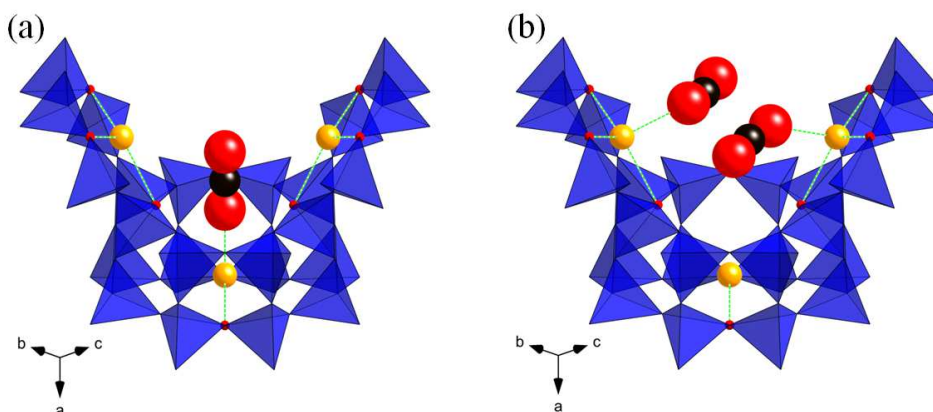


Figure 7.35. Adsorption sites for CO_2 in Na-Rho, as determined by Rietveld refinement of the synchrotron X-ray diffraction data at 298 K, with an equilibrium pressure of 0.1 bar. In adsorption (a) site A the $\text{O}=\text{C}=\text{O}$ molecules adopt end-on coordination with Na^+ (orange spheres) in the S8R site, whereas (b) in site B they directly coordinate a S6R Na^+

Notably, simulation of adsorption of CO_2 in zeolite Na-A at levels up to 3 molecules per α -cage suggests all CO_2 molecules interact with 2 (or 3) Na^+ cations, and the CO_2 molecules interact most strongly with cations in S6R and S8R sites.²⁰ Similarly, the presence of strong CO_2 adsorption sites has been postulated via simulation of CO_2 adsorption into sodium ferrierite.²¹

Sodium cations in the D8R adjust their position as this adsorption occurs (Figure 7.36) so the crystallographic $\text{Na}^+ - \text{Na}^+$ distance, at $1.73(1) \text{ \AA}$, precludes occupancies above 50%, and so supports a model where there is 1 Na^+ per D8R window.

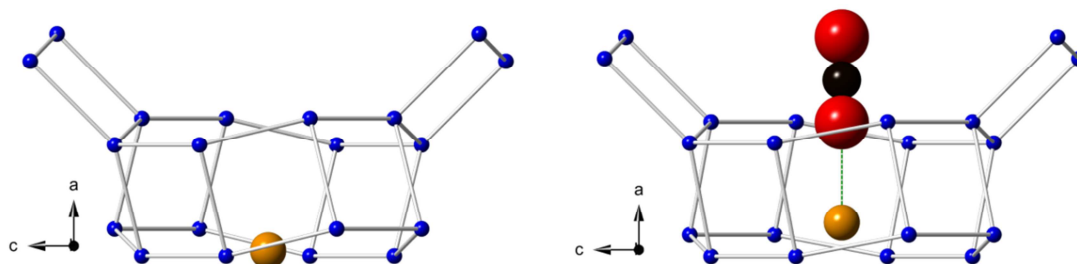


Figure 7.36. Simplified structural representation of movement of Na^+ within site II as CO_2 is adsorbed at 0.1 bar, 298 K (right) onto a dehydrated Na-Rho (left).

At 0.2 bar CO_2 there is a slight expansion in the unit cell (to $14.63480(6) \text{ \AA}$), but it is not possible to locate all the adsorbed CO_2 molecules, probably because some are disordered within the α -cage and disrupt the ordering scheme at sites A and B. Upon reducing the equilibrium pressure to 0.045 bar, there is a small reduction in the unit cell parameter again (to $14.62190(6) \text{ \AA}$) but the refined site occupancies remain unchanged. This is to be expected from the shallow desorption branch observed in the low pressure isotherms shown in Figure 7.32. It is only when the sample is opened to vacuum that the unit cell begins to contract sharply, as the steep part of the desorption branch is descended. The decrease of the unit cell is plotted against time of evacuation in Figure 7.37. Refinement indicates that after a few minutes evacuation the amount of ordered CO_2 in the pores has decreased, but the relative occupancy of the two sites stays unchanged.

Two possible arrangements of Na^+ cations and CO_2 molecules in the Na-Rho structure at 298 K and 0.1 bar are shown in Figure 7.38, taking into account possible arrangements of Na^+ cations and CO_2 molecules derived from the refinements.

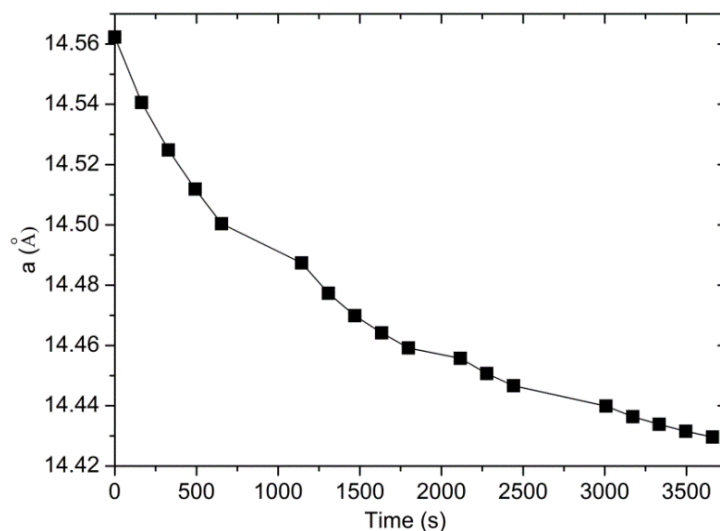


Figure 7.37. Unit cell parameter variation with time as Na-Rho pre-loaded with CO_2 at 0.045 bar and 298 K was subject to evacuation.

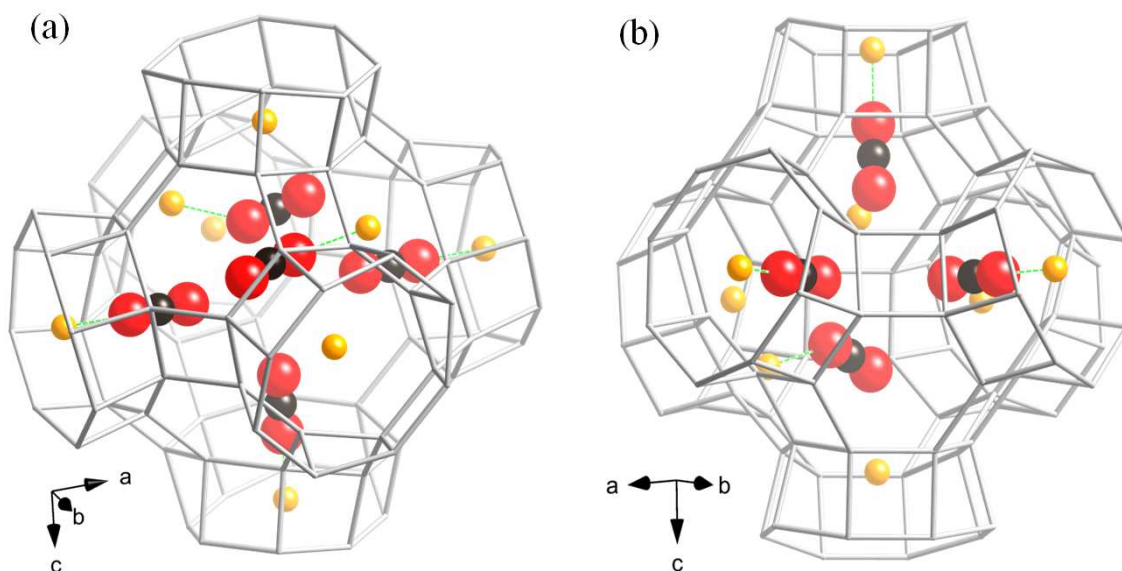


Figure 7.38. Two possible arrangements (a) and (b) of Na^+ cations and CO_2 molecules within an α -cage of Na-Rho that is in equilibrium with 0.1 bar of CO_2 at 298 K. These are based on the refined structure and a consideration of possible arrangements of cations and CO_2 molecules, given the observed statistical occupancies.

For diffusion of CO_2 through the Na-form of zeolite Rho, it is clear that the cations must move away from the sites that they occupy in the window sites of the dehydrated zeolite. That the site occupancies measured by diffraction do not change during the adsorption/desorption process in zeolite Na-Rho indicates that the cations can

rapidly move back to their original site once the CO_2 molecule has diffused through. It is suggested that Na^+ cations can move from S8R sites to vacant S6R sites, and back again, in the presence of CO_2 molecules, thereby allowing CO_2 molecules to diffuse through the window sites. One possible mechanism for CO_2 adsorption on Na-Rho is presented in Figure 7.39.

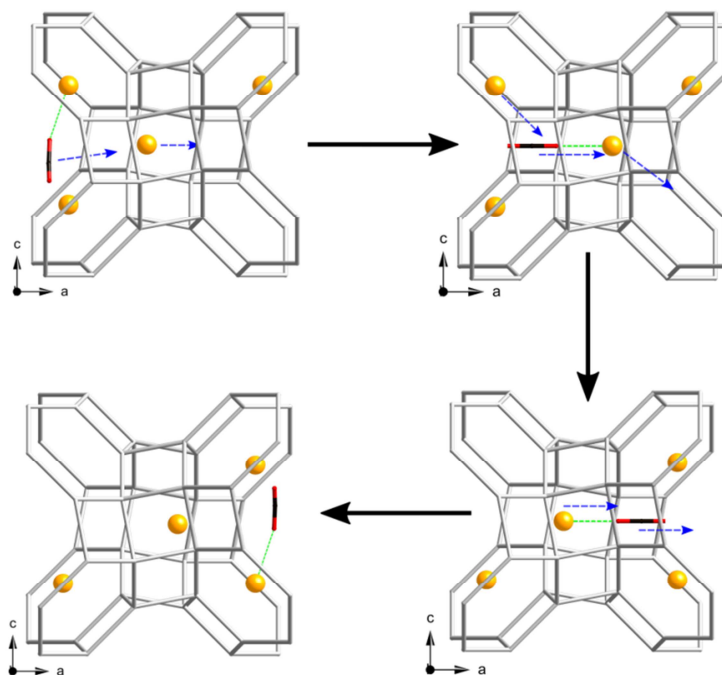


Figure 7.39. Postulated cooperative mechanism by which CO_2 molecules (represented by red and black ‘sticks’) could pass through a window site between α -cages in zeolite Na-Rho, where a Na^+ (yellow sphere) occupies one of the S8R sites in the window.

(iii) Comparison of ethane uptake on Na-Rho with that on H-Rho

The adsorption behaviour of ethane on Na-Rho at 298 K was compared with that over H-Rho. Whereas ethane is taken up by H-Rho (at 0.7 bar, the uptake is 1.65 mmol g^{-1}), it is effectively blocked from adsorption into Na-Rho (Figure 7.40). Ethane is a larger molecule than CO_2 , 3.90 \AA compared to 2.98 \AA (for the smaller dimension of CO_2 via a 2-centre Lennard-Jones model), so this may be due to the restricted size of the S8R opening in the presence of cations in the windows elsewhere in the structure or due to the physical presence of the cations. The lower interaction energies of cations with hydrocarbons than with carbon dioxide may not be enough to enable cations to move

away from their window blocking locations. The resultant effect is high selectivity for Na-Rho for CO₂ over ethane in mixtures, similarly to that observed previously for Na,Cs-Rho for CO₂/CH₄ mixtures.¹¹

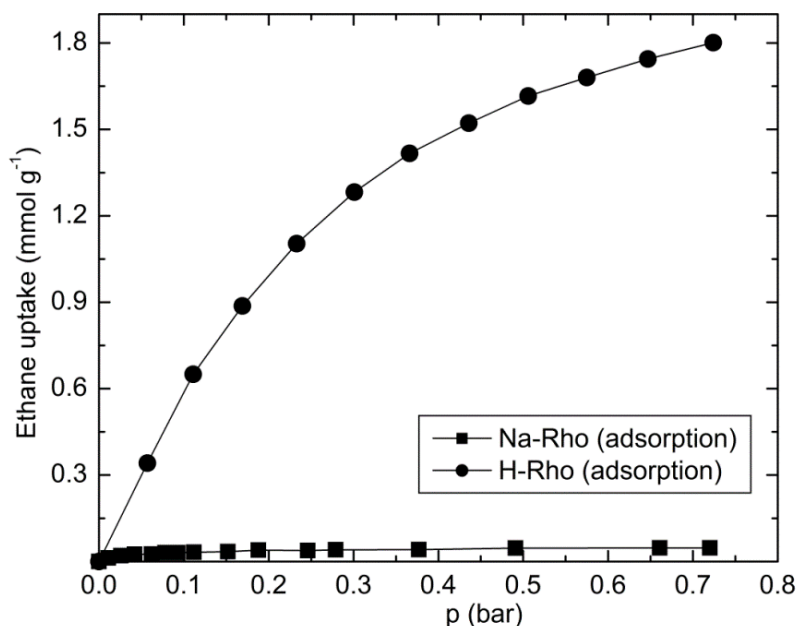


Figure 7.40. Ethane adsorption on H-Rho and Na-Rho at 298 K.

7.10. High Pressure CO₂ Adsorption and CO₂/CH₄ Selectivity Studies

Study of a range of single cation forms of Rho at pressures below 1 bar shows that the cation type strongly affects the adsorption behaviour, which is a function of cation location and charge density. The resultant effects on the flexible framework include a volume decrease of up to 7% compared to the fully symmetric form.²² Adsorption on Rho shows the uptake of CO₂ at pressures up to 1 bar decreased strongly in the order Li > Na > K > Cs > Ca, and the hysteresis increased. Cs-Rho and Ca-Rho show very low CO₂ adsorption at 1 bar at 298 K, while for K-Rho there is very large hysteresis observed (see Figure 7.23). Recent studies have shown that in small pore structures where cages are linked by S8R windows, when cations occupy sites in these windows (like in Cs-, K-, and Ca-Rho), it is possible to achieve high and selective uptake of CO₂ over gases such as N₂ or small hydrocarbons.^{11,22} The Cs,Na-Rho shows high selectivity to CO₂ over CH₄ and N₂.^{10,11} In this part of the study, in collaboration with Instituto de Tecnologia Quimica in Valencia, the behaviour of univalent Cs-, K-Rho and divalent Ca-Rho at pressures up to 9 bar for the uptake of CO₂ and CH₄, by gravimetric adsorption and by *in situ* PXRD was investigated.

CO₂ and CH₄ adsorption isotherms obtained for Ca-, Cs-, K- and Na-Rho are shown in Figure 7.41. The theoretical CO₂/CH₄ equilibrium selectivity factor (α) was calculated from single component isotherms using equation 4.3 in chapter 4. For all samples high pressure CO₂ adsorption increases gradually with increasing pressure up to 9 bar. The CH₄ uptake is low on all samples, and the ‘selectivities’ are 11–12 for Ca-Rho, 20–15 for Cs-Rho, 50–20 for K-Rho and 150–25 for Na-Rho at 1–9 bar and 298 K. Cs-Rho, K-Rho and Na-Rho adsorb less CO₂ when adsorption temperature increases, while Ca-Rho shows higher adsorption of CO₂ at higher temperature (333 K) which indicates a kinetic dependence on the adsorption uptake for this material. Na-Rho possesses the highest CO₂/CH₄ ‘selectivity’ ever reported for a zeolite. For Na-Rho CO₂ adsorption at high pressure stays very high (between 5.7 and 5.0 mmol g⁻¹) for all adsorption temperatures investigated whereas for CH₄ it is unchanged and at very low level. The high selectivity for CO₂ over CH₄ for Rho samples arises because the methane interacts much more weakly and does not reduce the barrier for migration of cations away from blocking positions.

To investigate the behaviour of these materials during CO₂ adsorption, *in situ* PXRD with high pressure CO₂ adsorption on Cs-Rho was measured (Figure 7.42). PXRD data of Cs-Rho reveals the different behaviour for Cs-Rho compared to Na-Rho during CO₂ adsorption. For Na-Rho, the unit cell increases and decreases gradually as CO₂ is adsorbed and desorbed and the Na⁺ cation location in the cell changes only slightly (see Figure 7.33). For Cs-Rho, by contrast, the structure exists as a mixture of two different structural forms of the zeolite, $I\bar{4}3m$ and $Im\bar{3}m$ (Figure 43), the relative amounts of which change with increased CO₂ uptake (100% of $I\bar{4}3m$ for dehydrated decreases to *ca.* 80% for 1 bar, *ca.* 50% for 2bar, *ca.* 8% for 3 bar and 0% for 4 bar and 5 bar).

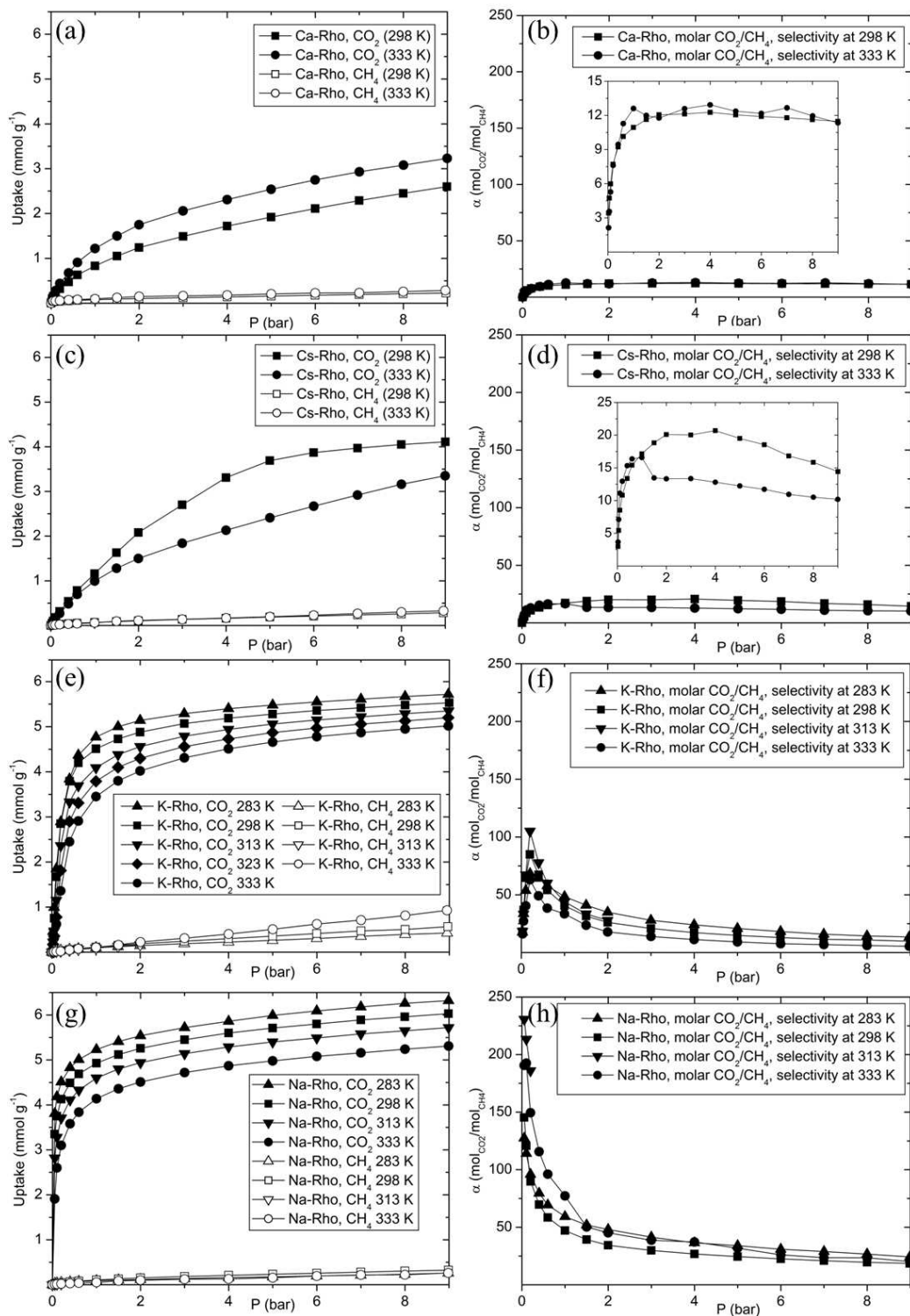


Figure 7.41. (a), (c), (e), (g) CO₂ and CH₄ adsorption isotherms of Cs-Rho at temperature between 298 K and 333 K, and (b), (d), (f), (h) CO₂/CH₄ equilibrium selectivity factor according to volumetric and gravimetric measurements of Ca-, Cs-, K- and Na-Rho. Data collected at Instituto de Tecnología Química in Valencia.

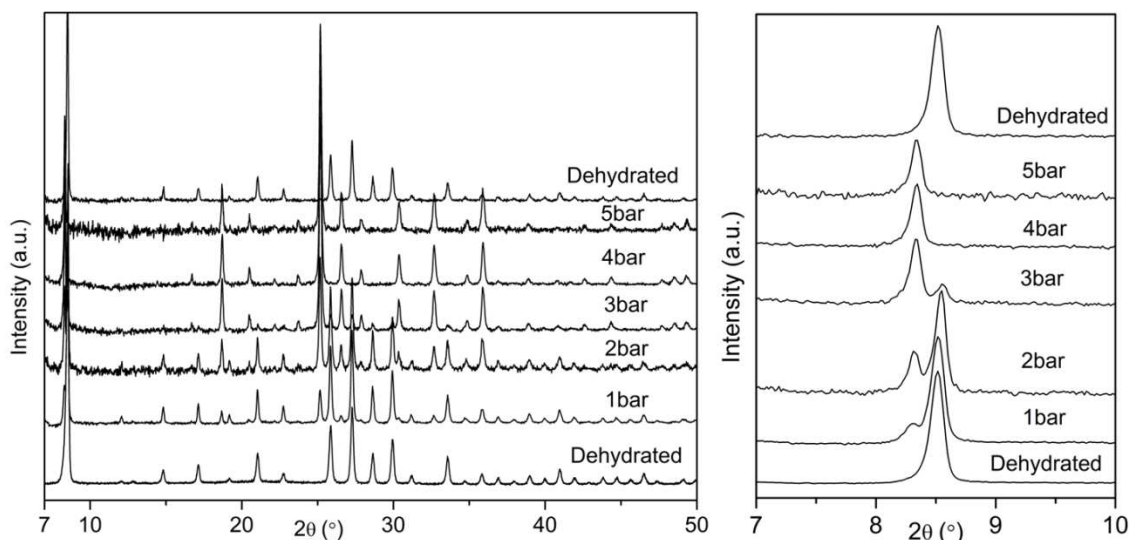


Figure 7.42. In situ PXRD of Cs-Rho during CO_2 adsorption up to 5 bar. The inset on right show magnified images of first peak. The (offset) patterns have been collected at 298 K using the same operating conditions. Data collected at Instituto de Tecnologia Quimica in Valencia.

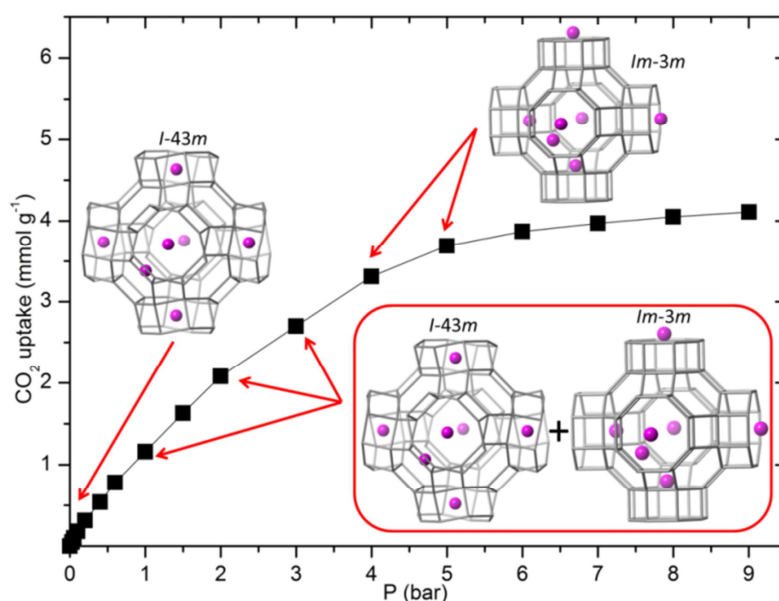


Figure 7.43. CO_2 adsorption isotherm of Cs-Rho showing the changes of the sample symmetry during high pressure CO_2 adsorption.

Structural changes during CO_2 adsorption for Cs-Rho were investigated by Rietveld refinement. Due to the increasing amount of the second phase ($Im\bar{3}m$), that results in overlapping reflections the structure refinement and location of Cs^+ cations and CO_2 in samples with 1 bar, 2 bar and 3 bar of CO_2 were impossible to obtain. The Rietveld

analysis was conducted on the dehydrated Cs-Rho and at a CO₂ pressure of 4 bar, where only one phase is visible. Crystallographic details from Rietveld analysis of these samples are given in the appendix. Final observed, calculated and difference Rietveld plots for the powder data refinement are presented in Figure 7.44. Refined unit cell parameters, cation locations and occupancies in dehydrated Cs-Rho and Cs-Rho in equilibrium with 4 bar of CO₂, obtained by Rietveld analysis of laboratory powder X-ray data collected at 298 K are presented in Table 7.9.

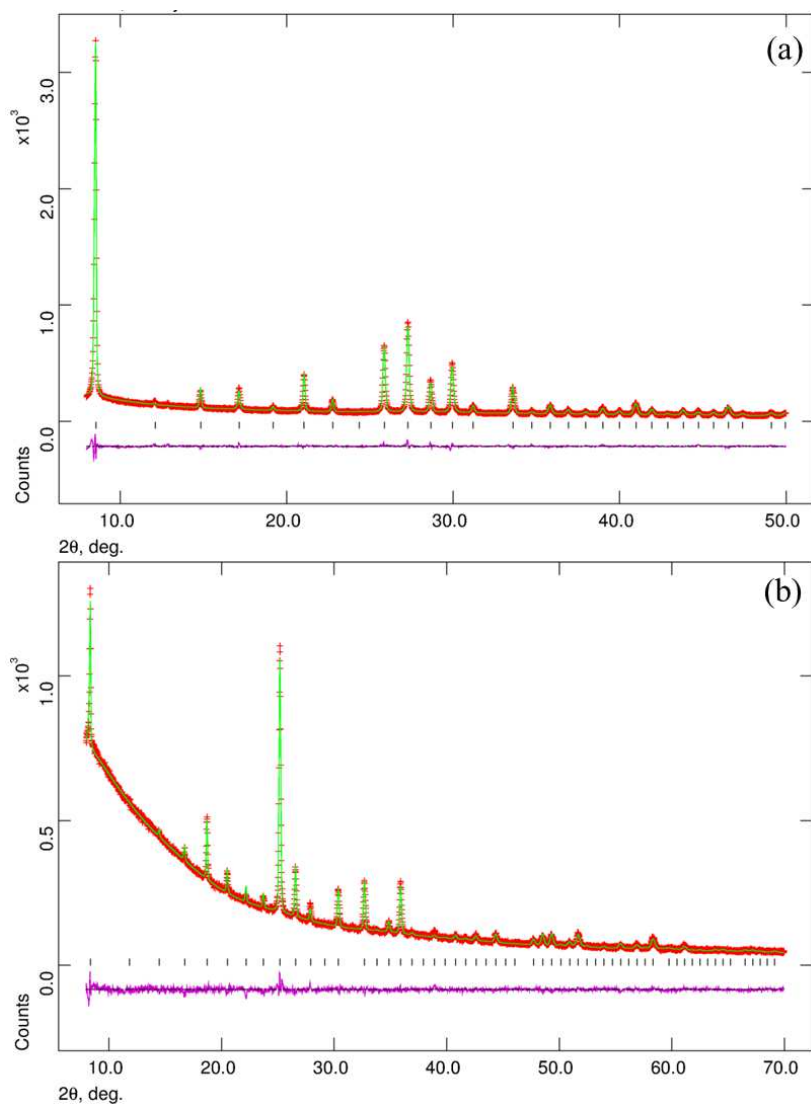


Figure 7.44. Final observed, calculated and difference Rietveld plots for the powder data refinement of (a) dehydrated Cs-Rho and (b) Cs-Rho in equilibrium with 4 bar of CO₂.

Possible arrangements of Cs⁺ cations and CO₂ molecules of dehydrated Cs-Rho and Cs-Rho in equilibrium with 4 bar of CO₂ are given in Figure 7.45. The refinement results

obtained on dehydrated Cs-Rho are similar to those described in section 7.3 (see Figure 7.20 and Table 7.5), where the structure adopts $I\bar{4}3m$ symmetry, cations occupy D8R (6 Cs⁺ per unit cell) and S6R (3 Cs⁺ per unit cell) and $a = 14.5817(1)$ Å. It was difficult to locate the CO₂ molecules from the PXRD laboratory data of Cs-Rho with 4 bar of CO₂, but strong electron density in the middle of α -cage was clearly visible. The only refined CO₂ position is close to the plane of D8R window sites. The Rietveld refinement reveals that all Cs⁺ cations, when 4 bar of CO₂ is adsorbed, move from D8R sites to S8R sites (Table 7.9), while the Cs⁺ window cations in S6R remain in the same position. The Cs–O distances are 3.34(1) Å for the Cs⁺ cations in S8R site and 3.31(2) Å for the Cs⁺ cations in S6R site. The Cs–O distance between Cs⁺ cations in S8R site and the closest O atom from CO₂ is 3.64(2) Å. It can be concluded that the changes in PXRD pattern of Cs-Rho with 4 bar of CO₂ result from a migration of the Cs from a D8R site to a S8R site (Table 7.9), with a corresponding lattice expansion ($a = 14.5817(1)$ Å for the dehydrated sample and $a = 14.9991(6)$ Å for Cs-Rho with 4 bar of CO₂) and symmetry change from $I\bar{4}3m$ to $Im\bar{3}m$. This concerted change within crystals arises as the Cs⁺ achieves coordination with CO₂ molecules when in the S8R site, and subsequent CO₂ diffusion is easier.

Due to the mixture of two phases in Cs-Rho during CO₂ adsorption a schematic diagram presenting the CO₂ uptake on Cs-Rho from a thermodynamic point of view has been prepared (Figure 7.46). For pressures below 2 bar, $I\bar{4}3m$ symmetry is more stable due to better coordination of framework oxygen atoms with caesium atoms. When pressure increases above 2 bar CO₂ molecules adsorb more easily on caesium cations which occupy S8R sites. When caesium cations move from D8R site to S8R, the D8R unit becomes more symmetric and $Im\bar{3}m$ symmetry becomes more stable.

Table 7.9. Refined unit cell parameters, cation locations and occupancies in Cs-Rho and Cs-Rho in equilibrium with 4 bar of CO₂, obtained by Rietveld analysis of laboratory X-ray data collected at 298 K.

Sample	Unit cell parameter /Å	Space group	O··O /Å	Site I		Site II		Site III	
				Frac. Occup.	Cations/unit cell	Frac. Occup.	Cations/unit cell	Frac. Occup.	Cations/unit cell
Cs-Rho	14.5817(1)	$I\bar{4}3m$	2.88	1.00	6.00	-	-	0.42(3)	3.39(2)
Cs-Rho (4bar)	14.9991(6)	$Im\bar{3}m$	3.92	-	-	0.53(2)	6.36(2)	0.19(2)	3.07(3)

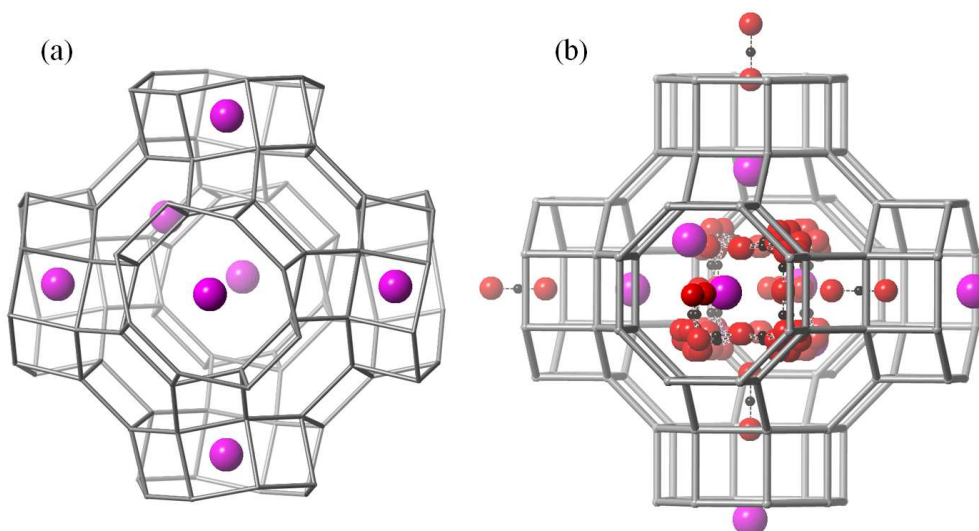


Figure 7.45. Possible arrangements of Cs^+ cations and CO_2 molecules within an α -cage of Cs-Rho that is (a) dehydrated and (b) in equilibrium with 4 bar of CO_2 at 298 K. These are based on the refined structure.

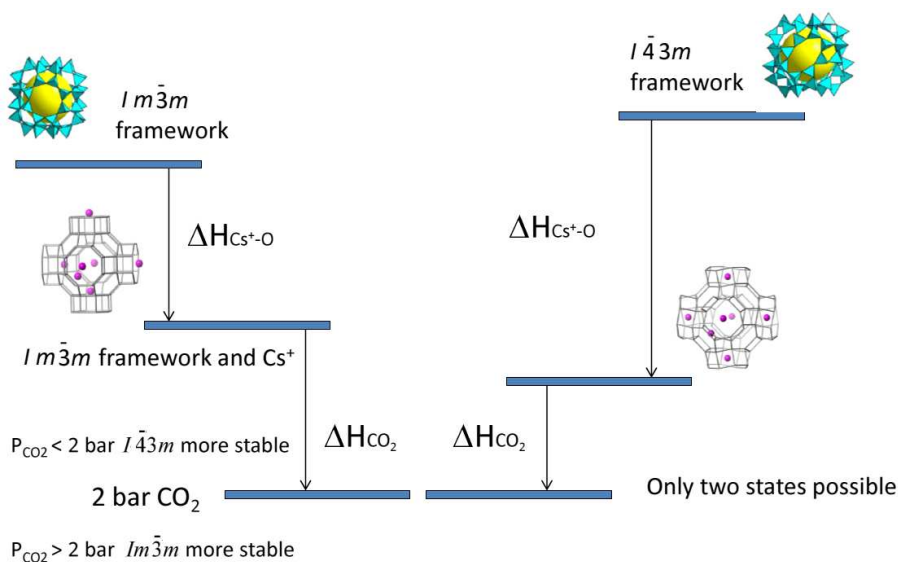


Figure 7.46. A schematic diagram presenting the CO_2 uptake on Cs-Rho from a thermodynamic point of view.

Highly selective CO_2 adsorption behaviour of many forms of zeolite Rho can be attributed to the ability of CO_2 to mediate ‘trapdoor motion’ (described previously by Reisner *et al.*,²³ for migration of Cd^{2+} in the presence of water) of the cation positions away from the S8R windows to allow adsorbate passage between cages, whereas molecules that interact less strongly (for example CH_4) do not permit this.

7.11. Comparison of Zeolite Rho with SAPO(RHO)

Chemico-physical and adsorption properties of aluminosilicate H-Rho and Na-Rho were compared with silicoaluminophosphate H-SAPO(RHO) and Na-SAPO(RHO). The H-SAPO(RHO) for this study was prepared by hydrothermal synthesis and ion exchanged as described in chapter 4.

PXRD was used to identify the crystallinity of the as-prepared hydrated H-SAPO(RHO) and to investigate the changes of zeolite structure caused by removing the template and the ion exchange with sodium. The PXRD pattern of as-prepared H-SAPO(RHO) shows well-resolved and sharp diffraction peaks in the region of $5.0\text{--}50.0^\circ 2\theta$ (Figure 7.47). The H-SAPO(RHO) reflections of the as-prepared hydrated sample are associated with $I23$ cubic symmetry with the unit cell parameters $a = 15.1102(1) \text{ \AA}$.

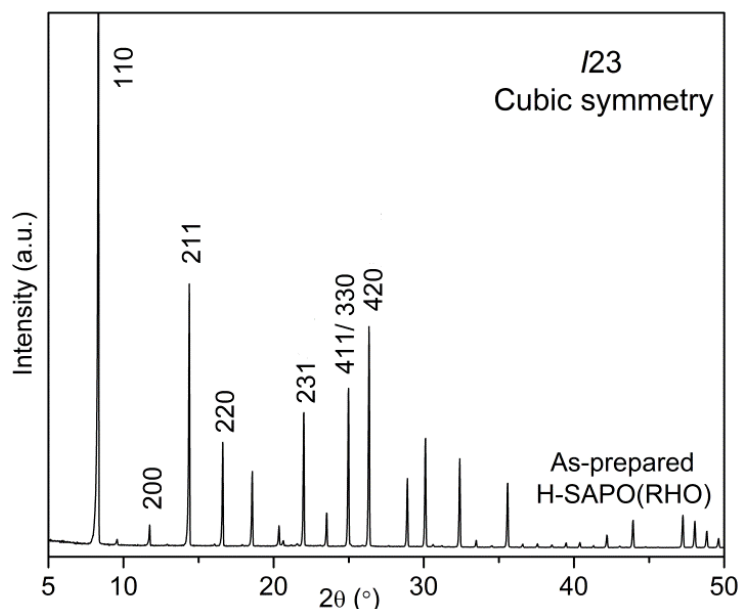


Figure 7.47. PXRD pattern of as prepared H-SAPO(RHO) indexed according to the cubic $I23$ symmetry.

TGA was used to determine the most effective temperature for template removal or H-SAPO(RHO) (Figure 7.48a). The first weight loss of *ca.* 5% before 400 K is attributed to desorption of physisorbed water. In the higher temperature range from 400 K to 900 K, the second weight loss of around 17% (three stages) is related to the removal of template (diethyl amine; DEA). The TGA suggests that the lowest temperature at which the DEA is completely removed is 823K. The H-SAPO(RHO) was found to be stable to template removal without loss of crystallinity (Figure 7.48b).

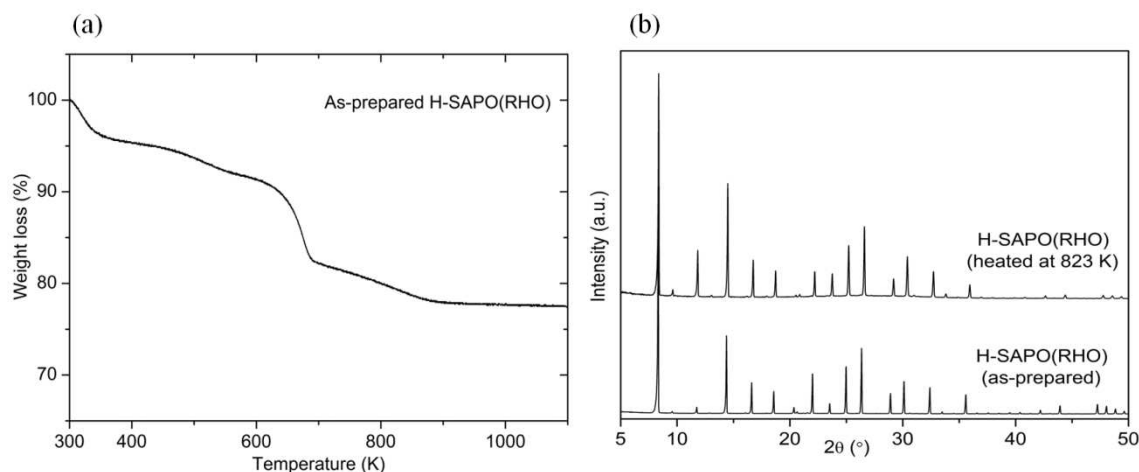


Figure 7.48. (a) TGA curve of as-prepared H-SAPO(RHO) and (b) PXRD patterns of as-prepared H-SAPO(RHO) and H-SAPO(RHO) after template removal. The (offset) patterns have been collected at 298 K using the same operating conditions.

Hydrogen cations in SAPO(RHO), heated at 823 K, were exchanged for Na^+ cations. The ion exchange of SAPO(RHO) is described in chapter 4. The degree of ion exchange was measured using X-ray energy dispersive spectroscopy (EDX). The EDX confirms that H^+ cations were exchanged for Na^+ cations in SAPO(RHO). No other elements apart from the framework O, Si, Al, P and extra-framework Na are visible in the EDX spectra (Figure 7.49). The EDX analysis of the SAPO(RHO) (after template removal) gives an estimated unit cell composition of $\text{H}_4\text{Si}_4\text{Al}_{24}\text{P}_{20}\text{O}_{96}$ and $\text{Na}_4\text{Si}_4\text{Al}_{24}\text{P}_{20}\text{O}_{96}$ for the ion exchanged sample (Table 7.10). EDX analysis gives Si/Al ratios of 0.17 for both samples. The formula for the derivation of the unit cell composition is given in chapter 4.

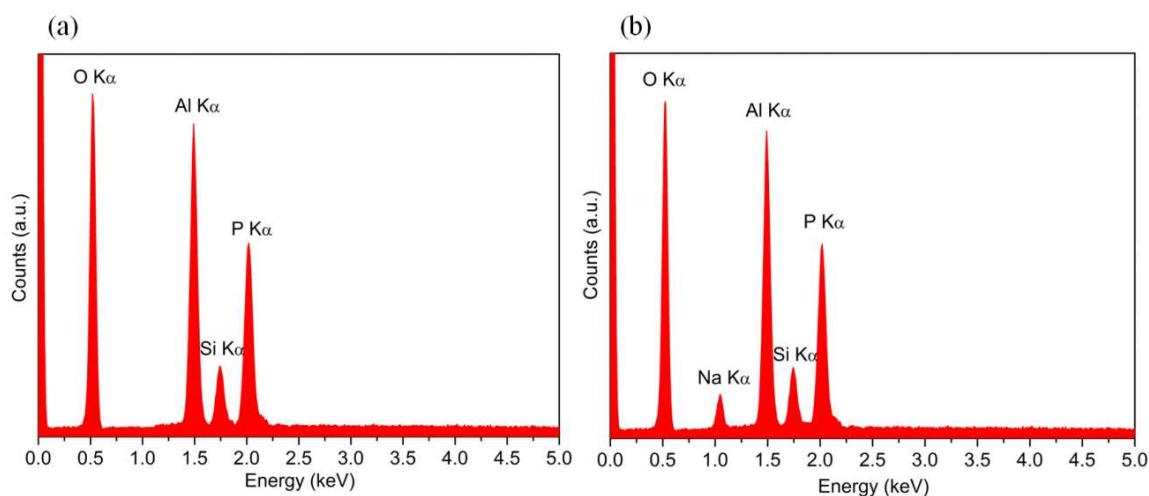


Figure 7.49. EDX spectra of (a) H-SAPO(RHO) and (b) Na-SAPO(RHO).

Table 7.10. EDX analysis of SAPO(RHO) before and after ion exchange.

Sample	Atomic %					Unit cell formula of dehydrated samples
	O	P	Si	Al	Na	
H-SAPO(RHO)	74 ± 1	11 ± 1	2 ± 0.5	13 ± 1	N.D.	H ₄ Si ₄ Al ₂₄ P ₂₀ O ₉₆
Na-SAPO(RHO)	72 ± 1	11 ± 1	2 ± 0.5	13 ± 1	2 ± 0.5	Na ₄ Si ₄ Al ₂₄ P ₂₀ O ₉₆

Values for oxygen are semi-quantitative

N.D. – not detected

Morphology of H- and Na-SAPO(RHO) samples was investigated by SEM analysis. The SEM micrograph of H-SAPO(RHO) (Figure 7.50a) indicates that the synthesis gave 12 μm rhombic dodecahedron crystals, similar to that of H-SAPO(RHO) reported by Su *et al.*²⁴ The ion exchange does not have an influence on the shape and size of the crystals which is confirmed by the SEM micrograph of ion exchanged Na-SAPO(RHO) (Figure 7.50b).

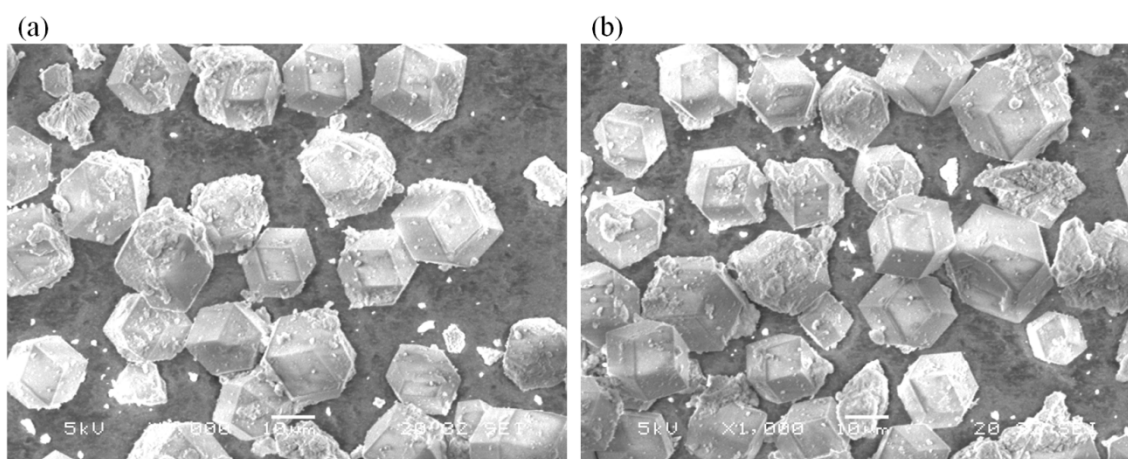


Figure 7.50. SEM micrographs of (a) H-SAPO(RHO) and (b) Na-SAPO(RHO).

PXRD pattern of Na-SAPO(RHO) compared to H-SAPO(RHO), heated at 823 K, (Figure 7.51a) confirms that the ion exchanged sample remains crystalline. Its porosity was monitored by N₂ adsorption at 77 K. The N₂ uptake decreases from 11 mmol g⁻¹ for H-SAPO(RHO) to 1.2 mmol g⁻¹ for Na-SAPO(RHO) at p/p₀ = 0.9 (Figure 7.51b), these values are very similar to those obtained for zeolite Rho (see Figure 7.7b).

Calcined, dehydrated H-SAPO(RHO) structure has been reported previously in the *I23* space group, to permit ordering of Al and P (and Si, which substitutes for P).²⁵ Figure 7.52 presents the PXRD patterns of hydrated and dehydrated Na-SAPO(RHO) samples. For the hydrated Na-SAPO(RHO) the structure adopts cubic *I23* symmetry. Upon dehydration Na-SAPO(RHO) remains this symmetry, but the structure tilts similarly to the Rho zeolite.

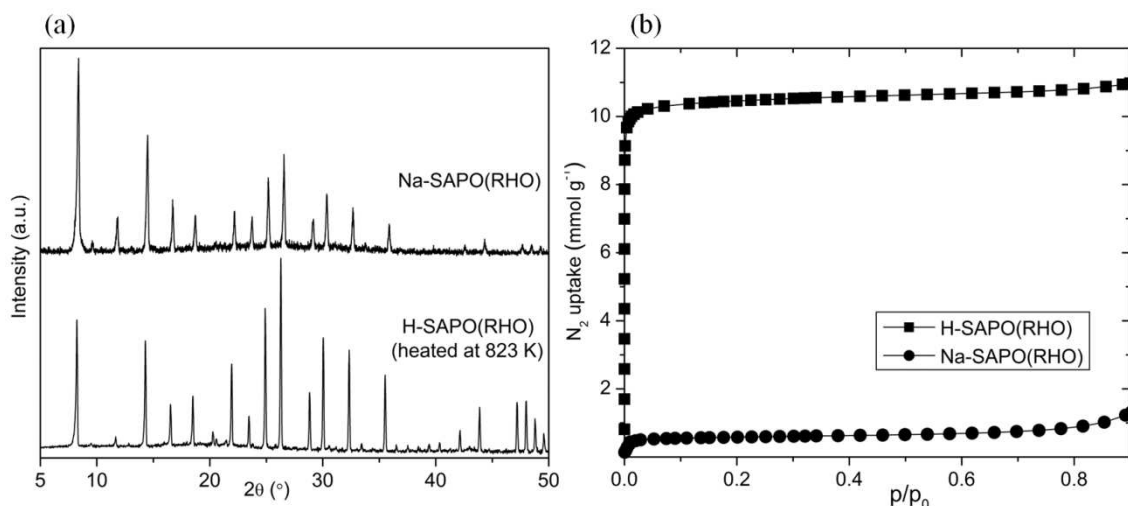


Figure 7.51. (a) PXRD patterns and (b) N_2 adsorption isotherms of H-SAPO(RHO), heated at 923 K, and ion exchanged Na-SAPO(RHO). The (offset) patterns have been collected at 298 K using the same operating conditions and the N_2 isotherms were recorded at 77 K.

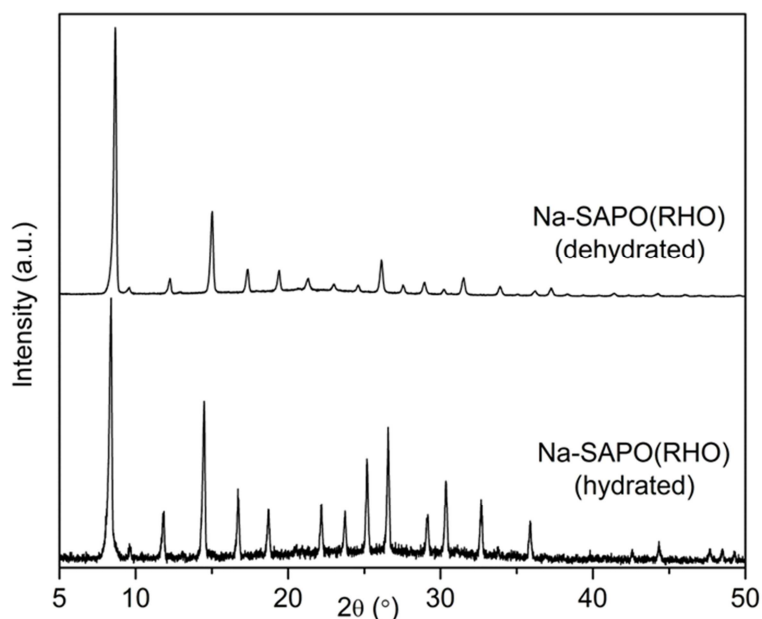


Figure 7.52. PXRD patterns of hydrated and dehydrated Na-SAPO(RHO). The (offset) patterns have been collected at 298 K using the same operating conditions.

Structure of Na-SAPO(RHO) upon dehydration was investigated by Rietveld analysis. The final observed, calculated and difference Rietveld plot for the laboratory powder data of Na-SAPO(RHO) is shown in Figure 7.53. Crystallographic details from the Rietveld analysis of dehydrated Na-SAPO(RHO) are given in the appendix. Rietveld refinement gives the structure of Na-SAPO(RHO) which is shown in Figure 7.54. For

Na-SAPO(RHO) all of the reflections are associated with cubic $I23$ symmetry and the unit cell parameter is $a = 14.4817(2)$ Å. The Na^+ cation positions are located at the sites close to the plane of S8R site. It has been found that there are 4 Na^+ per unit cell which gives 2 Na^+ per α -cage. Na–O distances in the S8R sites are $2.59(2)$ Å.

Similarly to H-Rho, H-SAPO(RHO) has very high pore volume but does not show strong adsorption of CO_2 at conditions relevant to carbon capture from flue gases (Figure 7.55a). The CO_2 adsorption is of Type I, and shows no hysteresis. Direct comparison of H-SAPO(RHO) with H-Rho shows H-SAPO(RHO) to be a weaker adsorbent, 1.1 mmol g^{-1} against 1.7 mmol g^{-1} for H-Rho at 0.1 bar. The CO_2 adsorption isotherm for Na-SAPO(RHO) shows Type I behaviour with hysteresis, which indicates physisorption with strong interactions between CO_2 molecules and the Na-SAPO(RHO) structure (Figure 7.55b). The uptake of CO_2 for Na-SAPO(RHO) is lower than for Na-Rho, 1.0 mmol g^{-1} and 3.2 mmol g^{-1} at 0.1 bar, respectively. Low CO_2 uptake for both samples, H-SAPO(RHO) and Na-SAPO(RHO) in comparison with H-Rho and Na-Rho, is due to a lower overall anionic charge on the framework in the SAPO materials compared to that of the aluminosilicates. The consequence of this is lower electrostatic interactions and also less cations may be introduced to the structure.

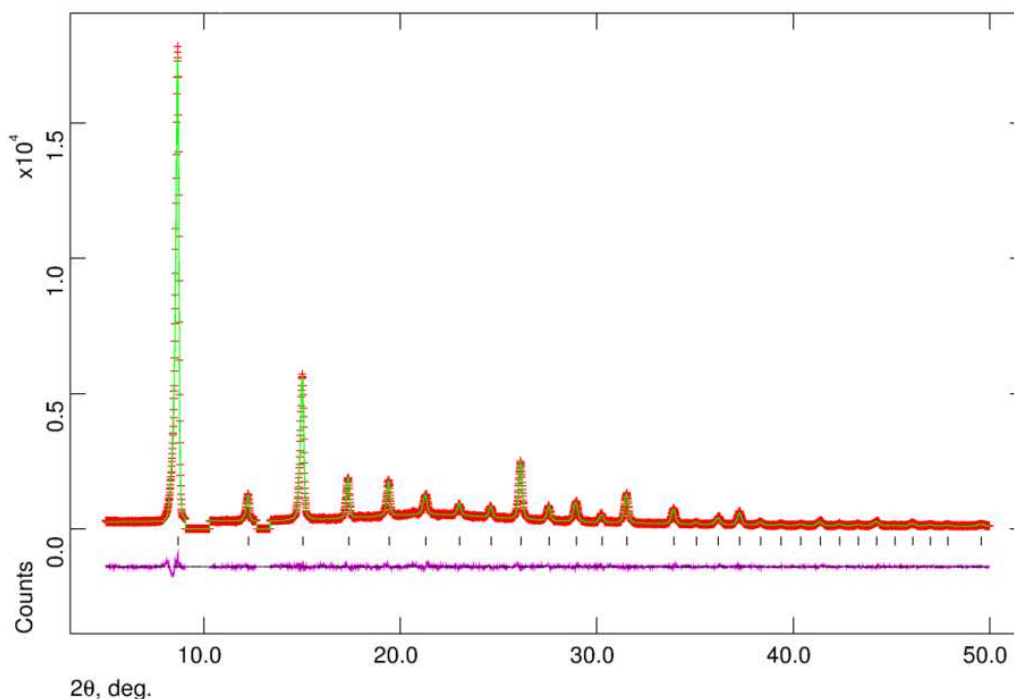


Figure 7.53. Final observed, calculated and difference Rietveld plot for the powder data refinement of dehydrated Na-SAPO(RHO).

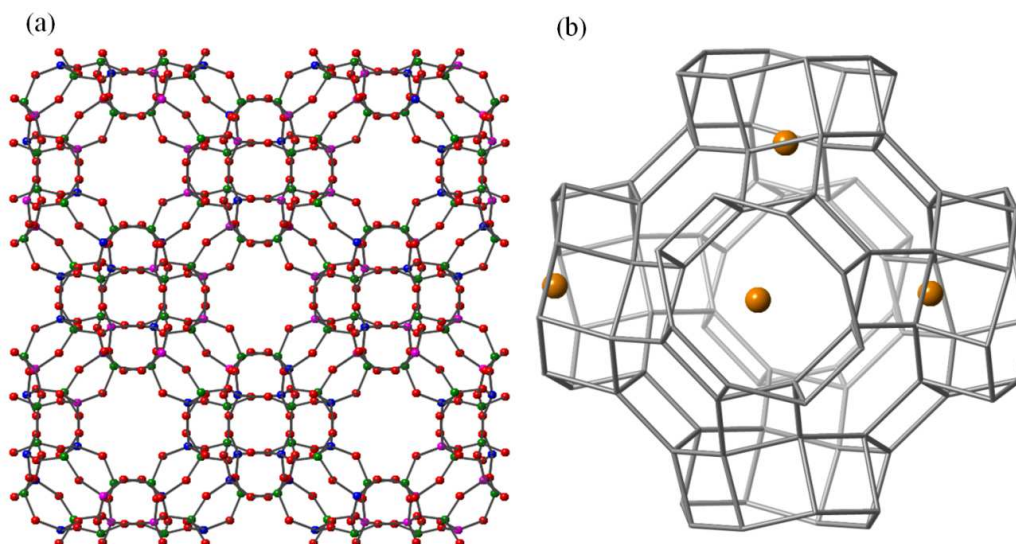


Figure 7.54. (a) Framework structure of Na-SAPO(RHO) in $I23$ symmetry showing an α -cages surrounded by double 8-membered ring (D8R) (Al atoms in green, P atoms in pink, Si atoms in blue and O atoms in red) and (b) possible cation distributions in one α -cage surrounded by double 8-membered ring of dehydrated Na-SAPO(RHO), both determined from Rietveld analysis of laboratory X-ray powder diffraction data.

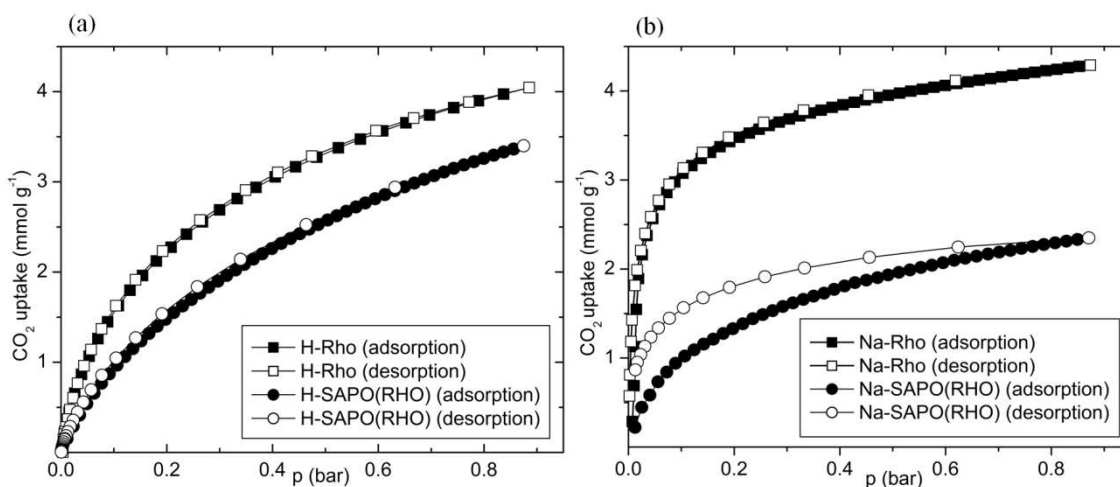


Figure 7.55. CO₂ sorption isotherms at 298 K for (a) H-SAPO(RHO) and H-Rho, and (b) Na-SAPO(RHO) and Na-Rho.

Additional analysis was carried out in collaboration with Instituto de Tecnologia Quimica in Valencia. High pressure (up to 9 bar) adsorption measurements for CH₄ and CO₂, and CO₂/CH₄ equilibrium selectivity factor were measured for H- and Na-SAPO(RHO) (Figure 7.56). H-SAPO(RHO) adsorbs more CO₂ at 9 bar and 298 K and 333 K than Na-SAPO(RHO), 5.8 mmol g⁻¹ and 4.5 mmol g⁻¹ for H-SAPO(RHO), and

4.8 mmol g⁻¹ and 4.0 mmol g⁻¹ for Na-SAPO(RHO) respectively, while Na-SAPO(RHO) shows higher selectivity than H-SAPO(RHO) at 298 K and 333 K. The α factor is plotted against pressure in Figure 7.56c,d. The CO₂/CH₄ equilibrium selectivity factor (α) was calculated from single component isotherms using equation 4.3 from chapter 4. The ‘selectivities’ from 8 to 3 at 298 K and 333 K for H-SAPO(RHO) and from 50 to 5 at 298 K and 20 to 5 at 333 K for Na-SAPO(RHO) are obtained at pressure ranges of 1–9 bar. The selectivity for CO₂/CH₄ is higher for Na-SAPO(RHO) because of the presence of cations in S8R sites which interact very weakly with CH₄ but strongly with CO₂.

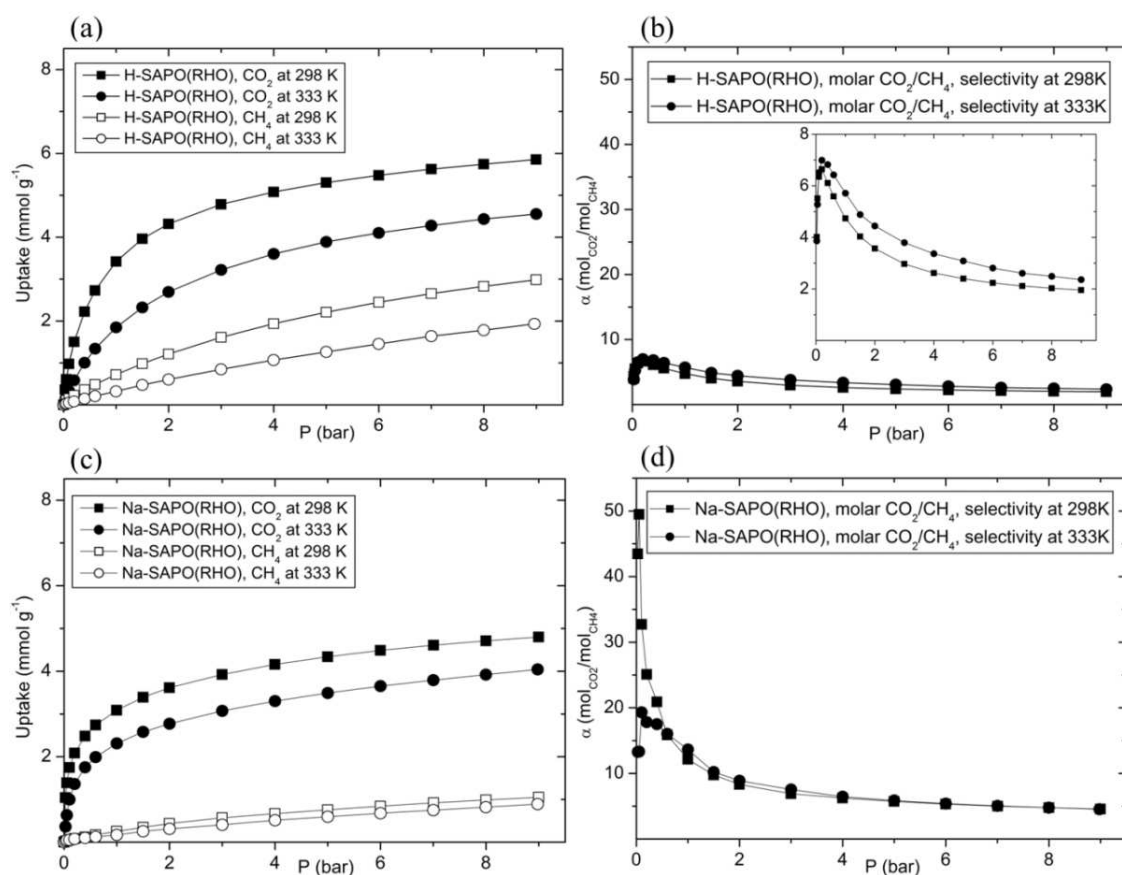


Figure 7.56. (a), (c) CO₂ and CH₄ adsorption isotherms and (b), (d) CO₂/CH₄ equilibrium selectivity factor according to volumetric and gravimetric measurements of H- and Na-SAPO(RHO) at 298 K and 333 K. Data collected at Instituto de Tecnologia Quimica in Valencia.

7.12. Conclusions

Univalent cationic forms of zeolite Rho show remarkable CO₂ adsorption behaviour that results from a combination of its flexible framework structure, the distribution of extra-

framework cations over different sites and the mobility of those cations that occupy window sites between α -cages.

H-Rho has the highest pore volume of all Rho samples examined, but does not show strong adsorption of CO₂ at conditions relevant to carbon capture from flue gases. Adsorption is of Type I, and shows no hysteresis. H-SAPO(RHO) interacts with CO₂ more weakly than the aluminosilicate, due to its lower framework charge. US-Rho, in which there are extra-framework Al species, also takes up less CO₂ at 0.1 bar and 298 K than H-Rho. Nitridation of H-Rho was unsuccessful.

The highest values of CO₂ adsorption for zeolite Rho are observed on the lithium form. Li⁺ cations are expected to occupy S6R sites in the α -cage, and so leave window sites free of cations. As a result the CO₂ adsorption isotherms at 298 K do not show hysteresis and all the Li⁺ cations in the S6R sites are accessible for CO₂ adsorption. The ability of Li-Rho to admit CO₂, even though the opening of the windows is only 1.90 Å, indicates that there is sufficient framework flexibility and interaction at 298 K to permit CO₂ diffusion.

In contrast to the Li-Rho behaviour, the Na-, K-, NH₄- and Cs-forms of Rho show hysteresis in their CO₂ adsorption isotherms ($\text{Na}^+ = \text{NH}_4^+ < \text{K}^+ < \text{Cs}^+$), with the adsorption at 298 K and 0–1 bar decreasing in the order $\text{Na}^+ > \text{K}^+ = \text{NH}_4^+ > \text{Cs}^+$. In all these cases cations occupy window sites in the dehydrated form, as ‘sentinels’, either in D8R or S8R sites, so there must be cation displacement to allow CO₂ uptake to occur. In Na-Rho the cations occupy S8R sites in the windows, in K- and NH₄-Rho both D8R and S8R sites are occupied and in Cs-Rho all the D8R sites are occupied. The movement of larger cations to S8R sites (as observed in this study to occur for Cs⁺ cations at pressures greater than 1 bar in Cs-Rho) results in a decrease in the coordination of the cation by framework oxygen atoms and a distortion away from $I\bar{4}3m$ to $Im\bar{3}m$.

Unprecedented selectivity of Cs-Rho, K-Rho, Ca-Rho and Na-Rho to CO₂ over CH₄ and the high ratio of single component adsorption uptakes of CO₂ to ethane reported here results from the ability of cations to move to allow the passage of CO₂ molecules into Rho whilst the larger size (4 Å) and particularly the lower interaction of hydrocarbons results in their exclusion.

Sodium cations in fully-exchanged Na-Rho remain in S8R and S6R positions during adsorption and CO₂ molecules occupy two positions, in each of which the O=C=O molecule adopts end-on coordination with one Na⁺ cation and may interact with another. The stronger of these adsorption sites involves one cation in a S8R site: the other involves interaction with a Na⁺ cation in a S6R site. Upon desorption of CO₂ from Na-Rho at 298 K, there is a gradual decrease in the single unit cell *a* parameter within the *I* $\bar{4}$ 3*m* space group indicating a concerted structural change. For Cs-Rho, by contrast, the structure exists as a mixture of two different structural forms of the zeolite, *I* $\bar{4}$ 3*m* and *Im* $\bar{3}$ *m*, the relative amounts of which change with increased CO₂ uptake. Cs⁺ cations move from D8R to S8R and they stay in these sites.

Na-SAPO(RHO) adsorbs less CO₂ than Na-Rho, however it shows high CO₂/CH₄ selectivity at high pressure.

Fully exchanged Na-Rho is the most promising CO₂ adsorbent of those studied, when taking into account cost, uptake, selectivity and kinetics. Furthermore, the Na-Rho single component CO₂ and CH₄ isotherms suggest high selectivity is possible at elevated pressure. Adsorption occurs on S8R and S6R sites: that these two adsorption sites exist is a consequence of both framework and extra framework composition, so that manipulation of these can give rise to ‘adsorption site engineering’. It should therefore be possible to modify chemical composition to optimise CO₂ uptake with this knowledge of the structural chemistry of Rho.

Information gathered in this study demonstrates what is likely to be a widespread and important mechanism for CO₂ adsorption and optimisation of selectivity in adsorption processes over many zeolite types.

References

1. Robson H. E., Shoemaker D. P., Ogilvie R. A. and Manor P. C., *Adv. Chem. Ser.*, **1973**, 106-115
2. Chatelain T., Patarin J., Fousson E., Soulard M., Guth J. L. and Schulz P., *Microporous Mater.*, **1995**, 4, 231-238
3. Corbin D. R., Abrams L., Jones G. A., Eddy M. M., Stucky G. D. and Cox D. E., *J. Chem. Soc., Chem. Commun.*, **1989**, 0, 42-43

4. Corbin D. R., Abrams L., Jones G. A., Eddy M. M., Harrison W. T. A., Stucky G. D. and Cox D. E., *J. Am. Chem. Soc.*, **1990**, *112*, 4821-4830
5. Corbin D. R., Stucky G. D., Eddy M. M., Prince E. E., Abrams L. and Jones G. A., *Abstr. Pap. Am. Chem. Soc.*, **1987**, *193*, 300-INOR
6. McCusker L. B. and Baerlocher C., '*Proceedings of the Sixth International Zeolite Conference*', Butterworths, UK, **1984**
7. Barrer R. M. and Rosenblat M. A., '*Proceedings of the Sixth International Zeolite Conference*', Butterworth Scientific, UK, **1984**
8. Johnson G. M., Reisner B. A., Tripathi A., Corbin D. R., Toby B. H. and Parise J. B., *Chem. Mater.*, **1999**, *11*, 2780-2787
9. McCusker L. B., *Zeolites*, **1984**, *4*, 51-55
10. Araki S., Kiyohara Y., Tanaka S. and Miyake Y., *J. Colloid Interf. Sci.*, **2012**, *388*, 185-190
11. Palomino M., Corma A., Jorda J. L., Rey F. and Valencia S., *Chem. Commun.*, **2012**, *48*, 215-217
12. Corbin D. R., 7 169 212 B1, US Patent, **2007**
13. Parise J. B., Abrams L., Gier T. E., Corbin D. R., Jorgensen J. D. and Prince E., *J. Phys. Chem.*, **1984**, *88*, 2303-2307
14. Johnson G. M., Tripathi A. and Parise J. B., *Chem. Mater.*, **1999**, *11*, 10-12
15. Schoedel R., Neubauer H. D. and Vogt F., Ger. Offen. 4,331,003, Leuna-WerkB GmbH, **1995**
16. Yu Z. W., Zheng A. M., Wang Q. A., Chen L., Xu J., Amoureux J. P. and Deng F., *Angew. Chem. Int. Edit.*, **2010**, *49*, 8657-8661
17. Dogan F., Hammond K. D., Tompsett G. A., Huo H., Conner W. C., Auerbach S. M. and Grey C. P., *J. Am. Chem. Soc.*, **2009**, *131*, 11062-11079
18. Srasra M., Delsarte S. and Gaigneaux E., *Top. Catal.*, **2009**, *52*, 1541-1548
19. Garrone E., Bonelli B., Lamberti C., Civalieri B., Rocchia M., Roy P. and Arean C. O., *J. Chem. Phys.*, **2002**, *117*, 10274-10282
20. Zukal A., Arean C. O., Delgado M. R., Nachtigall P., Pulido A., Mayerová J. and Čejka J., *Micropor. Mesopor. Mat.*, **2011**, *146*, 97-105
21. Pulido A., Nachtigall P., Zukal A., Domínguez I. and Čejka J., *J. Phys. Chem. C*, **2009**, *113*, 2928-2935

22. Lozinska M. M., Mangano E., Mowat J. P. S., Shepherd A. M., Howe R. F., Thompson S. P., Parker J. E., Brandani S. and Wright P. A., *J. Am. Chem. Soc.*, **2012**, *134*, 17628-17642
23. Reisner B. A., Lee Y., Hanson J. C., Jones G. A., Parise J. B., Corbin D. R., Toby B. H., Freitag A., Larese J. Z. and Kahlenberg V., *Chem. Commun.*, **2000**, *0*, 2221-2222
24. Su X., Tian P., Li J. Z., Zhang Y., Meng S. H., He Y. L., Fan D. and Liu Z. M., *Micropor. Mesopor. Mat.*, **2011**, *144*, 113-119
25. Tian P., Su X. O., Wang Y. X., Xia Q. H., Zhang Y., Fan D., Meng S. H. and Liu Z. M., *Chem. Mater.*, **2011**, *23*, 1406-1413

8. General Conclusions and Future Work

8.1. General Conclusions

The aim of this PhD study was to examine inorganic porous solids, with and without framework modification, for use in the removal of CO₂ from flue gas at ambient temperature and pressure. The CO₂ uptakes at 0.1 bar and 298 K on materials prepared in this study are presented in Figure 8.1.

Initially the mesoporous silicas, SBA-1 and SBA-2 were investigated. They were chosen due to their uniform, large ordered cages of controllable dimensions with small windows. They also possess high hydrophobicity, compared to zeolites and metal organic frameworks (MOFs), which is a potential advantage for CO₂ adsorption from flue gas. It was found that the CO₂ sorption performance of SBA-1 and SBA-2 depends on the size, surface chemistry of the pores, connectivity and accessibility of the network. SBA materials possess large pore volume, however the silica framework does not interact strongly with CO₂. Reducing the pore size of mesoporous silicas by calcination at different temperatures resulted in low adsorption of N₂ so that these mesoporous silicas acted as molecular sieves but it did not enhance their CO₂ uptake at low pressure. Furthermore, modification of the silica framework by nitridation had a stronger effect than calcination on the final connectivity of the SBA porous network but only slightly increased the CO₂ uptake. Nevertheless, nitrated samples also showed high CO₂ over N₂ selectivity. SBA-1 and SBA-2 were nitrated for the first time in this study. The SBA and NSBA are not good candidates for CO₂ capture and storage from flue gas at ambient temperature and pressure but they may have reasonably high uptake at high pressures and low temperatures. Additionally, experimental results of SBA-2 obtained in this study helped to validate a realistic and atomistic model of SBA-2 and simulate its synthesis, an approach that may be applied to understand the synthesis, structure and adsorption performance of other mesoporous silicas.

Zeolites are well known as good CO₂ adsorbents. In zeolites used in industry (for example zeolite Y or 13X) much of the open space is inaccessible to CO₂ because some parts of their structures cannot admit it. The zeolites chabazite, ZK-5 and Rho,

chosen in this study have a larger fraction of their pore volume accessible but still have relatively small cages that facilitate strong interactions with adsorbed molecules, even at the highest levels of pore filling. In this study, six zeolites were prepared that had a higher reversible CO₂ uptake at 0.1 bar and 298 K than benchmark zeolite 13X (Figure 1.8).

H-forms of all of the zeolites and SAPOs studied gave low (0.6 mmol g⁻¹ for H-chabazite, 0.6 mmol g⁻¹ for H-ZK-5, 0.8 mmol g⁻¹ for SAPO H-STA-14, 1.6 mmol g⁻¹ for H-Rho, for 1.2 mmol g⁻¹ H-SAPO(RHO)) uptakes of CO₂ at flue gas conditions. The isotherms were reversible and of Type-I, so that the low uptakes arise from weak interactions of the CO₂ with the framework. The lowest uptakes were observed for H-chabazite, due to crystal instability in the H-form. Furthermore, US-Rho, which contains extra-framework Al species, took less CO₂ at 0.1 bar and 298 K than H-Rho (1.6 mmol g⁻¹ for H-Rho and 0.6 mmol g⁻¹ for US-Rho), and attempts to nitride zeolite Rho were unsuccessful.

The highest values of CO₂ adsorption on chabazite (Si/Al = 3.0), ZK-5 (Si/Al = 4.16) and Rho (Si/Al = 3.9) were observed for the lithium forms. In all cases the uptakes were higher than for benchmark zeolite 13X. The lithium cations in these structures occupy sites away from the windows to the zeolite cages and so leave these windows free of cations and accessible to CO₂. As a result the CO₂ isotherms at 298 K of Li-forms do not show hysteresis. Li-ZK-5 possesses the highest CO₂ uptake in this study (Figure 8.1). The highest uptake results primarily from the high charge density of Li⁺ and also the small cation size, leaving additional pore space available.

Na- and K-chabazite show uptakes (at 0.1 bar and 298 K) comparable with zeolite 13X, with uptake increasing with cation content. *In situ* PXRD studies of fully exchanged Na- and K-chabazite with CO₂ adsorbed show that upon dehydration, the diffraction patterns of both materials show peak broadening and loss of intensity, which is reversible upon rehydration. An electron diffraction study showed that the changes visible on PXRD patterns occur due to the small size of the crystals rather than degradation of the structure. The diffraction peaks also sharpen upon CO₂ adsorption.

As expected from the structure determination, where K⁺ cations are found to fully occupy the single eight-membered ring windows between cages, there is no N₂ uptake at

77 K. However, the CO₂ uptake indicates that K⁺ cations move in the presence of CO₂, due to the strong interaction of K⁺ with the quadrupole of CO₂. Indeed, structural analysis of dehydrated K-chabazite with adsorbed CO₂ reveals that 1 K⁺ or 2 K⁺ per unit cell move to S6R sites. The K-chabazite of this study is not selective to CO₂ over CH₄, probably because K⁺ cations can migrate either permanently or momentarily away from the single eight-membered ring windows even in the presence of CH₄. If there is more than 9 K⁺ per unit cell (Si/Al < 3.0) any residual cations will start occupying S6R and K⁺ from S8R will not be able to move so readily, whereupon they act as ‘trapdoors’ that will still allow the passage of CO₂ molecules into chabazite whilst the larger size (4 Å) and lower interaction of hydrocarbons results in their exclusion.

Structural changes upon dehydration are even more visible for Na-chabazite which upon prolonged dehydration under a vacuum changes its rhombohedral $R\bar{3}m$ symmetry to a mixture of rhombohedral $R\bar{3}m$ symmetry and monoclinic $C2/m$ symmetry (in contrast to the Li-, Ca- and K-chabazite which remain rhombohedral) and the CO₂ adsorption isotherm at 298 K shows a step and hysteresis. The phase mixture for Na-chabazite observed in this study has not been previously reported. The distortion disappears with decreasing cation concentration. Na-chabazite prepared in this study possesses a composition where the number of Na⁺ cations does not allow for a complete change of the rhombohedral $R\bar{3}m$ symmetry to monoclinic $C2/m$ symmetry but remains as a mixture of these two phases. The structure of Na-chabazite during CO₂ adsorption was characterised by *in situ* synchrotron PXRD, although due to time restrictions the Na-chabazite structure transformation during dehydration was not observed, although dehydration was probably achieved. A model of Na-chabazite with adsorbed CO₂ in rhombohedral $R\bar{3}m$ symmetry was determined. On the basis of this and other evidence the stepped CO₂ isotherm and hysteresis are thought to result from a phase mixture where the monoclinic Na-chabazite shows ‘breathing’ behaviour.

In Ca-chabazite the cations do not occupy S8R window sites and are found in S6R and D6R sites. The cations in the D6R site are inaccessible, so only the cations in S6R sites are available to interact with CO₂, which makes the uptake of CO₂ on this material slightly lower than for the Li-form.

Zeolite ZK-5, a polytype of chabazite, is an example of a stable rigid small pore zeolite with a high pore volume. All cationic forms are accessible to N_2 at 77 K, indicating that intercage windows do not contain cations. The CO_2 isotherms are all of Type-I and fully reversible, and uptake on the Li-form at 0.1 bar and 298 K was the highest observed in this study.

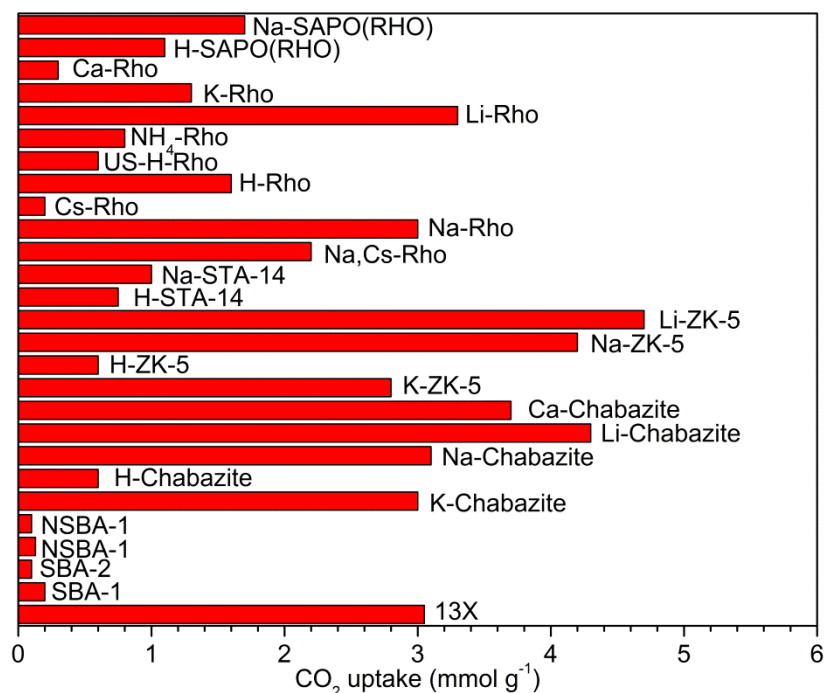


Figure 8.1. CO_2 uptake at 0.1 bar and 298 K on materials prepared in this study.

Framework structures of cationic forms of zeolite Rho show more remarkable flexibility upon dehydration than zeolites chabazite or ZK-5, because they distort and change symmetry from $Im\bar{3}m$ to $I\bar{4}3m$.

Na-, K-, NH_4 - and Cs-forms of Rho show hysteresis in their CO_2 adsorption isotherms ($Na, NH_4 < K < Cs$), with the adsorption at 298 K and 0–1 bar decreasing in the order $Na > K, NH_4 > Cs$. In all these cases cations occupy window sites in the dehydrated form, as ‘sentinels’, either in D8R or S8R sites, so there must be cation displacement to allow CO_2 uptake to occur. In Na-Rho the cations occupy S8R sites in the windows, in K- and NH_4 -Rho both D8R and S8R sites are occupied and in Cs-Rho all the D8R sites are occupied. By contrast, adsorption of CO_2 on Li-Rho is fully reversible, which results from the location of Li^+ cations in S6R sites away from the intercage windows.

Sodium cations in fully-exchanged Na-Rho remain in S8R and S6R positions during adsorption and CO₂ molecules occupy two positions, in each of which the O=C=O molecule adopts end-on coordination with one Na⁺ and may interact with another. The CO₂ molecules are able to act to mediate the displacement of Na⁺ cations in Na-Rho (and the NH₄⁺ and K⁺ forms) away from window sites where they block molecular transport, leading to a proposed mechanism that involves a CO₂-mediated migration from a window site to a vacant α -cage site. *In situ* synchrotron PXRD study showed that the Na⁺ cations move slightly to adopt better coordination with adsorbed CO₂ and indicates that after allowing CO₂ molecules to pass through the window, they return to their starting position.

Selectivity of Na-Rho, K-Rho, Cs-Rho and Ca-Rho to CO₂ over CH₄ even at high pressure ($P < 10$ bar) and the high ratio of single component adsorption uptakes of CO₂ to ethane over Na-Rho results from the ability of cations to move to allow the passage of CO₂ molecules into Rho whilst the lower interaction of hydrocarbons and their larger size (4 Å) result in their exclusion. It was also found that the movement of larger Cs⁺ cations in Cs-Rho from D8R window sites to S8R sites results in a decrease in the coordination of the cation by framework oxygen atoms, a distortion away from $I\bar{4}3m$ to $Im\bar{3}m$ and an increase in CO₂ uptake. For Ca-Rho the increase in CO₂ uptake as temperature increases suggests that kinetic rather than thermodynamic factors predominate.

According to measurements, when taking into account cost, uptake, selectivity and kinetics, from all materials prepared in this study, Na-Rho possesses the most potential as an adsorbent for the selective uptake of CO₂ at reasonable rates and with accessible uptake capacity at low partial pressures and ambient temperatures. Adsorption occurs on S8R and S6R sites: that these two adsorption sites exist is a consequence of both framework and extra-framework composition, so that manipulation of these can give rise to ‘adsorption site engineering’. It should therefore be possible to modify chemical composition to optimise CO₂ uptake with this knowledge of the structural chemistry of Rho.

The unique framework, structure of pore surface, and cation type and loading of zeolites are responsible for their excellent gas uptake capacity and selectivity. The cage access is

controlled by the size of the cation and the occupancy degree of the window. The results gathered in this study broaden the knowledge of chabazite and Rho structures by *in situ* CO₂ adsorption on these materials. The mechanism of ‘gating’ presented in this study is likely to be widespread for a range of zeolites where extra-framework cations occupy window sites between cages. Where previously these have been viewed simply as barriers to adsorption, their ability to move to allow CO₂ (or other molecules) to pass opens up a wide range of structures to more detailed examination for selective separations.

8.2. Future Work

Future work should involve understanding, broadening and developing the effect of cation gating in zeolites, so that it can be applied in a range of industrially important separations.

The role of crystal chemistry in controlling the performance of Rho should be investigated further. This should include varying the framework composition and preparing other univalent, divalent and mixed cation forms. So far, most work has been performed on templated Rho (Si/Al \approx 4.0), but it is also possible to prepare Rho with higher or lower framework Al content, which will result in higher or lower charge-balancing cation contents. Higher cation contents will give additional binding sites, whereas lower Al content will impart higher hydrothermal stability. Divalent and mixed cation forms of Rho will enable uptake and selectivity to be tuned by controlling the cations in the windows and in the cages. By introducing divalent cations at partial occupancy in the window sites these will act to reduce the window diameter of the whole structure (Rho is a very flexible structure) so that molecular sieving as well as cation gating can be introduced. Mixed cation forms will enable control to be exerted over diffusion rates and selectivity (Na,K; Na,Ca) or uptake (Na,Li). In the first case the cation content will control the ‘gate opening’ pressure whereas in the second the effect of the Li⁺ is to enhance uptake, because Li⁺ occupies positions away from the windows, in the cages, where it interacts strongly with adsorbed molecules.

In the case examined here, selectivities have been calculated from the single component isotherms. Although the nature of the proposed ‘chemoselective’ adsorption is such that molecules will be selected ‘one-by-one’, this selectivity should be measured in mixed

gases to simulate real conditions. Similarly, the effects of water vapour or trace impurities on the selectivity should be measured to assess applicability in industrial conditions.

D8R windows present in Rho are a key element of the cation gating shown by that zeolite, so the gating behaviour of the other zeolites that contain these windows (merlinoite, ECR-18) should be studied. Merlinoite, topology type MER (Figure 8.2a), contains D8R windows separating paulingite (*pau*) cages, and is expected to show similar gating behaviour to Rho in three dimensions through both D8R and S8R windows. ECR-18 (synthetic paulingite, topology type PAU, Figure 8.2b) is related to Rho (containing rho cages linked via D8Rs and *pau* cages, among others) and the initial structural studies indicate the framework distorts in a similar way to that of Rho. ECR-18 possesses high CO₂ uptake for as-prepared and unmodified Na-form (Figure 8.2c), and a very complex structure, which will require careful ion exchange and characterisation to optimise for selective uptake of CO₂.

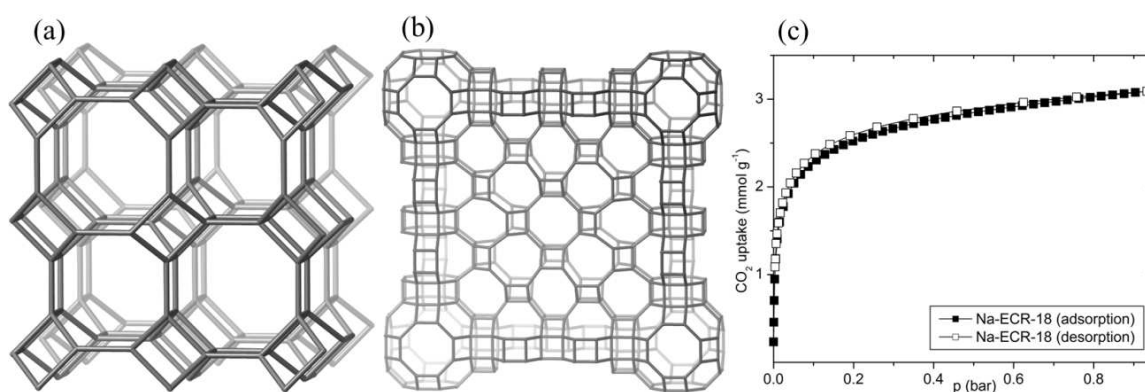


Figure 8.2. (a) Topology type MER contains D8R windows separating paulingite (*pau*) cages, (b) topology type PAU containing rho cages linked via D8Rs and *pau* cages, and (c) CO₂ sorption isotherms for Na-ECR-18 collected at 298 K.

It is expected that future work will permit an understanding of the structural control of selective adsorption to be obtained, and via that will indicate the best adsorbents for industrially-important industrial separations.

Appendix

Contents:

A1. Deconvolutions of ^{29}Si MAS NMR spectra

A1.1. Mesoporous silicas (Chapter 3)

A1.2. Zeolite chabazite (Chapter 5)

A1.3. Zeolite ZK-5 (Chapter 6)

A1.4. Zeolite Rho and zeolite Y (Chapter 7)

A2. Crystallographic details of dehydrated samples

A2.1. Zeolite chabazite (Chapter 5)

A2.2. Zeolite ZK-5 (Chapter 6)

A2.3. Zeolite Rho and Na-SAPO(RHO) (Chapter 7)

A3. Fractional atomic coordinates, occupancies and isotropic displacement parameters (in \AA^2) for dehydrated samples

A3.1. Zeolite chabazite (Chapter 5)

A3.2. Zeolite ZK-5 (Chapter 6)

A3.3. Zeolite Rho and Na-SAPO(RHO) (Chapter 7)

A1. Deconvolutions of ^{29}Si MAS NMR spectra

A1.1. Mesoporous silicas (Chapter 3)

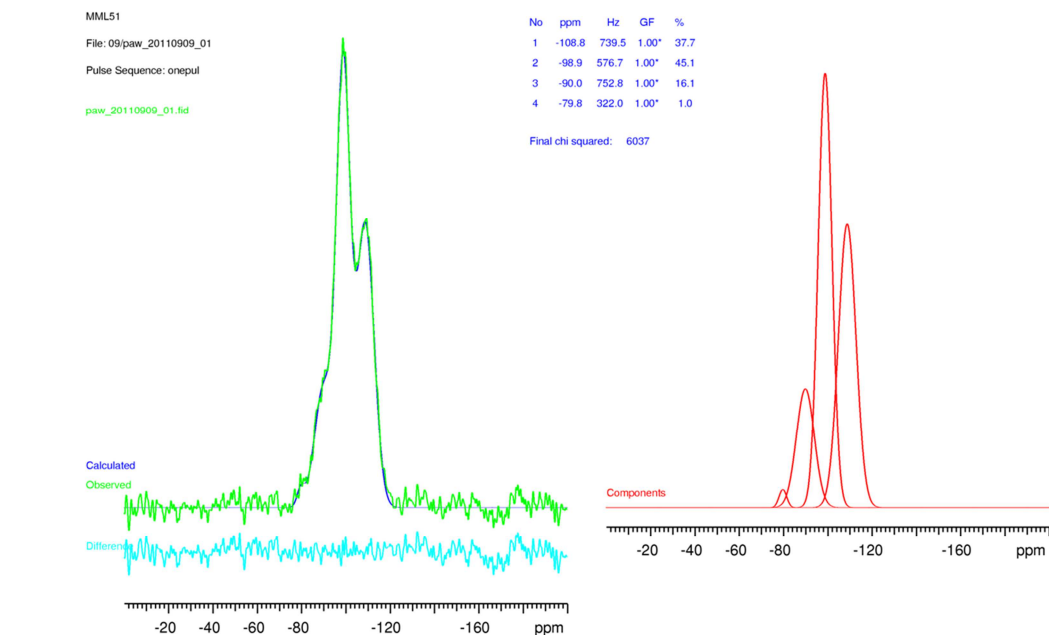


Figure A1.1. Deconvolution of the ^{29}Si MAS NMR spectrum of SBA-2 (as-prepared).

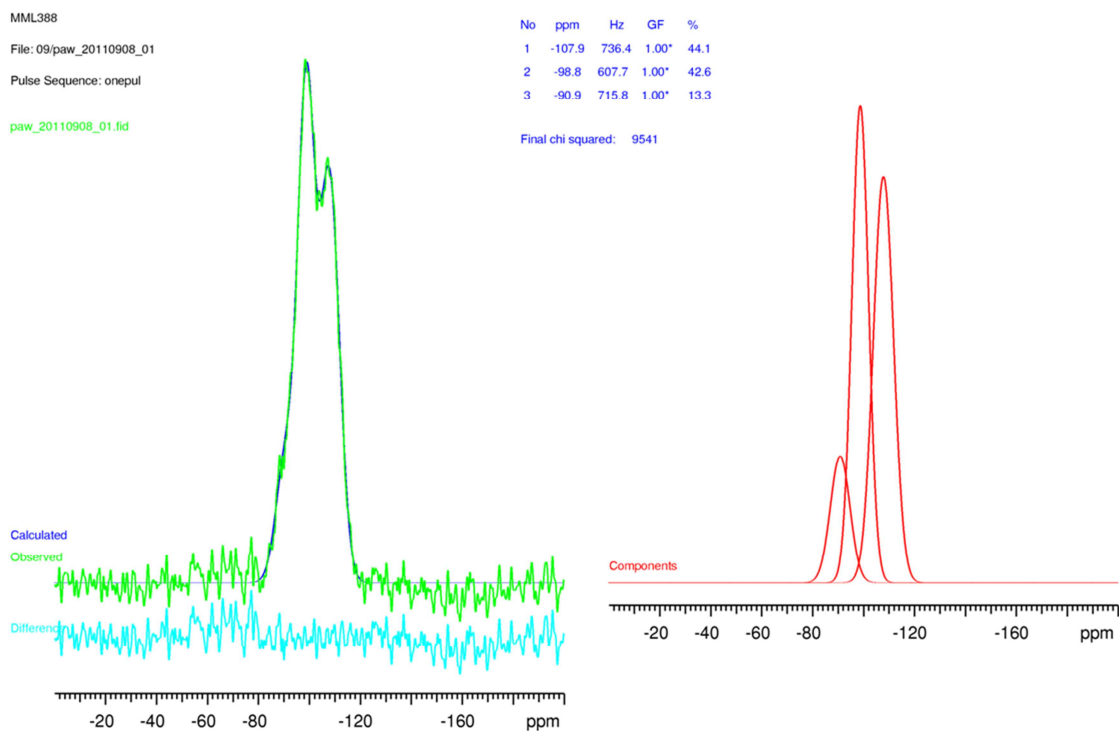


Figure A1.2. Deconvolution of the ^{29}Si MAS NMR spectrum of SBA-2(823).

Appendix

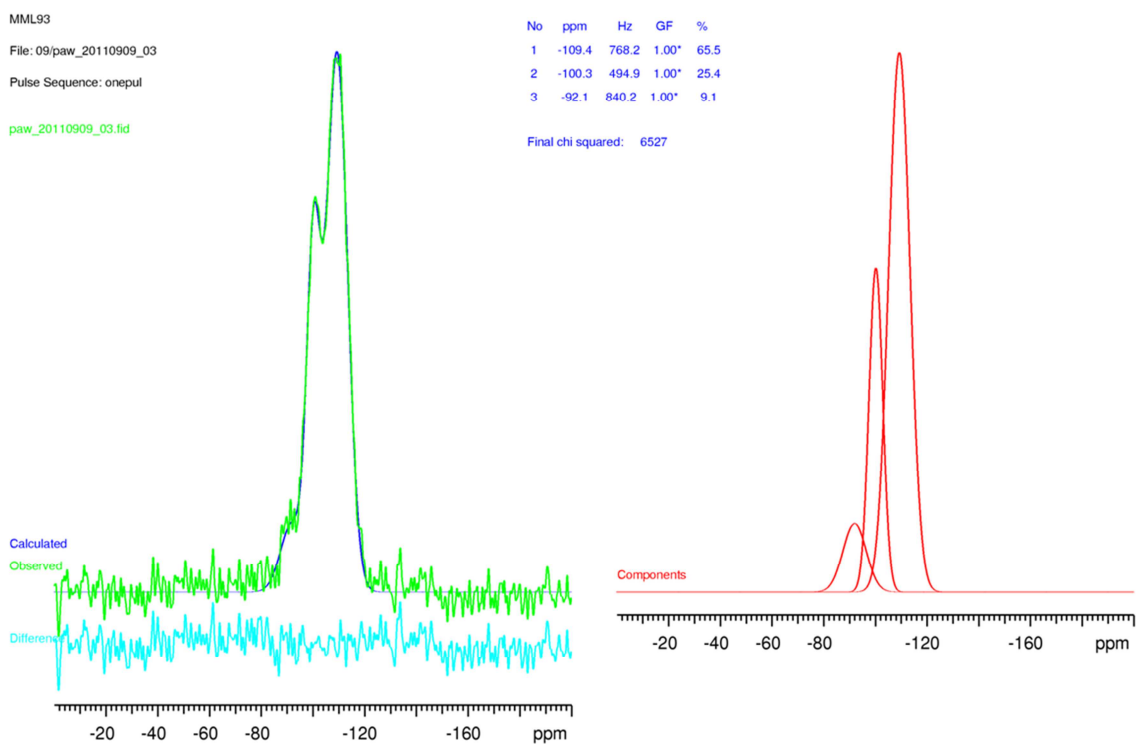


Figure A1.3. Deconvolution of the ^{29}Si MAS NMR spectrum of SBA-2(973).

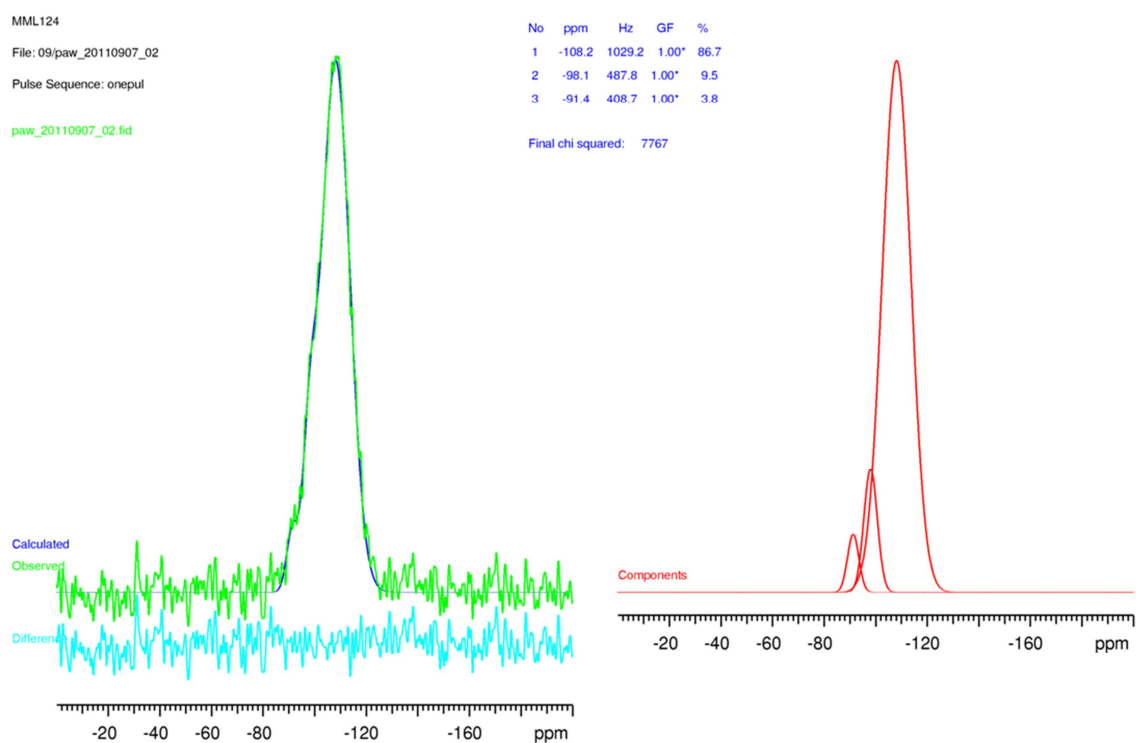


Figure A1.4. Deconvolution of the ^{29}Si MAS NMR spectrum of SBA-2(1073).

A1.2. Zeolite Chabazite (Chapter 5)

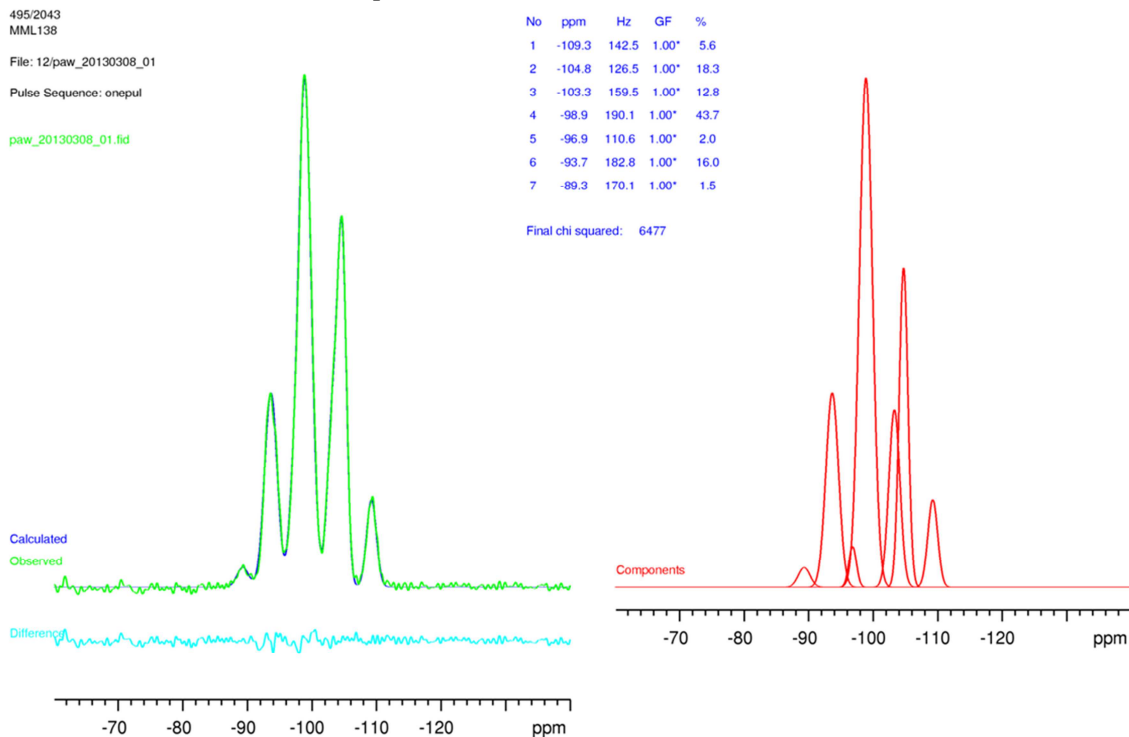


Figure A1.5. Deconvolution of the ^{29}Si MAS NMR spectrum of K-chabazite (as-prepared).

A1.3. Zeolite ZK-5 (Chapter 6)

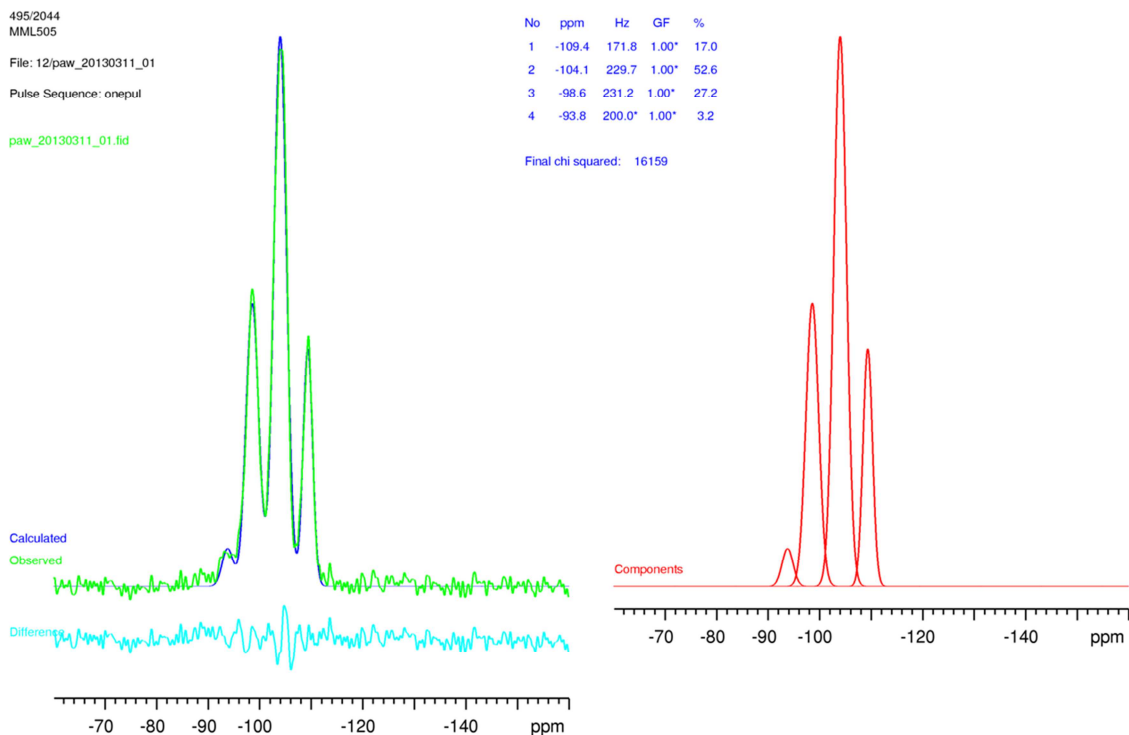


Figure A1.6. Deconvolution of the ^{29}Si MAS NMR spectrum of K-ZK-5 (as-prepared).

A1.4. Zeolite Rho and zeolite Y (Chapter 7)

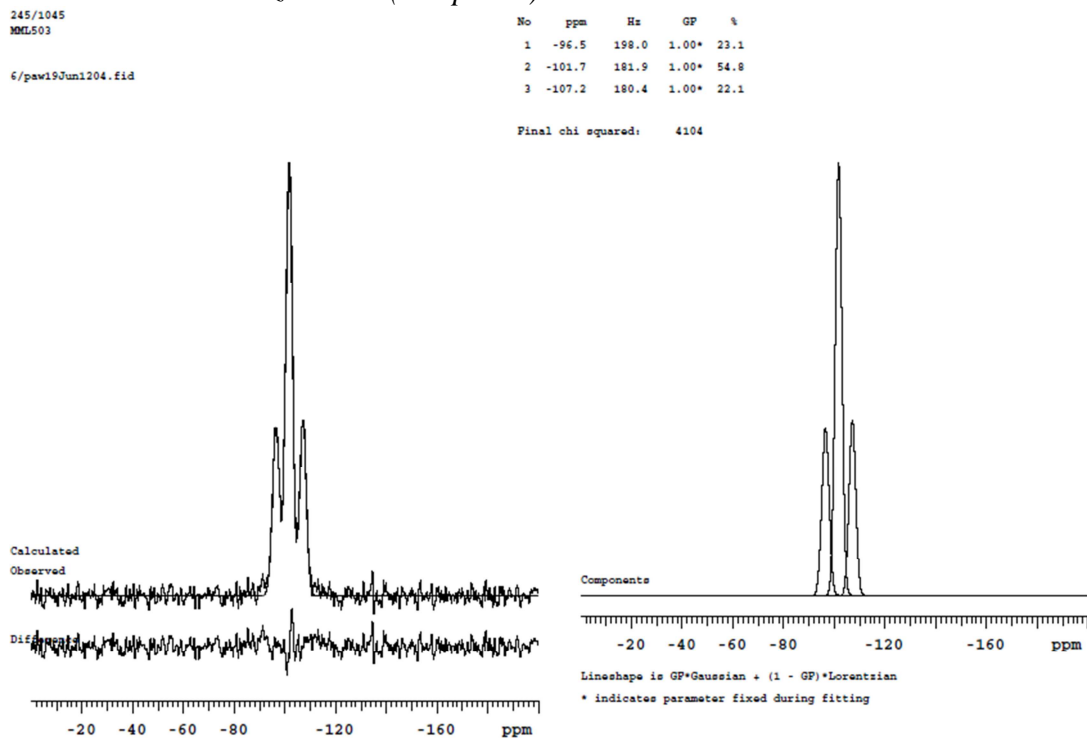


Figure A1.7. Deconvolution of the ^{29}Si MAS NMR spectrum of Na,Cs-Rho (as-prepared).

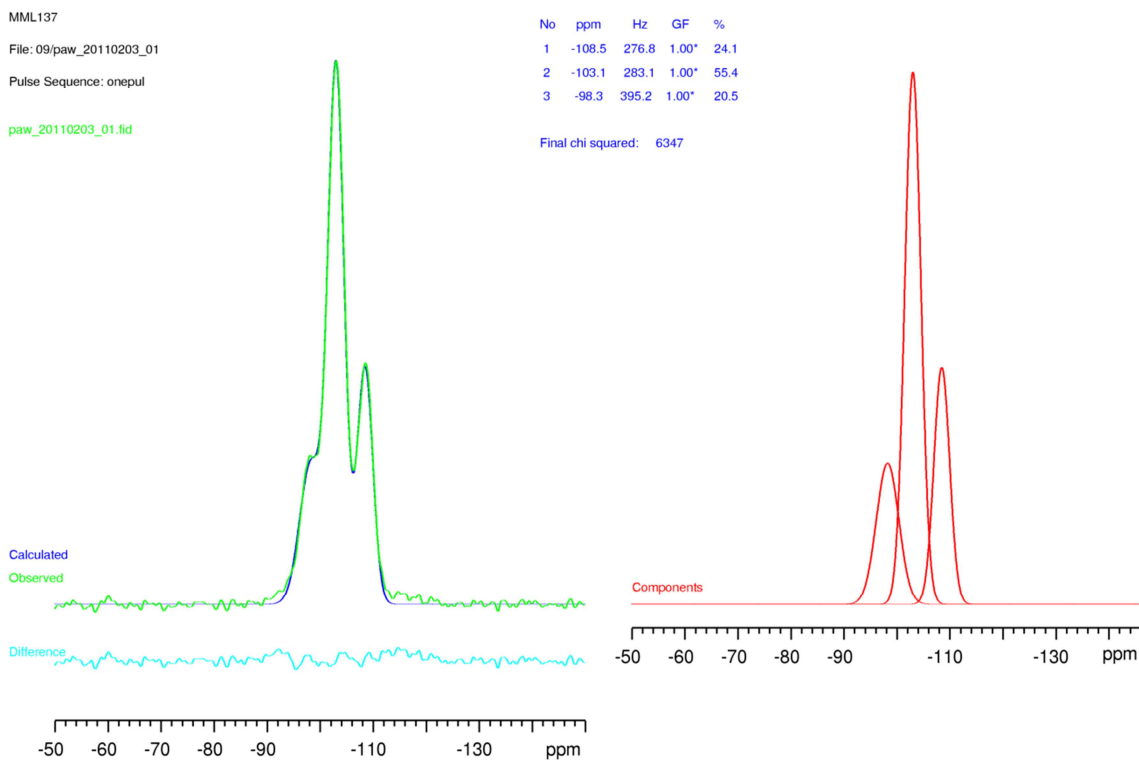


Figure A1.8. Deconvolution of the ^{29}Si MAS NMR spectrum of H-Rho.

Appendix

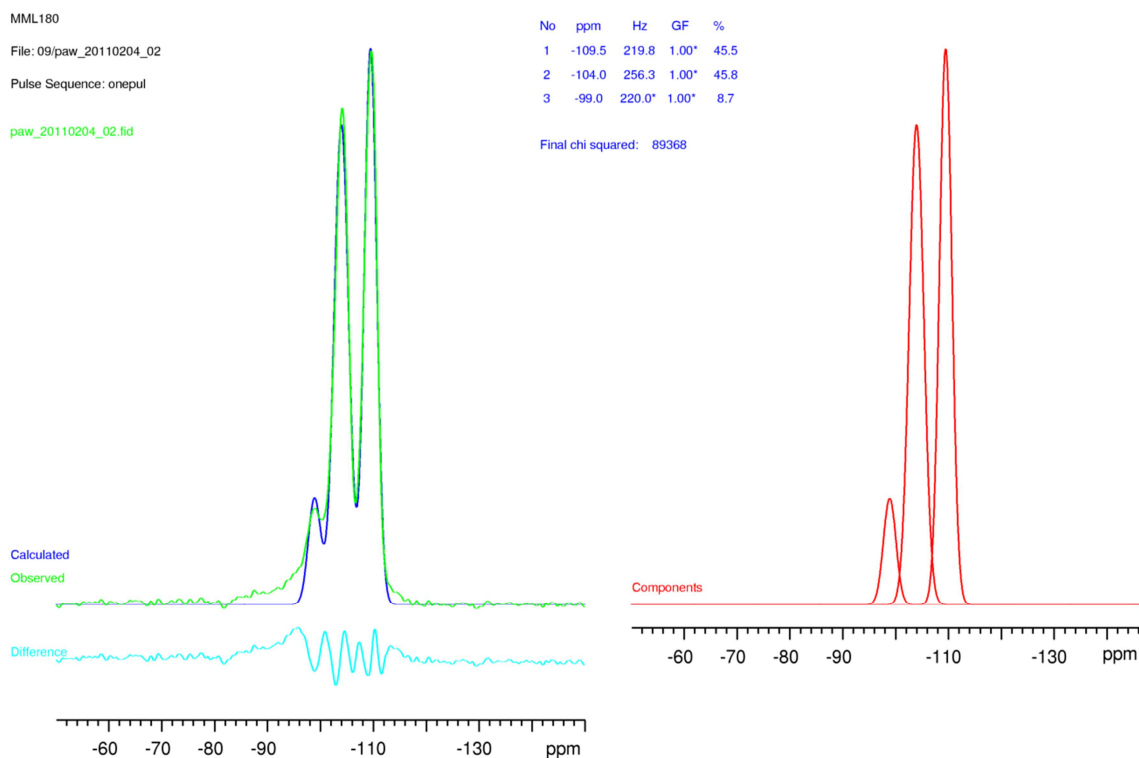


Figure A1.9. Deconvolution of the ^{29}Si MAS NMR spectrum of ST1-H-Rho(743) (ST1-first steaming with low water flow rate).

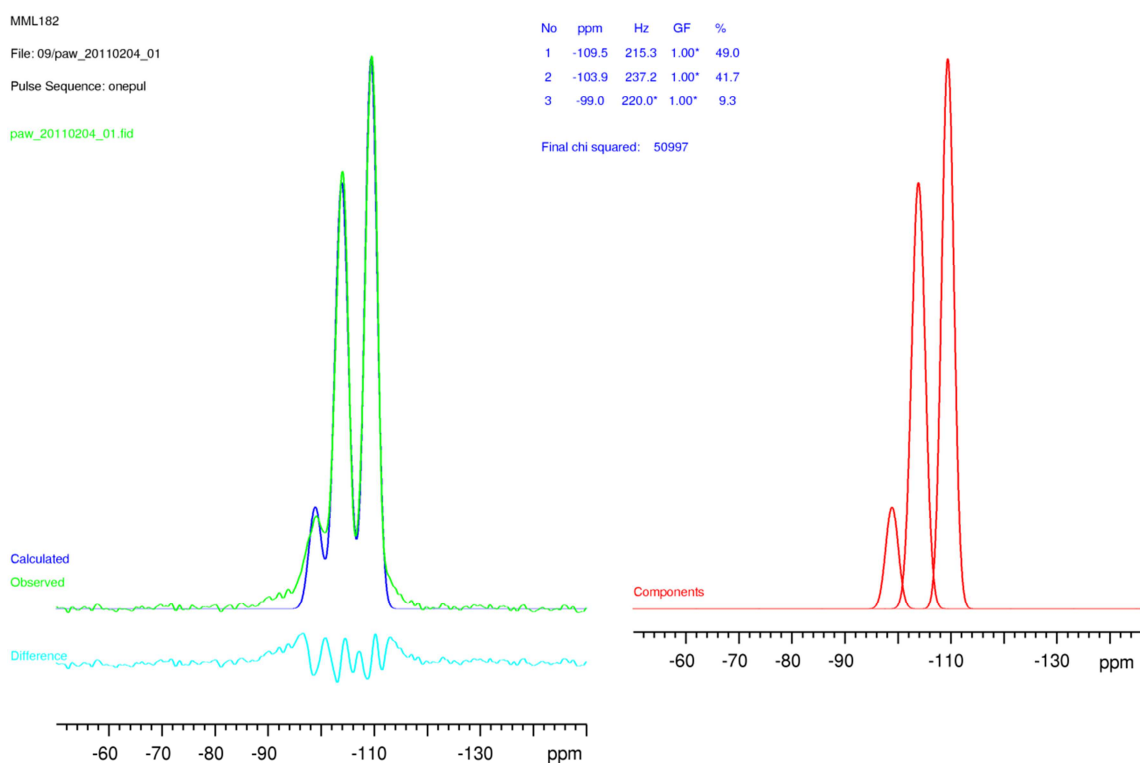


Figure A1.10. Deconvolution of the ^{29}Si MAS NMR spectrum of ST1-H-Rho(773) (ST1-first steaming with low water flow rate).

Appendix

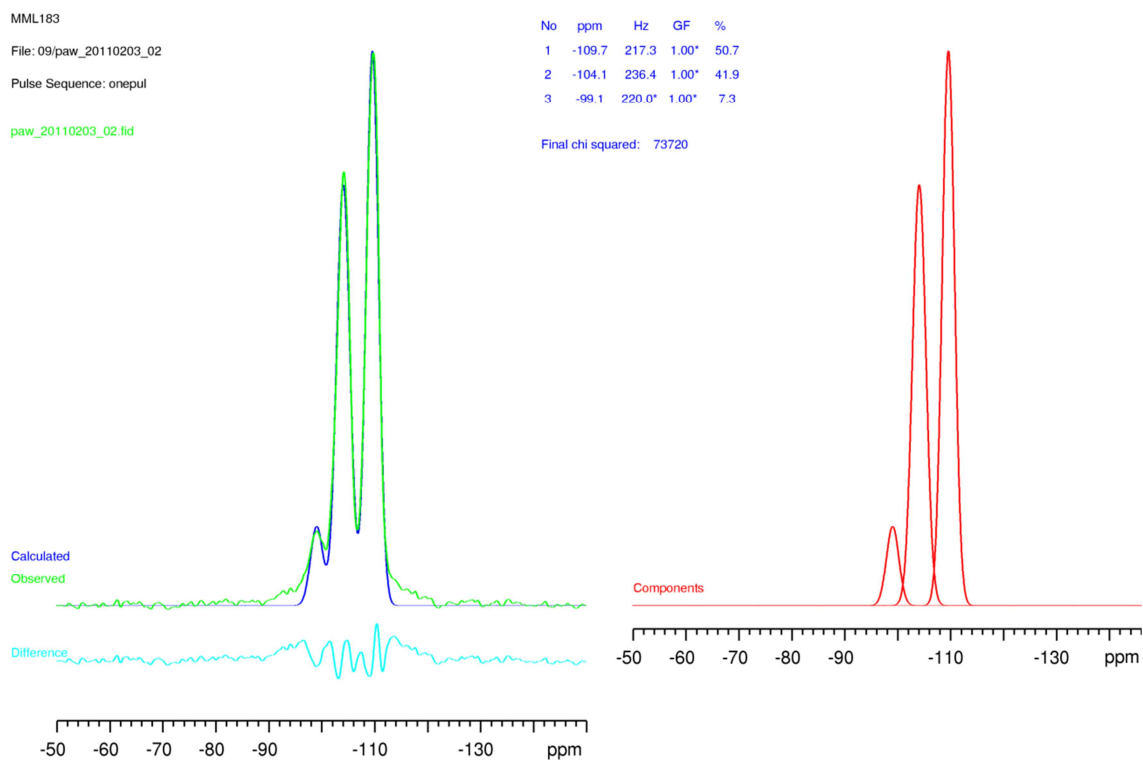


Figure A1.11. Deconvolution of the ^{29}Si MAS NMR spectrum of ST1-H-Rho(823) (ST1-first steaming with low water flow rate).

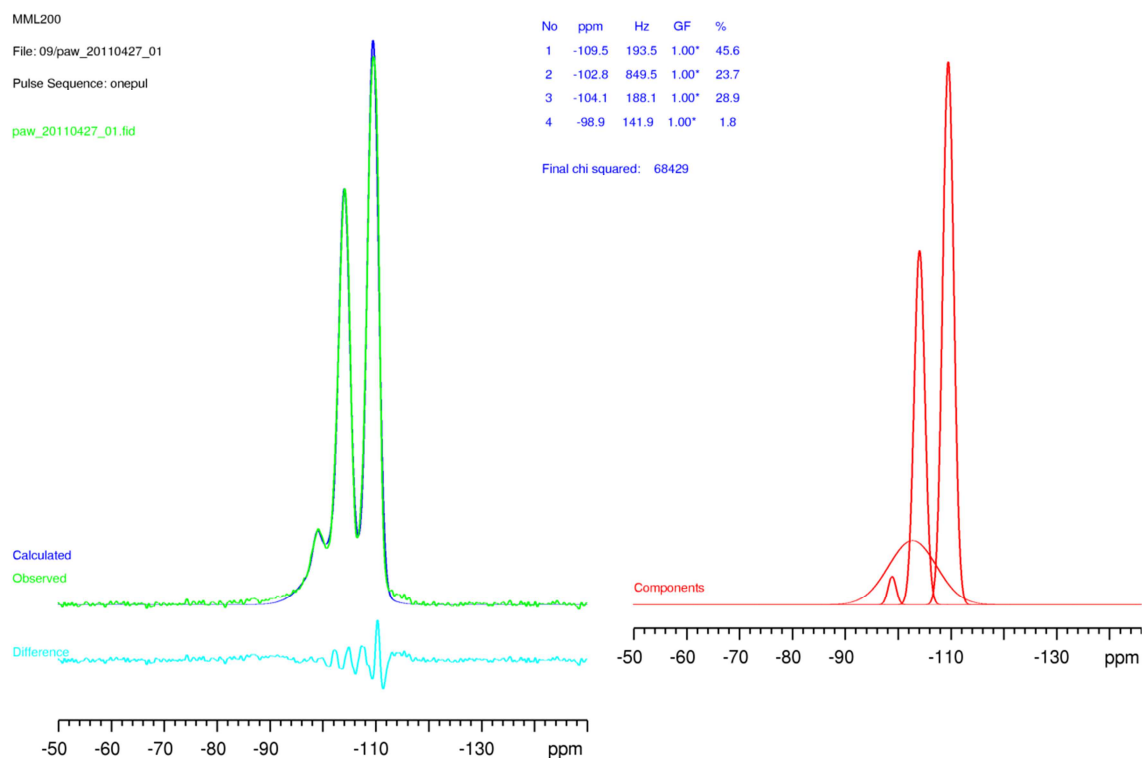


Figure A1.12. Deconvolution of the ^{29}Si MAS NMR spectrum of ST1-H-Rho(743) (ST2-second steaming with low water flow rate).

Appendix

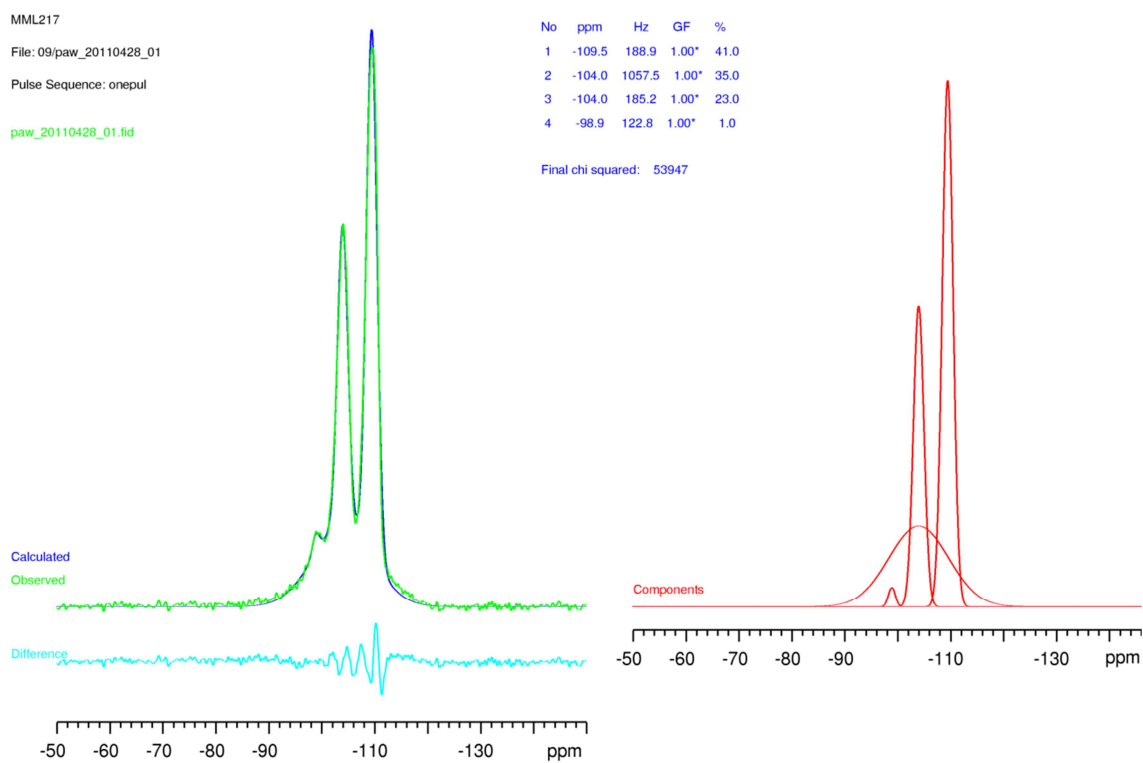


Figure A1.13. Deconvolution of the ^{29}Si MAS NMR spectrum of ST1-H-Rho(773) (ST2-second steaming with low water flow rate).

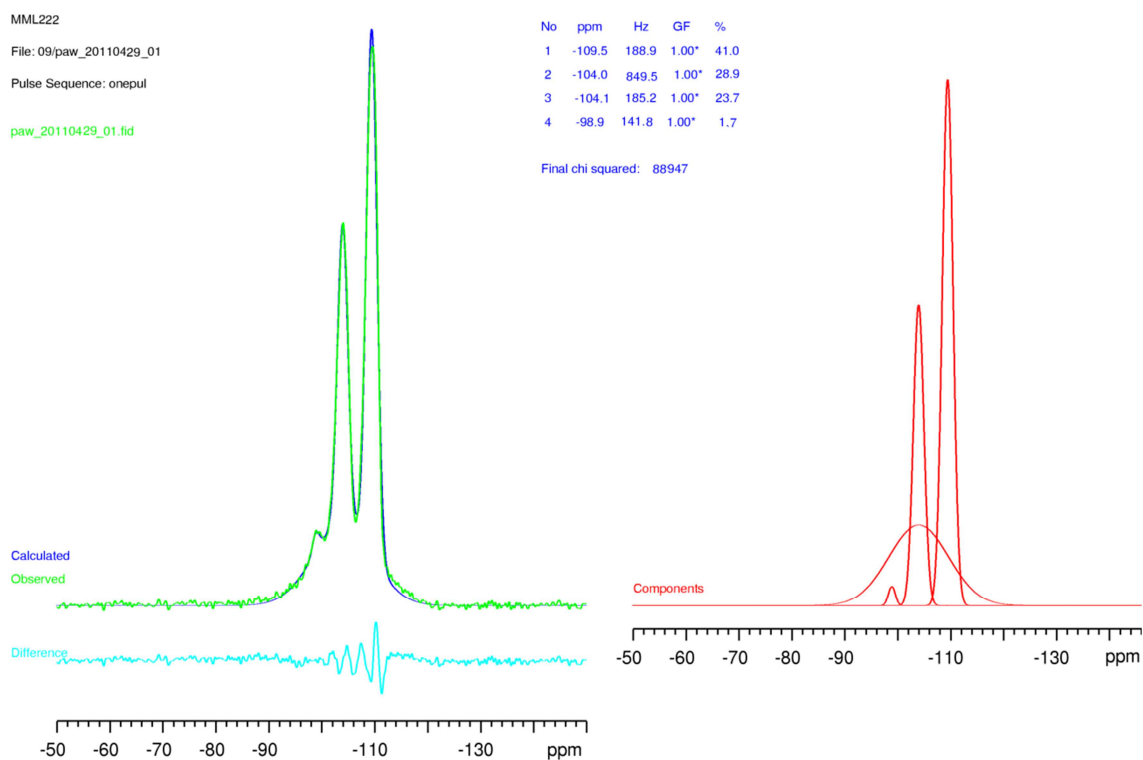


Figure A1.14. Deconvolution of the ^{29}Si MAS NMR spectrum of ST1-H-Rho(823) (ST2-second steaming with low water flow rate).

Appendix

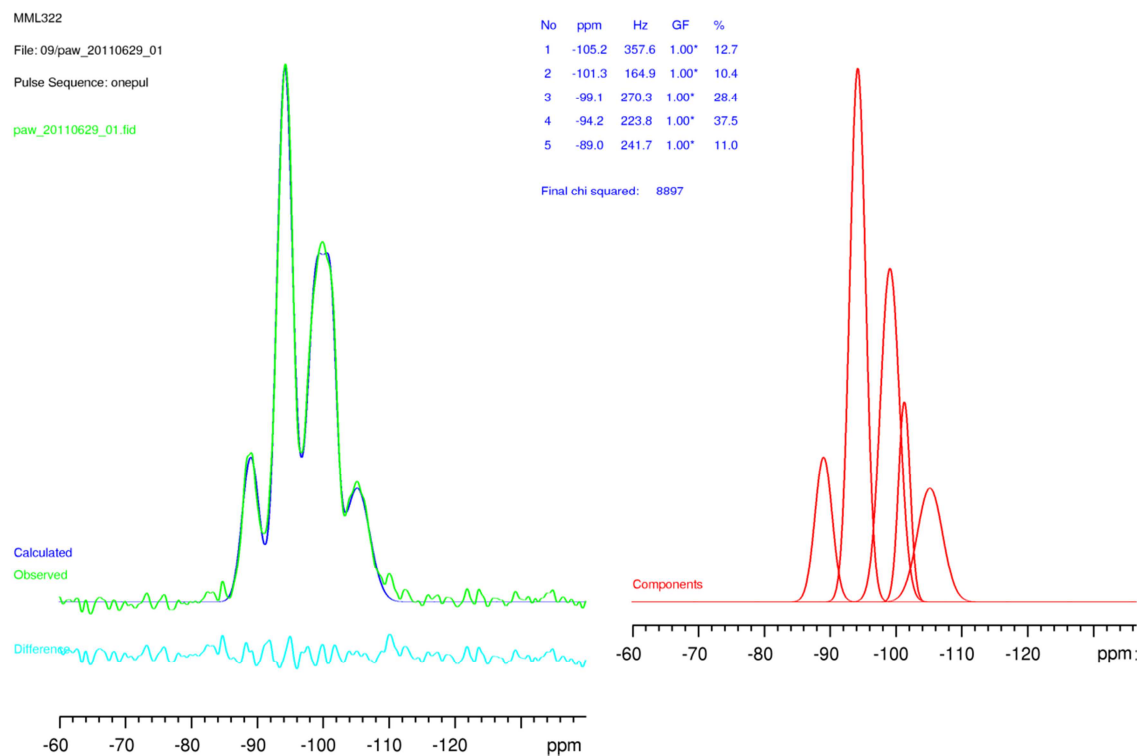


Figure A1.15. Deconvolution of the ^{29}Si MAS NMR spectrum of zeolite H-Y.

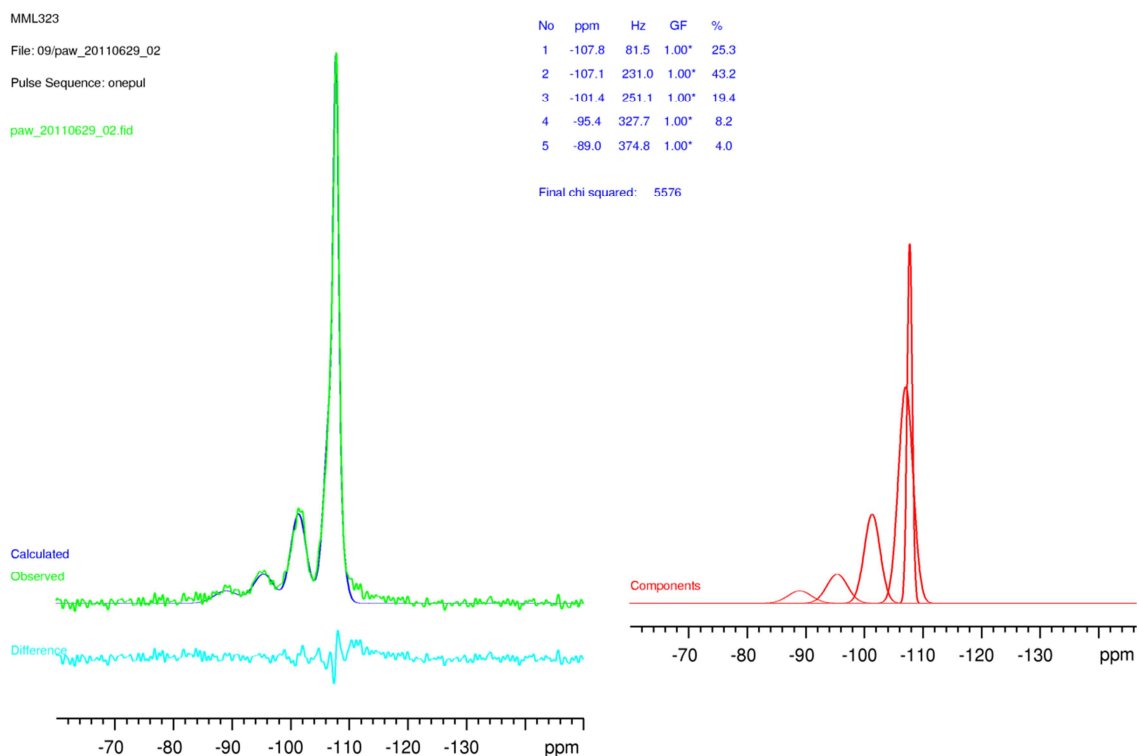


Figure A1.16. Deconvolution of the ^{29}Si MAS NMR spectrum of zeolite US-Y.

A2. Crystallographic details of dehydrated samples

A2.1. Zeolite chabazite (Chapter 5)

	K-chabazite	Li-chabazite	Ca-chabazite	Na,H-chabazite
Unit cell	$K_9Al_9Si_{27}O_{72}$	$Li_{8.5}Na_{0.3}K_{0.2}Al_9Si_{27}O_{72}$	$Ca_{4.4}K_{0.2}Al_9Si_{27}O_{72}$	$Na_{7.8}H_1K_{0.2}Al_9Si_{27}O_{72}$
Temperature/K	298	298	298	298
Space group	$R\bar{3}m$	$R\bar{3}m$	$R\bar{3}m$	$R\bar{3}m$
X-ray source	Cu	Cu	Cu	Cu
Diffractometer	Stoe	Stoe	Stoe	Stoe
Wavelength (Å)	1.54056	1.54056	1.54056	1.54056
a/ Å	13.7285(14)	13.60126(3)	13.6099(7)	13.4427(12)
c/ Å	14.666(5)	15.1909(6)	15.4113(14)	15.5434(19)
Volume/Å³	2393.8(10)	2433.73(15)	2472.20(35)	2432.5(6)
R_p	0.0877	0.0554	0.0414	0.0608
R_{wp}	0.1127	0.0706	0.0555	0.0786
χ²	2.120	6.542	3.504	3.051

	Na-chabazite	Na-chabazite (1 bar)	K-chabazite (1 bar)	K-chabazite (5 bar)
Unit cell	$Na_{8.8}K_{0.2}Al_9Si_{27}O_{72}$	$Na_{8.8}K_{0.2}Al_9Si_{27}O_{72} \cdot xCO_2$	$K_9Al_9Si_{27}O_{72} \cdot 9CO_2$	$K_9Al_9Si_{27}O_{72} \cdot 9CO_2$
Temperature/K	298	298	298	298
Space group	$R\bar{3}m$	$R\bar{3}m$	$R\bar{3}m$	$R\bar{3}m$
X-ray source	Beamline I11	Beamline I11	Cu	Cu
Diffractometer	Synchrotron	Synchrotron	PANalytical	PANalytical
Wavelength (Å)	0.827159(2)	0.827159(2)	1.54056	1.54056
a/ Å	13.5537(9)	13.69108(3)	13.8646(12)	13.8584(14)
c/ Å	15.4529(17)	15.2838(5)	14.6090(25)	14.6747(27)
Volume/Å³	2458.4(5)	2481.06(11)	2432.0(6)	2440.8(7)
R_p	0.0816	0.0669	0.0478	0.0241
R_{wp}	0.1062	0.0851	0.0629	0.0327
χ²	6.202	4.971	2.533	2.234

A2.2. Zeolite ZK-5 (Chapter 6)

	K-ZK-5	Na-ZK-5	Li-ZK-5
Unit cell	$K_{18.8}Al_{18.6}Si_{77.4}O_{192}$	$Na_{16.6}K_2Al_{18.6}Si_{77.4}O_{192}$	$Li_{17.8}K_{0.8}Al_{18.6}Si_{77.4}O_{192}$
Temperature/K	298	298	298
Space group	$Im\bar{3}m$	$Im\bar{3}m$	$Im\bar{3}m$
X-ray source	Cu	Cu	Cu
Diffractometer	Stoe	Stoe	Stoe
Wavelength (Å)	1.54056	1.54056	1.54056
a/ Å	18.6552(5)	18.6142(2)	18.5985(3)
Volume/Å³	6492.3(5)	6449.6(2)	6433.3(3)
R_p	0.607	0.0333	0.0445
R_{wp}	0.0783	0.0475	0.0598
χ²	8.651	2.888	2.512

A2.3. Zeolite Rho and Na-SAPO(RHO) (Chapter 7)

	Na,Cs-Rho	NH₄-Rho	H-Rho	Na-Rho
Unit cell	$Na_{6.8}Cs_{3.0}Al_{9.8}Si_{38.2}O_{96}$	$(NH_4)_{9.8}Al_{9.8}Si_{38.2}O_{96}$	$(AlO_4H_9)_{0.6}H_{9.3-6}Al_{9.3}Si_{38.7}O_{96}$	$Na_{9.8}Al_{9.8}Si_{38.2}O_{96}$
Temperature/K	298	298	298	298
Space group	$I\bar{4}3m$	$I\bar{4}3m$	$Im\bar{3}m$	$I\bar{4}3m$
X-ray source	Cu	Cu	Cu	Cu
Diffractometer	Stoe	Stoe	Stoe	Stoe
Wavelength (Å)	1.54056	1.54056	1.54056	1.54056
a/ Å	14.5307(4)	14.7018(2)	15.0352(2)	14.3771(2)
Volume/Å³	3068.06(24)	3177.72(11)	3398.82(14)	2971.74(9)
R_p	0.0663	0.0451	0.0353	0.0384
R_{wp}	0.0870	0.0587	0.0471	0.0536
χ²	1.141	2.568	1.588	1.944

Appendix

	Cs-Rho	Li-Rho	K-Rho	Ca-Rho
Unit cell	$\text{Cs}_{9.8}\text{Al}_{9.8}\text{Si}_{38.2}\text{O}_{96}$	$\text{Li}_{9.8}\text{Al}_{9.8}\text{Si}_{38.2}\text{O}_{96}$	$\text{K}_{9.8}\text{Al}_{9.8}\text{Si}_{38.2}\text{O}_{96}$	$\text{Ca}_{4.9}\text{Al}_{9.8}\text{Si}_{38.2}\text{O}_{96}$
Temperature/K	298	298	298	298
Space group	$I\bar{4}3m$	$I\bar{4}3m$	$I\bar{4}3m$	$I\bar{4}3m$
X-ray source	Cu	Cu	Cu	Cu
Diffractionmeter	Stoe	Stoe	Stoe	Stoe
Wavelength (Å)	1.54056	1.54056	1.54056	1.54056
a/ Å	14.5947(3)	14.2448(2)	14.5951(2)	14.0462(1)
Volume/Å³	3108.77(21)	2890.48(11)	3109.00(14)	2776.92(11)
R_p	0.0595	0.0415	0.0372	0.0487
R_{wp}	0.0800	0.0560	0.0514	0.0682
χ²	1.494	2.641	1.329	1.889
	Na,H-Rho (50%Na)	Li,H-Rho (50%Li)	Na-Rho	Na-Rho (0.1 bar)
Unit cell	$\text{Na}_{4.5}\text{H}_{5.3}\text{Al}_{9.8}\text{Si}_{38.2}\text{O}_{96}$	$\text{Li}_{5.2}\text{H}_{4.6}\text{Al}_{9.8}\text{Si}_{38.2}\text{O}_{96}$	$\text{Na}_{9.2}\text{Al}_{9.8}\text{Si}_{38.2}\text{O}_{96}$	$\text{Na}_{9.2}\text{Al}_{9.8}\text{Si}_{38.2}\text{O}_{96} \cdot 10.1\text{CO}_2$
Temperature/K	298	298	298	298
Space group	$I\bar{4}3m$	$I\bar{4}3m$	$I\bar{4}3m$	$I\bar{4}3m$
X-ray source	Cu	Cu	Beamline I11	Beamline I11
Diffractionmeter	Stoe	Stoe	Synchrotron	Synchrotron
Wavelength (Å)	1.54056	1.54056	0.827159(2)	0.827159(2)
a/ Å	14.3447(2)	14.4239(5)	14.41336(10)	14.62823(6)
Volume/Å³	2951.72(11)	3000.86(32)	2994.30(6)	3130.23(4)
R_p	0.0330	0.0512	0.0770	0.0559
R_{wp}	0.0447	0.0687	0.1034	0.0715
χ²	2.010	3.969	2.258	6.141
	Na-Rho (0.2 bar)	Na-Rho (0.045 bar)	Na-Rho (evac)	Cs-Rho
Unit cell	$\text{Na}_{9.2}\text{Al}_{9.8}\text{Si}_{38.2}\text{O}_{96} \cdot 10.8\text{CO}_2$	$\text{Na}_{9.2}\text{Al}_{9.8}\text{Si}_{38.2}\text{O}_{96} \cdot 9.8\text{CO}_2$	$\text{Na}_{9.2}\text{Al}_{9.8}\text{Si}_{38.2}\text{O}_{96} \cdot 6.0\text{CO}_2$	$\text{Cs}_{9.8}\text{Al}_{9.8}\text{Si}_{38.2}\text{O}_{96}$
Temperature/K	298	298	298	298
Space group	$I\bar{4}3m$	$I\bar{4}3m$	$I\bar{4}3m$	$I\bar{4}3m$
X-ray source	Beamline I11	Beamline I11	Beamline I11	Cu
Diffractionmeter	Synchrotron	Synchrotron	Synchrotron	PANalytical
Wavelength (Å)	0.827159(2)	0.827159(2)	0.827159(2)	1.54056
a/ Å	14.63480(6)	14.62190(6)	14.56328(12)	14.5817(1)
Volume/Å³	3134.45(4)	3126.164(35)	3088.72(8)	3100.43(17)
R_p	0.0580	0.0549	0.0853	0.0343
R_{wp}	0.0737	0.0689	0.1115	0.0447
χ²	8.292	8.985	6.510	2.619
	Cs-Rho (4 bar)	Na-SAPO(RHO)		
Unit cell	$\text{Cs}_{9.8}\text{Al}_{9.8}\text{Si}_{38.2}\text{O}_{96} \cdot x\text{CO}_2$	$\text{Na}_4\text{Si}_4\text{Al}_{24}\text{P}_{20}\text{O}_{96}$		
Temperature/K	298	298		
Space group	$Im\bar{3}m$	$I23$		
X-ray source	Cu	Cu		
Diffractionmeter		Stoe		
	<i>PANalytical</i>			
Wavelength (Å)	1.54056	1.54056		
a/ Å	14.9991(6)	14.4817(2)		
Volume/Å³	3374.4(4)	3037.09(23)		
R_p	0.0200	0.0455		
R_{wp}	0.0277	0.0624		
χ²	1.811	2.094		

A3. Fractional atomic coordinates, occupancies and isotropic displacement parameters (in Å²) for dehydrated samples

A3.1. Zeolite chabazite (Chapter 5)

K-chabazite	x	y	z	Occup.	Multipl.	Uiso
Si1	0.99961(11)	0.22453(14)	0.10725(12)	0.75	36	0.0236(21)
Al1	0.99961(11)	0.22453(14)	0.10725(12)	0.25	36	0.0236(21)
O1	0.90391(26)	0.09609(26)	0.1276(4)	1.0	18	0.092(4)
O2	0.9763(5)	0.3097(5)	0.1667	1.0	18	0.092(4)
O3	0.12119(20)	0.2423(4)	0.13565(27)	1.0	18	0.092(4)
O4	0.0	0.2523(4)	0.0	1.0	18	0.092(4)
K (S8R)	0.5	0.5	0.0	1.0	9	0.060(5)

Li-chabazite	x	y	z	Occup.	Multipl.	Uiso
Si1	1.00233(22)	0.22659(19)	0.10150(18)	0.75	36	0.0167(6)
Al1	1.00233(22)	0.22659(19)	0.10150(18)	0.25	36	0.0138(6)
O1	0.91493(22)	0.08507(22)	0.1111(5)	1.0	18	0.0075(13)
O2	0.9586(4)	0.2920(4)	0.1667	1.0	18	0.0075(13)
O3	0.12852(24)	0.2569(5)	0.1414(5)	1.0	18	0.0265(13)
O4	0.2654(4)	0.2654(4)	0.0	1.0	18	0.0265(13)
Li(S6R)	0.0	0.0	0.1386(30)	0.790(2)	6	0.068(24)
K (S8R)	0.5	0.5	0.0	0.05(1)	9	0.036(31)

Ca-chabazite	x	y	z	Occup.	Multipl.	Uiso
Si1	0.99936(33)	0.23073(28)	0.10123(28)	0.75	36	0.0286(10)
Al1	0.99936(33)	0.23073(28)	0.10123(28)	0.25	36	0.0286(10)
O1	0.9070(4)	0.0930(4)	0.1050(6)	1.0	18	0.0353(17)
O2	0.9724(7)	0.3058(7)	0.1667	1.0	18	0.0353(17)
O3	0.1209(4)	0.2417(7)	0.1311(7)	1.0	18	0.0353(17)
O4	0.0	0.2738(7)	0.0	1.0	18	0.0353(17)
Ca (D6R)	0.0	0.0	0.0	0.33(3)	3	0.011(11)
Ca (S6R)	0.0	0.0	0.1625(6)	0.59	6	0.006(4)

Na,H-chabazite	x	y	z	Occup.	Multipl.	Uiso
Si1	1.0015(4)	0.23929(30)	0.10514(25)	0.75	36	0.0101(7)
Al1	1.0015(4)	0.23929(30)	0.10514(25)	0.25	36	0.0101(7)
O1	0.8982(4)	0.1018(4)	0.0933(6)	1.0	18	0.0218(18)
O2	0.9913(7)	0.3247(7)	0.1667	1.0	18	0.0218(18)
O3	0.1208(4)	0.2415(9)	0.1105(7)	1.0	18	0.0218(18)
O4	0.0	0.2622(7)	0.0	1.0	18	0.0218(18)
Na (S8R)	0.5	0.5	0.0	0.343(4)	9	0.045(6)
Na (S6R)	0.0	0.0	0.1221(9)	0.8309(7)	6	0.045(6)

Appendix

Na-chabazite	x	y	z	Occup.	Multipl.	Uiso
Si1	1.0053(4)	0.23699(29)	0.10472(24)	0.75	36	0.0328(6)
Al1	1.0053(4)	0.23699(29)	0.10472(24)	0.25	36	0.0328(6)
O1	0.8923(4)	0.1077(4)	0.1131(6)	1.0	18	0.0328(6)
O2	0.9921(6)	0.3255(6)	0.1667	1.0	18	0.0328(6)
O3	0.11817(31)	0.2362(6)	0.1199(5)	1.0	18	0.0328(6)
O4	0.0	0.2785(6)	0.0	1.0	18	0.0328(6)
Na (S6R)	0.0	0.0	-0.1609(10)	0.8108(2)	6	0.0328(6)
Na (S8R)	0.5	0.5	0.0	0.4999(1)	9	0.0328(6)
K (S8R)	0.5	0.5	0.0	0.0255(4)	9	0.0328(6)

Na-chabazite (1 bar)	x	y	z	Occup.	Multipl.	Uiso
Si1	1.00017(21)	0.22912(16)	0.10114(15)	0.75	36	0.0070(4)
Al1	1.00017(21)	0.22912(16)	0.10114(15)	0.25	36	0.0070(4)
O1	0.90424(22)	0.09576(22)	0.1182(4)	1.0	18	0.0070(4)
O2	0.9790(4)	0.3124(4)	0.1667	1.0	18	0.0070(4)
O3	0.12002(20)	0.2399(4)	0.12799(35)	1.0	18	0.0070(4)
O4	0.0	0.2765(4)	0.0	1.0	18	0.0070(4)
Na (S8R)	0.5	0.5	0.0	0.5928(5)	9	0.0070(4)
Na (S6R)	0.0	0.0	-0.1664(10)	0.4886(4)	6	0.0070(4)
K (S8R)	0.5	0.5	0.0	0.025(3)	9	0.0070(4)
C100	0.7909(21)	0.3346(19)	0.7192(9)	0.2257(3)	36	0.0070(4)
O100	0.3678(13)	0.5574(12)	0.2041(7)	0.2257(3)	36	0.0070(4)
O101	0.5138(12)	0.3931(11)	-0.0217(9)	0.2257(3)	36	0.0070(4)
C200	0.0	0.0	-0.2478(17)	0.3756(3)	6	0.0070(4)
O200	0.0	0.0	-0.1757(17)	0.3756(3)	6	0.0070(4)
O201	0.0	0.0	-0.3189(16)	0.3756(3)	6	0.0070(4)
O300	0.4858(11)	0.5142(11)	0.0707(7)	0.2140(9)	18	0.0070(4)
C400	0.5	0.5	0.0	0.2140(9)	9	0.0070(4)

K-chabazite (1bar)	x	y	z	Occup.	Multipl.	Uiso
Si1	1.0015(4)	0.22776(32)	0.10809(27)	0.75	36	0.0268(10)
Al1	1.0015(4)	0.22776(32)	0.10809(27)	0.25	36	0.0268(10)
O1	0.8990(4)	0.1010(4)	0.1336(7)	1.0	18	0.0268(10)
O2	0.9820(6)	0.3155(6)	0.1667	1.0	18	0.0268(10)
O3	0.11565(24)	0.2312(5)	0.1368(5)	1.0	18	0.0268(10)
O4	0.0	0.2437(9)	0.0	1.0	18	0.0268(10)
K (S8R)	0.5	0.5	0.0	0.555(6)	9	0.0268(10)
K (S6R)	0.0	0.0	0.2411(13)	0.666(7)	6	0.0268(10)
C100	0.6880(35)	0.1990(34)	0.756(4)	0.2439	36	0.0268(10)
O100	0.2046(17)	0.5883(26)	0.2184(20)	0.2439	36	0.0268(10)
O200	0.5818(28)	0.4837(30)	-0.0588(21)	0.2439	36	0.0268(10)

K-chabazite (5 bar)	x	y	z	Occup.	Multipl.	Uiso
Si1	1.00232(35)	0.22993(32)	0.10729(26)	0.75	36	0.0239(10)
Al1	1.00232(35)	0.22993(32)	0.10729(26)	0.25	36	0.0239(10)
O1	0.8973(4)	0.1027(4)	0.1316(7)	1.0	18	0.0239(10)
O2	0.9818(6)	0.3153(6)	0.1667	1.0	18	0.0239(10)
O3	0.11382(24)	0.2275(5)	0.1343(5)	1.0	18	0.0239(10)
O4	0.0	0.2477(8)	0.0	1.0	18	0.0239(10)
K (S6R)	0.0	0.0	0.2392(10)	0.8333	6	0.0239(10)
K (S8R)	0.5	0.5	0.0	0.44444	9	0.0239(10)
C100	0.6843(29)	0.190(4)	0.746(4)	0.26157	36	0.0239(10)
O100	0.2031(15)	0.5861(28)	0.2282(16)	0.26157	36	0.0239(10)
O200	0.5749(25)	0.4812(30)	-0.0590(19)	0.26157	36	0.0239(10)

Appendix

A3.2. Zeolite ZK-5 (Chapter 6)

K-ZK-5	x	y	z	Occup.	Multipl.	Uiso
Si1	0.08553(19)	0.20122(25)	0.32019(23)	0.81	96	0.025
Al1	0.08553(19)	0.20122(25)	0.32019(23)	0.19	96	0.025
O1	0.1205(4)	0.1205(4)	0.3092(6)	1.0	48	0.025
O2	0.2496(5)	0.2496(5)	0.4058(4)	1.0	48	0.025
O3	0.0	0.1745(5)	0.3369(5)	1.0	48	0.025
O4	0.25	0.1034(4)	0.3966(4)	1.0	48	0.025
K (S6R)	0.1474(7)	0.1474(7)	0.1474(7)	0.238(7)	12	0.025
K (S8R)	0.0	0.25	0.5	0.853(6)	16	0.025

Na-ZK-5	x	y	z	Occup.	Multipl.	Uiso
Si1	0.08385(8)	0.20394(10)	0.32309(9)	0.81	96	0.0106(7)
Al1	0.08385(8)	0.20394(10)	0.32309(9)	0.19	96	0.0106(7)
O1	0.13190(14)	0.13190(14)	0.31533(25)	1	48	0.0114(8)
O2	0.24823(18)	0.24823(18)	0.39876(21)	1	48	0.0114(8)
O3	0	0.18055(21)	0.32971(21)	1	48	0.0114(8)
O4	0.25	0.10156(15)	0.39844(15)	1	48	0.0114(8)
Na (S8R)	0	0.25	0.5	0.636(5)	16	0.08
Na (S6R)	0.18470(32)	0.18470(32)	0.18470(32)	0.536(4)	12	0.08
K (S8R)	0	0.25	0.5	0.166(1)	12	0.08

Li-ZK-5	x	y	z	Occup.	Multipl.	Uiso
Si1	0.08666(9)	0.20174(10)	0.31858(10)	0.82	96	0.0168(6)
Al1	0.08666(9)	0.20174(10)	0.31858(10)	0.18	96	0.0168(6)
O1	0.12540(15)	0.12540(15)	0.31887(25)	1	48	0.0010(9)
O2	0.25395(16)	0.25395(16)	0.38925(17)	1	48	0.0010(9)
O3	0	0.19453(21)	0.32168(21)	1	48	0.0010(9)
O4	0.25	0.10972(14)	0.39028(14)	1	48	0.0010(9)
Li (S6R)	0.1898(7)	0.1898(7)	0.1898(7)	1	16	0.0013(9)
K (S8R)	0	0.25	0.5	0.089(5)	12	0.0013(9)

A3.3. Zeolite Rho and Na-SAPO(RHO) (Chapter 7)

Na,Cs-Rho	x	y	z	Occup.	Multipl.	Uiso
Si1	0.27074(19)	0.12177(18)	0.42222(19)	0.7583	48	0.0057(5)
Al1	0.27074(19)	0.12177(18)	0.42222(19)	0.2417	48	0.0057(5)
O1	0.03240(18)	0.21390(20)	0.3860(4)	1	48	0.0057(5)
O2	0.21427(28)	0.21427(28)	0.4004(5)	1	24	0.0057(5)
O3	0.13080(31)	0.13080(31)	0.62651(23)	1	24	0.0057(5)
Cs (D8R)	0	0	0.5	0.426(3)	6	0.0410(18)
Na (S8R)	0	0	0.6119(22)	0.252(11)	12	0.0410(18)
Na (S6R)	0.3093(13)	0.3093(13)	0.3093(13)	0.317(18)	8	0.0410(18)

NH₄-Rho	x	y	z	Occup.	Multipl.	Uiso
Si1	0.26669(12)	0.11731(12)	0.41560(11)	0.8	48	0.00781(34)
Al1	0.26669(12)	0.11731(12)	0.41560(11)	0.2	48	0.00781(34)
O1	0.02527(22)	0.20870(18)	0.38617(22)	1	48	0.0113(7)
O2	0.20425(22)	0.20425(22)	0.3930(4)	1	24	0.0113(7)
O3	0.13318(21)	0.13318(21)	0.62312(29)	1	24	0.0113(7)
N (D8R)	0.5	0	0	0.323(6)	6	0.043(5)
N (S8R)	0.3721(8)	0	0	0.677(6)	12	0.043(5)

H-Rho	x	y	z	Occup.	Multipl.	Uiso
Si1	0.25	0.10312(6)	0.39688(6)	0.8	48	0.0133(4)
Al1	0.25	0.10312(6)	0.39688(6)	0.2	48	0.0239(4)
O1	0	0.21903(16)	0.38108(15)	1	48	0.0161(7)
O2	0.16596(11)	0.16596(11)	0.37341(16)	1	48	0.0161(7)

Appendix

Na-Rho	x	y	z	Occup.	Multipl.	Uiso
Si1	0.27362(10)	0.12385(13)	0.42438(11)	0.8	48	0.0113(4)
Al1	0.27362(10)	0.12385(13)	0.42438(11)	0.2	48	0.0113(4)
O1	0.03744(20)	0.21140(18)	0.38652(20)	1	48	0.0054(6)
O2	0.21712(21)	0.21712(21)	0.40581(33)	1	24	0.0054(6)
O3	0.11924(23)	0.11924(23)	0.62544(30)	1	24	0.0054(6)
Na (S8R)	0.3861(6)	0	0	0.541(6)	12	0.08
Na (S6R)	0.3137(5)	0.3137(5)	0.3137(5)	0.389(10)	8	0.08
Cs-Rho	x	y	z	Occup.	Multipl.	Uiso
Si1	0.27143(29)	0.11954(26)	0.42005(26)	0.8	48	0.0054(22)
Al1	0.27143(29)	0.11954(26)	0.42005(26)	0.2	48	0.0054(22)
O1	0.02843(21)	0.21565(27)	0.3867(5)	1	48	0.0110(33)
O2	0.2074(4)	0.2074(4)	0.3976(7)	1	24	0.0110(33)
O3	0.1363(4)	0.1363(4)	0.63070(29)	1	24	0.0110(33)
Cs (D8R)	0	0	0.5	1	6	0.0126(12)
Cs (S6R)	0.18016(28)	0.18016(28)	0.18016(28)	0.424(3)	8	0.0126(12)
Li-Rho	x	y	z	Occup.	Multipl.	Uiso
Si1	0.27832(11)	0.12668(13)	0.42742(13)	0.8	48	0.0148(4)
Al1	0.27832(11)	0.12668(13)	0.42742(13)	0.2	48	0.0148(4)
O1	0.22477(24)	0.22477(24)	0.39901(30)	1	48	0.0144(8)
O2	0.11406(18)	0.11406(18)	0.63046(28)	1	24	0.0144(8)
O3	0.04128(20)	0.21391(18)	0.38431(19)	1	24	0.0144(8)
Li (S6R)	0.2910(11)	0.2910(11)	0.2910(11)	1	8	0.080(14)
K-Rho	x	y	z	Occup.	Multipl.	Uiso
Si1	0.26970(13)	0.11998(15)	0.41845(14)	0.8	48	0.0199(5)
Al1	0.26970(13)	0.11998(15)	0.41845(14)	0.2	48	0.0199(5)
O1	0.21046(26)	0.21046(26)	0.3987(4)	1	48	0.0164(9)
O2	0.13070(24)	0.13070(24)	0.62170(26)	1	24	0.0164(9)
O3	0.03037(20)	0.21158(18)	0.38604(27)	1	24	0.0164(9)
K (D8R)	0.5	0	0	0.343(4)	6	0.1052(30)
K (S8R)	0.3631(5)	0	0	0.571(3)	12	0.1052(30)
Ca-Rho	x	y	z	Occup.	Multipl.	Uiso
Si1	0.27607(30)	0.12874(29)	0.43300(30)	0.8	48	0.0366(8)
Al1	0.27607(30)	0.12874(29)	0.43300(30)	0.2	48	0.0366(8)
O1	0.23174(35)	0.23174(35)	0.4084(5)	1.0	24	0.0339(14)
O2	0.11559(29)	0.11559(29)	0.6174(5)	1.0	24	0.0339(14)
O3	0.0447(7)	0.20424(28)	0.3881(4)	1.0	48	0.0339(14)
Ca (D8R)	0.5	0.0	0.0	0.772(8)	6	0.357(6)
Na-Rho (50%)	x	y	z	Occup.	Multipl.	Uiso
Si1	0.27391(11)	0.12478(13)	0.42537(12)	0.8	48	0.0114(4)
Al1	0.27391(11)	0.12478(13)	0.42537(12)	0.2	48	0.0114(4)
O1	0.03853(22)	0.20883(19)	0.38515(19)	1	48	0.0079(6)
O2	0.21989(22)	0.21989(22)	0.40053(28)	1	24	0.0079(6)
O3	0.11977(17)	0.11977(17)	0.62212(28)	1	24	0.0079(6)
Na (D8R)	0.5	0	0	0.269(6)	6	0.129(9)
Na (S6R)	0.4013(14)	0	0	0.241(3)	12	0.129(9)
Li-Rho (50%)	x	y	z	Occup.	Multipl.	Uiso
Si1	0.27483(17)	0.12429(23)	0.42265(21)	0.8	48	0.0288(7)
Al1	0.27483(17)	0.12429(23)	0.42265(21)	0.2	48	0.0288(7)
O1	0.2150(4)	0.2150(4)	0.3970(4)	1	48	0.0247(12)
O2	0.12144(31)	0.12144(31)	0.6302(4)	1	24	0.0247(12)
O3	0.03462(33)	0.21627(30)	0.38325(29)	1	24	0.0247(12)
Li (S6R)	0.2807(19)	0.2807(19)	0.2807(19)	0.65(3)	8	0.021(21)

Appendix

Na-Rho						
(synchrotron)	x	y	z	Occup.	Multipl.	Uiso
Si1	0.27429(15)	0.12260(18)	0.42518(17)	0.8	48	0.0132(5)
All	0.27429(15)	0.12260(18)	0.42518(17)	0.2	48	0.0132(5)
O1	0.0388(3)	0.2113(2)	0.3868(3)	1	48	0.0045(8)
O2	0.2194(3)	0.2194(3)	0.4039(5)	1	24	0.0045(8)
O3	0.1170(3)	0.1170(3)	0.6275(4)	1	24	0.0045(8)
Na (S8R)	0.3869(9)	0	0	0.5	12	0.0490(5)
Na (S6R)	0.3103(8)	0.3103(8)	0.3103(8)	0.389(8)	8	0.0490(5)

Na-Rho						
(0.1bar)	x	y	z	Occup.	Mult.	Uiso
Si1	0.26879(10)	0.11856(12)	0.41920(11)	0.8	48	0.0064(2)
All	0.26806(10)	0.11889(12)	0.41992(11)	0.2	48	0.0064(2)
O1	0.0302(2)	0.20921(18)	0.38306(24)	1	48	0.0085(5)
O2	0.2092(2)	0.2092(2)	0.3916(3)	1	24	0.0085(5)
O3	0.1276(2)	0.1276(2)	0.6274(3)	1	24	0.0085(5)
Na (S6R)	0.3084(6)	0.3084(6)	0.3084(6)	0.4	8	0.053(3)
Na (S8R)	0.4408(5)	0	0	0.5	12	0.053(3)
OC1	0.3828(7)	0	0	0.5	12	0.053(3)
OC2	0.2306(7)	0	0	0.5	12	0.053(3)
CO1	0.3074(7)	0	0	0.5	12	0.053(3)
OC3	0.3683(7)	0.4863(15)	0.3683(7)	0.171(1)	24	0.053(3)
CO2	0.3489(7)	0.5597(15)	0.3711(18)	0.0855(5)	48	0.053(3)
OC4	0.3206(7)	0.6306(15)	0.3849(18)	0.0855(5)	48	0.053(3)

Na-Rho						
(0.2 bar)	x	y	z	Occup.	Mult.	Uiso
Si1	0.26897(11)	0.11871(13)	0.41890(11)	0.8	48	0.0063(3)
All	0.26897(11)	0.11871(13)	0.41890(11)	0.2	48	0.0063(3)
O1	0.0299(2)	0.2093(2)	0.3831(2)	1	48	0.0097(5)
O2	0.2084(2)	0.2084(2)	0.3912(4)	1	24	0.0097(5)
O3	0.1277(2)	0.1277(2)	0.6272(3)	1	24	0.0097(5)
Na (S6R)	0.3071(6)	0.3071(6)	0.3071(6)	0.4	8	0.047(3)
Na (S8R)	0.4421(5)	0	0	0.5	12	0.047(3)
OC1	0.3817(8)	0	0	0.5	12	0.047(3)
OC2	0.2301(8)	0	0	0.5	12	0.047(3)
CO1	0.3065(8)	0	0	0.5	12	0.047(3)
OC3	0.3682(6)	0.4729(12)	0.3682(6)	0.2011(11)	24	0.047(3)
CO2	0.3488(6)	0.5463(12)	0.3653(17)	0.1005(6)	48	0.047(3)
OC4	0.3205(6)	0.6172(12)	0.3790(17)	0.1005(6)	48	0.047(3)

Na-Rho						
(0.045 bar)	x	y	z	Occup.	Mult.	Uiso
Si1	0.26912(10)	0.11894(12)	0.41927(11)	0.8	48	0.0057(2)
All	0.26912(10)	0.11894(12)	0.41927(11)	0.2	48	0.0057(2)
O1	0.0311(2)	0.2097(2)	0.3821(2)	1	48	0.0083(5)
O2	0.2102(2)	0.2102(2)	0.3939(3)	1	24	0.0083(5)
O3	0.1295(2)	0.1295(2)	0.6246(3)	1	24	0.0083(5)
Na (S6R)	0.3072(6)	0.3072(6)	0.3072(6)	0.4	8	0.068(3)
Na (S8R)	0.4369(5)	0	0	0.5	12	0.068(3)
OC1	0.3963(8)	0	0	0.5	12	0.068(3)
OC2	0.2451(8)	0	0	0.5	12	0.068(3)
CO1	0.3211(8)	0	0	0.5	12	0.068(3)
OC3	0.3697(7)	0.4795(15)	0.3697(7)	0.1589(11)	24	0.068(3)
CO2	0.3503(7)	0.5530(15)	0.3706(19)	0.0795(5)	48	0.068(3)
OC4	0.3220(7)	0.6239(15)	0.3844(19)	0.0795(5)	48	0.0677(25)

Appendix

Na-Rho (evac.)	x	y	z	Occup.	Mult.	Uiso
Si1	0.26950(15)	0.12045(19)	0.42100(18)	0.8	48	0.0031(3)
Al1	0.26950(15)	0.12045(19)	0.42100(18)	0.2	48	0.0031(3)
O1	0.0333(3)	0.2088(3)	0.3799(4)	1	48	0.0062(7)
O2	0.2126(3)	0.2126(3)	0.3962(5)	1	24	0.0062(7)
O3	0.1293(3)	0.1293(3)	0.6223(5)	1	24	0.0062(7)
Na (S6R)	0.3167(10)	0.3167(10)	0.3167(10)	0.4	8	0.078(4)
Na (S8R)	0.4266(10)	0	0	0.5	12	0.078(4)
OC1	0.4059(17)	0	0	0.363(4)	12	0.078(4)
OC2	0.2528(17)	0	0	0.363(4)	12	0.078(4)
CO1	0.3294(17)	0	0	0.363(4)	12	0.078(4)
OC3	0.3837(20)	0.546(5)	0.3837(20)	0.0792(16)	24	0.078(4)
CO2	0.3643(20)	0.619(5)	0.3935(34)	0.0396(8)	48	0.078(4)
OC4	0.3360(20)	0.690(5)	0.4072(34)	0.0396(8)	48	0.078(4)

Cs-Rho (PANalytical)	x	y	z	Occup.	Mult.	Uiso
Si1	0.27067(34)	0.12098(29)	0.42026(30)	0.8	48	0.0088(23)
Al1	0.27067(34)	0.12098(29)	0.42026(30)	0.2	48	0.0088(23)
O1	0.02953(26)	0.21718(35)	0.3845(6)	1.0	48	0.0072(33)
O2	0.2086(5)	0.2086(5)	0.3954(8)	1.0	24	0.0072(33)
O3	0.1353(5)	0.1353(5)	0.6310(4)	1.0	24	0.0072(33)
Cs (D8R)	0.0	0.0	0.5	1.0	6	0.0229(13)
Cs (S6R)	0.17726(31)	0.17726(31)	0.17726(31)	0.423(6)	8	0.0229(13)

Cs-Rho (4 bar)	x	y	z	Occup.	Mult.	Uiso
Si1	0.25	0.10191(27)	0.39809(27)	0.8	48	0.0458(27)
Al1	0.25	0.10191(27)	0.39809(27)	0.2	48	0.0458(27)
O1	0.0	0.2205(5)	0.3827(5)	1.0	48	0.0200(28)
O2	0.1702(4)	0.1702(4)	0.3692(5)	1.0	48	0.0200(28)
Cs (D8R)	0.0	0.0	0.5	0.001(4)	6	0.0312(16)
Cs (S8R)	0.3500(5)	0.3500(5)	0.3500(5)	0.1921(34)	16	0.0312(16)
Cs (S6R)	0.5	0.1499(4)	0.5	0.531(5)	12	0.0312(16)
OC1	0.4075(22)	0.0	0.0	0.431(18)	12	0.010(13)
OC2	0.2480(22)	0.0	0.0	0.431(18)	12	0.010(13)
CO1	0.3278(22)	0.0	0.0	0.431(18)	12	0.010(13)
OC3	0.3844(21)	0.505(9)	0.3844(21)	0.1151(32)	48	0.010(13)
CO2	0.3650(21)	0.578(9)	0.399(6)	0.0575(16)	96	0.010(13)
OC4	0.3367(21)	0.649(9)	0.413(6)	0.0575(16)	96	0.010(13)

Na-SAPO(RHO)	x	y	z	Occup.	Mult.	Uiso
Si1	0.2631(5)	0.4240(4)	0.1253(4)	0.2	24	0.0430(5)
Al1	0.2849(5)	0.1256(4)	0.4261(5)	1.0	24	0.0430(5)
P1	0.2631(5)	0.4240(4)	0.1253(4)	0.8	24	0.0430(5)
O1	0.0414(4)	0.2049(6)	0.3797(9)	1.0	24	0.0294(6)
O2	0.0309(4)	0.3910(10)	0.2253(6)	1.0	24	0.0294(6)
O3	0.2192(5)	0.2144(5)	0.3914(6)	1.0	24	0.0294(6)
O4	0.1353(5)	0.1168(6)	0.6153(5)	1.0	24	0.0294(6)
Na (S8R)	0.3838(24)	0.0	0.0	0.324(12)	12	0.2321(3)